A Tri-Axial Electromagnetic Induction Tool for Hydraulic Fracture Diagnostics

Final Scientific Report

Reporting Period Start Date October 1, 2014
Reporting Period End Date September 30, 2018

Principal Author(s):
Mukul M. Sharma
Javid Shiriyev
Peng Zhang
Dave Glowka
Jeff Gabelmann
Robert Houston

December 2018

DOE Award Number: DE-FE0024271

Prime Contract:

The University of Texas at Austin
PI: Mukul M. Sharma, Professor
200 E. Dean Keeton St. Stop C0300
Austin, Texas 78712

(512) 471-3257
msharma@mail.utexas.edu

Subcontractor:

E-Spectrum Technologies, Inc.
PI: Robert Houston
12725 Spectrum Technologies
San Antonio, TX 78249

(844) 693-8665
rhouston@espectech.com

Disclaimer

Acknowledgement

Sections of this report contain figures and text that have been published in PhD dissertations by Dr. Javid Shiriyev and Dr. Peng Zhang as well as in the following published papers:

Shiriyev, J., Y. Brick, P. Zhang, A. E. Yilmaz, C. Torres-Verdin, M. M. Sharma, T. Hosbach, M. A. Oerkfitz, and J. Gabelmann, "Experiments and Simulations of a Prototype Tri-Axial Electromagnetic Induction Logging Tool for Open-Hole Hydraulic Fracture Diagnostics", Geophysics, vol. 83, issue 3, pp. D73-D81, 05/2018.

Zhang, P., J. Shiriyev, C. Torres-Verdin, M. M. Sharma, Y. Brick, J. Massey, and A. E. Yilmaz, "Fracture Diagnostics Using a Low Frequency Electromagnetic Induction Method", 50th US Rock Mechanics / Geomechanics Symposium, Houston, Texas, U.S.A. June 26-29, 2016, American Rock Mechanics Association, 06/2016.

Contributions made by all authors and co-authors of these papers is duly acknowledged. Some figures and text in this report are from these publications.

Abstract

The monitoring and diagnostics of induced fractures are important for the real-time performance evaluation of hydraulic fracturing operations. Previous electromagnetic (EM) based studies show that single backbone tri-axial induction logging tools are promising candidates for real-time monitoring and diagnosis of fractures in open-hole wells. To support the development of field deployable tools, the concept must be tested in experiments, in a controllable environment, before it is tested under field-like conditions. To this end, we have developed numerical tools which can simulate any wellbore environment while logging hydraulic fractures with the induction tool. We have designed and built a prototype induction tool and performed two sets of tests to compare with numerical simulation results. The computational and experimental setup consists of tri-axial transmitter- and receiver-coils in co-axial, co-planar and cross-polarized configurations. Both lab and shallow earth measurements are shown to be in good agreement with simulations for all examined cases. The average relative and maximum discrepancies of the measured signals from the simulated ones were lower than 3% and 10%, respectively. With the prototype tool, strong signals sensitive to the fracture's surface area and dip-angle were measured in co-axial coil configuration, while weaker signals sensitive to the fracture's aspect ratio were observed in the co-planar configuration. Cross-polarized signals are also shown to be strong and sensitive to the fracture's dip. Lastly, we resolved the detectable components of the signal tensor to obtain parameters of simplified fracture geometries. The inversion algorithm, a derivative free directional search model, uses an objective function defined as a combination of co-axial and cross-polarized signals from different tool spacings to provide a well behaved global minimum. The robustness of inversion algorithm is tested on synthetic data for single cluster fractures in homogeneous and heterogeneous background electrical conductivity. All the effective model parameters for different cases, fracture conductivity (width), propped area (length) and dip-angle, are shown to be recovered with sufficient accuracy. We also evaluated the effect of multiple neighboring fractures and suggested a multi-cluster inversion algorithm that can accurately recover the proppant distribution in each fracture. Based on these results we provide a downhole tool design, with detailed specifications, that can effectively recover far-field proppant distribution in hydraulic fractures.

Table of Contents

Executive Summary

A new downhole fracture diagnostic prototype tool that maps electrically conductive proppant has been designed, built and tested. In addition, numerical models have been formulated to simulate the tool so that the downhole measurements can be inverted to obtain the propped fracture length, height and orientation.

The electrical resistivity of a candidate proppant, calcined petroleum coke (CPC), was measured for a range of stresses, particle sizes and mixtures with sand. The results show that the effective resistivity of the proppant decreases as the confining stress increases, due to the better contact between the CPC particles under higher stress. Pure CPC shows an electrical resistivity of around $2 \times 10^{-4}\ \Omega \cdot m$ when the confining stress is above 3000 psi. This is approximately 10,000 times larger than the conductivity of the shale. Particle size does not play a noticeable role in the measured results. The effective resistivity increases with an increasing weight percentage of sand when sand is mixed with CPC. The electrical resistivity stays reasonably low ($\sim 6 \times 10^{-4}\ \Omega \cdot m$) when up to 50% sand is added.

Fracture hydraulic conductivity measurements on CPC show that when sand is added, the measured fracture conductivity increases because of the higher mechanical strength of sand. Even when using pure CPC, the measured fracture conductivity is above $4\ \mathrm{md \cdot ft}$ under a confining stress of 6000 psi, which means that the fracture is infinitely conductive for a typical field-scale fracture.

The extremely high electrical conductivity of the CPC coupled with good hydraulic conductivity at stress, its ready availability in large quantities and its relatively low cost make it an excellent candidate for use as a diagnostic proppant.

Two numerical schemes are implemented to solve Maxwell's equations in 3-D for fracture geometries of interest. The method of moment solution of surface integral equations provides very accurate results with a node spacing less than ten. A typical run takes about one minute when a single core is used for the computation. The fracture is simulated as a low impedance sheet. Variations in permittivity and conductivity for more complex fracture geometries can also be handled using this simulation. Since it is fast and includes all relevant fracture parameters, it is better suited for use with the inversion analysis. The axial hybrid method can easily handle heterogeneous background formation conductivity and production casing. A typical run can be conducted with a few hundred basis functions and the total run-time is a few seconds. The numerical results are validated and the computational requirements for a typical fracture simulation are reported. The scattered fracture signals at 10^5 S/m casing conductivity and 30 relative magnetic permeability is tiny compared to the scattered casing signals making it very challenging to detect fractures in cased-hole applications when using induction tools.

A prototype fracture diagnostics tool, consisting of co-axial, co-planar, and cross-polarized configurations of transmitter and receiver coils operated at 1 kHz, was designed and built. Initial tests were conducted to confirm the component properties and detectability range. Then, the prototype tool was tested in-air using a specially designed experimental setup with scaled targets that emulate propped hydraulic fractures. Tests were also conducted with the target buried underground in a near-surface trench. The measured results for both in-air and near-surface tests were in excellent agreement with those simulated by the integral equation-based numerical model (average relative differences of less than 3% with a maximum difference of 10%). This agreement

increases the confidence in the results of existing numerical studies which also cover conditions beyond those considered in the experiments. The high signal to noise ratios (over 100) of the measured signals indicate that the new EM induction tool can be used to extract the propped length (or area), orientation and width of propped hydraulic fractures in open-hole applications.

Each pair of transmitters and receivers exhibits sensitivity to different properties of conductive fractures. The co-axial coil configuration signals are strong (>100 μV) and highly sensitive to the fracture's surface area (or length). A combination of signals from the co-axial and cross-polarized configurations (both >100 μV) can enable estimation of the fracture's dip-angle. The co-planar configuration signals, however, are of relatively lower magnitude (only >10 μV) and, while theoretically are sensitive to the fractures' aspect ratios, might be too low to be sensed in a realistically noisy environment. While the design of (x, y)-oriented transmitter coils that can deliver greater power is challenging, due to geometrical constraints and heating considerations, improved sensitivity to the aspect ratio may be obtained by modifying the tool's design and operating mode.

A hybrid stochastic inversion algorithm was developed to process tri-axial induction data to estimate the geometry and conductivity of hydraulic fractures. It is shown that this inversion analysis can successfully provide good estimates of fracture length, conductivity and dip-angle. The approximation based linear regression is also shown to be a very efficient inversion technique for single orthogonal fractures. When neighboring fractures are considered in the inversion, the hybrid inversion model provides excellent results. In all cases, good agreement is obtained between the true and estimated fracture parameters suggesting that a tri-axial EM tool has excellent potential to map the proppant distribution in hydraulic fractures. The following conclusions are obtained from this inversion study:

- By using a mono-axial transmitter coil and tri-axial receiver coils, it is possible to recover the effective properties of hydraulic fractures; two coil configurations (co-axial and cross-polarized) and two coil spacings (short and long) are essential to provide a complete description of fracture geometries and conductivities.
- For fractures that are assumed to be circular, parameters such as fracture conductivity and radius were shown to be recovered very accurately. For fractures that are assumed to be elliptical, we recover the effective radius for a circle which has the same area as the ellipse. When the proppant concentration varies radially in a fracture, the inverted conductivity value is approximately equal to the average conductivity of the fracture. In all these cases, the calculated dip-angle is always close to the true value. We demonstrated the potential of the induction tool for monitoring proppant settling in the fracture.
- For heterogeneous rocks, an accurate estimate of fracture parameters is obtained only after the subtraction of the differential signals with and without a hydraulic fracture. This highlights the importance of logging the well before and after fracturing operations.
- To invert the results for multiple fractures in a time efficient manner, five fractures should be included in each forward model run. This approach is shown to provide a very accurate estimation of fracture parameters in a given stage.

Chapter 1: Introduction

While traditional hydrocarbon recovery techniques are not applicable in shales because of their very small matrix permeability, a recent combination of hydraulic fracturing treatments with horizontal drilling has led to a breakthrough in hydrocarbon production. To evaluate the outcomes and performance of such hydraulic fracturing treatments, induced propped fractures must be monitored, appraised and quantified. Indeed, unpropped portions of induced fractures can close under high net stress shortly after fracing and flowback and may not contribute to well productivity (Sharma and Manchanda, 2015). It is, therefore, important to determine the spatial distribution of proppants for successful fracture diagnostics.

1.1. Fracture Diagnostic Methods Explored In The Industry

Conventional fracture diagnostic techniques are based on sensing physical events that occur during fracture growth or fluid propagation. There are a few categories of fracture diagnostic methods applied or currently being explored in the industry. They are summarized in the following sub-sections of this chapter.

1.1.1. Tiltmeters

Tiltmeters are one of the earlier diagnostic methods that have been used for fracture mapping. The method is based on a simple principle: a created fracture induces deformation in the surrounding rock, which can be detected either on the surface or downhole (Fig. 1.1) (Warpinski and Branagan, 1989).

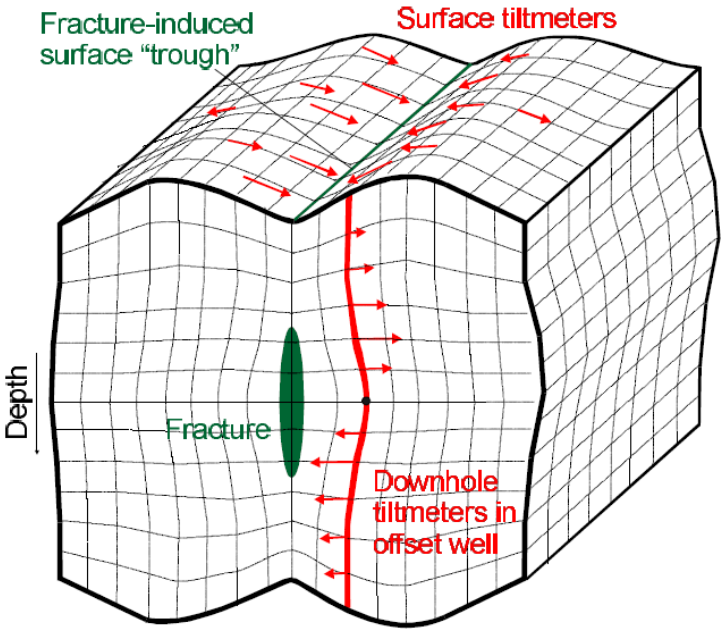

Figure 1.1: Principle of tiltmeter fracture mapping (From Cipolla and Wright, 2000)

An array of surface tiltmeters measures the tilt of the earth at several locations, from which the fracture azimuth can be obtained. However, surface tiltmeters cannot accurately measure fracture length and height, because they are typically very far from the created fractures deep under the ground (Cipolla and Wright, 2000; Warpinski, 1996). Downhole tiltmeters are placed in one or a few monitor wells next to the treatment well. They are near the depth of the fracture so the deformation in the proximity of the fracture can be captured. Although downhole tiltmeters are significantly more sensitive to fracture dimensions than surface tiltmeters (Wright et al, 1998a, 1998b), they are more difficult to implement in the field (limited location of observation wells) and provide no direct information about proppant distribution. Hence, while they may provide some information about the orientation of created hydraulic fractures, they are seldom used to infer propped fracture geometries.

1.1.2. Tracers

Another category of diagnostic methods in the petroleum industry relies on proppant tracers or fluid tracers that can be dissolved in water or hydrocarbons. They are typically pumped into the well with the fracturing fluids, and then detected based on various mechanisms depending on the unique properties of the tracer.

Radioactive tracers, which are usually coated on the proppant or sometimes dissolved in the fracturing fluids, emit gammy rays that can be detected by radiation sensors. However, this method fails to provide fracture information at distances more than a few inches from the wellbore (Gore and Terry, 1956; Scott et al., 2010; Warpinski 1996). These radioactive tracers also involve environmental and safety concerns for operators. An alternate non-radioactive ceramic proppant that contains a high thermal neutron capture compound has proven effective in evaluating fracture height (Grae et al., 2012; Saldungaray et al., 2012; Duenckel et al., 2011). Unfortunately, this method also focuses on near-wellbore proppant detection, due to the small depth of investigation of neutron logs.

Chemical tracers carried by the fracturing fluids can potentially overcome the limitation of radioactive tracers and allow far-field fracture detection. These chemical tracers travel deep into the reservoir with the fluids during pumping. The recorded tracer concentrations during flowback and historical production data can reveal important information about the effectiveness of different fracture stages. However, the complexity in the fracture and reservoir geometry, coupled with data limitations, complicates the estimation of these properties (Elahi and Jafarpour, 2018). Due to the non-uniqueness of the results, they offer a more qualitative than quantitative characterization of the proppant distribution. Nonetheless, analysis of tracer returns provides a clear indication of which fracture stages hydrocarbon is being produced from. This technology can also be used to determine hydrocarbon cross flow between wells due to hydraulic communication (Catlett et al., 2013; Mayerhofer et al., 2011).

1.1.3. Pressure Monitoring

Pressure data from surface or downhole gauges are often available in a hydraulic fracture treatment. Pressure monitoring is recognized as a low-cost fracture diagnostic method without particular requirements for the fracturing fluid or proppant properties and downhole instrumentation.

There are different ways of utilizing the pressure data to diagnose fractures. For example, poroelastic effects can result in pressure increases in wells with fractures next to a stimulated well. These pressure signals acquired in one or multiple monitor wells on the same pad can be used to determine the geometry of induced fractures as well as their orientation (Kampfer and Dawson, 2016). This pressure interference method requires that the horizontal wells be in reasonable proximity both in the vertical and lateral directions. Limited natural fractures and faults are also desired for the successful implementation of this approach (Dawson and Kampfer, 2016).

Pump shutdown or valve closure at the conclusion of a hydraulic fracture treatment generates a series of pressure pulses, known as a water hammer. The different water hammer signature properties (Fig. 1.2) can be used to describe the fracture connection to the wellbore (Iriarte et al., 2017). History matching of field data with simulations reveals that the water hammer signature can be correlated to fracture spacing, length and stimulated reservoir volume (Carey et al., 2015, 2016).

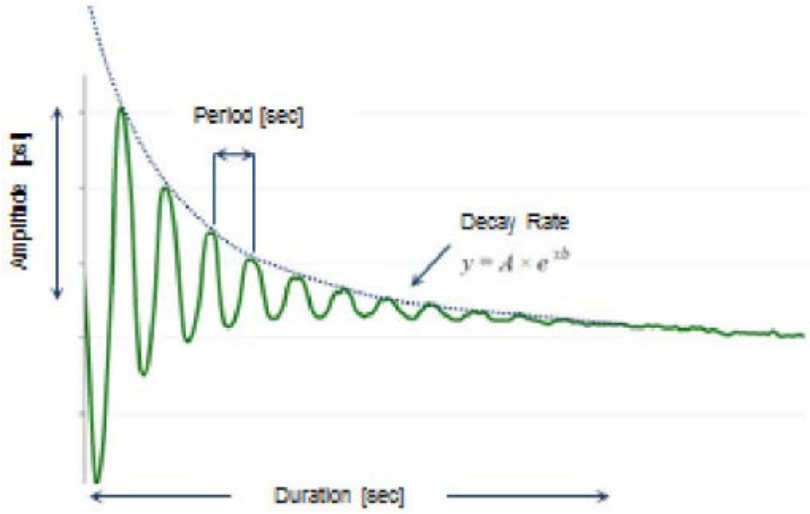

Figure 1.2: Water hammer signature properties: amplitude, period, decay rate and duration. (From Iriarte et al., 2017)

Pressure monitoring does not impact completion efficiency, which makes it easy to implement and advantageous in terms of costs. However, these methods rely on limited surface or downhole pressure measurements which make the extraction of fracture geometry very challenging. The solutions are often non-unique and they provide very limited insight into proppant distribution in the fracture.

1.1.4. Borehole microseismic

Fracture propagation results in micro-earthquakes or microseisms, which can be detected by receivers in an adjacent monitor well or on the surface (Fig. 1.3). The locations of the microseisms are obtained from inversion by using an appropriate velocity model. With more than twenty years of development, borehole microseismic monitoring can efficiently provide extensive information on induced fracture geometry. Sophisticated data processing techniques can even provide real-time microseismic monitoring of hydraulic fracture treatments (Le Calvez et al.,

2007). This method has been the primary SRV identification technique and has been proved to be an effective tool for improving completion and reservoir management (Mayerhofer et al., 2010).

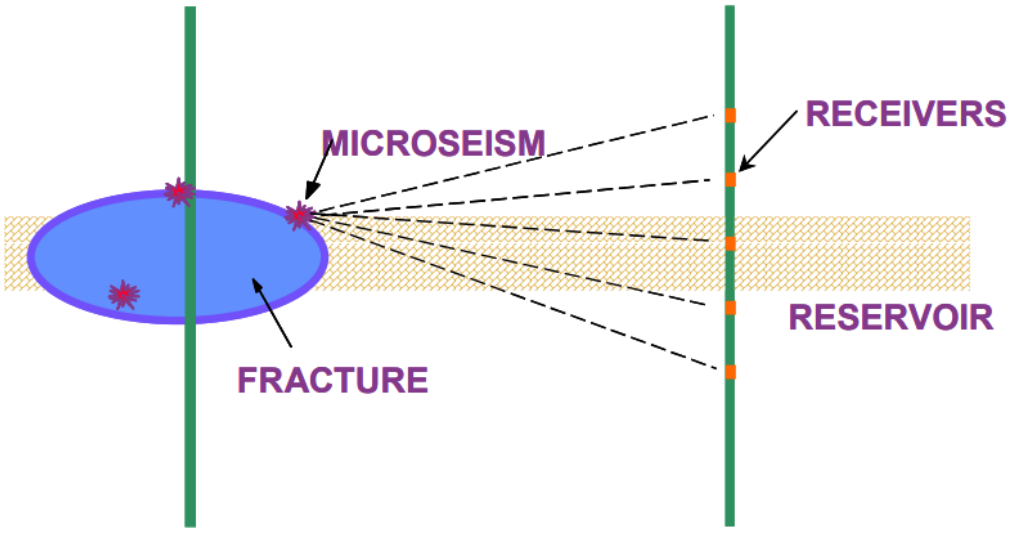

Figure 1.3: Borehole microseismic for fracture detection. (From Fisher et al., 2002)

Even so, microseismic measurements only capture a portion of the rock failure events and the results can be easily biased by adopting inaccurate velocity models. Moreover, this technique only focuses on seismic events associated with shear failure (Eisner et al., 2006; Warpinski and Du, 2010), without accounting for the dilation of the propped fracture and the fluid and proppant transport in it. Therefore, this technique provides very limited insight into the propped fracture geometry, which is the main factor controlling the effectiveness of a hydraulic fracturing treatment.

1.1.5. Fiber optics

More recent fiber optic based measurements (Sierra et al., 2008; Bhatnagar, 2016; Zhang and Zhu, 2017; Sookprasong et al., 2014) provide data that can be qualitatively interpreted to obtain the efficiency of proppant placement in different perforation clusters. In some studies, the data are also integrated with borehole microseismic monitoring to understand the fracture geometry (Webster et al., 2013; Haustveit et al., 2017). Fiber optics has the advantage of providing continuous wellbore monitoring capabilities during fluid injection, shut-in and production phases of fracturing operations and full-length wellbore characteristics are transmitted to the surface in real-time. However, it requires installation of expensive fiber on the outside of the casing, a process which can interfere with routine field operations. The single fiber optic cable temporarily/permanently installed in the well provides important diagnostic measurements (Fig. 1.4) such as temperature (DTS), acoustic (DAS), strain (DSS), etc. (Smolen and Spek, 2003).

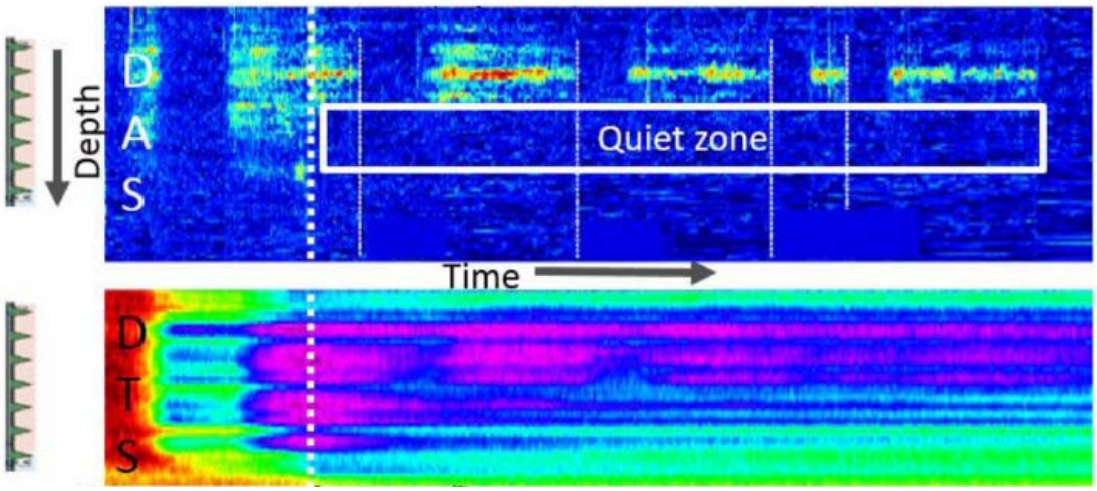

Figure 1.4: DAS and DTS results showing the lack of fluid and proppant entering the toe-side clusters (quite zone). (From Haustveit et al., 2017)

Monitoring with only DTS lacks the same correlation with proppant location, and in some applications, DAS/DTS data have been used to infer dominant perforation clusters that are taking most of the fracturing fluid and proppant (Sookprasong et al., 2014; Wheaton et al., 2016). Such measurements have been used to avoid frack-hits while fracturing and to determine and eliminate dominant clusters. DAS measurements have shown that fractures are heel dominated and that special steps may need to be taken to optimize the number of clusters per stage, spacing between clusters/stages and fracturing fluid injection rate to avoid non-uniform fluid/proppant distribution (Ugueto et al., 2016; Wu et al., 2017b).

1.2. Low Frequency Electromagnetic Induction Tool

So far we have reviewed a few categories of fracture diagnostic methods, and described the physics behind them. Unfortunately, none of these methods can track proppant distribution or map propped fracture geometry directly. A more promising alternative for proppant detection is to use techniques that rely on sensing electromagnetic (EM) fields scattered due to the contrast in EM material properties between propped fractures and the surrounding formation. Although the contrast in EM properties can be enhanced by increasing the proppant's electrical conductivity, magnetic permeability, electrical permittivity, or a combination of them (Heagy and Oldenburg, 2013), enhancing the conductivity contrast generally enables better detectability compared to the other alternatives (LaBrecque et al., 2016) and is more practical. In fact, numerous proppant types have been reported to exhibit large effective electrical conductivities (LaBrecque et al., 2016; Palisch et al., 2016; Zhang et al., 2016; Hoversten et al., 2015).

A variety of field data acquisition techniques can be implemented to sense the EM fields scattered from proppants that display a large electrical conductivity contrast over the background shale. One acquisition technique, employed in LaBrecque et al. (2016), Palisch et al. (2016), and Hibbs (2014), is to use receiver arrays densely deployed on the surface to sense the response to an electric current emitted into the subsurface by electrodes. While the spatially dense surface

receiver array allows for relatively extensive coverage of the stimulated area, this transmitter-receiver coupling is inherently depth limited. As the source-observer distance increases, EM fields are significantly attenuated by the overburden layers greatly obfuscating the signals of interest.

This limitation can be considerably mitigated by utilizing source/observers in the vicinity of propped hydraulic fractures. The electrically conductive proppant can then be mapped using a single-backbone, electromagnetic induction tool (Salies, 2012; Basu, 2014). This has the potential to offer a cheap (Gul and Aslanoglu, 2018) far-field proppant detection technique that can be executed from a single wellbore at any time during the well's life cycle. The method can provide a time-lapse analysis of fracture growth or closure which can decrease the uncertainties in reservoir parameters critical for long-term production forecasting (Balan et al., 2017) where data-driven analyses are not available (Eftekhari et al., 2018). Furthermore, the application of such measurements in the field can be incorporated with complex-fracture proppant transport models (Shrivastava and Sharma, 2018) to improve their reliability.

In Pardo and Torres-Verdin (2013), Basu and Sharma (2014), Yang et al. (2015), and Zhang et al. (2016) such a low-frequency induction tool, where both sources and observers (tri-axial induction coils) are placed on the same backbone, were numerically studied and found to be sensitive to various propped fracture properties in open-hole hole completion wells. These findings were corroborated by independent laboratory experiments in Yu et al. (2016) that used a scaled-down co-axial induction tool and scaled-up electrical conductivities to evaluate orthogonal fractures. According to numerical forward studies and parametric inversion analyses with synthetic data (Yang et al., 2015/2016), different transmitter/receiver coil configurations are sensitive to different propped fracture properties (area, shape and dip) and the best response occurs when the primary magnetic field is perpendicular to the plane of the target (Swift, 1988). In this report, we present results for an induction tool that we have developed and invert the data with fast and robust numerical forward and inversion models to obtain the propped fracture geometry. A complete set of validation experiments with a prototype tool are presented.

The low-frequency induction logging tool developed here (Fig. 1.1) is based on theoretical models presented by Salies (2012), Pardo and Torres-Verdin (2013), Basu and Sharma (2014), Yang et al. (2015), and Zhang et al. (2016). It includes a tri-axial transmitter (Tx) coil that generates EM fields and a tri-axial receiver coil set composed of two coils, Rx_1 and Rx_2, measuring the EM response of the surrounding formation to those fields (Dusterhoft et al., 1961). The measured total voltage on each of the receiver coils can be described as the superposition of two contributions: (i) a primary contribution corresponding to the fields in the shale formation in the absence of induced fractures and (ii) a secondary contribution that can be associated with fields arising due to the presence of a fracture filled with an electrically conductive proppant.

To formulate the tool's response, we denote $\mathbf{H}_v^{\{\mathrm{p,s,t}\}}(\mathbf{r})$ the {primary, secondary, total} magnetic field at point $\mathbf{r}$, excited by a transmitter coil oriented in the $v \in \{x, y, z\}$ direction. We follow the $\mathrm{e}^{j\omega t}$ time convention used in engineering. For all figures, the Cartesian coordinate system is defined such that the positive *z*-axis is the direction of a horizontal wellbore, and the positive *x*-axis is the vertical direction opposite to gravity (Fig. 1.1). The signals of interest, for a receiver set oriented in the $u \in \{x, y, z\}$ direction, are given by

$$\Delta U_{uv}^{\{p,s,t\}} = -j\omega\mu_0 A_{RX} N_{RX} \hat{\mathbf{u}} \cdot \left[\mathbf{H}_v^{\{p,s,t\}}(\mathbf{r}_{Rx2}) - \mathbf{H}_v^{\{p,s,t\}}(\mathbf{r}_{Rx1}) \left(\frac{l_1}{l_2} \right)^3 \right] \quad (1.1)$$

where $\Delta U_{uv}^{\{p,s,t\}}$ are the bucked voltages, A_{RX} is the area of the receiver coils positioned at $\mathbf{r}_{RX1}$ and $\mathbf{r}_{RX2}$, N_{RX} is number of turns in the receiver coils, μ_0 is free-space magnetic permeability, and $(l_1/l_2)^3$ is a bucking coefficient used to approximately cancel the dominant imaginary component of the primary field (Lovell, 1993). Bucking increases the tool's sensitivity to small variations in the total magnetic field but must be carefully calibrated: for thin coils, l_1 and l_2 are the distances between the receiver and the transmitter coil's center. For such simple geometries, bucking can yield close to perfect primary component cancellation for low frequency signals in air, accounting for the $1/R^3$ decay of the primary field at distance R from the source. In practice, however, the coils are of finite length and thus should be calibrated for optimal cancellation of the primary signal prior to data acquisition in the well.

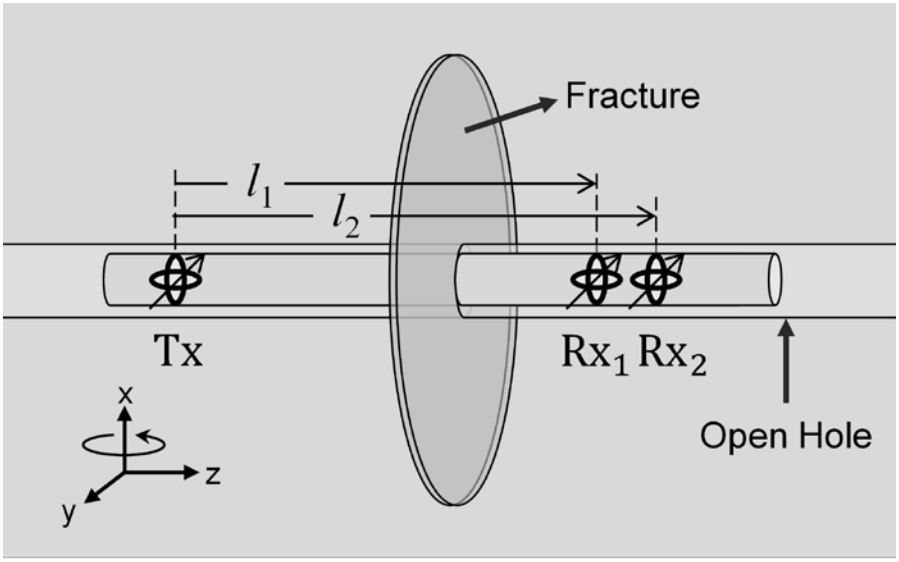

Figure 1.5: An electromagnetic induction logging tool with a single-spacing couple: tri-axial transmitter (Tx) and receiver/bucking (Rx_1/Rx_2) coils.

The utilization of a tri-axial receiver coil system allows acquisition of more parameters of the fractures. In the previous numerical study, co-axial measurements were shown to be sensitive to the fracture cross-sectional area but cannot differentiate fractures of the same area with different cross-sectional shapes or dips. Transverse co-polarized measurements can discern axially symmetric from asymmetric ones and cross-polarized measurements can quantify fracture dip-angle and become more sensitive as the dip-angle increases (Yang et al., 2015).

An actual measurement in the field involves two passes of the tool along the wellbore, before and after the hydraulic fracturing operation, during which the bucked signals $\Delta U_{uv}^{\mathrm{p}}$ (before the hydraulic fracturing) and $\Delta U_{uv}^{\mathrm{t}}$ (after the hydraulic fracturing) are recorded. The difference between these bucked signals is given by:

$$\Delta U_{uv}^{s} = \Delta U_{uv}^{t} - \Delta U_{uv}^{p} \quad (1.2)$$

This is referred as the "differential signal" in this report. Since the distance between transmitter and receiver coils dictates the depth of investigation of the tool, three receiver coil sets at different distances from the tri-axial transmitter coil have been suggested to investigate fractures far away from the wellbore (Fig. 1.2). The short spacing can detect smaller fractures but is insensitive to larger ones. The signals from the long spacing are inherently weak but can distinguish larger fractures. The upper bound of sensitivity was shown to be 10 m^2 for the short spacing and 1000 m^2 for the long spacing receiver couples.

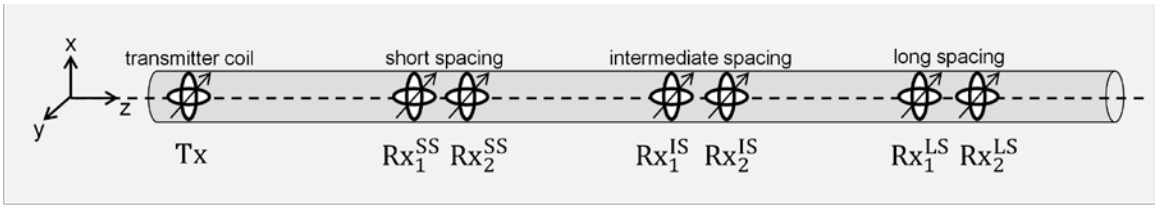

Figure 1.6: An electromagnetic induction logging tool with three spacings: short, intermediate and long spacing transmitter-receivers couples.

Table 1.1 shows nominal spacings used for the tool.

Short Spacing		**Intermediate Spacing**		**Long Spacing**	
l_1^{SS} (m)	l_2^{SS} (m)	l_1^{IS} (m)	l_2^{IS} (m)	l_1^{LS} (m)	l_2^{LS} (m)
1.2	1.5	5.0	5.6	18.0	19.2

Table 1.1: Nominal tool spacings, the distance between transmitter and receiver/bucking coils, for short, intermediate and long spacing.

1.3. PROBLEM STATEMENT

A new electromagnetic downhole induction tool that relies on the conductivity contrast between the proppant pack and the reservoir rock has never before been designed and built. Numerical models show that such measurements should enable us to detect proppant deep into the formation. The models used to interpret the results from the tool need to be computationally efficient so that these forward models can allow inversion algorithms to be implemented in a time efficient manner. To be able to judge the predictive value, and ultimately the potential of single backbone EM tools for propped fracture diagnosis, the detectability and differentiability of realistic signal levels corresponding to fractures of various geometries must be studied experimentally with realistically sized tri-axial coils.

A limited amount of previous work theoretically demonstrates the EM method's capability to detect and characterize propped fractures, but numerous gaps still exist before this technology can be deployed in the field. These include, for example, specifications of transmitting and receiving components, uncertainty in their positioning, the required resolution of the processed signals, their

sensitivity to the actual noise, etc. To bridge the gap between the theoretical proof of concept and a field deployable tool, the design, and testing of a lower-risk initial prototype is required. This testing should enable refining the tool specifications to guarantee its robustness while avoiding difficult and expensive down-hole measurements. In this study we have experimentally verified this technique and developed a list of recommended specifications and practices for a field deployable tool.

1.4. OBJECTIVES

The main objective of this study is to design, build and test a prototype tool, with suitable software and hardware, to demonstrate the use of electrically conductive proppant as a fracture diagnostic method. In addition, our goal is to demonstrate and test the proposed methodology in a lab and field-like scenario to validate the numerical forward models used both for the simulation of the experimental and downhole scenarios and as the cornerstone of an inversion analysis. The specific objectives are:

- To test the physical properties of a candidate proppant to demonstrate its potential in providing sufficient electrical conductivity and mechanical integrity;
- To build a prototype tool which is very close in design to a field deployable tool;
- To develop a numerical forward model that can be compared with experimental results and is fast/robust enough to be used in the inversion analysis;
- To develop a laboratory measurement technique that can emulate hydraulic fractures in a controlled environment;
- To conduct laboratory tests with the tool and compare its results with our numerical models to ensure that the tool response is captured accurately by the model.
- To test the tool in a controlled setting in the laboratory and in a simulated well test site to demonstrate that is can be used for fracture diagnostics;
- To develop an inversion algorithm that is automated, fast and robust and ready to be used in the field.

The prototype tool, design specifications and numerical models together with our results and conclusions in this report enable the design and manufacturing of a field deployable tool.

1.5. REPORT OUTLINE

The report is divided into six chapters. Chapter 2 presents and tests a candidate proppant to be used in the field. Then, a numerical model developed in Chapter 3 and its results are compared to the response of a prototype tool described in Chapter 4. A stochastic inversion algorithm is developed and described in Chapter 5 which is ready to use with field data. The last chapter uses both numerical and inversion models to demonstrate the capabilities of the tool and to make recommendations for field deployment.

Chapter 2 introduces a lab setup for measuring electrical resistivity of proppants. A candidate proppant, petroleum coke, is tested to evaluate both its electrical and hydraulic conductivity.

Chapter 3 describes two numerical algorithms used to compute the response of the tool to targets with good EM contrast. The models developed here allow the regions of different EM properties to be included around the tool with little computational effort. We effectively utilize surface integral equations for the open-hole application and an axial hybrid method for the computation of tool response inside the production casing.

In Chapter 4, we describe the experimental system, including the design of a particular prototype tool and target models and measurement procedures for tests in laboratory and field environments; importantly, the coil sizes and operation frequency are not scaled. The experimentally measured signals are described and compared to numerical simulations for various receiver and transmitter configurations. These fracture models have increased conductivity and reduced thickness, designed to provide signal levels similar to those expected from realistic propped fractures.

Chapter 5 develops a stochastic inversion algorithm for the full automated inversion of the tool's response. The model is validated with testing functions and used for the parametrized fracture model. We use synthetic data to evaluate the sensitivity of the signals to fracture electrical conductivity, size and dip-angle. The chapter also studies the effect of neighboring fractures on the recorded signals to accurately identify proppant distribution among the clusters of a stage.

In Chapter 6, we used numerical and forward models to evaluate the investigation area of the tool with the given optimized frequency and tool spacings. We further simulated inter-well deployment and showed the potential for the evaluation of proppant settling. Finally, we simulated and presented results for proppants with enhanced electrical permittivity and magnetic permeability.

Chapter 2: Electrical Resistivity & Hydraulic Conductivity of Petroleum Coke

2.1. BACKGROUND

As discussed in the last chapter, electromagnetic (EM) methods rely on proppants that demonstrate unique EM properties in high contrast with those of the formation. These properties can be electrical conductivity, electric permittivity, magnetic permeability, etc.

Prior to the developments of field applicable proppants, people have studied 'proppant analogs', which are materials that display unique EM properties but may not be acceptable for injection into deep reservoirs (LaBrecque et al., 2016). For example, steel shots (Symington, et al., 2010) exhibits a high relative permittivity of 10^7 at 100 Hz frequency. Small-scale field experiments at shallow depth indicate that this material shows a significant increase in the intrinsic phase response over that of the background. Coke breeze, as a conductive proppant analog, has been tested as a contrast agent as well. Mixing coke breeze with sand can reduce its consumption while keeping a reasonably high electrical conductivity (LaBrecque et al., 2016). However, the main problem for these materials is the lack of mechanical strength for withstanding high confining stress.

Recent advancements in proppant detection brought up a few new candidates that can potentially be applied in deep wells. Coke-breeze-coated sand slurry was expected to have an effective resistivity as low as $5 \times 10^{-4}\ \Omega \cdot \mathrm{m}$ when the volume of proppant in the slurry is above 70% (Hoversten et al., 2015). A ceramic proppant with an electrically conductive coating possesses the high mechanical strength of ceramic and was tested in a horizontal well 8000 feet deep (Palisch et al., 2016).

Effective Medium Theory was used to estimate the proppants' electrical resistivity (Berryman and Hoversten 2013). A better evaluation of proppant electrical resistivity requires a general and robust experimental method. Measurements on one or several types of conductive proppants in the lab can provide valuable information for numerical simulations, as well as help in selecting the desired proppant for field applications.

The effective electrical resistivity of the propped fracture is dictated by the proppant conductivity, distribution, as well as by factors such as in-situ stress in the reservoir. To better simulate a realistic situation, an experimental system (or method) for resistivity measurements on proppants should be able to:

- Conduct consistent and accurate measurements on different proppants;
- Apply a high enough confining pressure to simulate downhole conditions;
- Saturate the proppant with different fluids.
- Measure electrical resistivity as well as hydraulic conductivity of the proppant pack.

Although a few candidate proppants have been reported in the literature, the cost of applying these materials in large quantities remains high. So another important goal of our work is to find a material that is inexpensive while exhibiting contrasting EM properties relative to the formation rock. Proppants with high intrinsic conductivity are natural candidates for our application. Calcined petroleum coke (CPC), is one such material which is currently accessible in large quantities in the market. It is a byproduct of oil refining and more than 96% of its composition is carbon, which makes it a good electrical conductor. CPC is a dark material with a density of 2.03

g/cm^3 and a particle size of 150 - 400 μm. It is relatively inexpensive and comparable in cost to sand on a unit volume basis. The main scope of this chapter is building a general and effective experimental method, measuring the electrical resistivity of CPC and exploring the possibility of mixing it with sand for fracture diagnostics using EM methods.

For field applications, it is also very important to verify that CPC (mixed with sand) shows reasonable hydraulic conductivity, especially under high confining stress, in order to be used as a proppant. Some results on CPC's hydraulic conductivity under confining stress will also be presented.

2.2. ELECTRICAL RESISTIVITY OF PETROLEUM COKE

2.2.1. Experimental System

A resistivity core holder (Fig. 2.1) is used to conduct electrical resistivity/conductivity measurements on well-consolidated cores. The measurements are conducted using a four-point probe method, which minimizes the error introduced by contact resistance.

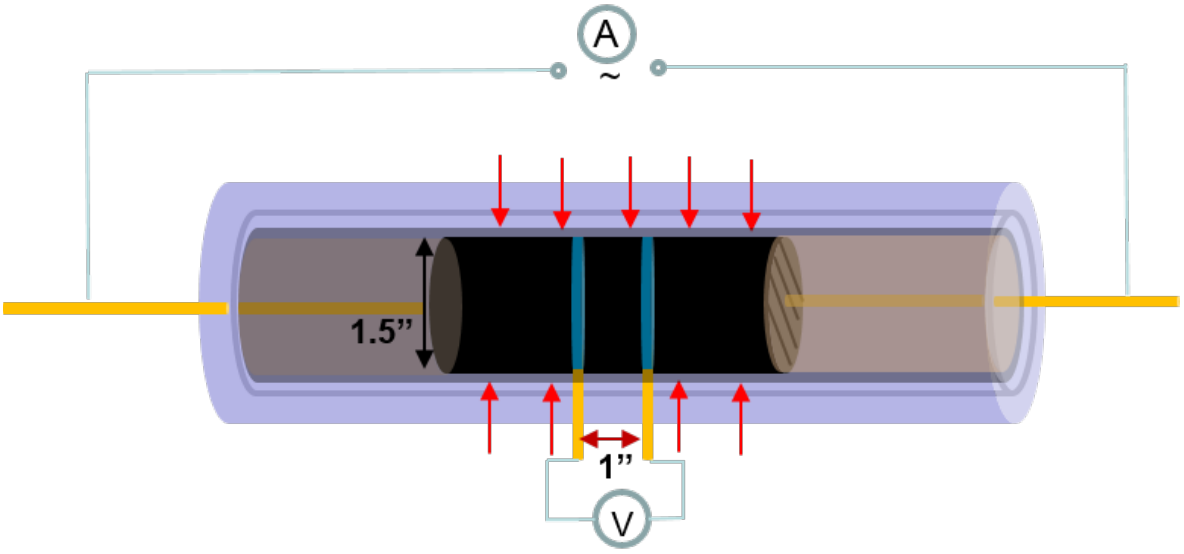

Figure 2.1: Configuration of the resistivity core holder. The yellow bars identify the electrodes, while the black cylinder and the red arrows represent the core and the confining pressure, respectively.

A core with a length of 5.08 cm (2 inches) and a diameter of 3.81 cm (1.5 inches), which is represented by the black cylinder in Fig. 2.1 is wrapped with a rubber sleeve and constrained by the end pieces of the core holder at both ends. Fluids can be injected through one of the current-carrying electrodes into the core. Confining pressure around the rubber sleeve is applied using a hydraulic pump, in order to prevent the fluid bypassing the core through the gap between the core and the robber sleeve. An alternating current I is applied via the current-carrying electrodes at the two ends. These current-carrying electrodes are isolated from the outer shell of the core holder

such that current is forced to flow through the core. A voltage U is measured on the voltage-sensing electrodes in the center (Fig. 2.1). These electrodes are connected to two ring electrodes which are directly in contact with the core. The spacing between the two voltage sensing electrodes is 2.54 cm (1 inch). The measured resistance can be obtained from Ohm's law (U/I). Assuming that the core has cross sectional area A and length l, the resistivity of the core is

$$R = \frac{U}{I}\frac{A}{l} \tag{2.1}$$

We proposed to adopt this setup for resistivity measurements on conductive proppants (Zhang et al., 2016). For this purpose, the core in the setup will be replaced by a proppant pack or a fractured core propped by proppant. Due to the fact that the resistivity core holder was initially designed for well consolidated cores, it's necessary to verify that it works properly for unconsolidated grains (e.g., sand or proppant). We used a sand pack which has a porosity of 25.2% for this verification. Brine of different concentrations was injected to saturate the sand pack (S_w=100%) and resistivity measurements were conducted using this resistivity core holder. The brine concentration c, resistivity R_w and measured resistivity of the sand pack R_o are listed in Table 2.1.

c (g/l)	36	70	100	150
$R_w\ (\Omega \cdot m)$	0.18	0.10	0.08	0.06
$R_o\ (\Omega \cdot m)$	0.86	0.54	0.44	0.29

Table 2.1: Measured resistivity of a brine saturated sand pack with different brine concentrations.

A plot of R_o vs R_w shows the measured resistivity of the sand pack R_o is proportional to the resistivity of brine that saturates the sand pack (Fig. 2.2). This is consistent with Archie's Law, which is a well-known relationship between the core resistivity and the resistivity of the saturating fluid:

$$R_o = F \cdot R_w \tag{2.2}$$

The formation factor F for this unconsolidated sand pack is about 4.55. The agreement with Archie's equation (Eq. 2.2) verifies the applicability of this core holder for resistivity measurements of unconsolidated grains.

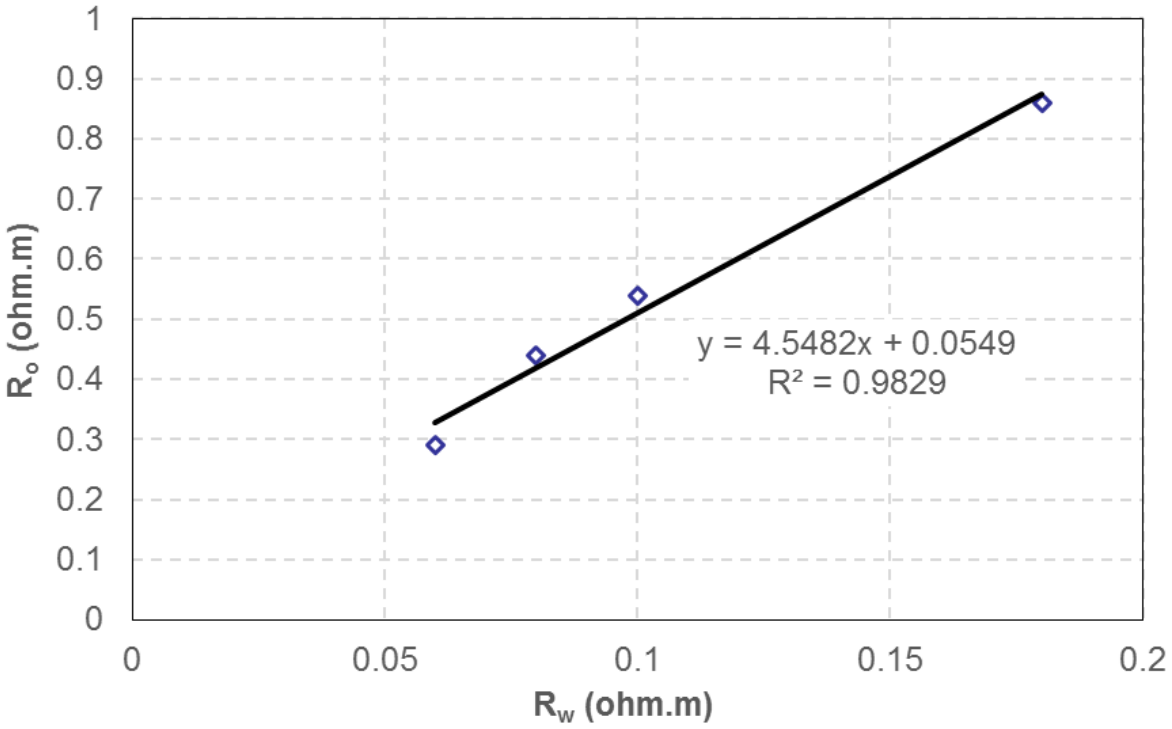

Figure 2.2: The measured resistivity of the sand pack $\boldsymbol{R_o}$ versus the resistivity of brine $\boldsymbol{R_w}$. A linear relationship is observed.

Next, we used the experimental system to conduct resistivity measurements on CPC. Our lab measurements mainly focused on this material and all the measurements were performed at room temperature. Although under reservoir conditions fluid temperature will be higher, room temperature experiments are expected to be very predictive, because the effective conductivity is dominated by that of the proppant instead of the fracturing fluid. The proppant resistivity was measured for both a cylindrical pack and a planar thin layer in a simulated fracture created in the core.

2.2.2. Resistivity of Bulk PC

The PC was packed in the rubber sleeve of the core holder with and without brine occupying the void space between the particles (Fig.2.1). In this case, the cross sectional area A equals $\pi D^2/4$, where D is the diameter of the cylinder (1.5 inch) and the length l is 1 inch. The particle size of the CPC is 70 – 100 mesh (150 – 210 μm). Eq. 2.1 is used to calculate the electrical resistivity. Fig. 2.3 shows the measured resistivity when no brine is present.

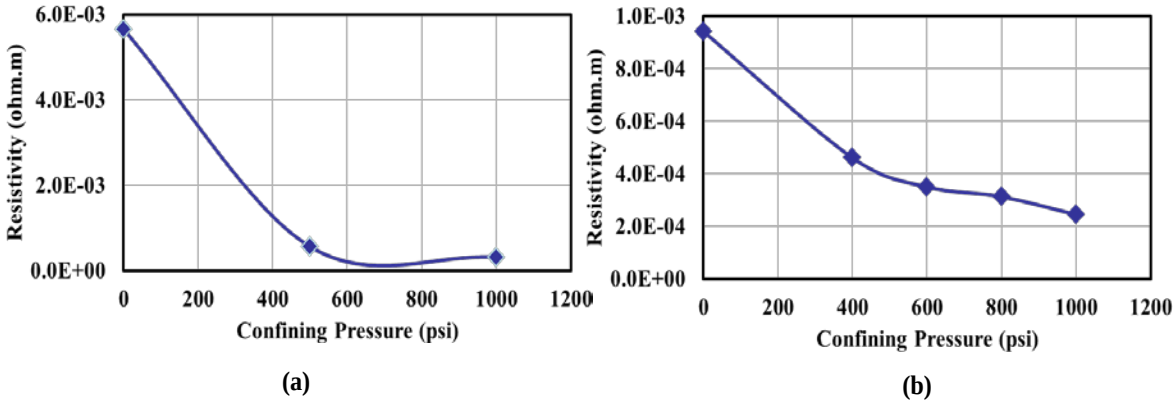

Figure 2.3: Electrical resistivity of the CPC pack at different confining pressure. No brine is present in the pore space in these two sets of measurements.

The initial packing condition affects the proppant's resistivity significantly when no extra confining pressure is applied. As shown in Fig. 2.3(a), the measured resistivity is about $6.0 \times 10^{-3}\ \Omega \cdot \mathrm{m}$ when the initial bulk density of CPC is $1.14\ \mathrm{g/cm^3}$, which corresponds to a porosity of 43.9%. However, when the initial bulk density is increased to $1.27\ \mathrm{g/cm^3}$ (37.6% porosity), the resistivity decreases to about $1.0 \times 10^{-3}\ \Omega \cdot \mathrm{m}$ (Fig. 2.3(b)). When a confining pressure is applied, the resistivity quickly decreases and reaches a plateau. End point values for Fig. 2.3(a) and Fig. 2.3(b) are $3.2 \times 10^{-4}\ \Omega \cdot \mathrm{m}$ and $2.4 \times 10^{-4}\ \Omega \cdot \mathrm{m}$ at 1000 psi. Even though the two curves have very different starting values, they eventually approach a similar number (Zhang et al., 2016).

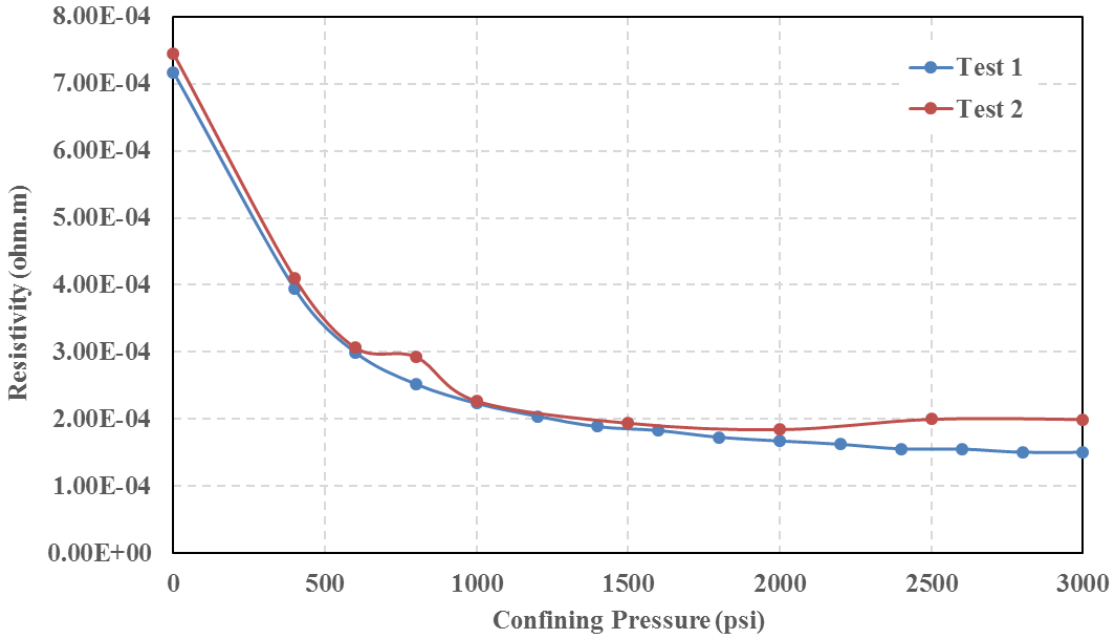

Figure 2.4: Electrical resistivity of the CPC pack with respect to confining pressure. Sea water was injected into the pack for both Test 1 and Test 2.

Fig. 2.4 shows two sets of measurements (blue and red curves) with the same initial PC bulk density of 1.27 g/cm^3. As opposed to the measurements shown in Fig. 2.3, here, sea water (35 g/L. NaCl solution) was injected into the proppant pack. Sea water has a resistivity of 0.2 $\Omega \cdot m$ at room temperature, which is several orders of magnitude greater than the resistivity of PC. Hence similar results are expected when sea water fills the void space between the particles. The measured resistivity starts from about $7.0 \times 10^{-4}\ \Omega \cdot m$ when no confining pressure is applied. End point values for Test 1 and Test 2 are 1.5×10^{-4} and $1.9 \times 10^{-4}\ \Omega \cdot m$, as the confining pressure reaches 3000 psi (Fig. 2.4). Note that, unlike the smooth decrease of the blue curve, some humps can be observed in the red curve. We interpret this as the result of the simplification in our calculations: the rubber sleeve shrinks under pressure, which gives us an apparent higher resistivity because the change of the cross sectional area is not accounted for in the calculations (Zhang et al., 2016). Shrinking of the rubber sleeve also leads to the break of the seals on the core holder and therefore leaks develop as the confining pressure increases. Higher confining pressures could be achieved with sea water (Fig. 2.4 compared to Fig. 2.3).

Apart from the intrinsic conductivity, the contact between the CPC particles is the most important factor that controls the pack's resistivity. This justifies the role that initial bulk density plays. As the confining pressure increases, the contact improves, which leads to a lower resistivity. However, as the confining pressure rises to ~1000 psi this effect reaches the saturation point, thereby explaining why all the results converge at high confining pressure to the same value of $\sim 2 \times 10^{-4}\ \Omega \cdot m$.

2.2.3. Resistivity of CPC in a Fracture

A second set of measurements was conducted on the proppant in a fractured sandstone core, mimicking proppant in a hydraulic fracture. The core has the same dimensions as that of the proppant pack in Subsection 2.2.1 and the initial fracture width w_f is set to be 3 mm (Fig. 2.5). Confining pressure was applied as well. PC of particle size 40 – 70 and 70 – 100 mesh, corresponding to 210 – 420 and 150 -210 μm were used. In order to explore the possibility of using a mixture of PC and sand in the field, a few combinations of these two materials (0 wt% sand, 25 wt%, 50 wt% and 75 wt% sand) were tested. Again Eq. 2.1 is used to calculate the electrical resistivity. The cross sectional area A in this case is $D \cdot w_f$.

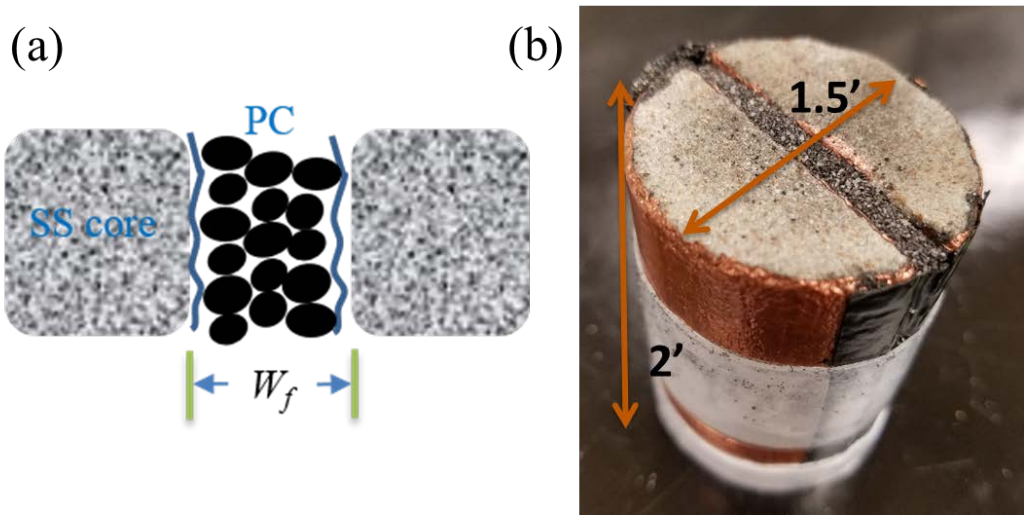

Figure 2.5: (a) A schematic of proppant in a fracture of width w_f. (b) A fractured sandstone core propped by CPC. The core length and diameter are 2' and 1.5', respectively.

For the CPC with a particle size of 210 – 420 μm (40 – 70 mesh), no sea water was injected in the test. The measured electrical resistivities at various confining pressures are shown in Fig. 2.6 and 2.7. Different curves represent the resistivity of CPC mixed with different proportions of sand. The O-ring seal at the voltage sensing electrodes of the core holder is not very consistent, due to the deformation of the rubber sleeve at elevated pressures. The end point pressure on different curves denotes the highest confining pressure achieved. The end point values of the measured resistivity are listed in Table 2.2.

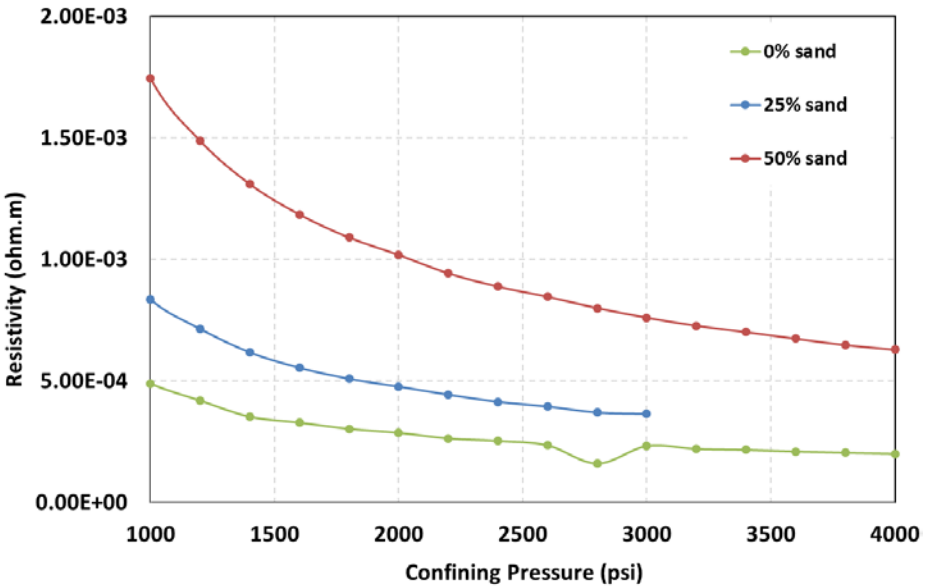

Figure 2.6: Measured resistivity of CPC (40 – 70 mesh) at various confining pressures. The green, blue and red curves represent the CPC mixed with 0%, 25% and 50% sand, respectively.

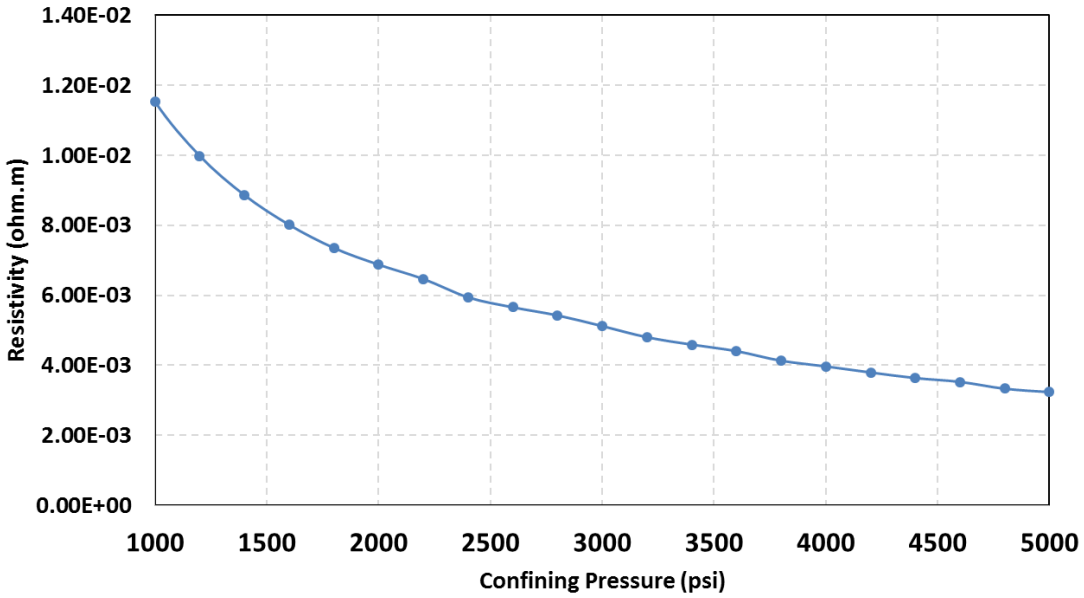

Figure 2.7: Measured resistivity of CPC (40 – 70 mesh) mixed with 75% sand at various confining pressures.

0% sand	$1.99 \times 10^{-4}\ \Omega \cdot m$ @4000 psi
25% sand	$3.64 \times 10^{-4}\ \Omega \cdot m$ @3000 psi
50% sand	$6.28 \times 10^{-4}\ \Omega \cdot m$ @4000 psi
75% sand	$3.24 \times 10^{-3}\ \Omega \cdot m$ @5000 psi

Table 2.2. The measured electrical resistivity of CPC (40–70 mesh) - sand mixtures at different confining pressure.

Similar to the results of the proppant pack, for a given composition of PC-sand mixture, the electrical resistivity decreases with increasing confining pressure, due to better contact between the CPC particles. The electrical resistivity of pure CPC filled fracture is $1.99 \times 10^{-4}\ \Omega \cdot m$ under a confining pressure of 4000 psi, which is close to that of a CPC pack (Fig. 2.6). This resistivity is about four orders of magnitude lower than the typical resistivity of shale, which makes it a suitable candidate material that can be tracked using EM methods.

As the weight percentage of sand increases, the effective resistivity of the mixture increases. This is because sand, as a very resistive material, fills the gap between the PC particles and

prevents direct contact between them. The effective resistivity of the mixture remains quite low till 50% sand is mixed with CPC (Fig. 2.6). However, when the weight percentage of sand reaches 75%, the measured resistivity is substantially higher ($3.24 \times 10^{-3}\ \Omega \cdot m$ at a confining pressure of 5000 psi). At this high percentage of sand, the high resistivity will have an adverse impact its effectiveness in field applications (Fig. 2.7).

A CPC sample with a smaller particle size of 150 -210 μm (70 -100 mesh) was also tested (Fig. 2.8 and 2.9). Sea water was injected to saturate the proppant, in order to achieve a higher confining pressure in our apparatus. Since the minor effect of sea water on the effective resistivity of the proppant has been verified in 2.2.1, the difference in the measured resistivity (if there is any) can be attributed to the smaller particle size in this set of measurements.

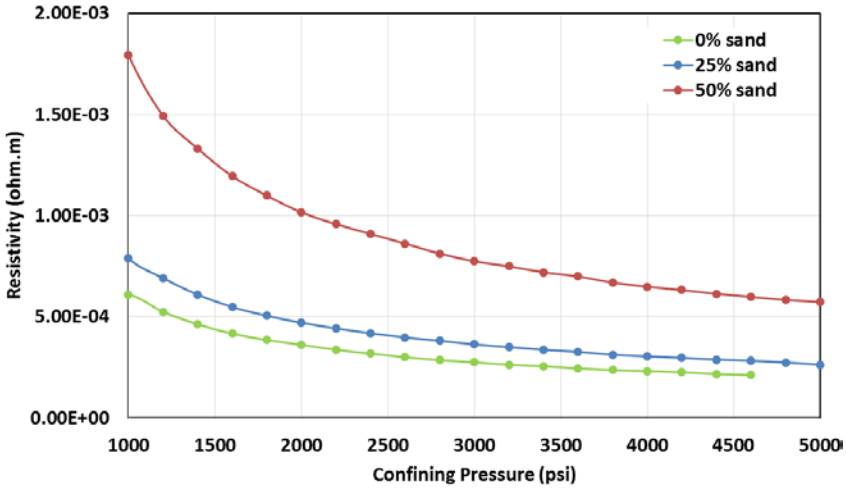

Figure 2.8: Measured resistivity of CPC (70 – 100 mesh) at various confining pressures. The green, blue and red curves represent the CPC mixed with 0%, 25% and 50% sand, respectively.

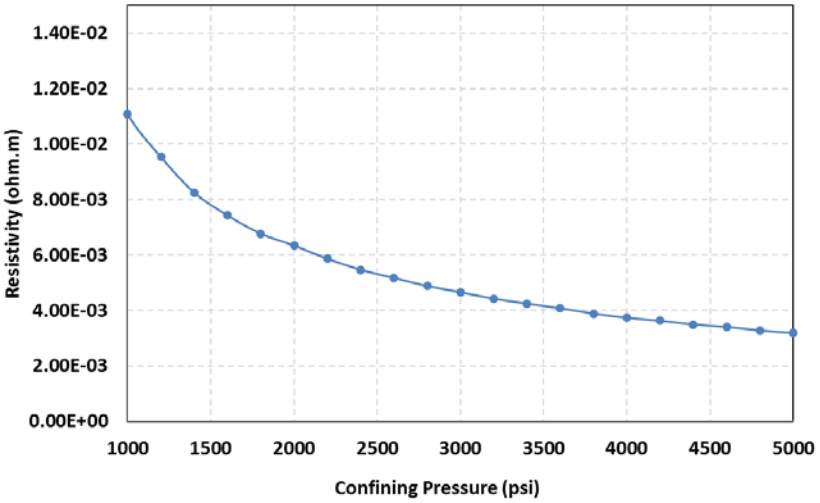

Figure 2.9: Measured resistivity of CPC (70 – 100 mesh) mixed with 75% sand at various confining pressures.

The results show a few similarities to those obtained with the CPC with a larger particle size. The end point values of the measured resistivity are listed in Table 2.3. The measured resistivity of different CPC-sand mixture at high pressure remains close to the previous results, which means the particle size doesn't affect the effective resistivity much. Again, the mixture stays highly conductive when up to 50 wt% sand is added. However, when 75 wt% sand is added, the electrical resistivity is one order of magnitude higher, which makes it questionable for field applications.

0% sand	$2.12 \times 10^{-4}\ \Omega \cdot m$ @4600 psi
25% sand	$2.64 \times 10^{-4}\ \Omega \cdot m$ @5000 psi
50% sand	$5.73 \times 10^{-4}\ \Omega \cdot m$ @5000 psi
75% sand	$3.18 \times 10^{-3}\ \Omega \cdot m$ @5000 psi

Table 2.3: The measured electrical resistivity of CPC (70–100 mesh) - sand mixture at different confining pressure.

2.3. HYDRAULIC CONDUCTIVITY OF PETROLEUM COKE

2.3.1. Experimental System

We measured the hydraulic conductivity of fractures propped by PC (or PC – sand mixtures) using an experimental method shown in Fig. 2.10. Details of the application of this apparatus for fracture conductivity measurements has been reported earlier (Wu, et al., 2017). A Berea sandstone core of 1'' diameter by 8'' length was prepared with a fracture width of 1mm. The fracture was filled with proppant and then the core was placed inside a Hassler sleeve core holder and evacuated to remove trapped air. Confining closure stress was applied for 24 hours. After that a 3% brine solution was pumped from the accumulator through the core at a range of constant flow rates Q. For each closure stress applied, the pressure drop ΔP across the core was measured and used to calculate the fracture conductivity using Darcy's Law

$$Q = \frac{k_f \cdot w_f \cdot D}{\mu_f} \cdot \frac{\Delta P}{L} \tag{2.3}$$

where w_f, D and L represent the fracture width, core diameter and length, and k_f and μ_f stands for the fracture permeability and fluid viscosity, respectively.

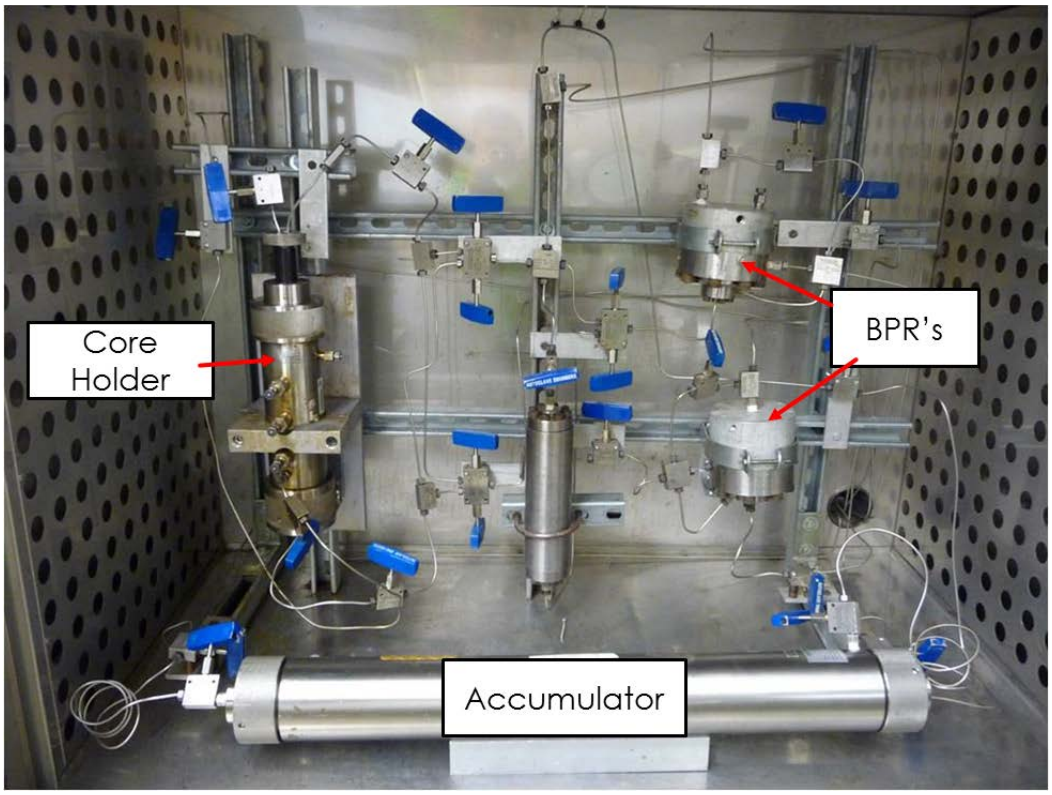

Figure 2.10: Experimental method for fracture conductivity measurements. Fluid is injected from the accumulator into the core. The back pressure regulators (BPR's) are used to adjust the flow rates. A confining stress is applied on the core.

2.3.2. Hydraulic Conductivity of PC in a Fracture

Pure CPC, pure sand with the same particle size and PC – sand mixtures are tested for comparison. The measured fracture conductivity $k_f \cdot w_f$ for 40 – 70 mesh and 70 – 100 mesh proppants are shown in Fig 2.11 and 2.12. Fig. 2.11 (b) and Fig. 2.12 (b) are the normalized fracture conductivities with respect to the ones under 2000 psi closure stress. For both cases, as the weight percentage of sand increases, the measured fracture hydraulic conductivity under a given confining stress increases. This indicates sand has a higher mechanical strength or lower compressibility than PC does. The actual mechanism for this phenomenon should be explored in the future by conducting mechanical tests on the sand and PC particles. Comparison between Fig. 2.11 and 2.12 indicates that the fracture propped by 40 – 70 mesh grains has an overall higher conductivity.

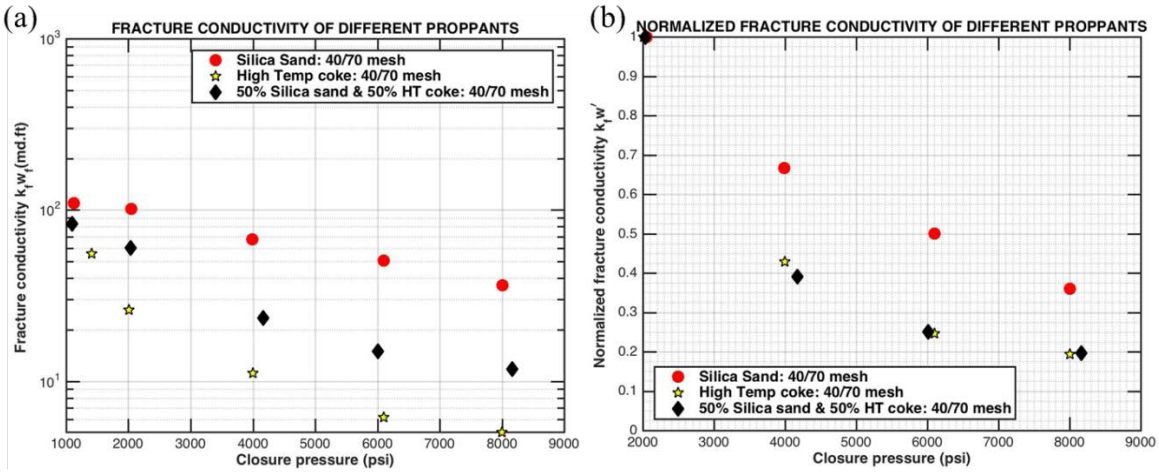

Figure 2.11: (a) The measured fracture conductivities for different proppants (40 – 70 mesh) at various confining stresses. (b) Fracture conductivities normalized by the conductivity at 2000 psi confining stress.

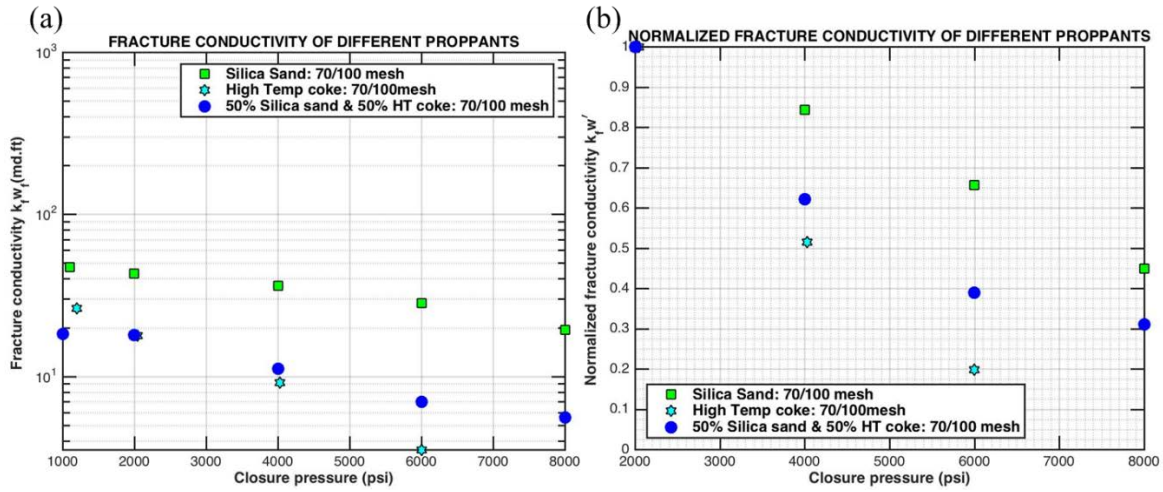

Figure 2.12: (a) The measured fracture conductivities for different proppants (70 – 100 mesh) at various confining stresses. (b) Fracture conductivities normalized by the conductivity at 2000 psi confining stress.

To better interpret the results, we calculated the dimensionless fracture conductivity by assuming a matrix permeability of 10^{-4} md and a fracture half-length of 250 ft. For the worst case observed, when pure PC (70 – 100 mesh) is under a confining stress of 6000 psi, the measured fracture conductivity is about 4 $\text{md} \cdot \text{ft}$. The corresponding dimensionless fracture conductivity is given by:

$$F_{CD} = (k_f \cdot w_f)/(L_f \cdot k_{matrix}) = 160.$$

Using this value in a few fracture productivity models (e.g., Friehauf and Sharma (2009) and Prats (1961)), it can be concluded that the stimulation ratio J/J_0 reaches a maximum, which means that the fracture acts as an infinitely conductive fracture for any F_{CD} value above 100

(Fig.2.13). Therefore, the application of CPC (or CPC – sand mixture) for fracture diagnostics using EM methods will also assure good productivity of the fractured well even at an elevated effective stress of 6000 psi.

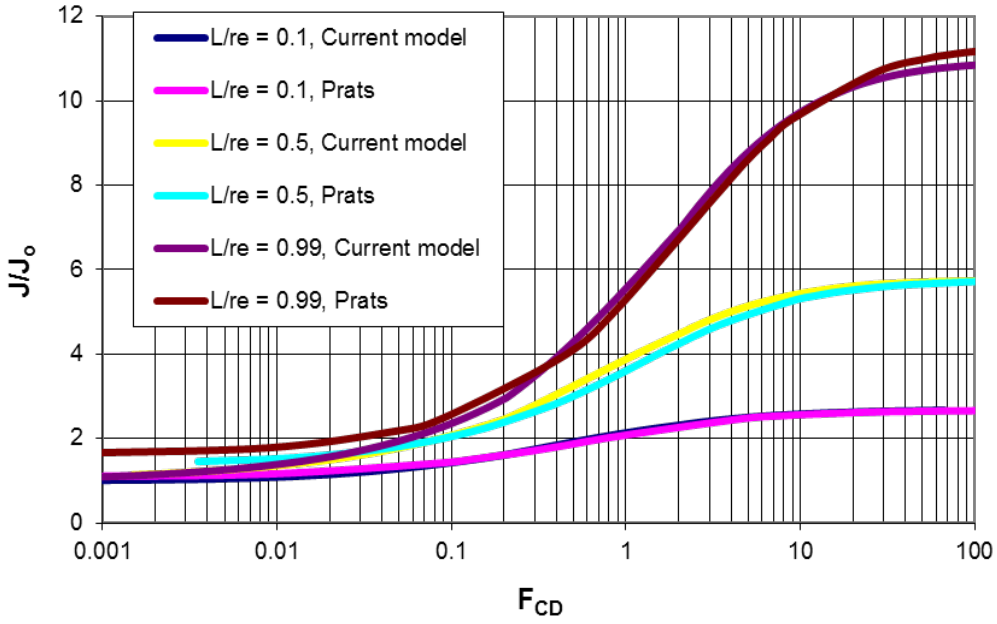

Figure 2.13: Stimulation ratio versus dimensionless fracture conductivity from two models. 'Current model' and 'Prats' represents Friehauf's and Prats's model, respectively.

2.4. CONCLUSION

A resistivity core holder was used to measure the electrical resistivity of a candidate proppant (CPC) for a range of stresses, particle sizes and mixtures with sand. The results show that the effective resistivity of the proppant decreases as the confining stress increases, due to the better contact between the PC particles under higher stress. Pure CPC shows an electrical resistivity of around $2 \times 10^{-4}\ \Omega \cdot m$ when the confining stress is above 3000 psi. Particle size does not play a noticeable role in the measured results. The effective resistivity increases with an increasing weight percentage of sand when sand is mixed with CPC. This is because sand, as a non-conductive material, prevents the direct contact between CPC particles and changes the current path. The electrical resistivity stays reasonably low ($\sim 6 \times 10^{-4}\ \Omega \cdot m$) when up to 50% sand is added. This is of great significance because in field applications, when a huge quantity of proppant is pumped, adding sand can reduce the consumption of PC and therefore, the cost of hydraulic fracture operations and diagnostics.

Fracture hydraulic conductivity measurements on CPC show that when sand is added, the measured fracture conductivity increases, probably because of the higher mechanical strength of sand. Even when using pure PC, the measured fracture conductivity is above $4\ \text{md} \cdot \text{ft}$ under a confining stress of 6000 psi, which means that the fracture is infinitely conductive for a typical

field-scale fracture. Therefore, CPC is a good candidate for fracture diagnostics not only due to its low electrical resistivity, but also due to its high conductivity to fluid flow at elevated stress.

When more sand is mixed with the CPC, it leads to a trade-off between a higher electrical resistivity and higher fracture conductivity. When applying this proppant in the field, the ratio of CPC to sand should be tailored according to the field conditions (e.g., reservoir depth and in situ stresses) to assure the fractures propped by this proppant is conductive enough to both current and fluid flow.

Chapter 3: Numerical Modeling of Electrically Conductive Targets

In this chapter, numerical modeling tools we developed are presented to simulate the induction tool response while logging propped fractures both in open- and cased-hole applications. We are using methods which can simulate proppant distribution in fractures with arbitrary geometry which are not necessarily orthogonal to the wellbore. Wellbores may contain casing and/or fluid in the wellbore which may have electromagnetic properties that are very different than that of the proppant and background formation.

We develop two numerical models to simulate the tool's response in a time-efficient manner. The first model is based on the implementation of impedance boundary conditions to the surface integral equations and solving this system with a method of moments (MOM) (Rao et al., 1982; Qian et al., 2007). The convergence, validation, possible approximation and computation time analyses are shown in the following subsections. The second model is based on the axial hybrid method which simulates transversely isotropic media (Zhang et al., 1999; Wang et al., 2009). The model is mainly used to understand the behavior of the tool's response inside a production casing, and some analyses of the numerical features are shown at the end. In both cases, the governing equations are discussed in detail.

3.1. Literature Review

While logging a well with an induction tool, the tool is pulled along the wellbore and transmitter coils are excited at certain sampling points. The solution of the induction tool response to the propped fractures has to consider many excitation points. Therefore, a frequency domain computation is ideal for the analyses of the suggested single frequency tool where the system matrix obtained after deploying a numerical technique is usually independent of excitations. Once this matrix is inverted or factorized, it can be used to obtain solutions to all excitations. Moreover, since the frequency-domain methods solve Maxwell's equations at each frequency, they can deal with dispersive media[1] easily.

Maxwell's equations in the frequency domain can be solved in 3-D using one of several numerical methods. The family of finite difference and finite element methods solves Maxwell's equations or their weak form representations directly but requires the solution domain to be truncated and treated carefully so that the truncated computational domain mimics the original open space. The method of moments, on the other hand, solves Maxwell's equations indirectly by dealing with integral equations formulated using the fundamental solution to a point source which is known as a Green's function. This simulation method is especially well suited for our analysis because it confines the computational domain to the anomalous conductivity region only.

The classical method of moment solution of the volume electric field integral equations is limited to small-scale problems because the integral equation methods yield fully populated matrices. In Yang et al. (2014; 2015), an adaptive integral method is used to accelerate the solution to the induction problem by making use of the translational invariance of Green's functions. Approximately 150, 1500 and 1800 minutes are spent on filling matrices, and the memory requirement is 1.6, 13 and 34 GB for solving a problem with 20,729, 120,000 and 320,000

[1]The medium is called dispersive if electromagnetic properties are dependent on the frequency of the field.

unknowns, respectively. This is still computationally intensive especially if we consider the inversion analysis which requires multiple runs of the forward model to determine the fracture parameters. Moreover, high conductivity contrast between the fracture and formation cannot be easily handled because of the failure in convergence in the iterative procedure.

While simulating an open-hole induction tool response, Zhang et al. (2016) has shown negligible effects of the wellbore fluid on the results by testing different sizes of circular fractures with and without a borehole. This is due to the very high electrical conductivity contrast between the proppant filled fracture and the rock formation. In the same paper, a single thin bulk volume of a constant effective thickness was shown to be equivalent of a thin complex fracture showing that signal responses depend on fracture total volume rather than on fracture complexity. Removing the borehole not only significantly decreases the number of unknowns boosting the speed of the forward model but also allows deploying integral equations to be solved on the surface of the fracture.

The number of unknowns resulting from surface discretization is significantly smaller than that from volume discretization; therefore, the method of moments is much more efficient when it deals with surface integral equations (SIE). It enables meshing the surface with a typical element length that is not dictated by the penetration depth inside the conductive fracture as would be required for a volumetric integral equation solution. In this current work, we are using surface integral equations for simulating the open-hole application of the induction tool. This technique allows simulation of all fracture parameters listed in Yang et al. (2016): fracture location, conductivity, size, shape factor and dip-angle.

To avoid an outrageous increase in the number of unknowns when a casing pipe is introduced to the computational domain tremendous speed up can be obtained by decreasing the dimensions of the problem. In cylindrical coordinates, the ϕ-direction of the problem can be eliminated by use of a Fourier series, and the set of 2D problems can be solved with different types of numerical solvers. Although we lose the capability of simulating the fracture parameters such as shape factor and dip-angle, this technique provides a very practical solution to the original large problem. In this report, we use the axial hybrid method to solve the reduced 2D problem where the numerical solution is obtained in the wellbore direction, and a family of normalized Bessel functions is used to describe the EM fields in the radial direction (Gianzero et al., 1985; Pai, 1991; Li and Shen, 1993).

3.2. OPEN-HOLE SIMULATION OF INDUCTION TOOL

In this application of induction tools, the thickness of fractures is much smaller than their length and skin depth. This allows us to make the assumption of a zero thickness surface for the fracture models, rather than a very thin volume (Yang et al., 2015; Zhang et al., 2016), facilitating the use of surface integral equations (Ren et al., 2016). The magnetic fields $\mathbf{H}_v^{\mathrm{sca}}(\mathbf{r})$ are computed in two main steps: 1) by discretizing the surface with triangular elements to calculate the surface currents on the anomalous region of conductivity by applying an impedance boundary condition; and 2) calculating the scattered fields on the observation points induced by these currents.

A model to simulate responses for a given perfectly electrically conductive (PEC) geometry was formulated and described earlier in Rao et al. (1982). In this work, an impedance boundary condition is implemented due to the finite conductivity and thickness of fractures as described in

Lindell (1992). Before proceeding to numerical results, the basic steps of the computation are shown below. First, we start with the formulation of an integral equation for the problem under consideration. Second, the equation is expanded and tested with the same basis functions to convert the integral form of equations into the linear system of equations. Finally, the matrix equation is solved for the unknown coefficients and the desired magnetic fields are calculated. In all formulations presented below, the reservoir is assumed to be homogeneous and is assigned a constant conductivity.

3.2.1. Surface Integral Equation with Impedance Boundary Condition

The electromagnetic field generated by a time-harmonic source, a source oscillating with a single frequency, defined by volume electric current density $\mathbf{J}$ and volume magnetic current density $\mathbf{M}$ satisfies Maxwell's equations:

$$\nabla \times \mathbf{E} = -j\omega\mu\mathbf{H} - \mathbf{M} \tag{3.1}$$

$$\nabla \times \mathbf{H} = j\omega\tilde{\varepsilon}\mathbf{E} + \mathbf{J} \tag{3.2}$$

$$\nabla \cdot (\tilde{\varepsilon}\mathbf{E}) = \rho_e \tag{3.3}$$

$$\nabla \cdot (\mu\mathbf{H}) = \rho_m \tag{3.4}$$

If we assume that both electric and magnetic fields exist only due to the electric source then the problem can be formulated as follows:

$$\mathbf{E} = -j\omega\mathbf{A} - \nabla\varphi \tag{3.5}$$

$$\mathbf{H} = \frac{1}{\mu}\nabla \times \mathbf{A} \tag{3.6}$$

where the second component of the right-hand side in Eq. 3.5 can be represented in terms of $\mathbf{A}$ as well. For the given surface, the solution of $\mathbf{A}$ and φ are given by:

$$\mathbf{A}(\mathbf{r}) = \mu \iint_S \mathbf{J}_s(\mathrm{r}')G_{\mathrm{R}}(\mathbf{r},\mathbf{r}')\,dS' \tag{3.7}$$

$$\varphi(\mathbf{r}) = -\frac{1}{j\omega\tilde{\varepsilon}} \iint_S \nabla' \cdot \mathbf{J}_s(\mathbf{r}')G_{\mathrm{R}}(\mathbf{r},\mathbf{r}')\,dS' \tag{3.8}$$

in terms of surface current $\mathbf{J}_s$. Here, $\mathbf{r}$ and $\mathbf{r}'$ are observer and source points, respectively; and the Green's function is given as:

$$G_{\mathrm{R}}(\mathbf{r},\mathbf{r}') = \frac{e^{-jk|\mathbf{r}-\mathbf{r}'|}}{4\pi|\mathbf{r}-\mathbf{r}'|} \tag{3.9}$$

The wavenumber is given as:

$$k = \sqrt{\omega^2 \mu \tilde{\varepsilon}} \tag{3.10}$$

and the complex permittivity is defined as:

$$\tilde{\varepsilon} = \varepsilon - j\frac{\sigma}{\omega} \tag{3.11}$$

As can be seen from the equations above, if we find $\mathbf{J}_s$ then we can calculate the electromagnetic field on any observation point. To calculate $\mathbf{J}_s$, we need to apply impedance boundary conditions on the surface of the fracture. This boundary condition is similar to the PEC condition but with non-zero fields on both sides of the surface:

$$\hat{\mathbf{n}} \times \hat{\mathbf{n}} \times \left(\mathbf{E}^{\mathrm{sca}} + \mathbf{E}^{\mathrm{inc}}\right) = -Z_s \mathbf{J}_s \tag{3.12}$$

where $\hat{\mathbf{n}}$ is the unit normal vector of the surface, and Z_s is a surface impedance assigned to the target. Finite thickness and conductivity of fracture can be incorporated to the surface impedance as shown in Lindell (1992):

$$Z_s = \left[\sigma t + \frac{j}{\eta_{\mathrm{o}}}(\varepsilon_r - 1)k_{\mathrm{o}} t\right]^{-1} \tag{3.13}$$

The inverse of this equation is referred as the shunt admittance. For the more generalized impedance boundary condition, one can refer to the study by Qian et al. (2007). In cases when the fracture model has a relative permittivity of one, only the first part of the right-hand side is non-trivial. After taking the cross product of both sides of Eq. 3.12 with a normal vector and substituting the expressions for the electric field and surface impedance, the integral equation can be formulated as follows:

$$\hat{\mathbf{n}} \times (j\omega\mathbf{A} + \nabla\varphi) + \frac{\hat{\mathbf{n}} \times \mathbf{J}_s}{\sigma t} = \hat{\mathbf{n}} \times \mathbf{E}^{\text{inc}} \tag{3.14}$$

To solve Eq. 3.14, Rao-Wilton-Glisson (RWG) basis functions (Rao et al., 1982) are defined on triangular patches (Fig. 3.1) used to discretize the surface, and then surface currents $\mathbf{J}_s$ are approximated as follows:

$$\mathbf{J}_s(\mathbf{r}) \cong \sum_{n=1}^{N} l_n \mathbf{\Lambda}_n(\mathbf{r}) \tag{3.15}$$

In Fig 2.1, the plus or minus sign designation of the triangles is determined by the choice of a positive current reference direction for the nth edge, the reference for which is assumed to be from T_n^+ to T_n^-. The same figure includes the equation for the vector basis function and its divergence associated with the n^{th} edge.

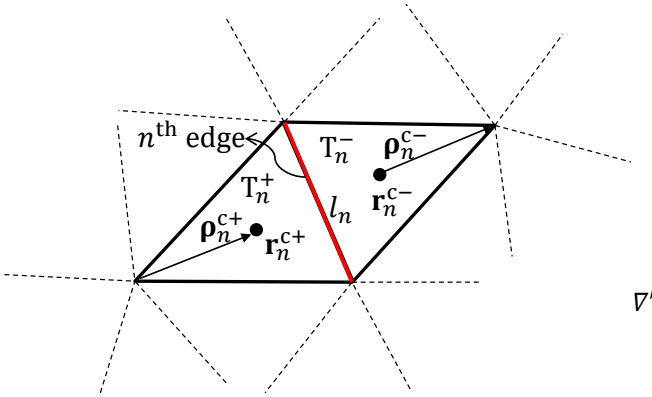

$$\mathbf{\Lambda}_n(\mathbf{r}) = \begin{cases} \frac{l_n}{2A_n^+}\boldsymbol{\rho}_n^+ & \mathbf{r} \in T_n^+ \\ \frac{l_n}{2A_n^-}\boldsymbol{\rho}_n^- & \mathbf{r} \in T_n^- \\ 0 & \text{otherwise} \end{cases}$$

$$\nabla' \cdot \mathbf{\Lambda}_n(\mathbf{r}') = \begin{cases} \frac{l_n}{A_n^+} & \mathbf{r} \in T_n^+ \\ -\frac{l_n}{A_n^-} & \mathbf{r} \in T_n^- \\ 0 & \text{otherwise} \end{cases}$$

Figure 3.1: The equations of vector RWG basis function and its divergence for a given common edge (red) of two triangular elements.

We substitute Eq. 3.15 into 3.14 and test all components of equation with the same RWG testing functions (Davidson, 2011) as in the equation shown below:

$$\begin{aligned} \langle \mathbf{f}, \mathbf{\Lambda}_m \rangle &= \frac{l_m}{2}\left(\frac{1}{A_m^+} \iint_{\mathrm{T}_m^+} \mathbf{f} \cdot \boldsymbol{\rho}_m^+ \, dS + \frac{1}{A_m^-} \iint_{\mathrm{T}_m^-} \mathbf{f} \cdot \boldsymbol{\rho}_m^- \, dS \right) \\ &\cong \frac{l_m}{2}\left(\mathbf{f}(\mathbf{r}_m^{\mathrm{c}+}) \cdot \boldsymbol{\rho}_m^{\mathrm{c}+} + \mathbf{f}(\mathbf{r}_m^{\mathrm{c}-}) \cdot \boldsymbol{\rho}_m^{\mathrm{c}-}\right) \end{aligned} \tag{3.16}$$

where $\mathbf{f}$ can be $\mathbf{A}$, $\nabla\varphi$, $\frac{\mathbf{J}_s}{\sigma t}$ or $\mathbf{E}^{\text{inc}}$. The testing procedure results in a system of linear equations for the coefficients I_n which can be written as a matrix equation:

$$\left(\underline{\underline{\mathbf{Z}}} + \underline{\underline{\mathbf{B}}}\right)\underline{\mathbf{I}} = \underline{\mathbf{V}}^{\text{inc}} \tag{3.17}$$

where the $N \times N$ matrix $\mathbf{Z}$ stores Eq. 3.18; $\mathbf{B}$ is the $N \times N$ correction matrix to the $\mathbf{Z}$'s near diagonal elements due to the impedance boundary condition and filled with Eq. 3.19; and $\mathbf{V}^{\text{inc}}$ is a $N \times 1$ vector storing the tested primary field shown in Eq. 3.20:

$$Z_{mn} = j\omega\mu\left(\mathbf{A}^{+}_{mn}\cdot\frac{\boldsymbol{\rho}^{\text{c}+}_{m}}{2} + \mathbf{A}^{-}_{mn}\cdot\frac{\boldsymbol{\rho}^{\text{c}-}_{m}}{2} + \phi^{-}_{mn} - \phi^{+}_{mn}\right) \tag{3.18}$$

$$B_{mn} = \frac{\boldsymbol{\Lambda}_n(\mathrm{r}^{\text{c}+}_{m})}{\sigma(\mathbf{r}^{\text{c}+}_{m})t(\mathbf{r}^{\text{c}+}_{m})}\cdot\frac{\boldsymbol{\rho}^{\text{c}+}_{m}}{2} + \frac{\boldsymbol{\Lambda}_n(\mathbf{r}^{\text{c}-}_{m})}{\sigma(\mathbf{r}^{\text{c}-}_{m})t(\mathbf{r}^{\text{c}-}_{m})}\cdot\frac{\boldsymbol{\rho}^{\text{c}-}_{m}}{2} \tag{3.19}$$

$$V^{\text{inc}}_{m} = \mathbf{E}^{\text{inc,c}+}_{m}\cdot\frac{\boldsymbol{\rho}^{\text{c}+}_{m}}{2} + \mathbf{E}^{\text{inc,c}-}_{m}\cdot\frac{\boldsymbol{\rho}^{\text{c}-}_{m}}{2} \tag{3.20}$$

Where

$$\mathbf{A}^{\pm}_{mn} = \iint_{S}\boldsymbol{\Lambda}_n(\mathbf{r}')G_{\text{R}}(\mathbf{r}^{\text{c}\pm}_{m},\mathbf{r}')\,dS' \tag{3.21}$$

$$\phi^{\pm}_{mn} = \frac{1}{k^2}\iint_{S}\nabla'\cdot\boldsymbol{\Lambda}_n(\mathbf{r}')G_{\text{R}}(\mathbf{r}^{c\pm}_{m},\mathbf{r}')\,dS' \tag{3.22}$$

and the corresponding incident electric fields (Balanis, 2005) are given as:

$$E^{\text{inc}}_{r} = E^{\text{inc}}_{\theta} = 0 \tag{3.23}$$

$$E^{\text{inc}}_{\phi} = M_{\text{TX}}\frac{\omega\mu k\sin\theta}{4\pi|\mathbf{r}-\mathbf{r}'|}\left[1+\frac{1}{jk|\mathbf{r}-\mathbf{r}'|}\right]e^{-jk|\mathbf{r}-\mathbf{r}'|} \tag{3.24}$$

where the fields are also multiplied with the rotation matrix to change to Cartesian coordinates. A Gaussian quadrature rule is applied to numerically solve the integral equations of Eq. 3.21 and 3.22. To avoid the singularity due to the Green's function, when $\mathbf{r}^{c\pm}_{m} = \mathbf{r}'$, the order of quadrature can be selected as 2, 4 and 6 (Fig. 3.2). To use the other orders of quadrature, the singularity in the center of a triangle can be avoided as shown in Kaur and Yilmaz (2011). In all presented results, the order of quadrature is selected to be 2.

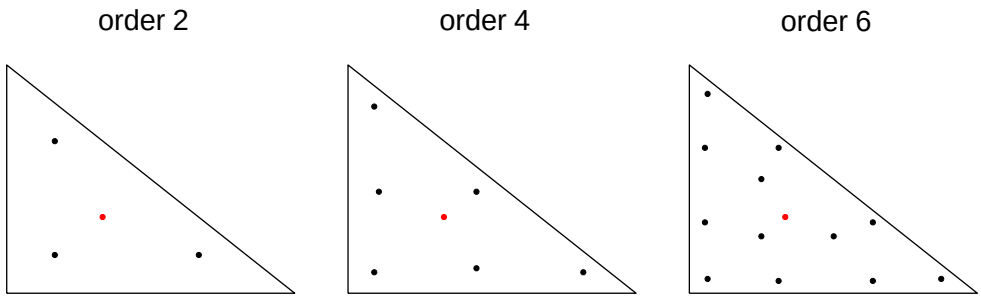

Figure 3.2: Gaussian quadrature of order 2, 4, and 6 for standard triangles: red dots are singularity points (center of triangles) and black dots are the points where integrals (Eqs. 3.21 and 3.22) are calculated.

The left-hand side of Eq. 3.17 is filled, factorized (LU-factorization) and stored for the next solution step. In the solution step, for each right-hand side of the same equation, unknowns are determined which are used to numerically compute $\mathbf{H}^{\text{sca}}$ with the following equation:

$$\mathbf{H}^{\text{sca}} = \iint_S \nabla G_{\text{R}}(\mathbf{r}, \mathbf{r}') \times \mathbf{J}_s(\mathbf{r}')\, dS' \tag{3.25}$$

where

$$\nabla G_{\text{R}}(\mathbf{r}, \mathbf{r}') = -\frac{G_{\text{R}}}{|\mathbf{r} - \mathbf{r}'|^2}(1 + jk|\mathbf{r} - \mathbf{r}'|)(\mathbf{r} - \mathbf{r}') \tag{3.26}$$

As in the matrix filling step, Gaussian quadrature of order 2 is used to solve the integral in Eq. 3.25.

3.2.2. Mesh Convergence

In this subsection, we are trying to understand the desired mesh density to get the required level of accuracy. The term λ is introduced which defines node spacing on the inner and outer circumferences of the circular fracture, e.g. the distance between two adjacent nodes on the circumference is equal to radius over λ. The node spacing factor, λ, is sampled in between 2 and 20. In Fig. 3.3, the absolute signal levels for small and large fracture sizes have been shown both for short and long spacing transmitter-receiver couples and for the node spacing factor of 20.

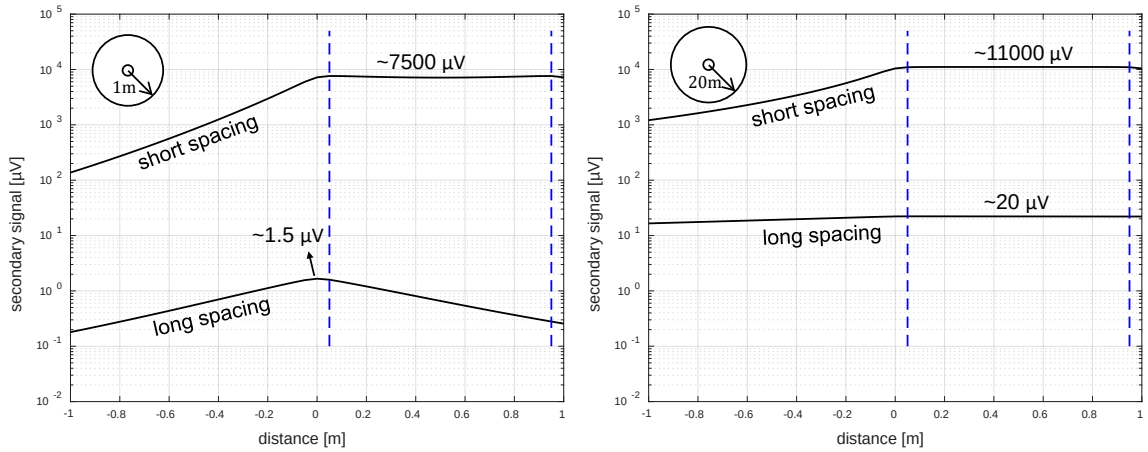

Figure 3.3: Absolute secondary signal levels for short ($\boldsymbol{l_{TR} = 1\ m}$) and long ($\boldsymbol{l_{TR} = 18\ m}$) spacing transmitter-receiver couples. Left and right plots show results for 1 **m** and 20 **m** outer radius orthogonal and circular fractures, respectively. In both cases, fracture inner radius is 6 **cm**, conductivity is 333 $\boldsymbol{S/m}$ and thickness is 5 **mm**; background (rock) conductivity is 0.333 $\boldsymbol{S/m}$; tool is operated at 1 **kHz** frequency with transmitting magnetic dipole moment of 1500 $\boldsymbol{A \cdot m^2}$; cross-sectional area of receiver is 30 $\boldsymbol{cm^2}$ and it has 600 turns.

The model with a division factor of 20 is the finest mesh and is selected to be the base case in the convergence analysis. The blue dashes in Fig. 3.3 show the interval where the values lying between those dashes are compared to the base case. The equation below defines the error in any iteration,

$$\epsilon = \frac{1}{N}\sqrt{\sum_{i=1}^{N}\left(U_{zz,i}^{\mathrm{sca}}(\lambda) - U_{zz,i}^{\mathrm{sca}}(20)\right)^2} \tag{3.27}$$

This error, ϵ, is shown in Fig. 3.4.

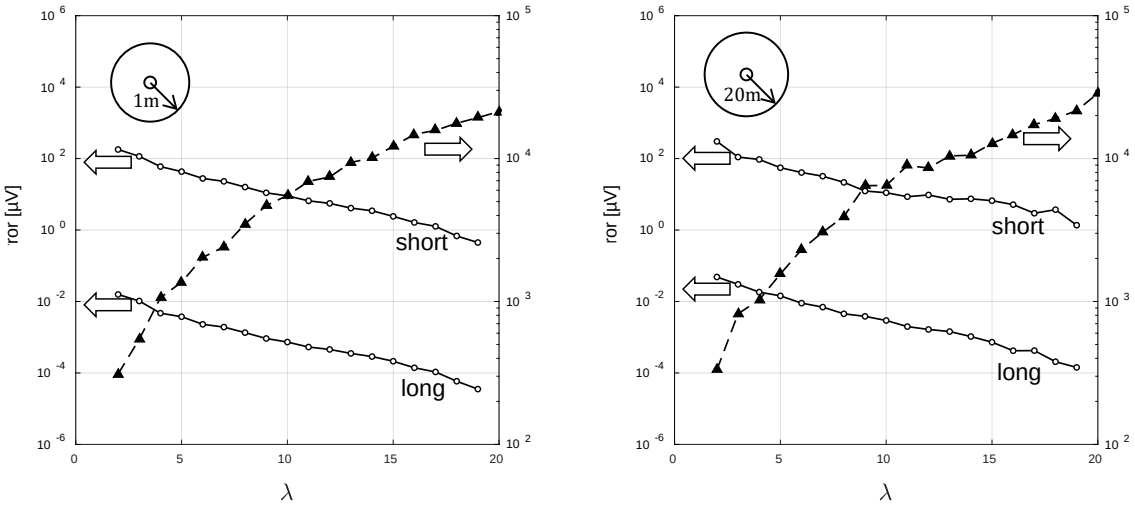

Figure 3.4: Convergence rate of the secondary signals with respect to the node spacing factor for short ($\boldsymbol{l_{TR} = 1\ m}$) and long ($\boldsymbol{l_{TR} = 18\ m}$) spacing transmitter-receiver couples. Left and right plots show results for 1 $\mathbf{m}$ and 20 $\mathbf{m}$ outer radius orthogonal and circular fractures, respectively. In both cases, fracture inner radius is 6 $\mathbf{cm}$, conductivity is 333 $\mathbf{S/m}$ and thickness is 5 $\mathbf{mm}$; background (rock) conductivity is 0.333 $\mathbf{S/m}$; tool is operated at 1 $\mathbf{kHz}$ frequency with transmitting magnetic dipole moment of 1500 $\mathbf{A \cdot m^2}$; cross-sectional area of receiver is 30 $\mathbf{cm^2}$ and it has 600 turns.

As it can be seen on the left plots of Fig. 3.3 and 3.4 the relative error is around 0.1% for short spacing and 0.05% for long spacing when the division factor is 10. This relative error percentage further decreases for the right plots of Fig. 3.3 and 3.4 suggesting that coarser meshes can be used to minimize the computation time which will be a factor to consider when multiple runs are required such as in the inversion analysis.

3.2.3. Model Validation

The solution of surface integral equations is compared to analytical and numerical models. First, analytical equations for the scattered magnetic field are shown where a plane wave is propagating toward a PEC sphere, and then the same case is simulated with our numerical model. Later, scattered signals are computed for a representative fracture model and compared to the numerical results of Yang et al. (2015).

3.2.3.1. Fields Calculated for Conducting Sphere

In this section, an analytical solution for the scattering of a plane wave by a conducting sphere is presented and compared to the results of the numerical tool. Given the PEC sphere with radius a at the origin of a spherical coordinate system and a plane wave propagating in the positive z-direction (Fig. 3.4), the scattering magnetic field outside of the sphere can be calculated with the following equations:

$$H_r^{\text{sca}} = H_0 \frac{\sin\phi}{j(kr)^2} \sum_{n=0}^{\infty} b_n n(n+1) \breve{H}_n^{(2)}(kr) P_n^1(\cos\theta) \tag{3.28}$$

$$H_\theta^{\text{sca}} = -H_0 \frac{\sin\phi}{kr} \sum_{n=1}^{\infty} \left[a_n \breve{H}_n^{(2)}(kr) \frac{P_n^1(\cos\theta)}{\sin\theta} + b_n j \breve{H}_n^{(2)\prime}(kr) \frac{dP_n^1(\cos\theta)}{d\theta} \right] \tag{3.29}$$

$$H_\phi^{\text{sca}} = -H_0 \frac{\cos\phi}{kr} \sum_{n=1}^{\infty} \left[a_n \breve{H}_n^{(2)}(kr) \frac{dP_n^1(\cos\theta)}{d\theta} + b_n j \breve{H}_n^{(2)\prime}(kr) \frac{P_n^1(\cos\theta)}{\sin\theta} \right] \tag{3.30}$$

where

$$a_n = -j^{-n} \frac{2n+1}{n(n+1)} \frac{\breve{J}_n'(ka)}{\breve{H}_n^{(2)\prime}(ka)} \tag{3.31}$$

$$b_n = -j^{-n} \frac{2n+1}{n(n+1)} \frac{\breve{J}_n(ka)}{\breve{H}_n^{(2)}(ka)} \tag{3.32}$$

A detailed explanation of these equations can be found in Jin (2010), subsection 7.4.3.

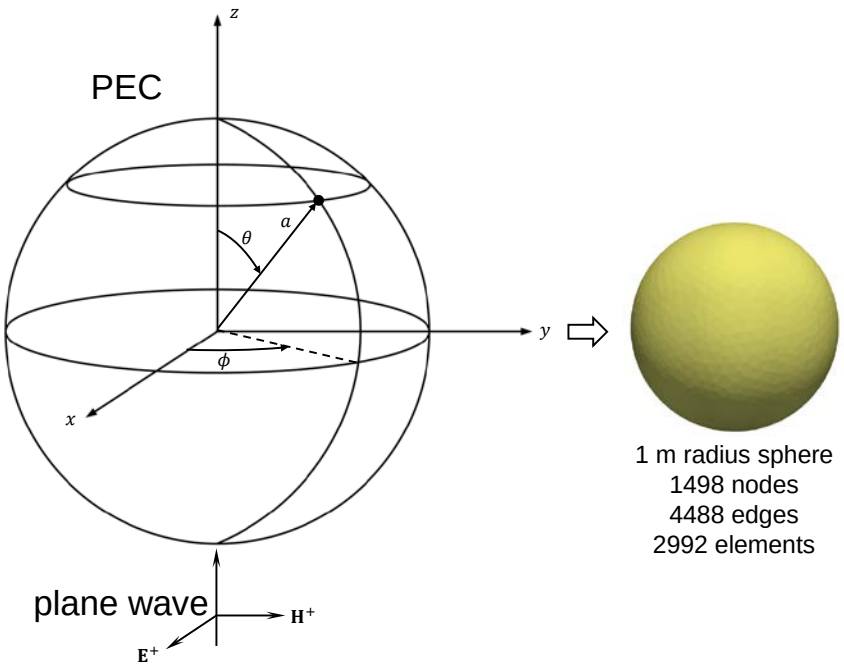

Figure 3.5: Plane wave scattering by a conducting sphere: a PEC sphere with radius $\boldsymbol{a}$ located at the center of spherical coordinate system and plane waves propagating in the positive *z*-direction; numerical surface discretization generated for the solver is shown to the right.

In the numerical calculations, to fill the vector $\underline{\mathbf{V}}^{\text{inc}}$, incident electric field is calculated with the following set of equations:

$$E_r^{\text{inc}} = E_0 \frac{\cos\phi}{j(kr)^2} \sum_{n=0}^{\infty} j^{-n}(2n+1)\check{J}_n(kr)P_n^1(\cos\theta) \tag{3.33}$$

$$E_\theta^{\text{inc}} = E_0 \frac{\cos\theta\cos\phi}{kr} \sum_{n=0}^{\infty} j^{-n}(2n+1)\check{J}_n(kr)P_n(\cos\theta) \tag{3.34}$$

$$E_\phi^{\text{inc}} = -E_0 \frac{\sin\phi}{kr} \sum_{n=0}^{\infty} j^{-n}(2n+1)\check{J}_n(kr)P_n(\cos\theta) \tag{3.35}$$

For the comparison, the PEC sphere is selected to be 1 m in radius (Fig. 3.4), observer points are on the $r = 2\,\text{m}$, $0 < \theta < \pi$ and $\phi = 90°$ line, the background is air (zero electrical conductivity), frequency is 100 MHz, and $E_0 = 1$ where $H_0 = E_0/\eta$. Fig. 3.6 shows results for both real and imaginary components of the scattered magnetic field. Note that since ϕ is selected to be 90 degrees, H_ϕ^{sca} is always zero as can be seen in Eq. 3.30. The sufficient level of the agreement obtained for both components of the magnetic field increases the confidence in the

numerical tool. In the next subsection, further validation study is carried for the representative model and incident signals.

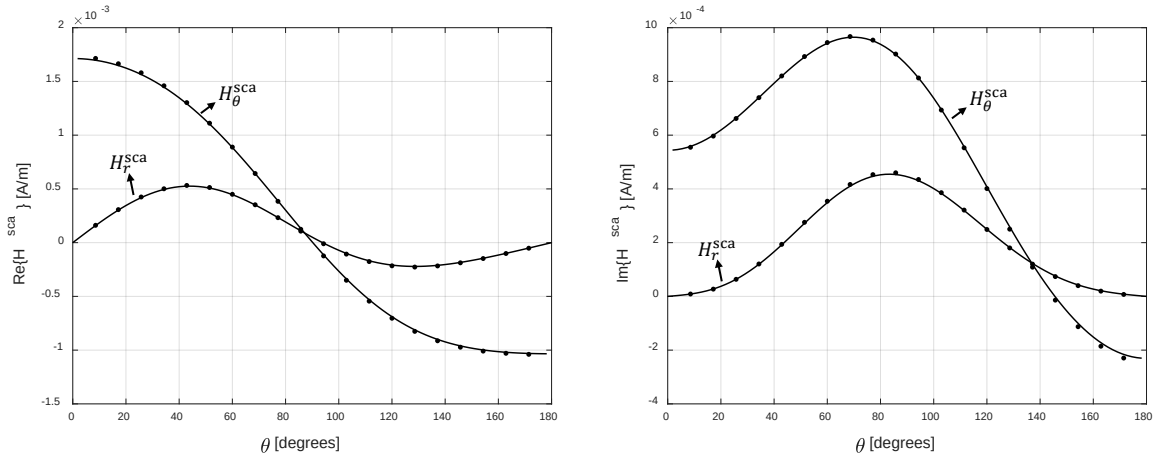

Figure 3.6: Comparison of analytical (solid line) and SIE solution (dots) of scattering from a meter radius PEC sphere; real (left) and imaginary (right) components of scattered magnetic fields are calculated for the observation points on the $\boldsymbol{r = 2\ \mathrm{m},\ 0 < \theta < \pi}$ and $\boldsymbol{\phi = 90°}$ line.

3.2.3.2. Numerical Results for a Representative Model

The iterative solution of the volume integral equations (Yang et al., 2015) was tested. The simulated orthogonal fracture model is a circle with an outer radius of 3 m, inner radius of 10 cm, thickness of 5 mm, and conductivity of 30 S/m. The background formation has a uniform conductivity of 0.333 S/m. The tool is operated at 100 Hz frequency with 1500 $\mathrm{A \cdot m^2}$ magnetic dipole moment on the transmitter coil. The receiver coil has 30 $\mathrm{cm^2}$ cross-sectional area and 600 wire turns. The spacing between transmitter and receiver coil is 1.2 m.

In the generated volume mesh, there are 57,808 unknowns, and the solution for VIE is obtained in about 2 minutes with 512 parallel processors. There are 6420 unknowns in the generated surface mesh, and the solution for SIE is obtained in a minute with a single processor. Numerical results are shown in Fig. 3.7 where signal levels are shown with a solid line for the solution of surface integral equations (SIE) and absolute differences with the VIE are shown with dashed lines. For the real (blue) and imaginary (black) component of secondary signals it shows very good agreement for both numerical results, with a maximum discrepancy of less than 5%. It is important to note the significant dominance of real components over the imaginary signals.

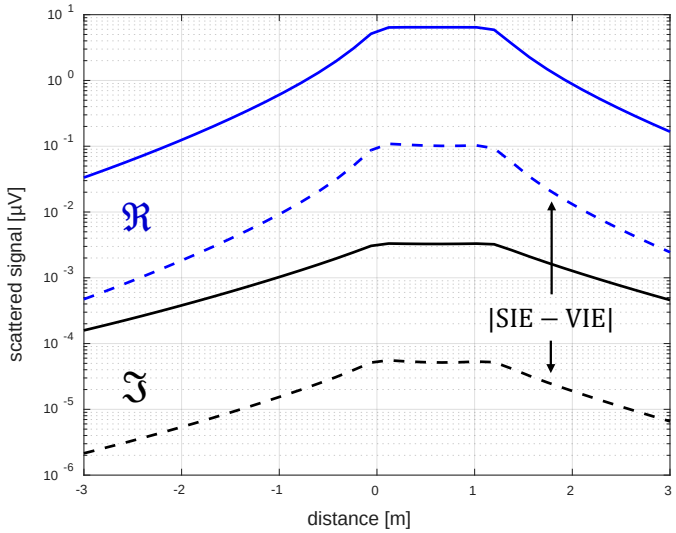

Figure 3.7: Comparison of SIE and VIE solutions of scattering from a representative fracture model; solid lines show the real (blue) and imaginary (black) components of absolute secondary (scattered) signals for the SIE solution; dashed lines show the absolute differences between both solutions.

3.2.4. In-Phase and Quadrature Components of Signals

Following the observation made in the previous section (high ratio of real and imaginary components), in this section, the parameters affecting this ratio are investigated. Fig. 3.8 shows the signal levels at the middle of the hump (Fig. 3.7) for the different conductivity of fracture and background formation at the operating frequency of 1 kHz. The fracture conductivity ranges between 10 and 10^4 S/m, and the background conductivity ranges between 10^{-2} and 1 S/m. The fracture is 1 m in radius and is assumed to be an orthogonal circle with 10 cm of inner radius and 5 mm thickness. The magnetic dipole moment of the transmitter coil is 1500 $A \cdot m^2$. The receiver coil has 30 cm^2 cross-sectional area and 600 wire turns. The spacing between the transmitter and receiver coil is 1 m.

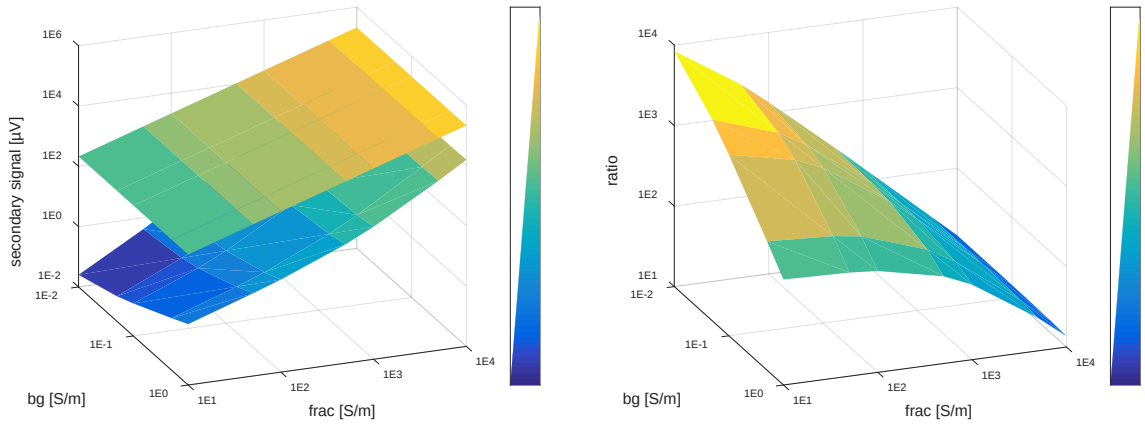

Figure 3.8: The relationship between real and imaginary components of secondary signals with changing background (bg) and fracture (frac) conductivity: left plot shows both real and imaginary components on upper and lower surfaces, respectively; right plot shows the ratio between them.

An increase in the background conductivity does not affect the real component; however, it increases the imaginary component of the signal. An increase in the fracture conductivity increases both real and imaginary components. The ratio between them $|\Re(U^{\mathrm{sca}})/\Im(U^{\mathrm{sca}})|$ stays above 10 for the selected region clearly showing the dominance of real components in the absolute signals. This may lead to a simplification in the forward model which is described in the next subsection.

3.2.5. Approximation of Surface Currents

In the previous section, the dominance of the real component is shown for an operating frequency of 1 kHz. If the magnitude of the signal is of interest, then the accurate calculation of only the real component is sufficient for the detailed analysis. It can be achieved with the simplification in the boundary condition shown in Eq. 3.12. If the scattered electric field is eliminated surface currents can be approximated as follows:

$$\mathrm{J}_{\boldsymbol{s}} \approx -\hat{\mathrm{n}} \times \hat{\mathrm{n}} \times \boldsymbol{G}\mathrm{E}^{\mathbf{inc}} \tag{3.36}$$

This procedure does not require inversion of the matrices and reduces computational time. The accuracy level is shown for orthogonal and rotated fracture models with metallic conductivity (the conductivity and thickness of 34.6 MS/m and 25.4 μm, respectively) and smaller size (this type of model is used in the next chapter). Transmitter coil is operated at 1 kHz frequency, and the magnetic dipole moment is 12 A · m^2; receiver coil has the cross section of 30 cm^2 with 600 turns. The background has zero conductivity and the distance between transmitter and receiver coils is 1 m. Fig. 3.9 shows secondary signal magnitude for co-axial coil configuration and 10 cm radius orthogonal fracture. The relative error introduced due to the surface current approximation is always less than 1% along the sampling interval.

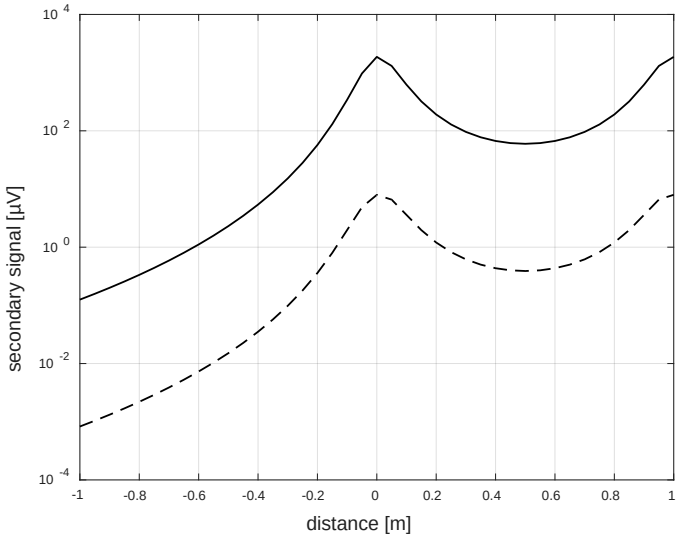

Figure 3.9: Magnitude of secondary signals when surface currents are approximated: solid line shows the full SIE solution; dashed line shows the difference between the approximation-based solution and full computation. The fracture model is orthogonal and coils are in co-axial configuration.

Fig. 3.10 shows secondary signal magnitude for the co-axial (left) and cross-polarized (right) coil configurations and for 20 cm radius fracture rotated 30˚ about the *x*-axis. The relative error introduced due to the surface current approximation is always less than 10% for the co-axial coil configuration. For the cross-polarized configuration, however, approximation simulates the trend only; there is a poor quantitative match.

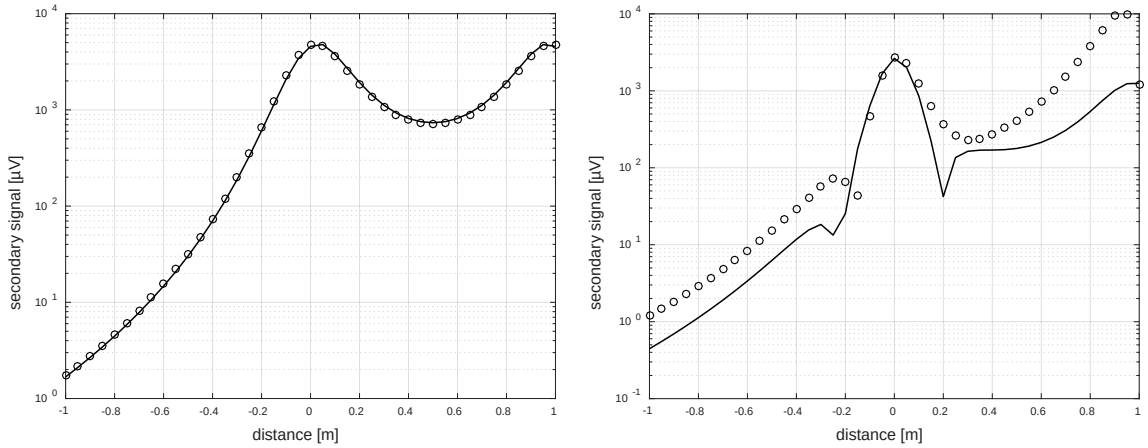

Figure 3.10: Magnitude of secondary signals when surface currents are approximated: solid line shows the full SIE solution; and circle markers show the approximation based solution. The fracture model is rotated and coils are in co-axial (left) and cross-polarized (right) configurations.

3.2.6. Computational Time

In this section, the computational time required for a typical run is explored. Fig. 3.11 shows the time required for the full numerical solution of SIE with an impedance boundary condition. Its solution has two stages: filling the impedance matrix and solving it for every excitation point. The first step dominates the computation time because integral equations yield a full matrix. LU-factorization of the matrix occurs once in a typical run, hence, for multiple excitation points, the total sampling time (factorization + solution for all excitations) is divided by the number of excitation points which is equal to 82 in this case. This step can be further accelerated by using numerical iterative solvers or parallelization.

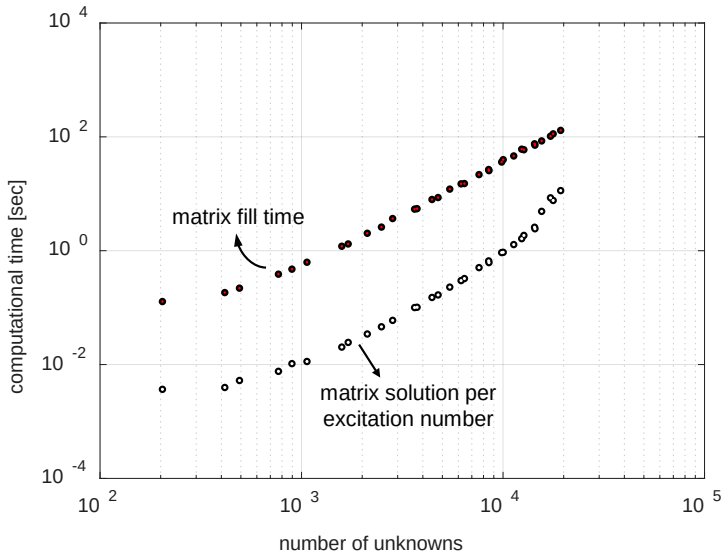

Figure 3.11: Computation time for the different number of surface unknowns: red filled circles show matrix fill-times which includes the application of impedance boundary condition as well, and empty circles show matrix solution times for each sampling point.

A typical run for the fracture size of 20 m yields 5,000-10,000 unknowns with λ being equal to 10. This problem can be solved in a minute. For the inversion analysis, the speed can be further increased by using coarser meshes.

3.3. Simulation of Induction Tool Response in Production Casing

In this computation, the set of 2D problems emerging from the Fourier series expansion is solved with an axial hybrid method where the wellbore axis (z-axis) is solved numerically and the radial part is solved analytically. After solving the generalized eigenvalue problem, normalized Bessel and Hankel functions are used to describe the fields in the radial direction. Amplitude and slope basis functions are defined over the discretized wellbore axis which allows the use of a coarse grid everywhere along the axis. This eliminates the need to refine the grid in the vicinity of the

fracture. Before proceeding to the numerical results, the detailed steps of the computation are shown below (Wang et al., 2009), and the results are compared to that of the surface integral equations.

3.3.1. Axial Hybrid Method

In any radial layer, the electric and magnetic fields in the *z*-direction can be expressed with the following governing equations:

$$\nabla_s^2 E_z + \frac{\partial}{\partial z}\sigma_s^{-1}\frac{\partial}{\partial z}\sigma_z E_z - j\omega\mu_o\mu_{r,s}\sigma_z E_z = \nabla_s \cdot (\mathbf{M}_s \times \hat{z}) \tag{3.37}$$

and

$$\nabla_s^2 H_z + \frac{\partial}{\partial z}\mu_{r,s}^{-1}\frac{\partial}{\partial z}\mu_{r,z} H_z - j\omega\mu_o\sigma_s\mu_{r,z} H_z = \sigma_s M_z - \frac{1}{j\omega\mu_o}\frac{\partial}{\partial z}\mu_{r,s}^{-1}\nabla \cdot \mathbf{M} \tag{3.38}$$

where the subscript s designates the transverse component and z shows the wellbore direction. Excluding the source terms in the above equations they can both be written in the following form:

$$\nabla_s^2 p_\eta^{-1} f_\eta + \frac{\partial}{\partial z} q_\eta^{-1}\frac{\partial f_\eta}{\partial z} + k_\eta^2 p_\eta^{-1} f_\eta = 0 \tag{3.39}$$

where $f_\eta = \{\sigma_z E_z, \mu_{r,z} H_z\}$, $p_\eta = \{\sigma_z, \mu_{r,z}\}$, $q_\eta = \{\sigma_s, \mu_{r,s}\}$, $k_\eta^2 = -j\omega\mu_o\{q_h p_e, q_e p_h\}$ and $\eta = \{e, h\}$. The ϕ variation of f_η is expressed in terms of a Fourier series. The solution of ρ dependence is obtained after solving the generalized eigenvalue problem, and it is in the form of a combination of normalized Bessel functions of the first kind $\hat{J}_n$ and the normalized Hankel function $\hat{H}_n^{(1)}$. To solve the z dependence, basis functions are defined over one-dimensional elements along the *z*-axis. Local shape functions of each element are defined in the interval of (z_n, z_{n+1}) as follows:

$$L_1 = \frac{z_{n+1} - z}{z_{n+1} - z_n} \tag{3.40a}$$

$$L_2 = \frac{z - z_n}{z_{n+1} - z_n} \tag{3.40b}$$

and all elements, except the first and last one, have four basis functions defined as follows:

$$g_{\eta,1}(z) = -2L_1^3 + 3L_1^2 \tag{3.41a}$$

$$g_{\eta,2}(z) = q_\eta(z)\Delta z(z)L_1^2 L_2 \tag{3.41b}$$

$$g_{\eta,3}(z) = -2L_2^3 + 3L_2^2 \tag{3.41c}$$

$$g_{\eta,4}(z) = -q_\eta(z)\Delta z(z)L_2^2 L_1 \tag{3.41d}$$

Fig. 3.12 shows these basis functions (Eq. 3.41) when q_η is unity. For the first element only 2.41c, d and for the last element only 2.38 a, b are defined. Each basis function is non-zero over two neighbor elements; $g_{\eta,1}$ and $g_{\eta,2}$ are non-zero on the neighbor element in the negative z-direction, and $g_{\eta,3}$ and $g_{\eta,4}$ are non-zero on the neighbor element in the positive z-direction. Hence, if we have N_n number of nodes, we get $N_e = N_n - 1$ number of elements and $N = 2(N_n - 2)$ total number of basis functions.

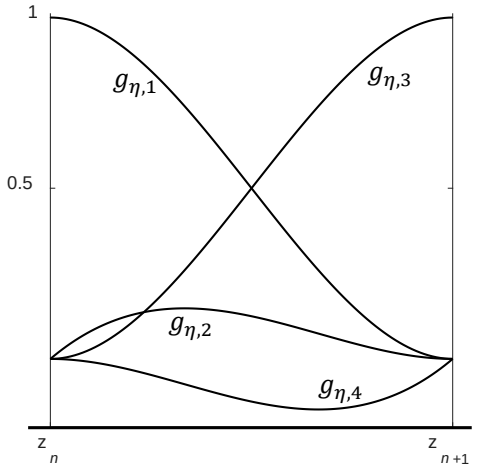

Figure 3.12: Basis functions defined over a one-dimensional element along the wellbore axis; relative permeability of one is used.

The solution of Eq. 3.39 is obtained after solving the generalized eigenvalue problem which is defined with the following equation:

$$\mathbf{A}_\eta \mathbf{C}_\eta = \mathbf{B}_\eta \mathbf{C}_\eta \mathbf{\Lambda}_\eta^2 \tag{3.42}$$

where $\mathbf{C}_\eta$ is the matrix of eigenvectors, $\mathbf{\Lambda}_\eta$ is the diagonal matrix of eigenvalues and $\mathbf{A}_\eta$ and $\mathbf{B}_\eta$ are defined as:

$$\mathbf{A}_\eta = -\int_{-\infty}^{\infty} \frac{1}{q_\eta} \frac{\partial \mathbf{g}_\eta(z)}{\partial z} \frac{\partial \mathbf{g}_\eta^t(z)}{\partial z} dz + \int_{-\infty}^{\infty} \frac{k_\eta^2}{p_\eta} \mathbf{g}_\eta(z) \mathbf{g}_\eta^t(z) dz \tag{3.43}$$

and

$$\mathbf{B}_\eta = \int_{-\infty}^{\infty} \frac{1}{p_\eta} \mathbf{g}_\eta(z) \mathbf{g}_\eta^t(z) dz \tag{3.44}$$

Integrals in Eq. 3.43 and 3.44 are solved analytically for each element. $\mathbf{A}_\eta$ and $\mathbf{B}_\eta$ are six-diagonal matrices and $N \times N$ in dimensions. It should be emphasized that the orthogonality relationship still holds for the numerical eigenmodes. Hence, the following equation must be satisfied:

$$\mathbf{C}_\eta^t \mathbf{B}_\eta \mathbf{C}_\eta = \mathbf{I} \tag{3.45}$$

Now, the solution to Eq. 3.39 for each layer can be expressed in the form of basis functions (Eq. 3.41), eigenvalues and eigenvectors (Eq. 3.42), and normalized Bessel and Hankel functions. Then, in each radial boundary, local transmission and reflection matrices are defined as:

$$\mathbf{T}_{l,l\pm1} = \left[\boldsymbol{\beta}_{(l\pm1)\mp}^{\pm} - \boldsymbol{\beta}_{(l)\pm}^{\mp} \mathbf{P}_{l,\underline{l\pm1}}\right]^{-1} \left[\boldsymbol{\beta}_{(l)\pm}^{\pm} - \boldsymbol{\beta}_{(l)\pm}^{\mp}\right] \tag{3.46}$$

and

$$\mathbf{R}_{l,l\pm1} = \mathbf{P}_{l,\underline{l\pm1}} \mathbf{T}_{l,l\pm1} - \mathbf{I} \tag{3.47}$$

where l represents the number of layer. In the above,

$$\boldsymbol{\beta}_{(k)\pm}^{\pm} = \begin{pmatrix} -j\frac{n}{\rho}\mathbf{D}_{he,l,k} & j\omega\mu_0 \mathbf{P}_{h,\underline{l},k} \boldsymbol{\chi}_{h,(k)\pm}^{\pm} \boldsymbol{\Lambda}_{h,k} \\ -\mathbf{P}_{e,\underline{l},k} \boldsymbol{\chi}_{e,(k)\pm}^{\pm} \boldsymbol{\Lambda}_{e,k} & -j\frac{n}{\rho}\mathbf{D}_{eh,l,k} \end{pmatrix} \boldsymbol{\Lambda}_k^{-2} \tag{3.48}$$

and

$$\mathbf{P}_{\eta,l,\underline{k}} = \mathbf{C}_{\eta,l}^t \int_{-\infty}^{\infty} \frac{1}{p_{\eta,k}} \mathbf{g}_{\eta,l} \mathbf{g}_{\eta,k}^t dz \, \mathbf{C}_{\eta,k} \tag{3.49}$$

$$\mathbf{P}_{\eta,\underline{l},k} = \mathbf{C}_{\eta,l}^{t} \int_{-\infty}^{\infty} \frac{1}{p_{\eta,l}} \mathbf{g}_{\eta,l} \mathbf{g}_{\eta,k}^{t} dz \, \mathbf{C}_{\eta,k} \tag{3.50}$$

$$\mathbf{D}_{he,l,k} = \mathbf{C}_{h,l}^{t} \int_{-\infty}^{\infty} \frac{1}{p_{h,l} q_{e,k}} \mathbf{g}_{\eta,l} \frac{\partial}{\partial z} \mathbf{g}_{\eta,k}^{t} dz \, \mathbf{C}_{e,k} \tag{3.51}$$

$$\mathbf{D}_{eh,l,k} = \mathbf{C}_{e,l}^{t} \int_{-\infty}^{\infty} \frac{1}{p_{e,l} q_{h,k}} \mathbf{g}_{e,l} \frac{\partial}{\partial z} \mathbf{g}_{h,k}^{t} dz \, \mathbf{C}_{h,k} \tag{3.52}$$

where $k = l$ or $l \pm 1$. Note that when $k = l$ $\mathbf{P}_{\eta,l,\underline{k}} = \mathbf{I}$ and $\mathbf{P}_{\eta,\underline{l},k} = \mathbf{I}$. In the outermost layer, there is no incoming wave. Starting with this we can calculate a generalized reflection matrix at the wellbore $\mathbf{Q}_1^+$ by using recursive relationships:

$$\mathbf{S}_{m,m+1} = \left[\mathbf{I} - \mathbf{R}_{m+1,m} \mathbf{Q}_{(m+1)-}^{+}\right]^{-1} \mathbf{T}_{m,m+1} \tag{3.53}$$

$$\mathbf{Q}_{(m)+}^{+} = \mathbf{R}_{m,m+1} + \mathbf{T}_{m+1,m} \mathbf{Q}_{(m+1)-}^{+} \mathbf{S}_{m,m+1} \tag{3.54}$$

along with the propagation relationship:

$$\mathbf{Q}_m^+(\rho_a) = \boldsymbol{\gamma}_m^-(\rho_a, \rho_b) \mathbf{Q}_m^+(\rho_b) \boldsymbol{\gamma}_m^+(\rho_a, \rho_b) \tag{3.55}$$

Where

$$\boldsymbol{\gamma}_m^+(\rho_a, \rho_b) = e^{-j\boldsymbol{\Lambda}_m(\rho_b - \rho_a)} \frac{\widehat{\mathbf{H}}_n^{(1)}(\boldsymbol{\Lambda}_m \rho_b)}{\widehat{\mathbf{H}}_n^{(1)}(\boldsymbol{\Lambda}_m \rho_a)} \tag{3.56}$$

$$\boldsymbol{\gamma}_m^-(\rho_a, \rho_b) = e^{-j\boldsymbol{\Lambda}_m(\rho_b - \rho_a)} \frac{\hat{\mathbf{J}}_n(\boldsymbol{\Lambda}_m \rho_a)}{\hat{\mathbf{J}}_n(\boldsymbol{\Lambda}_m \rho_b)} \tag{3.57}$$

For the magnetic dipole oriented in the wellbore direction and when $\rho' = \rho_{\mathrm{TX}} = \rho_{\mathrm{RX}}$:

$$\mathbf{b}_h = \frac{jM_{\mathrm{TX}}}{4p_{h,1}(z_{\mathrm{TX}})} \widehat{\mathbf{H}}_n^{(1)}\left(\boldsymbol{\Lambda}_{h,1}\rho'\right) \hat{\mathbf{J}}_n\left(\boldsymbol{\Lambda}_{h,1}\rho'\right) \boldsymbol{\Lambda}_{h,1}^2 \mathbf{C}_{h,1}^{t} \mathbf{g}_{h,1}(z_{\mathrm{TX}}) \tag{3.58}$$

and magnetic field will be given by:

$$H_z^{\mathrm{inc}} = \frac{1}{p_{h,1}(z_{\mathrm{RX}})} \mathbf{g}_{h,1}^{t}(z_{\mathrm{RX}}) \mathbf{C}_{h,1} \mathbf{b}_h \tag{3.59}$$

$$H_z^{\mathrm{sca}} = \frac{1}{p_{h,1}(z_{\mathrm{RX}})} \mathbf{g}_{h,1}^{t}(z_{\mathrm{RX}}) \mathbf{C}_{h,1} \mathbf{Q}_{h,1}^{+} \mathbf{b}_h \tag{3.60}$$

As in the previous method, Eq. 3.59 and 3.60 are solved for different excitation points.

3.3.2. Numerical Validation

The simulated orthogonal fracture model is a circle with an outer radius of 8 m, inner radius of 10 cm, thickness of 5 mm and conductivity of 333 S/m. The background (rock) formation has a uniform conductivity of 0.333 S/m. The tool is operated at 1 kHz frequency with 1500 $\mathrm{A \cdot m^2}$ magnetic dipole moment on the transmitter coil. The receiver coil has 30 $\mathrm{cm^2}$ cross-sectional area and 600 turns. The spacing between transmitter and receiver coils is 1.2 m for the short spacing and 17.8 m for the long coil spacing. For the method of moments, the total computation time is 70 seconds with 8220 unknowns and 82 sampling points.

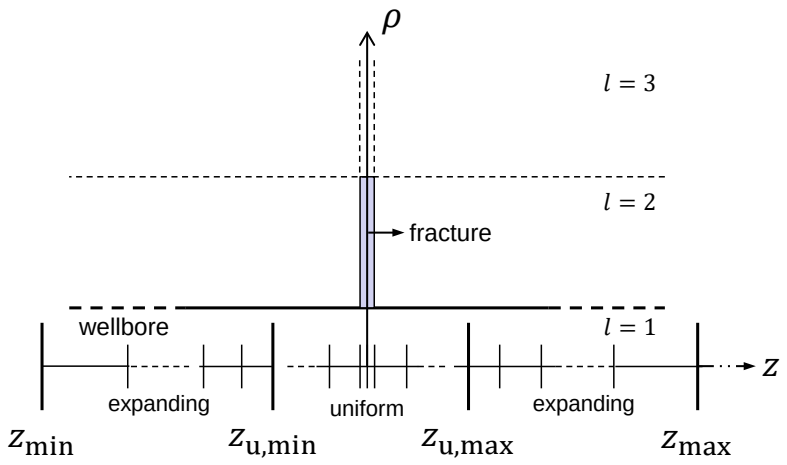

Figure 3.13: Meshing and radial layering scheme used in the axial hybrid method for the computation of fracture scattering in an open-hole completion.

The gridding scheme used in the mode matching technique is shown in Fig. 3.13. A uniform grid is implemented between -2 and 2 m with an element size of 10 cm. The 5 mm thickness of fracture is an additional orthogonal layer. The domain is truncated at 150 m on both expanding parts of the grid with a 1.25 length ratio between two adjacent elements. The total number of basis functions is 274. The solution with 82 sampling points and with this gridding scheme is obtained in 10 seconds.

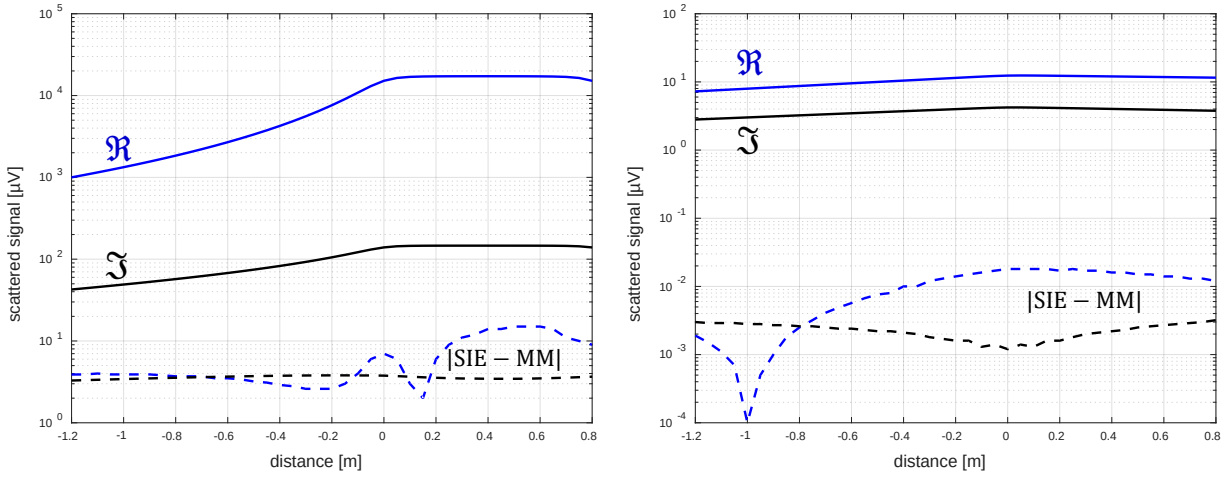

Figure 3.14: Comparison of MM and SIE solution of fracture scattering measured with short spacing (left plot) and long spacing (right plot) couples; solid lines show the real (blue) and imaginary (black) components of absolute secondary (scattered) signals for the SIE solution; dashed lines show the absolute difference between both solutions.

Numerical results are shown in Fig. 3.14 where signal levels are shown with a solid line for the solution of surface integral equations (SIE) and absolute differences with the mode matching (MM) are shown with dashed lines. For the real (blue) and imaginary (black) component of secondary signals, Fig. 3.14 shows very good agreement for both short and long spacing couples, with a maximum discrepancy of less than 3% for the peak signals.

3.3.3. Effect of Electromagnetic Properties of Casing on Differential Signals

An additional radial layer is added to the previously used scheme to include production casing material properties. Fig. 3.15 shows the meshing and layering scheme used for understanding the effect of the casing electrical conductivity and magnetic permeability on the scattered field from the fracture. The fracture is an additional layer orthogonal to the wellbore axis with the radius of 8 m, thickness of 5 mm and conductivity of 333 S/m (conductivity anywhere else is 0.333 S/m). The inner and outer radius of the casing pipe is 6.2 and 7 cm, respectively. The wellbore axis is discretized from -15 and 15 m, where the uniform part of the meshing is between -2 and 2 m with the ratio of element size of 1.25 in the expanding part. The total number of basis functions is 230. The tool operating frequency is 1 kHz and the transmitter magnetic dipole moment is 1500 $A \cdot m^2$. The number of turns on the receiver is 600 with 30 cm^2 cross-sectional area. The spacings between the transmitter and receiver coils are 1.2 and 1.5 m.

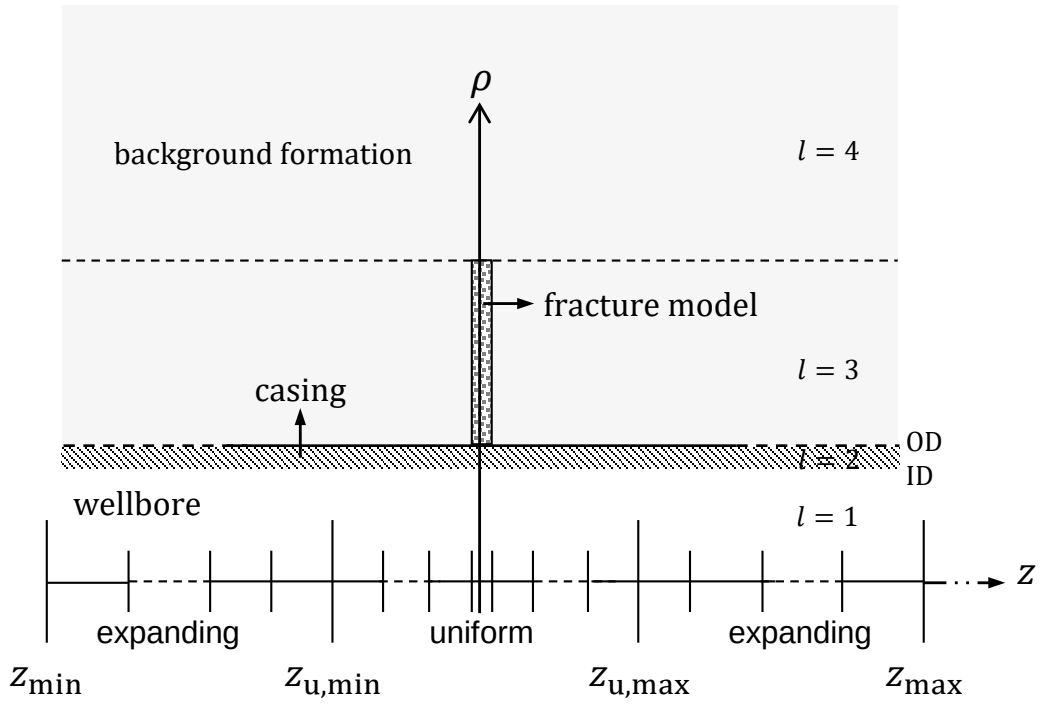

Figure 3.15: Meshing and radial layering scheme used in the axial hybrid method for the computation of fracture scattering in a cased-hole completion.

Fig. 3.16 shows the short spacing differential signals when the electrical conductivity of the casing pipe increases from 10^1 to 10^5 S/m, and the relative magnetic permeability is one. Fig. 3.17 shows the same signals when the relative magnetic permeability of the casing pipe increases from 1 to 30, and the electrical conductivity is 10^5 S/m. The left column plots show the differential signals from the casing (no-frac case), and the right column plots show the differential signals from the fracture (subtraction of frac and no-frac cases). For the given tool parameters and 0.333 S/m background (rock) conductivity, the real and imaginary components of incident signals are ~$4.4 \cdot 10^3$ μV and $3.4 \cdot 10^6$ μV, respectively.

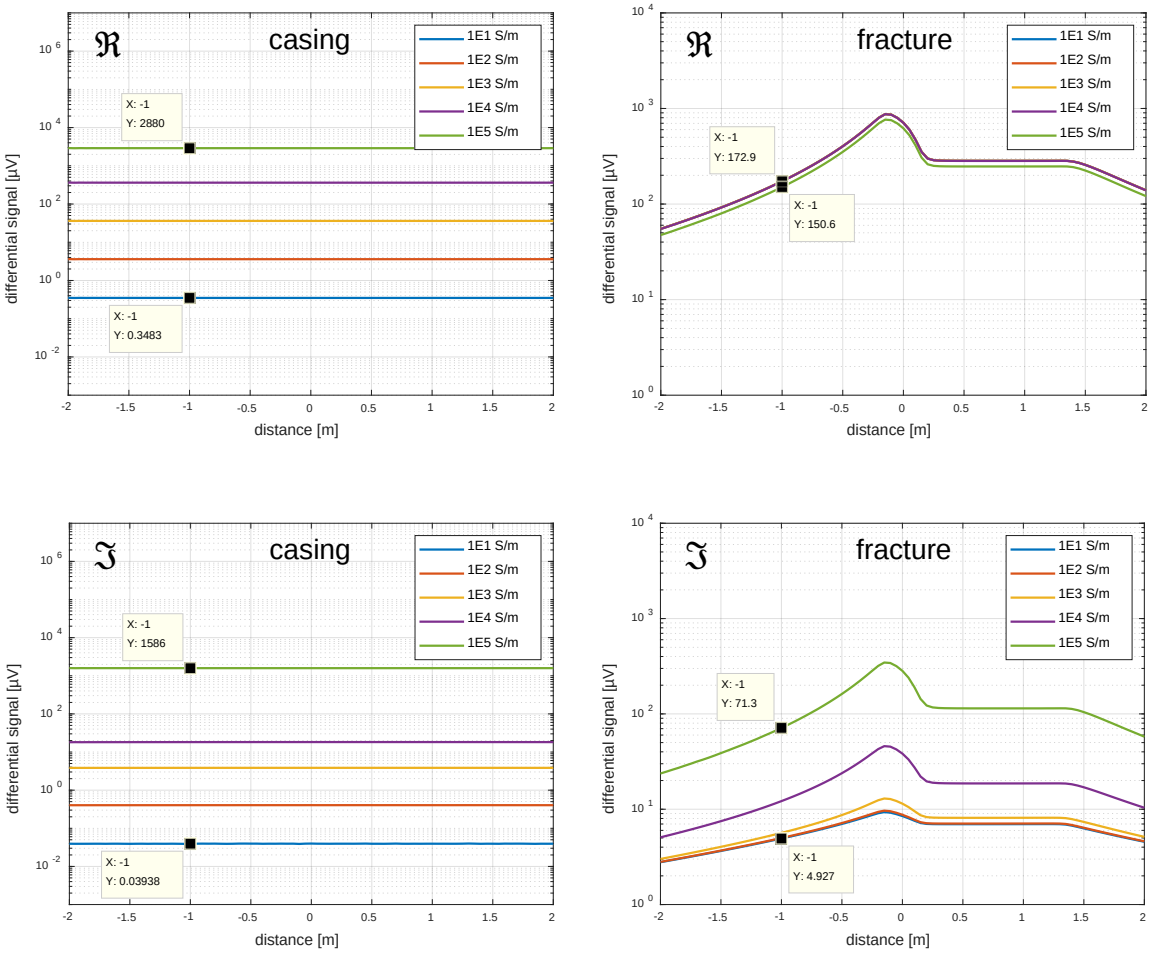

Figure 3.16: The effect of electrical conductivity of casing on the differential signals: left and right columns show differential signals for casing and fracture; and upper and lower plots show real and imaginary components of differential signals, respectively.

The increase in the electrical conductivity causes the scattered voltages from the casing to increase significantly suppressing the comparatively small fracture scattered voltages. For the 10^4 times increase in the electrical conductivity, real and imaginary components of primary signals increase ~10^4 and ~$4 \cdot 10^4$, respectively. The real components of the differential signals due to scattering by the fracture, however, are not affected by the increase. The imaginary components of fracture differential signals are increased ~15 times and get closer to the level of the real components.

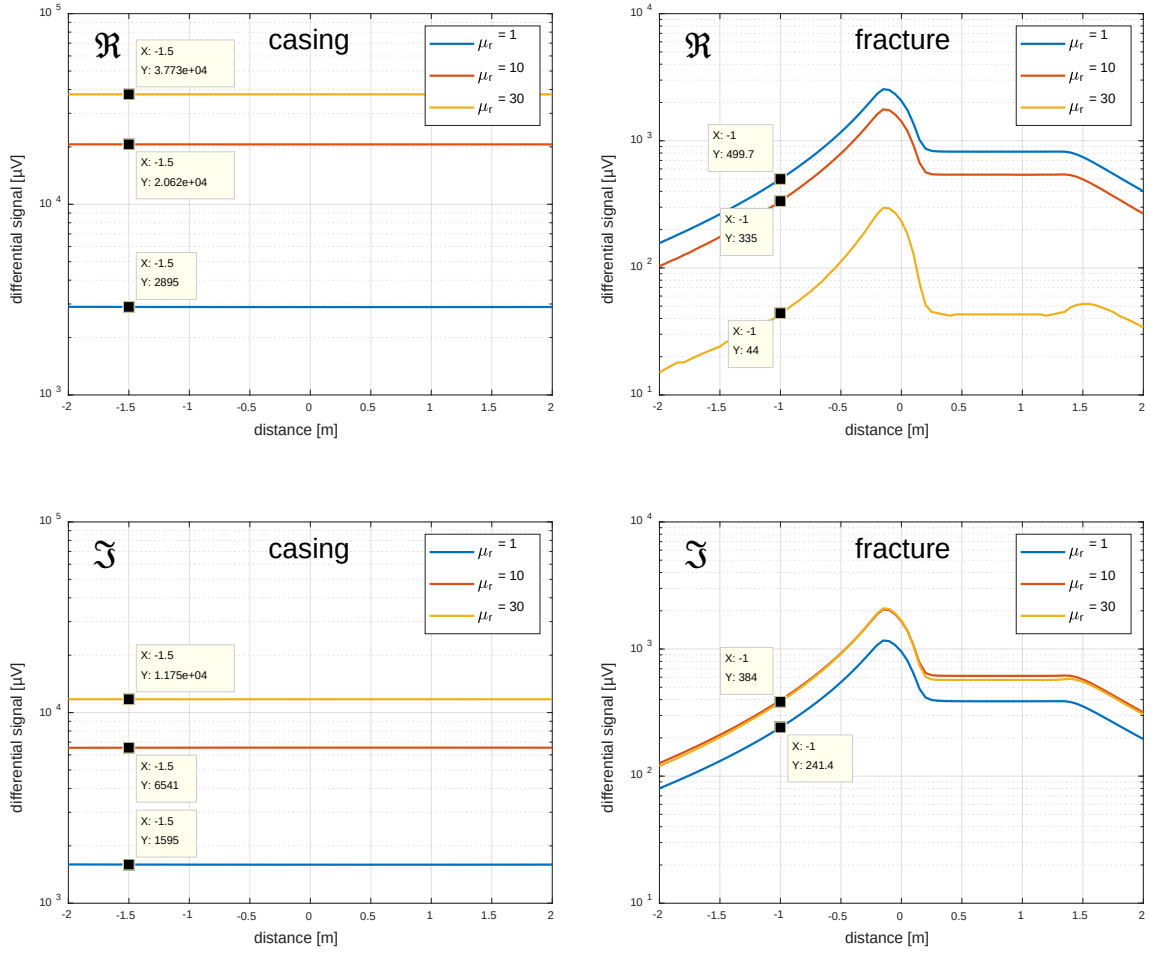

Figure 3.17: The effect of magnetic permeability of casing on the differential signals: left and right columns show differential signals for casing and fracture; and upper and lower plots show real and imaginary components of differential signals, respectively.

The same observation is made for the relative magnetic permeability increase which causes a significant increase in the primary signals. For the 30 times increase in the relative magnetic permeability, real and imaginary components of primary signals are increased ~15 and ~8 times, respectively. The real components of the differential signals due to the fracture scattering, however, are decreased ~11 times and there is only a slight increase (~1.6 times) in the imaginary components.

3.3.4. Computational Time

In this section, the computational time required for different runs are reported. Fig. 3.18 shows the time requirement for the solution steps of axial hybrid method for the different number of basis functions. The first step is the solution of the generalized eigenvalue problem; the second is the calculation of the generalized refraction matrix; and the third step is the solution for the scattered

signals at different sampling points. As indicated previously, a typical run can be completed with a few hundred basis functions.

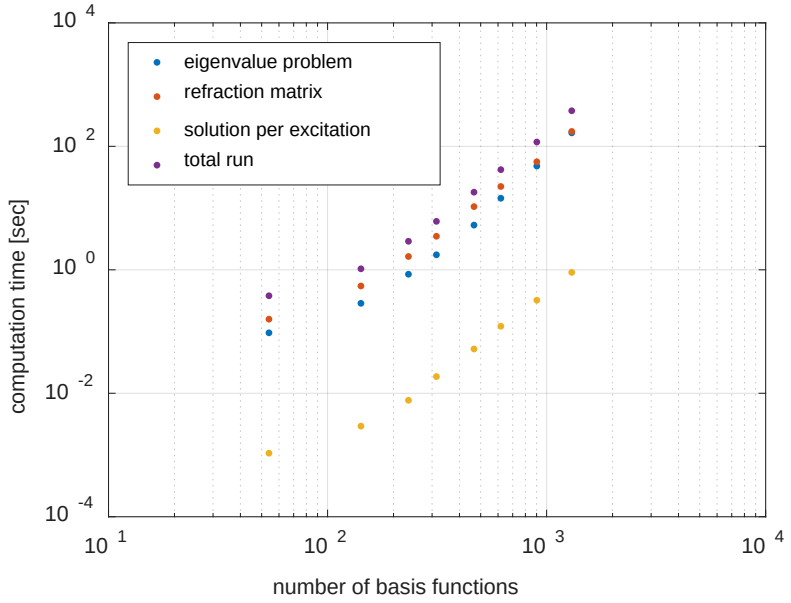

Figure 3.18: Computation time for different number of basis functions: blue dots show the generalized eigenvalue solution time for all layers; red dots show the generalized refraction matrix solution time; orange dots show the solution time for each sampling point and purple dots show the total run time for all 41 sampling points.

3.4. CONCLUSION

In this chapter, the formulation and numerical schemes that allow us to solve Maxwell's equations in 3-D for the fracture geometries of interest are presented. The numerical results are validated and the computational requirements for a typical fracture simulation are reported. The models allow us to include all the possible variations in electromagnetic properties inside and outside the fracture. An open-hole application of the induction tool can be best modeled with integral equations where the effect of fracture shape factor and rotation about the wellbore axis can be captured. A hybrid method can provide very time efficient results when the induction tool is logged inside the casing. The model development was done using Matlab. The key findings are:

- The method of moment solution of surface integral equations provides very accurate results with the node spacing less than ten and a typical run takes about one minute when a single core is used for the computation.
- The fracture is simulated as an impedance sheet and all the permittivity and conductivity variation can be handled using this simulation. Since it is fast and includes all relevant fracture parameters, it is better suited for use with the inversion analysis presented in Chapter 4.

- The axial hybrid method may easily include the variation in all electromagnetic properties of the media; heterogeneous background formation conductivity and production casing properties can be handled. A typical run can be conducted with a few hundred basis functions and the total run-time is a few seconds.
- The scattered fracture signals at 10^5 S/m casing conductivity and 30 relative magnetic permeability is tiny compared to the scattered casing signals making it very challenging to detect fractures in cased-hole applications when using induction tools.

Chapter 4: Design and Testing a Prototype Tri-axial Induction Logging Tool In-Air and in a Near Surface Trench

This chapter[2] introduces a new prototype tool which is designed and tested with scaled down fracture models. First, a review is provided on the physics of coil design, the essentials of the measurement set-up, and the theory of electromagnetic scaling. Then, the detailed specification of a developed field-sized prototype induction tool is shown and the design of two main experimental setups is presented. The tool works at the same operational frequency as in the field, and the tool sizes are selected based on the actual wellbore dimensions.

After the tool design was finalized, the tool coil and electronics was built and tested. The study comprises experiments in two different environments: (i) a laboratory environment where in-air measurements are performed, (ii) a field environment where measurements are performed near (below) the earth's surface. The first experimental setup enables easy calibration of the tool, as well as the insertion and removal of targets, thus, facilitating the gathering of data for a range of targets with various parameters. Fracture models of various sizes, shapes, and dip-angles are tested. This set-up was built in the laboratory of E-Spectrum Technologies, Inc. in San-Antonio, TX. The second setup enables measurement in a horizontal well close to the surface, in a lossy and more realistic earth background. This experiment was carried out in a test site in a ranch in Blanco County, TX. The measurements in both cases are compared to a numerical simulator introduced in the previous chapter. The results and set of conclusions are provided while discussing the potential capabilities of the current tool.

It should be noted that some of the work performed by E-Spectrum Technologies and described in this chapter was conducted under a Phase I Small Business Innovative Research/DOE grant (DE-SC0015774) and was documented in the final report, "An Enhanced Extremely Low Frequency Triaxial Induction Tool for Fracture Diagnostics in Open Wellbores," April 3, 2017 (E-Spectrum, 2017). The results are included here for completeness and because much of the work performed by UT under this project helped to guide the work of the Phase I SBIR work and also used the results to validate the computational methods developed under this project.

Additional work was, however, performed by E-Spectrum Technologies under this project, both prior to and after the Phase I SBIR project. This work, summarized in Appendix A, involved two primary tasks: (1) Analysis of an induction tool design created by a previous contractor, Gearhart Company, who left the project due to insolvency, and, (2) Recommendations on how to proceed with the tool design.

4.1. TOOL DESIGN

In this section, three main questions are answered: 1) how to design the most efficient low frequency transmitter and receiver coils which will work in a typical oil well, 2) how to test them in a controllable environment, and 3) how to represent large field scale fractures in a relatively small lab environment.

[2] The experimental set-ups shown in this chapter were first presented in Shiriyev et al. (2018).

4.1.1. Induction Coil Design

The magnetic dipole moment (or torque) is the main characteristic of a transmitter coil and determines the strength of induced magnetic fields. It is defined as:

$$M = \mu_{\mathrm{r,core}} NAI \tag{4.1}$$

given that the cross-sectional area of windings is small compared with the coil diameter, inductance is ignored and the operation frequency is low (Frischknecht, 1988). The emphasis is usually placed on achieving large moments to obtain detectable signals on a receiving component. This can be accomplished by increasing any component in the right-hand side of the equation above, and in the following three paragraphs, we discuss each one of them.

A typical transmitter coil does not have much flexibility in the cross-sectional area selection. It will be elongated along the wellbore direction (*z*-axis) to provide high magnetic dipole moments in restricted wellbore sizes (~4 inches). The elongations of *x*- or *y*-oriented transmitter coils allow an increase in the cross-sectional area of the coil. For the *z*-oriented coil, the elongation allows us to increase the number of turns.

The amount of current that can be driven through a wire at any frequency is limited by thermal considerations. To assure the endurance of a coil in a given environment, the minimization of power loss is essential. This is defined as:

$$P_{\mathrm{coil}} = \frac{1}{2} R_{\mathrm{coil}} |I_{\mathrm{coil}}|^2 \tag{4.2}$$

The minimization of power loss also limits increasing the number of turns by decreasing the cross-sectional area of the wire; the overall resistivity will increase limiting the maximum current. It can be avoided by sharing the current among parallel connected wires:

$$I_{\mathrm{coil}} = I_{\mathrm{coil},1} + \cdots + I_{\mathrm{coil},n} \tag{4.3}$$

where n represents the number of wires connected in parallel. Assuming that all coils are identical to each other, the total resistivity will be decreased in an amount equal to the number of parallel connections:

$$R_{\mathrm{coil}} = \frac{R_{\mathrm{wire},i}}{n} \quad \text{where} \quad R_{\mathrm{wire},i} = \frac{\rho_{\mathrm{wire},i} l_{\mathrm{wire},i}}{A_{\mathrm{wire},i}} \tag{4.4}$$

When the relative magnetic permeability of a core is equal to one, the coil is referred as an air-core coil. It describes an inductor that uses plastic, ceramic or other nonmagnetic forms as a core, as well as those that have only air inside the winding. These types of coils are often used at high frequencies because they are free from energy (or core) losses that occur in ferromagnetic cores due to hysteresis and eddy currents in the core material. The losses increase with an increase in the frequency. To increase the dipole moment of transmitter coils at low frequency we use, a core with a relative magnetic permeability more than one can be used. In general, long and slender shapes of coils allow the effective use of a magnetic core material (Frischknecht, 1988).

The transmitter coil suggested by Heagy and Oldenburg (2013) is a magnetically permeable core wrapped with several hundred turns of wire and has a magnetic dipole moment of 5,000 $A \cdot m^2$ in the frequency range of 1-100 Hz, and only several hundred $A \cdot m^2$ at frequencies above 500 Hz. Lastly, the best practice for the use of transmitter coils in wells requires the monitoring of input currents to take into account any possible changes in coil parameters. Factors that are likely to cause changes are temperature or humidity that may cause an expansion or contraction of coil windings and proximity to a conductive material that may cause electrical loading.

Design criteria to be used for transmitter coils can be applied to receiver coils in the same way. The main factors to consider in the design of receiving loops are the size, sensitivity and stability of loop characteristics, insensitivity to extraneous electric fields and disturbance of normal fields due to the loop itself. Correct measurements are not obtained if the probe significantly disturbs the fields in the vicinity of the model media; that is if the probe behaves as a secondary source. Receiver coils suggested in Heagy and Oldenburg (2013) are the magnetically permeable core wrapped with several thousand turns of wire. Magnetic fields in the order of 10^{-8} A/m can be detected with these coils. These receiver coils are directly connected to the recording apparatus which also contains an amplifier board to increase the power of a received signal. At low frequencies, this direct connection is not expected to introduce major errors (Frischknecht, 1988).

4.1.2. Experimental Set-up

In modeling moving source methods with targets placed in air, the coils can be fixed and the target may be placed on a moving carriage which moves by the coils. To avoid extraneous EM responses, large metallic parts or other conductive materials should not be used in the construction of mechanical parts that are within or near the working region. It is a good practice to construct carriages, tracks and other structures mostly of wood, plastic, concrete and other insulating materials. Measuring instruments should be placed far enough from the region so that their metal cases and chassis do not produce a response. In our experiment, we conduct frequency domain measurements. Therefore, several of the required functions used in the measurement circuit can be combined in one unit known as a lock-in-amplifier. The frequency range of most lock-in-amplifiers is below 100-200 kHz which suits for our application well (Frischknecht, 1988).

4.1.3. Electromagnetic Scaling

Both the laboratory and field experimental environments have space limitations for the electromagnetic targets. They must be of a significantly reduced size compared to the ones likely to be detected in an actual oil and gas formation while the tool parameters, such as coil size and

operation frequency, are kept similar to those expected in the field. Following the theory of EM scaling (Sinclair, 1948), it can be shown that similar signal magnitudes can be obtained only if the induction number defined as:

$$N^{\mathrm{i}} = \sigma\mu\omega l^2 \tag{4.5}$$

is kept invariant for all electric conductivities σ, magnetic permeabilities μ and spatial dimensions l in the system operated at an angular frequency of ω. For some components, however, this requirement can be relaxed. For example, the dimensions of coils do not need to be scaled if their radii are smaller than one-tenth of the distance between them (and neglecting the mutual interactions between the coils). This condition is satisfied for the coils in this work; l_1 and l_2 in Fig. 1.1 are kept more than ten times larger than the radius of coils. The conductivity of the background, if sufficiently lower than that of the propped fracture, has little effect on the resulting secondary fields. As for the propped fracture's conductivity, if the skin depth given as:

$$\delta = \sqrt{\frac{2}{\sigma\omega\mu}} \tag{4.6}$$

is sufficiently larger than the thicknesses of both the original and scaled propped fractures, it is sufficient to only scale the propped fracture's conductance, rather than its conductivity or thickness separately, to maintain similar signal levels (Frischknecht, 1988). At the operation frequency of 1 kHz and effective proppant conductivity of 333 S/m (Zhang et al., 2016), the skin depth is 872 mm – several times larger than the expected propped fracture thickness of 5 mm (Sharma and Manchanda, 2015). In this study, the propped fracture models are made of industrial aluminum foil with a mean conductivity of 34.6 MS/m at 20 ˚C temperature and a mean thickness of 25.4 μm. The skin depth of aluminum at an operating frequency of 1 kHz is 2.7 mm – much larger than the foil's thickness.

4.2. Building a Prototype Tool

In the design of the prototype tool, the goal is to keep the main characteristics the same as in the field deployable tool. Firstly, the operation frequency is selected to be 1 kHz, low enough to detect fractures a few tens of meters away from the wellbore. Secondly, transmitter and receiver coils are designed based on the physical constraints of wellbores. Lastly, the prototype tool can be carried and tested in different environments, especially in conductive backgrounds.

4.2.1. Transmitter and Receiver Coils

This sub-section describes the induction tool and the measurement equipment that were used in the experiments. Solenoidal coils are used for transmitting and receiving (Fig. 4.1). The coils

are designed to operate at the frequency of 1 kHz without overheating. The transmitter coils are made using a 16 AWG (American wire gauge) magnet wire and carry a nominal current of 2.3 A (*x*, *y*-oriented coil) and 4 A (*z*-oriented coil) which was sufficient to provide detectable differential signals. To enable the tool's passage in a narrow well, the coils are designed to be long in the wellbore direction: the *z*-oriented coil has a circular profile and a larger number of turns while the (*x*, *y*)-oriented coil is rectangular with a high aspect ratio. The *z*-oriented coil uses a magnetic core to provide an increased magnetic dipole moment. Table 4.1 summarizes the remaining properties of the transmitter coils. Note that, while the *x*- and *y*- oriented coils are single wires, *z*-oriented coil's current is distributed among three wires wound in parallel.

Orientation	***x*** and ***y***	***z***
Number of parallel connection	1	3
Total number of turns	90	114
Cross-sectional area [cm^2]	256	40
Height [cm]	40.4	32
Relative core permeability	air core	14

Table 4.1: Summary of the transmitter (Tx) coil properties.

As for the receiver coils, these are identical regardless of their orientation, made with an air core and 600 turns of a 32 AWG magnet wire. Their cross-sectional area and height are 30 cm^2 and 1.3 cm, respectively.

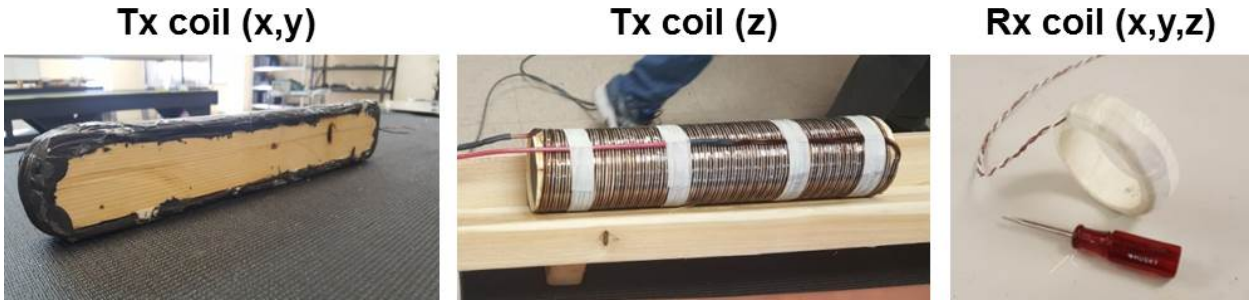

Figure 4.1: Tri-axial transmitter (Tx) and receiver (Rx) coils.

4.2.2. Measurement System

The circuit system used for the experiments is described schematically in Fig. 4.2. The Pre-Amp PCB (printed circuit board) connected to receiver coils (Rx_1 and Rx_2) includes the bucking and amplification of received signals. A bucking coefficient of $l_1^3/l_2^3 = 1/2$ is hardwired. The lengths l_1 and l_2 are fine-tuned during the tool's calibration to minimize the received signal when

operated in air with no target. The bucked signals are amplified by a factor of 100. The set-up allows having a single receiver measurement without any amplification factor.

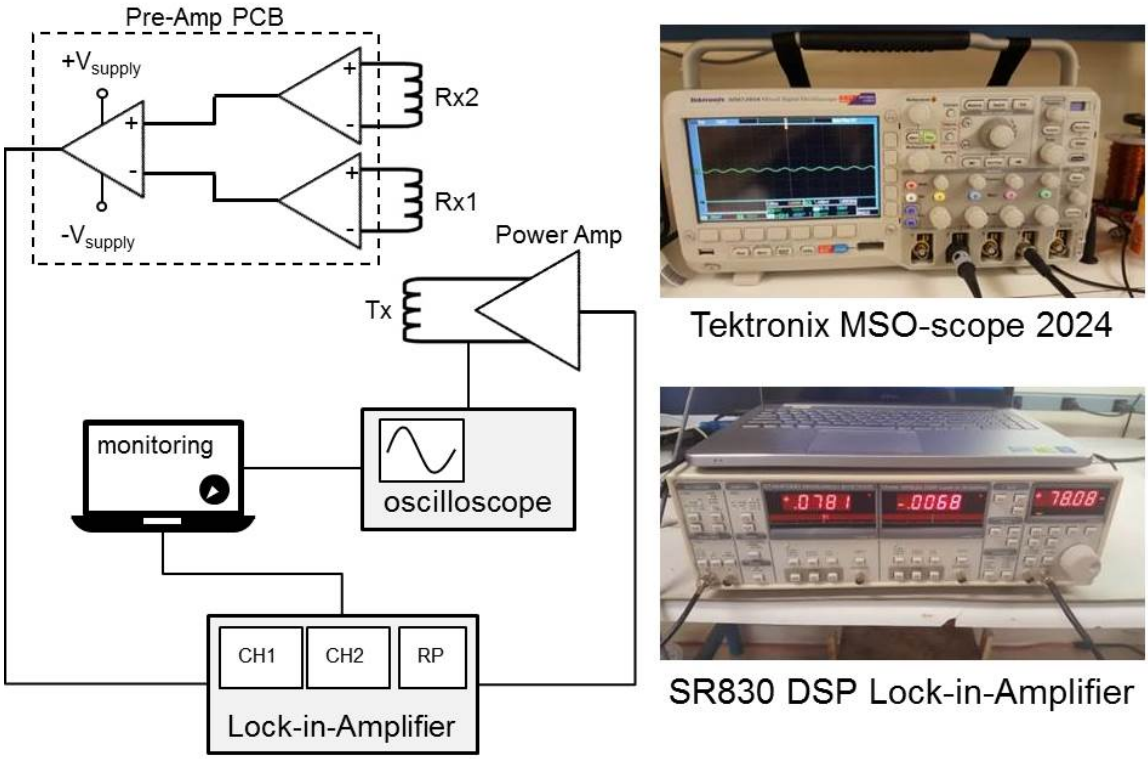

Figure 4.2: Block diagram of the prototype tool: transmitter (Tx) and receiver (Rx1 and Rx2) coils; pre-amp circuit board shown with dashed rectangle; monitoring laptop with full control over the circuit; oscilloscope for measuring the transmitter coil input current; and lock-in-amplifier for signal referencing and decomposition.

The lock-in-amplifier receives amplified bucked signals, with the voltage on the transmitter coil being its reference signal (Fig. 4.2). It outputs, in two separate channels, the bucked signal's in-phase and quadrature components with respect to the reference signal. If we assume the input current of the transmitter coil to be real ($\mathfrak{R}$) then the following rotation matrix multiplication can be used:

$$\begin{bmatrix} \mathfrak{R} \\ \mathfrak{I} \end{bmatrix} = \begin{bmatrix} -\sin\theta & -\cos\theta \\ \cos\theta & -\sin\theta \end{bmatrix} \begin{bmatrix} X \\ Y \end{bmatrix} \tag{4.7}$$

where θ is the reference phase. The transmitter coil input current is measured with an oscilloscope. At selected time instances the monitoring unit continuously displays and records: the time, reference signal, reference frequency, phase with respect to the reference signal and the two output channels (X and Y).

4.2.3. Coil Positioning

Data were collected to see how close the receiver coils can get to the transmitter coil. Fig. 4.3 shows the results both for the receiving and bucking coils in a co-axial coil configuration and data were gathered by measuring the voltage on a single receiver coil for two minutes (30 data at least) as a function of distance from the transmitter. Both receiver coils exist in the setup during the recordings; however, one is disconnected from the circuit board (Fig. 4.2) when the measurements are made for the other coil. The results showed half a meter to be a minimum distance to get the noise sufficiently low.

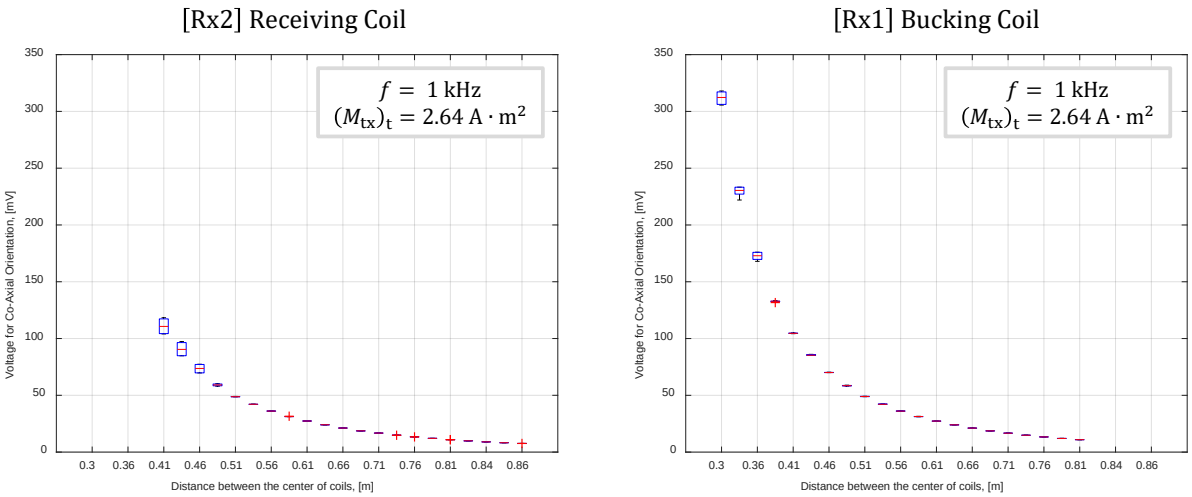

Figure 4.3: Box charts for measured incident signals at different transmitter-receiver coil spacing; left and right plots show results for receiving and bucking coils, respectively. Transmitting magnetic dipole moment is calculated using coil properties and measured input current.

4.2.4. Verification of Coil Parameters

The effective magnetic induction properties of the transmitter and receiver coils both for co-axial and co-planar coil configurations are estimated to be used as an input into the numerical simulation results. By measuring the voltage on a single receiver coil as a function of distance from the transmitter, for a given (measured) transmitter current, and fitting it to the theoretically expected curve, the multiplication of the receiver area and turn number by the transmitter's magnetic dipole moment ($A_{RX}N_{RX}M_{TX}$) is calculated. In this setup, only one receiver coil exists at a time.

The theoretical curve is calculated from the field equation (Balanis, 2005) of a small circular loop. For a given source and sink points, voltages of co-axial configuration can be calculated with the following equation for free space:

$$U_{zz}(z,z') = -j\omega\mu_o A_{\mathrm{RX}} N_{\mathrm{RX}} H_z(z,z') \tag{4.8}$$

where

$$H_z(z,z') = M_{\mathrm{TX}} \frac{jk}{2\pi(z-z')^2}\left[1+\frac{1}{jk(z-z')}\right] e^{-jk(z-z')} \tag{4.9}$$

z is an arbitrary point where the field is calculated (the center of a receiver coil) and z' (the center of a transmitter coil which is assumed to be the origin of the coordinate system) is the location of a point source oriented in the *z*-direction. For the co-planar coil configuration, voltages will be calculated for free space with:

$$U_{yy}(z,z') = -j\omega\mu_o A_{\mathrm{RX}} N_{\mathrm{RX}} H_y(z,z') \tag{4.10}$$

where

$$H_y(z,z') = -M_{\mathrm{TX}} \frac{k^2}{4\pi(z-z')}\left[1+\frac{1}{jk(z-z')}-\frac{1}{k^2(z-z')^2}\right] e^{-jk(z-z')} \tag{4.11}$$

Here, sampling is again along the *z*-direction and coils are oriented in the *y*-direction. The value of $A_{\mathrm{RX}}N_{\mathrm{RX}}M_{\mathrm{TX}}$ minimizing the error between measured and calculated data is selected as an input into the numerical model:

$$\sum_i \left[w_i\left(U_i - U_i^{\exp}\right)\right]^2 = 0 \tag{4.12}$$

where *w* is the weight factor and is larger for the middle part of the data because both short spacing data and long spacing data are not as reliable as the data at middle distances. For the short spacing, more deviation is expected because of noise (see the previous sub-section). For the long spacing receiver, the sensitivity of measurements may decrease because of the low signal levels.

In the measurements, signals are sampled at a rate of one sample per second, over a period of 30 seconds and averaged (shown as dots in Fig. 4.4). The magnetic dipole moments were extracted from the theoretical curves (solid line) such that the coefficient $A_{\mathrm{RX}}N_{\mathrm{RX}}M_{\mathrm{TX}}$ is ~21.7 Am^4 and ~13.5 Am^4 for the co-axial and co-planar configurations, respectively. These calculated values match the coil specifications very well.

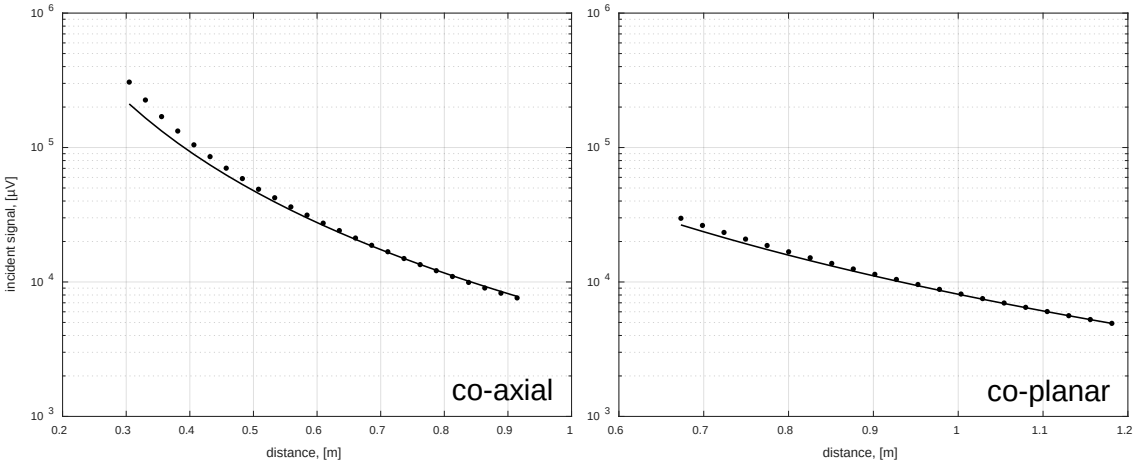

Figure 4.4: Estimation of transmitting and receiving moments: dots show measurements for co-axial (left) and co-planar (right) coil configurations; and solid line is the analytical solution with the best calculated moment coefficient.

4.2.5. Primary Bucked Signal

In this section, results are shown for the measurements before the fractures are in place. At each configuration, two receiver coils are placed inside the tool's inner shell (PVC pipe with a nominal size of 3 in. (~8 cm)) in a bucking configuration, at nominal distances l_1 and l_2 from the transmitter coils. The distance l_2 is tuned to minimize the magnitude at the lock-in amplifier's output. This tuning process is repeated for every test and if there is no other limitation l_1 and l_2 are not changed significantly. Once a minimum is obtained, the coils are fixed in place and the inner shell is inserted into an outer shell PVC pipe with a nominal size of 4 in. (~10 cm). No adjustments are made for centralizing the inner shell inside the outer shell. The test is conducted in a closed lab with a floor area of ~100 m^2 and a height of ~4 m during the daytime. Surrounding materials are all made of wood and plastic; metallic targets are at least 3 meters away both from the transmitter and receiver coils.

The transmitter coil input current (Fig. 4.5) and primary bucked signal (Fig. 4.6) are monitored over 10 minutes. Signals are sampled at a rate of one sample for every 5 seconds. No significant drift was observed during this period and the variation in the primary bucked signal which is normalized with respect to transmitter coil input current was not more than $1\ \mu V$ in the co-axial and co-planar configurations and not more than $0.2\ \mu V$ in the cross-polarized configuration.

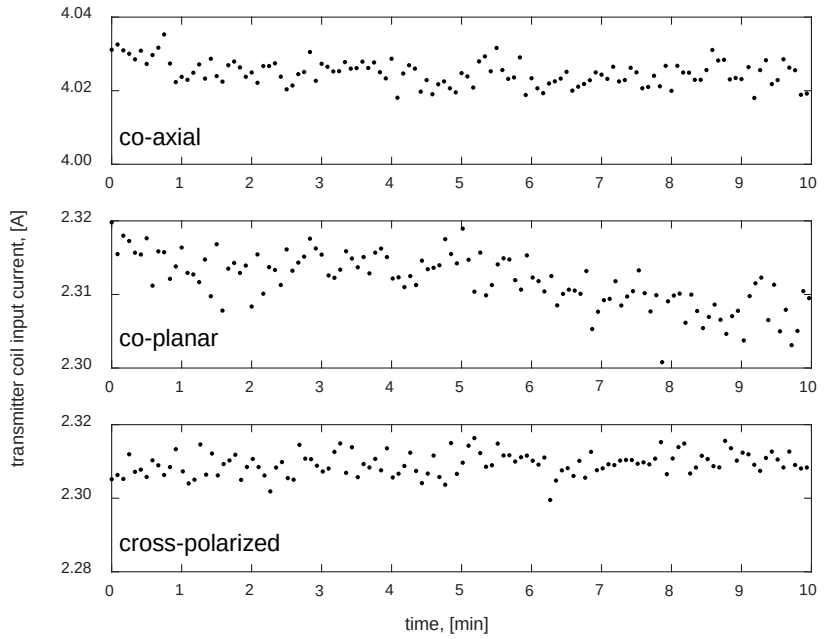

Figure 4.5: The variation in the measured transmitter input current over time; presented for the co-axial (upper), co-planar (middle) and cross-polarized (lower) coil configurations before the measurements with fracture models.

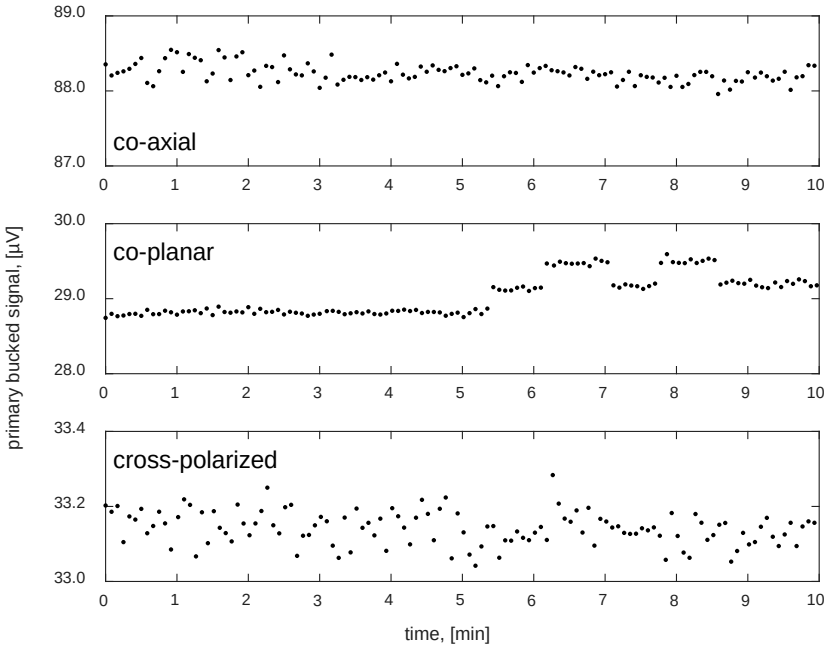

Figure 4.6: The variation in the measured primary bucked signal over time; presented for the co-axial (upper), co-planar (middle) and cross-polarized (lower) coil configurations before the measurements with fracture models; the data are normalized with respect to transmitter coil input current.

4.3. PROTOTYPE TOOL TESTING

In this section, the design of small scale and highly conductive targets, intended to produce a response close in magnitude to that of realistic field propped fractures, is explained. The set-ups used in the lab-air and shallow near-surface experiments are discussed.

4.3.1. In-Air Experiment

The laboratory in-air experiments include primary and total bucked signal measurement for various targets. To emulate various hydraulic fracture geometries in the lab, three sets of propped fracture models are used for the in-air experiments, Fig. 4.7: (a) circular fractures of three different radii, (b) elliptical fracture of three different aspect ratios, and (c) circular fractures with five different dip-angles.

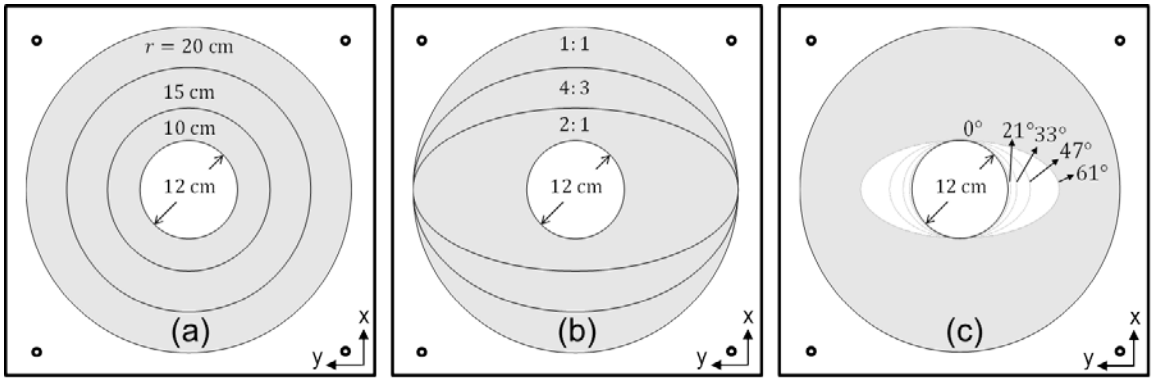

Figure 4.7: Fracture models used for laboratory experiments: (a) orthogonal fractures of various areas; (b) orthogonal fractures with various aspect ratios, the major radius is 20 cm; and (c) fractures of various dips rotated about the *x*-axis.

Measurements are acquired on a test bench at a height of roughly 1 m above the ground. The outer shell of the tool is held, by non-conductive (plastic) boxes, above the test bench (Fig. 4.8 and 4.9). Model targets are sandwiched between acrylic sheets that enable fixing them in a prescribed orientation and centralized with respect to the outer shell. After the tuning, the distances between the center of receivers and the center of transmitter coil are $l_1 = 0.96$ m and $l_2 = 1.21$ m for all coil configurations. Throughout the measurement, the tool is kept stationary and the signal is first measured without model fractures. A typical response for different configurations of coils is shown in Section 4.2.5. Then, the fracture model is moved within a range of [-0.4, 0.4] m with respect to the midpoint between the receiver coils, in 2.5 cm intervals. At each model target position, signals are sampled at a rate of one sample per second, over a period of 30 seconds and the mean signal value measured without the fracture is subtracted to obtain the differential signal.

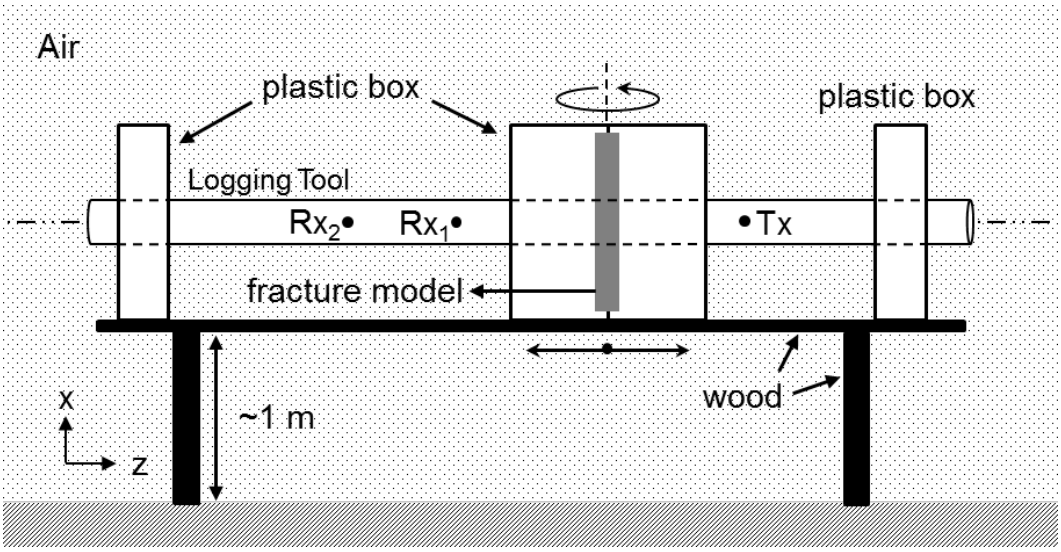

Figure 4.8: Laboratory experimental setup: an outer shell backbone (horizontal pipe) containing coils, fracture model inside a holder (middle box), and two outer shell backbone holders (left and right boxes).

Figure 4.9: Laboratory experimental setup at E-Spectrum Technologies, Inc.: top picture shows main set-up which allows moving fracture models across the center of receivers; during the tests, the surrounding of the tool was kept free of metal; bottom-left picture shows the plastic box which keeps fracture model in a given orientation; and bottom-right picture shows centralization of the fracture model with respect to the outer shell of the tool.

4.3.2. Near Surface Experiment

To evaluate the performance of the tool in a more realistic medium, experiments were conducted in a shallow subsurface site as well. The field experiment includes a tuning stage similar to that in the laboratory experiment and uses the magnetic inductance properties measured in those tests. After the tuning, the distances between the center of receivers and the center of the transmitter coil are $l_1 = 0.96$ m and $l_2 = 1.21$ m. Following the tuning, the tool is used underground, but near the surface, to detect a buried target. A single elliptical fracture model was placed at a certain dip-angle. This simulated fracture model was designed specifically for the near-surface field experiment, Fig. 4.10.

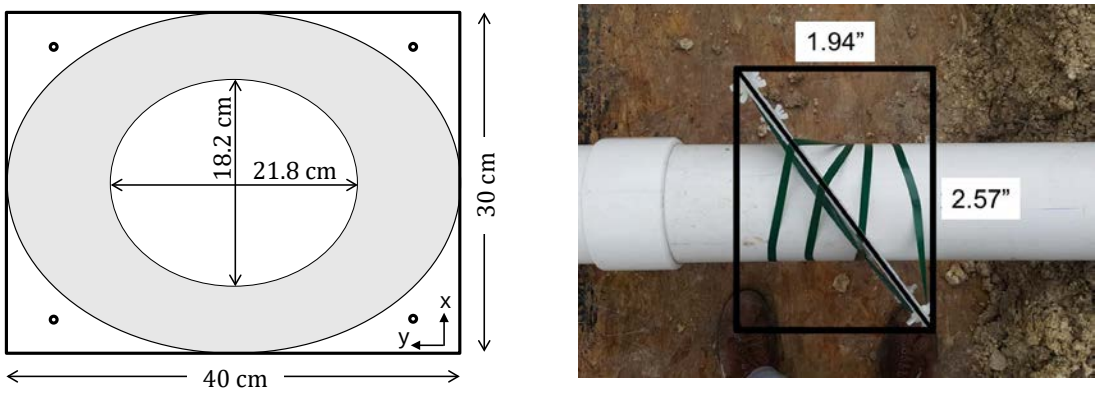

Figure 4.10: Fracture model used for near surface experiment: left figure is the elliptical fracture model which is designed to be 37˚ rotated about the *x*-axis; right figure is field taken picture to verify the dip-angle.

For this experiment, a 6-inch PVC pipe of 12 m length (serving as a well) was buried horizontally at a depth of 1 m below the surface (Fig. 4.11). An aluminum foil target (Fig. 4.10), sandwiched between acrylic sheets, was placed around and centralized with respect to the buried pipe at a dip-angle of 37˚ about the vertical axis (*x*-axis). While designed to be placed at the prescribed dip-angle, the positioning was also geometrically verified using an image taken at the test site. Here, the target is stationary and the tool (outer shell) is moved inside the buried pipe. The tool is lowered into a trench through an opening at the end of the buried pipe and is pushed such that the midpoint between receivers moves in the range [-0.5, 0.5] m with respect to the fracture’s center. No adjustments are made for centralizing the outer shell inside the buried pipe. Data is recorded at intervals of 5 cm and sampled in the same manner as in the laboratory experiment. Then, the primary signal (a measurement far away from the fracture model) is subtracted to obtain differential signals. The background formation conductivity is independently measured with an earth/ground tester (Fluke, 2006).

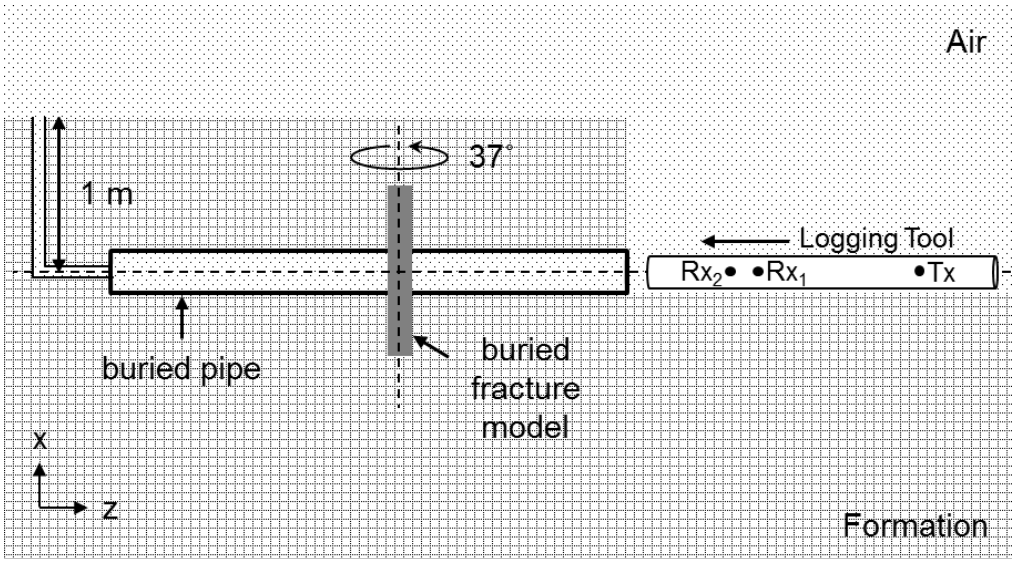

Figure 4.11: Near-surface field-experiment setup illustration: 6” PVC pipe buried together with the fracture model (Fig. 4.10); the tool is pushed and pulled inside the well with the plastic string attached from the transmitter coil end; and all cable connections are attached from the same end.

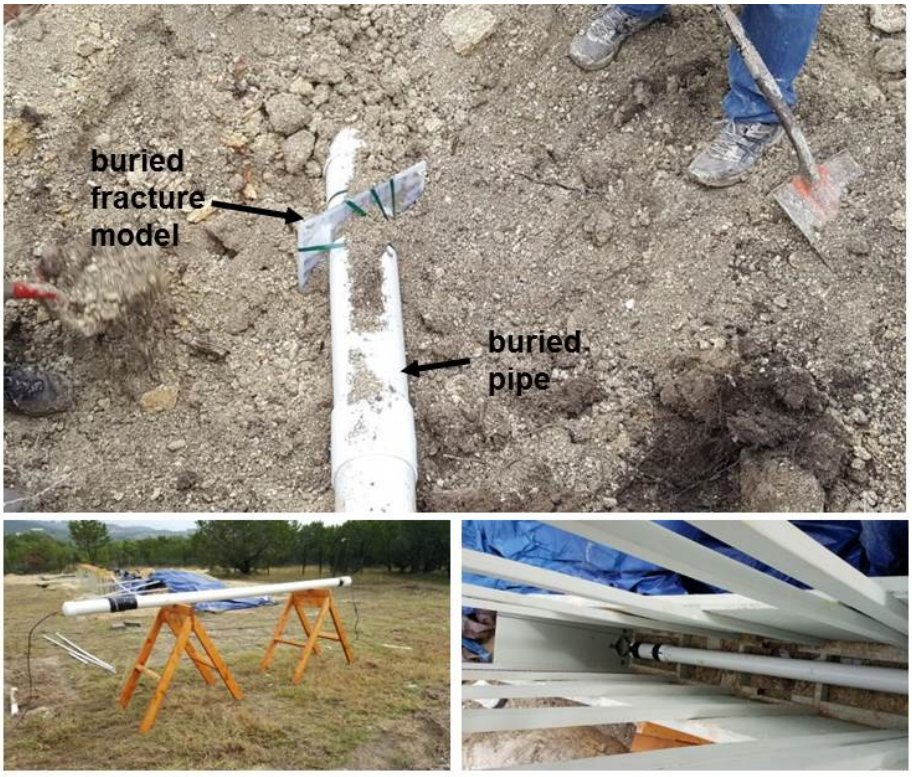

Figure 4.12: Near-surface field-experiment setup illustration: Top picture shows the 6” PVC pipe and fracture model before the hole is covered with soil; bottom-left picture shows the prototype tool on the surface before logging the well; and bottom-right picture shows the prototype tool just before it was pushed into the well.

4.4. RESULTS AND DISCUSSION

In the previous sections, details of a prototype tool, experiment set-ups, fracture model targets and measurements performed were discussed. In this section, the results of these experiments are summarized for different coil configurations, fracture parameters, and surrounding properties in magnitude and phase plots.

4.4.1. Investigation of Different Model Parameters

The differential signals obtained for the various coil configurations are summarized in Table 4.2 which lists typical signal levels observed around a fracture model for each coil configuration (table columns) and for the different parameter of fractures sets in Fig. 4.7 (table rows). It should be noted that, while the results are time averaged at each tool position, deviations from the average of up to 10 μV for strong signals (>100 μV) and 1 μV for weak signals (>10 μV) were observed and that signals weaker than 0.1 μV were not detectable.

Parameter	Co-axial	Co-planar	Cross-polarized
Surface Area	>100 μV	>10 μV	<1 μV
Aspect Ratio	>100 μV	>10 μV	<1 μV
Dip Angle	>100 μV	>100 μV	>100 μV

Table 4.2: Summary of maximum differential signal levels obtained for different fracture parameters and coil configurations.

In the following subsections, the signal magnitudes are plotted as a function of the distance between the location of the fracture model and the midpoint of receivers for the five cases corresponding to the: {co-axial, surface area}, {co-axial, aspect ratio}, {co-planar, aspect ratio}, {co-axial, dip-angle}, and {cross-polarized, dip-angle}. For each of the cases, the plots show both simulated (solid line) and the measured (circles) results. Excellent agreement between the signal magnitudes are observed for all the cases tested. The maximum error observed was less than 10% with most cases showing less than 1% error.

4.4.1.1. Circular Fracture Models

Beginning with the co-axial coil configuration, for which the measured signal levels are the largest (Table 4.2), Fig. 4.13 presents the signals measured for the model targets in Fig. 4.7(a). This configuration's sensitivity to the target's area is evident from the increase in the signal magnitude with the fracture area; however, fractures of greater aspect ratio can potentially produce similar signal levels in this coil configuration.

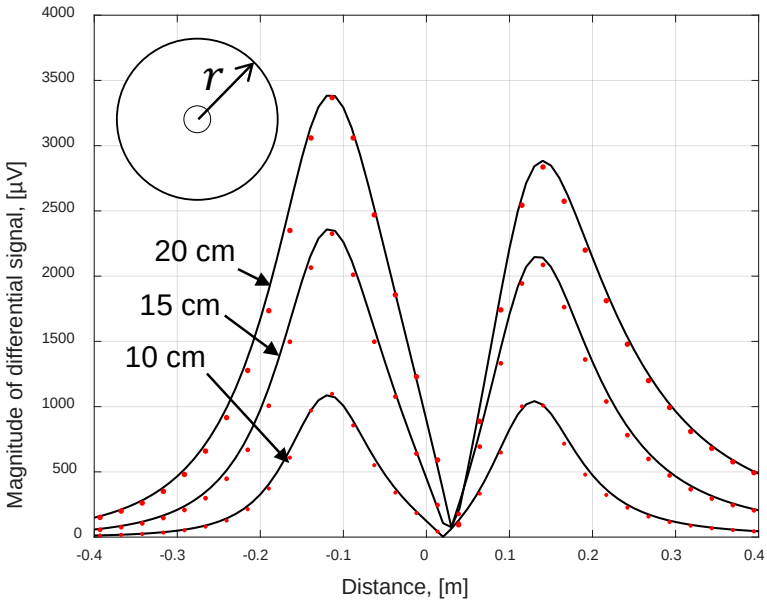

Figure 4.13: In-air test results for the co-axial (*zz*) coil configuration and for the fracture model targets in Fig. 4.7(a). Solid lines mark the simulated results, and red dots mark the measured signals.

4.4.1.2. Elliptical Fracture Models

Only the co-planar configuration measurements were shown to be sensitive to the symmetry of a fracture, Yang et al. (2015). Hence, additional information from this configuration can be used for the determination of the fracture aspect ratio. First, in Fig. 4.14, co-axial signals are shown for the targets of Fig. 4.7(b). As can be seen from the plot, the magnitude of signals is strong; however, symmetric fractures of an equivalent size can potentially produce similar signal levels in this coil configuration. In Fig. 4.15, co-planar signals are shown for the same target where the signals are much weaker than those in the co-axial configuration. It is evident that these signals are sensitive to the aspect ratio of the fractures.

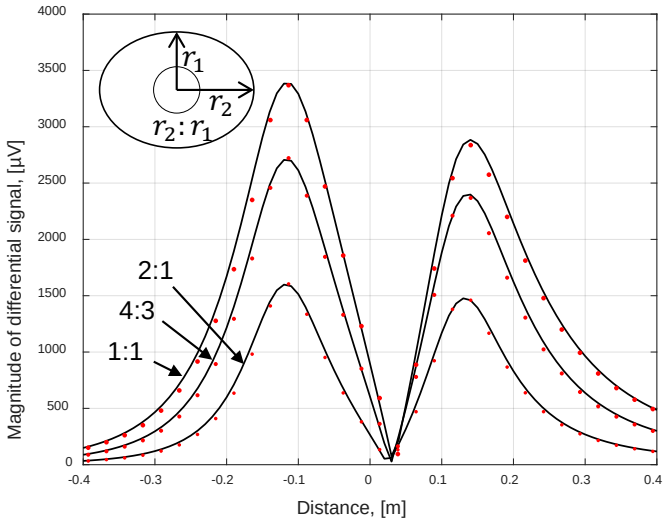

Figure 4.14: In-air test results for the co-axial (*zz*) coil configuration and for the fracture model targets in Fig. 4.7(b). Solid lines mark the simulated results, and red dots mark the measured signals.

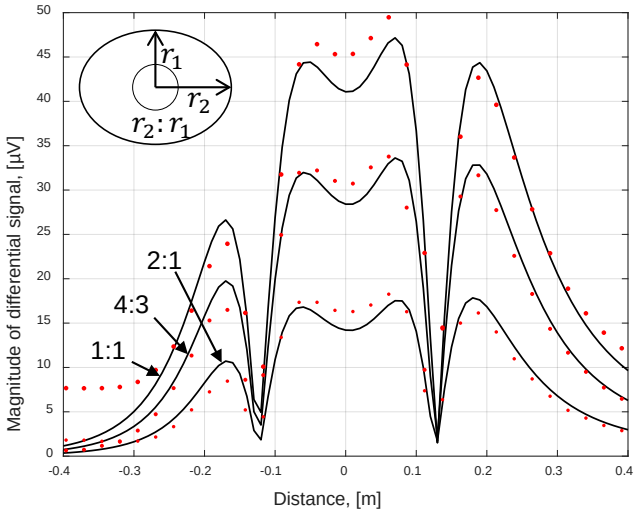

Figure 4.15: In-air test results for the co-planar (*yy*) coil configuration and for the fracture model targets in Fig. 4.7(b). Solid lines mark the simulated results, and red dots mark the measured signals.

4.4.1.3. Rotated Fracture Models

The response to the fracture's dip-angle (models are shown in Fig. 4.7-c) is demonstrated for both co-axial (Fig. 4.16) and cross-polarized configurations (Fig. 4.17). As the dip-angle increases, the received signals get weaker for the co-axial configuration and stronger for the cross-polarized

configuration. It should be noted that all three configurations show strong sensitivity to the dip-angle (Table 4.2).

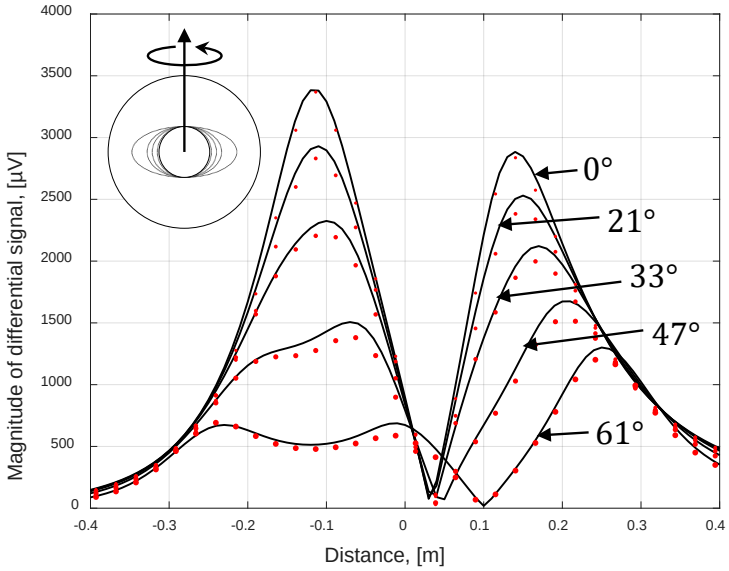

Figure 4.16: In-air test results for the co-axial (*zz*) coil configuration and for the fracture model targets in Fig. 4.7(c). Solid lines mark the simulated results, and red dots mark the measured signals.

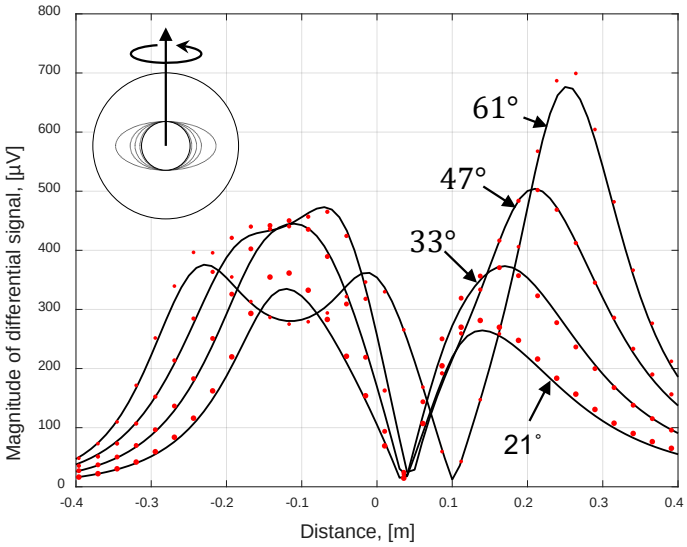

Figure 4.17: In-air test results for the cross-polarized (*zy*) coil configuration and for the fracture model targets in Fig. 4.7(c). Solid lines mark the simulated results, and red dots mark the measured signals.

4.4.2. Near Surface Field Experiment: Effect of Conductive Background

The signal magnitudes measured in the near-surface field experiment are presented next. During the measurements, soil conductivity in the range of 15-20 mS/m was measured (computed signals showed little dependence to the background conductivity). Only the co-axial configuration was used to produce the magnitude plot in Fig. 4.18. Once again, good agreement can be observed (<10 % of relative error) between the numerical and experimental results.

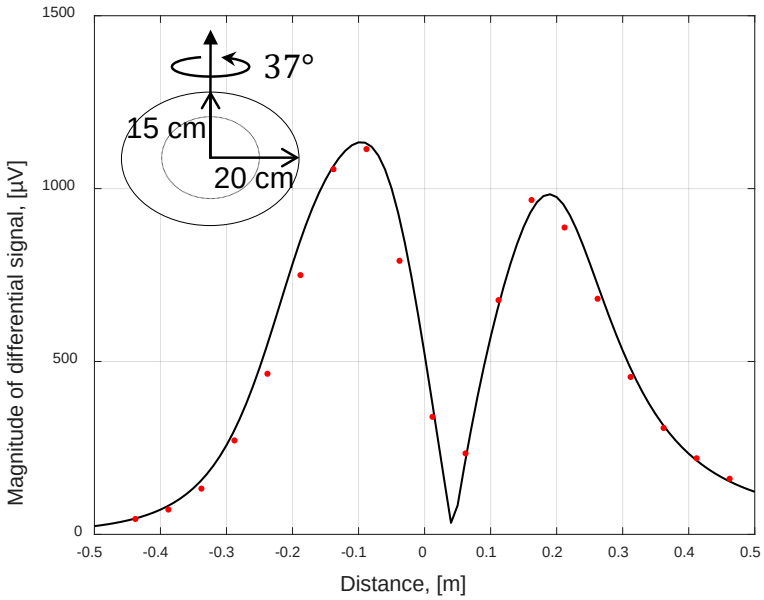

Figure 4.18: Near-surface buried target test results for the co-axial (*zz*) coil configuration and for the fracture model target in Fig. 4.10. Solid lines mark the simulated results, and red dots mark the measured signals.

4.4.3. Phase Plots

Finally, Fig. 4.19 presents the signals for all in-air lab and near-surface field tests (simulation – black dots, measurement – red dots) as polar plots. Examination of each of the sub-figures indicates that, while good agreement between the simulation and measurements was obtained for the magnitude, there is a phase mismatch between simulated and measured signals. The mismatch remains roughly constant across all measurements of a given coil configuration, and it can be attributed to the referencing; the simulated signals are referenced to the transmitter coil current while the measured signals are referenced to its voltage. Ideally, this should result in a phase difference of 90˚; however, the plots suggest that this mismatch ranges between 92˚ and 102˚, depending on the coils. This might not be an issue; as Fig. 4.19 shows that, for all studied cases, the in-phase (real) components with coil current dominate the quadrature (imaginary) components.

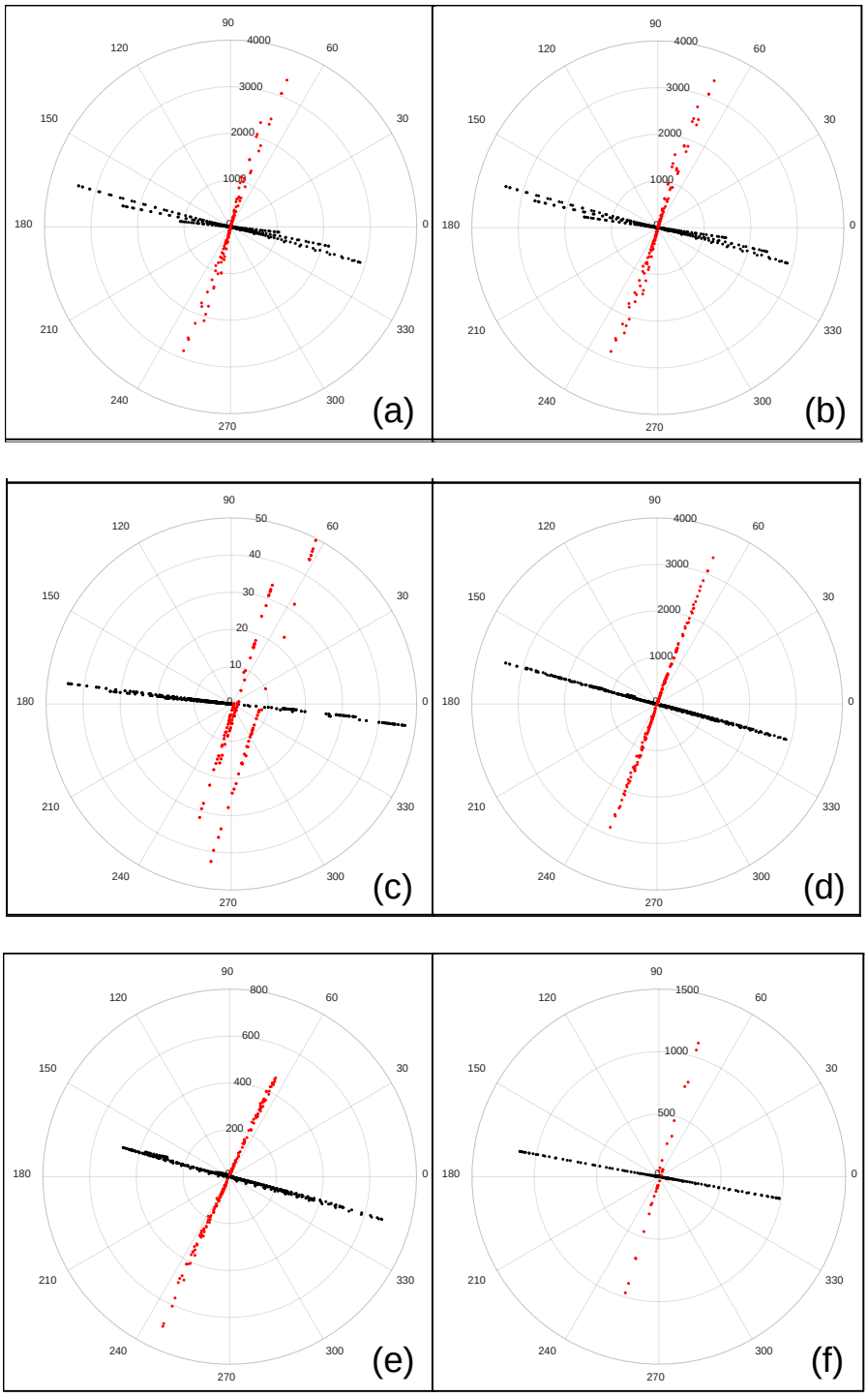

Figure 4.19: Phase plots for the air-tests: (a) co-axial coils with orthogonal fractures of different areas, (b) co-axial coils with orthogonal fractures of different aspect ratio, (c) co-planar coils with orthogonal fractures of different aspect ratio, (d) co-axial coils with different orientation of fractures, (e) cross-polarized coils with different orientation of fractures, and for the near-surface test (f) co-axial coils with the orthogonal fracture. Black and red dots identify the numerical simulations and field measurements, respectively.

4.4.4. Signal to Noise Ratio

In the previous magnitude plots, results are shown with average values at each sampling point. In this section, the variation of total signals with respect to their magnitude is shown for some specified cases (Fig. 4.20).

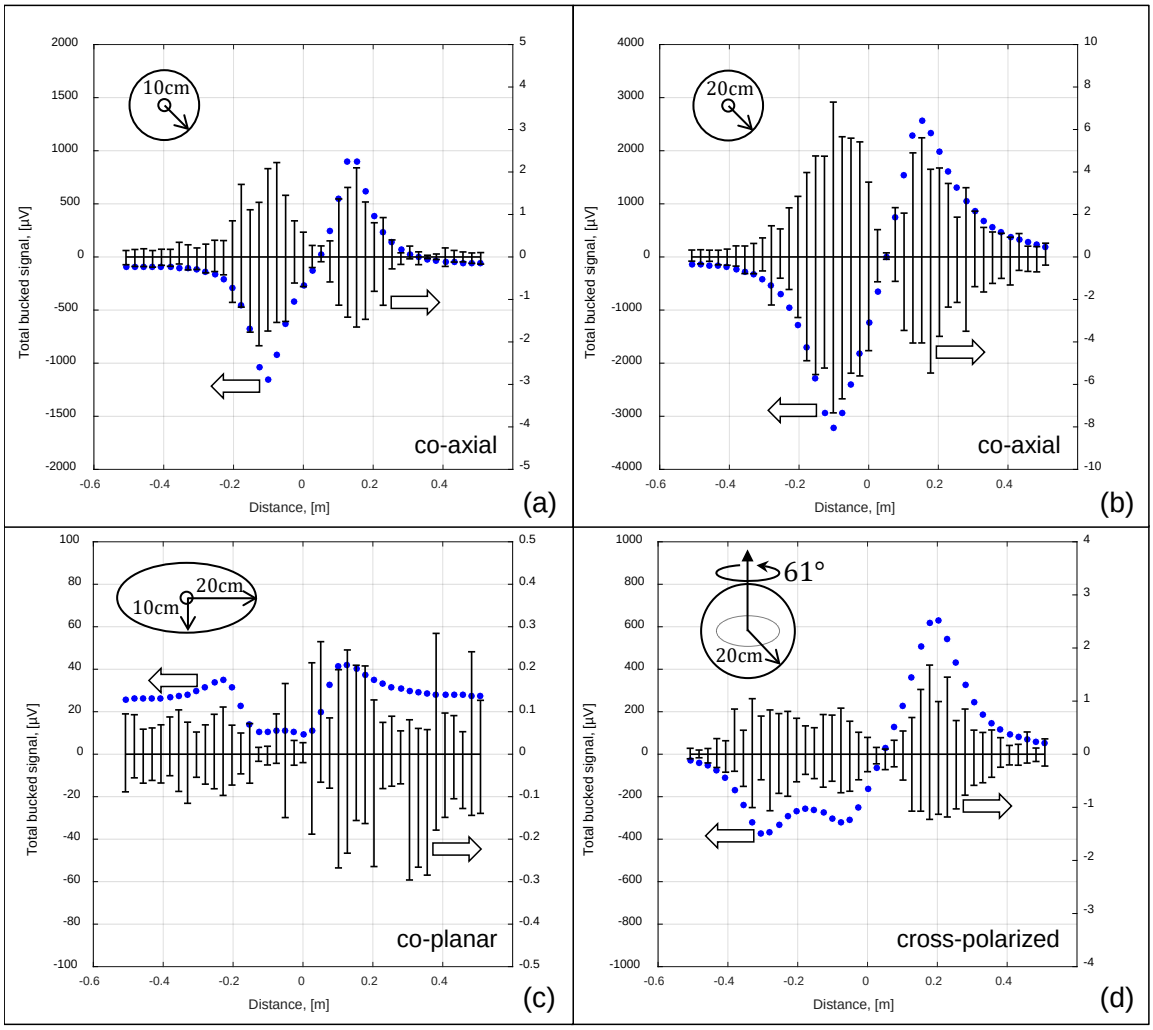

Figure 4.20: Signal to noise ratio of air tests: (a) co-axial measurements with 10 cm radius symmetric and orthogonal fracture model; (b) co-axial measurements with 20 cm radius symmetric and orthogonal fracture model; (c) co-planar measurements with 20 cm major and 10 cm minor radius elliptical and orthogonal fracture model; and (d) cross-polarized measurement with 20 cm radius and 61˚ rotated fracture model; the magnitude of total bucked signals is shown on the left axis and the variation of magnitude on the right axis.

As can be seen from Fig. 4.20, the variation of total signals is dependent on its magnitude. As the magnitude of the signal increases, the variation increases as well with the signal to noise ratio

being more than 100 for all coil configurations. The same type of plot for the near surface field test is shown in Fig. 4.21 where the signal to noise ratio is more than 100 again.

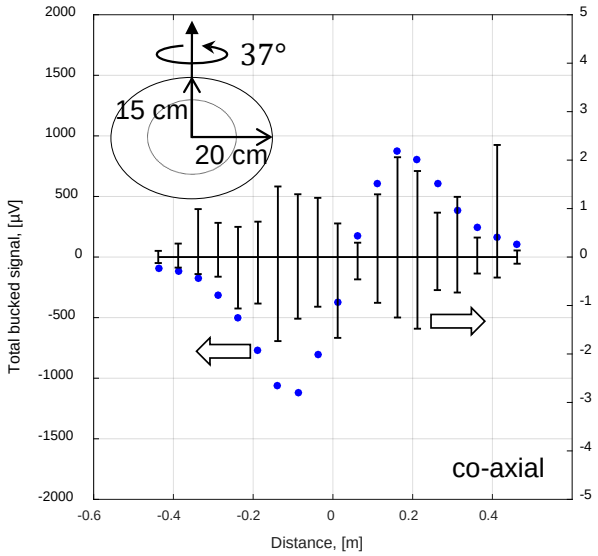

Figure 4.21: Signal to noise ratio of near-surface field test: co-axial measurements with the fracture model shown in Fig. 4.10; the magnitude of total bucked signals is shown on the left axis and the variation of magnitude on the right axis.

4.5. CONCLUSION

A prototype fracture diagnostics tool, consisting of co-axial, co-planar, and cross-polarized configurations of transmitter and receiver coils operated at 1 kHz, was designed and built. Initial tests were conducted to confirm the component properties and detectability range. Then, the prototype tool was tested in-air using a specially designed experimental setup with scaled targets that emulate propped hydraulic fractures. Tests were also conducted with the target buried underground in a near-surface trench. The measured results for both in-air and near-surface tests were in excellent agreement with those simulated by the integral equation-based numerical model (average relative differences of less than 3% with a maximum difference of 10%). This agreement increases the confidence in the results of existing numerical studies which also cover conditions beyond those considered in the experiments. The high signal to noise ratios (over 100) of the measured signals indicate that, indeed, an EM induction tool can be used to extract the propped length (or area), orientation and height of propped hydraulic fractures in open-hole applications.

Each pair of transmitters and receivers exhibits sensitivity to different properties of conductive fractures. The co-axial coil configuration signals are strong (>100 μV) and highly sensitive to the fracture's surface area (or length). A combination of signals from the co-axial and cross-polarized configurations (both >100 μV) can enable estimation of the fracture's dip-angle. The co-planar configuration signals, however, are of relatively lower magnitude (only >10 μV) and, while theoretically are sensitive to the fractures' aspect ratios, might be too low to be sensed in a realistically noisy environment. While the design of (x, y)-oriented transmitter coils that can deliver greater power is challenging, due to geometrical constraints and heating considerations,

improved sensitivity to the aspect ratio may be obtained by modifying the tool's design and operating mode, as will be explored in Chapter 5. Further research in Chapter 4 is dedicated to the development of parametric inversion techniques tailored to such tools.

Lastly, for the largest tested fracture model (circular model with 20 cm radius and orthogonal orientation), the scattered differential signals are approximately 100 times stronger than those produced by a circular hydraulic fracture of 1 m radius, 5 mm thickness (if the coil spacing is 1 meter, it can investigate fractures of ~1 meter radius) and the effective conductivity of 333 S/m (Zhang et al., 2016). However, the tool is expected to be operated downhole with a larger power supply, several hundred $A \cdot m^2$ (Heagy and Oldenburg, 2013) giving rise to greater currents. As a result, in the field, signal levels for short spacing coil couples are going to be close to those obtained in this experiment.

Chapter 5: Inversion of EM Data to Obtain Fracture Geometry and Conductivity

In this chapter, we develop an inversion algorithm for the estimation of fracture geometry and conductivity. The main goal is to have a time efficient simulation tool where the same analysis can be carried out with real field data. The knowledge of the fracture geometry and conductivity will help to improve the efficiency of fracturing operations, and in the long run, it will help completion engineers to design operations with the optimum number of stages and clusters. The results presented in this chapter also provide insight into the resolution obtained with the low frequency induction tool.

We developed a simulated annealing and neighbor-approximation based stochastic inversion algorithm, and first, examined it with a testing function to tune the optimization parameters. Then, several cases were run to invert the "measured data" and appraise the estimation of different fracture parameters such as conductivity, size, dip-angle, etc. An approximation-based direct inversion technique is also proposed for orthogonal fractures to minimize the computation time. Lastly, the effect of neighbor fractures is evaluated, and the inversion algorithm is utilized to recover the fracture distribution along the well for different stages. In the computations, nominal values are used for the tool. Our inversion results are shown to be robust and in agreement with the true values.

5.1. Literature Review

After logging the well with the induction tool, information on the proppant distribution in the fracture can be extracted in two different ways. The more practical and computationally less intensive approach is the parametrization of fractures. Yang et al. (2016) used circular (or elliptical) fractures to characterize the hydraulic fractures and utilized parametric inversion technique where the model parameters are evaluated independently in the given iteration. This technique leads to a small number of model parameters increasing time efficiency. The other approach is the generation of a conductivity map which provides information about the secondary fracture branches. In this case, one challenge is the intensive computational time required for the 3D volumetric solution of Maxwell's equations. The other challenge is the solution of the inherently under-determined problem where the number of model parameters will be dependent on the resolution requirements. In this chapter, we have selected the first approach with the main difference from the previously mentioned study (Yang et al., 2016) being our application of the multidimensional stochastic inversion technique which is based on simulated annealing and neighbor-approximation methods.

Typically, stochastic inversion techniques randomly select a starting point in the model space and moves are decided based on control parameters. Simulated annealing (Fouskakis and Draper, 2002; Sen and Stoffa, 1995) uses temperature as a control parameter for the search direction and jump distance which decreases the randomness of movements. In this study, we start with multiple models, and we use the neighbor approximation (Sambridge, 1999) to benefit from the data history and to avoid additional forward model runs. The tuning parameters are 1) the cooling schedule, 2) the model population and 3) the number of iterations.

5.1.1. Tensor of Detected Signal

In previous studies, Yang et al. (2015) and Zhang et al. (2016), it was shown that any electromagnetic induction tool aimed at fully diagnosing hydraulic fractures requires the use of a tri-axial transmitter and receiver coil system where a 3×3 tensor is measured for the scattered voltage at each sampling point:

$$\begin{bmatrix} V^{xx} & V^{xy} & V^{xz} \\ V^{yx} & V^{yy} & V^{yz} \\ V^{zx} & V^{zy} & V^{zz} \end{bmatrix}_i \tag{5.1}$$

where i is the index of the sampling point. The following model parameters: conductance, area, aspect ratio (shape), and dip-angle are sensitive to the different coil orientations. Co-axial measurements (V_{zz}) are sensitive to the fracture cross-sectional area until a certain saturation point but cannot differentiate fractures of the same area with different shapes or dip-angles. The short spacing can detect small fractures but cannot distinguish large ones. The signals on the long spacing receiver are inherently weak but can distinguish large fractures. The saturation limits for the short and long coil spacings were shown to be 10 m^2 and 1000 m^2, respectively. Co-planar measurements (V_{xx} or V_{yy}) can differentiate axially symmetric fractures from asymmetric ones, but they were found to be weak in the previous chapter. Cross-polarized measurements (off-diagonal components) can quantify fracture dip-angle and become more pronounced as the dip-angle increases (Yang et al., 2015). For an accurate estimation of all model parameters, we suggest using a combination of various orientations. In this study, we define an objective function in such a way that it includes all the signals from different coil spacings and configurations.

5.2. INVERSION TECHNIQUES

In this chapter, we will show results for a mono-axial transmitter (axis oriented in the wellbore direction) and tri-axial receiver coils. Two strong signals are obtained from each run of the tool: co-axial and cross-polarized signals. They are used in the cost function as follows:

$$E = \left(E_{zz} + E_{yz}\right)^{\text{short}} + \left(E_{zz} + E_{yz}\right)^{\text{long}} \tag{5.2}$$

This cost function combines all four signals effectively and enables a global search on the fracture parameters. The signal levels in the long coil spacing are inherently weaker than that of short spacing. Therefore, signals are normalized as follows to get an equal weight on the cost function for the short and long spacings:

$$E_{uv} = \sum_i \left(\frac{\Delta U_{uv}^{\mathrm{sca},i} - \Delta \widetilde{U}_{uv}^{\mathrm{sca},i}}{\Delta \widetilde{U}_{uv}^{\mathrm{sca},i}} \right)^2 \tag{5.3}$$

The tilde refers to the measured (true or observed) data. Fig. 5.1 shows the error map for a fracture with 8 m radius, 100 S/m conductivity and 30˚ dip-angle calculated with Eq. 5.2 where it is clearly seen that there is a global minimum at the true model parameters. For all our presentations here, "calculated data" (differential signal without tilde in Eq. 5.3) is generated using coarser surface meshes, a node spacing factor of four (ref. Chapter 2). For the "measured data", finer surface mesh, a node spacing factor of ten, is used with an additional one percent random noise.

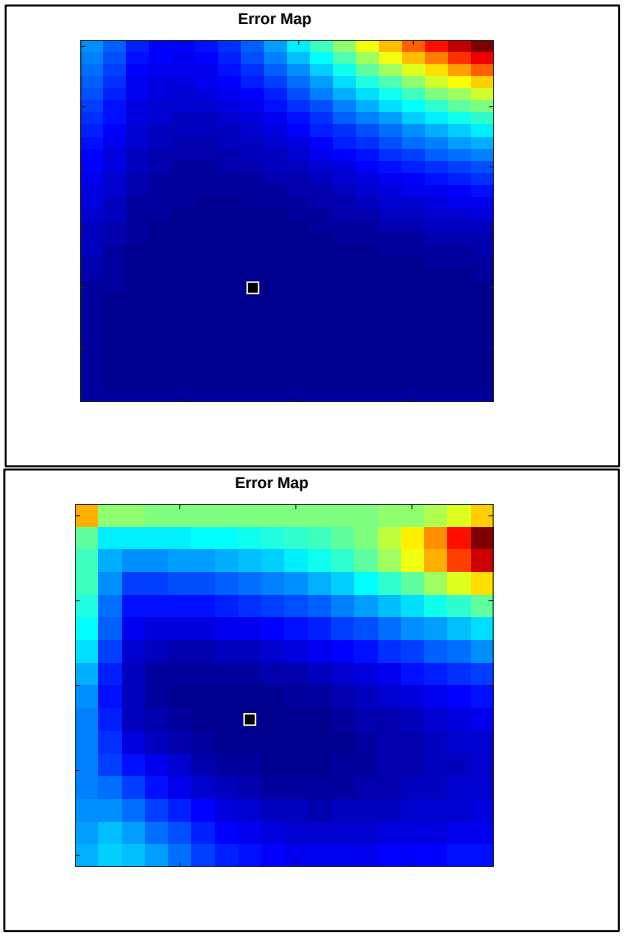

Figure 5.1: Error map calculated for the 8 m radius fracture with a thickness of 5mm, conductivity of 100 S/m and dip-angle of 30˚: upper plot is the fracture conductivity vs. fracture radius, and lower plot is the fracture dip-angle vs. fracture radius.

5.2.1. Derivative Free Directional Search

The main goal of the inversion algorithm is to minimize the error calculated using Eq. 5.2, and the work flow is outlined in Fig. 5.2. First, we define the limits for each individual model parameter. The lower bound is defined as $\mathbf{m}^{\min}$ and upper bound as $\mathbf{m}^{\max}$. Then the first population of models is randomly generated as follows:

$$\mathbf{m}^1 = \mathbf{m}^{\min} + r_{\mathrm{u}} \cdot \left(\mathbf{m}^{\max} - \mathbf{m}^{\min}\right) \tag{5.4}$$

where r_{u} is the random number generated from the uniform distribution. Errors for the population are then evaluated, and the production of new parameters for each model in the population is carried out as follows:

$$m_i^{\mathrm{new}} = m_i^{\mathrm{old}} \mp r_u \cdot T \cdot \Delta m_i \tag{5.5}$$

where T is the control temperature which gradually decreases according to the predefined schedule:

$$T = 0.01^{(i-1)/(N-1)} \tag{5.6}$$

When the iteration number, i is one, T is 1 and approaches 0.01 when i is equal to the maximum number of iterations which is shown with N in the equation above. The cooling schedule allows larger jumps at the beginning of the search and smaller jumps toward the end of the search. As a general rule, a faster cooling schedule may cause the solution to be stuck in a local minimum. A slower cooling schedule is more likely to find a global minimum at the cost of increasing the computation time.

To avoid additional forward model runs, due to the one-dimensional search, data history is used to approximate error to the closest neighbor point. The distance from the point of interest is calculated with the following equation:

$$\|m_{\mathrm{a}} - m_{\mathrm{b}}\| = \sqrt{\left((m_{\mathrm{a}} - m_{\mathrm{b}})^{\mathrm{T}} \cdot C \cdot (m_{\mathrm{a}} - m_{\mathrm{b}})\right)} \tag{5.7}$$

$$C_{ii} = \left(m_{i,max} - m_{i,min}\right)^{-2} \tag{5.8}$$

The condition of accepting a new point is defined as follows:

$$E(\mathbf{m}^{\mathrm{new}}) \leq E\left(\mathbf{m}^{\mathrm{old}}\right) \quad \text{or} \quad T > r_{\mathrm{u}} \tag{5.9}$$

Here, the temperature (T) is used to decide whether to keep a larger error model or not. At the beginning of the search, we have a high chance of accepting new models with larger errors which decreases almost to zero toward the end of the search. Finally, the algorithm is terminated when the maximum number of iterations is achieved.

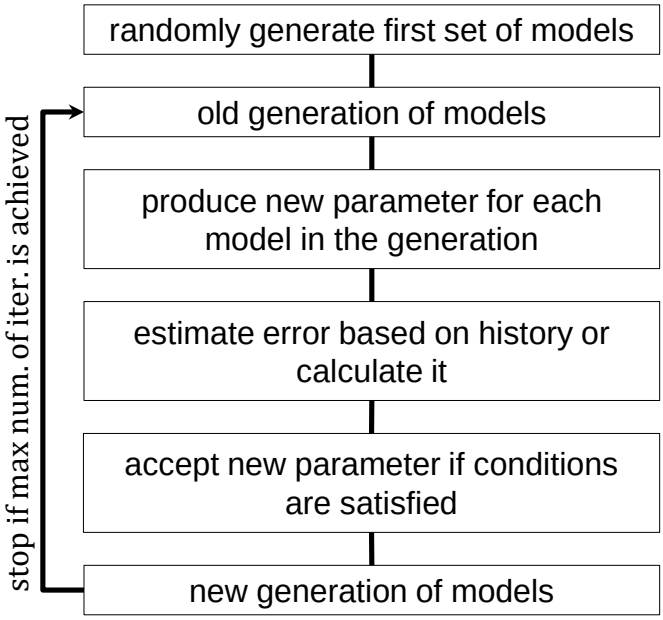

Figure 5.2: Flow diagram of simulated annealing and neighbor approximation based hybrid inversion algorithm.

To test the model the following equation is used as a testing function:

$$E = \left(1 - \prod_{i=1}^{N} \text{sign}\big(\text{sinc}(m_i)\big)\sqrt[4]{|\text{sinc}(m_i)|}\right)^2 \tag{5.10}$$

This testing function allows having a different number of model parameters, and Fig. 5.3 shows error plots for a one- and two-dimensional problem domain.

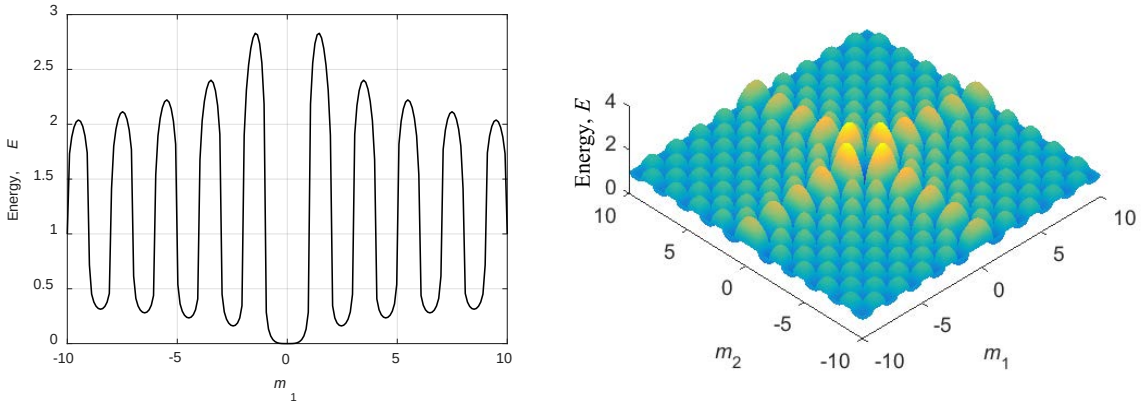

Figure 5.3: One- and two-dimensional plot of the testing function shown in Eq. 5.10.

The output of the algorithm for the test function is shown in Fig. 5.4. We start the search with 10 model samples. In the given iteration, the open black circles show errors for all models and the red filled circle is a model with the minimum error. In all dimensions, one to four, results converge to the global minima within 200 iterations. For the inversion analysis on synthetic data, we use a smaller population and iterations to lower the computation time.

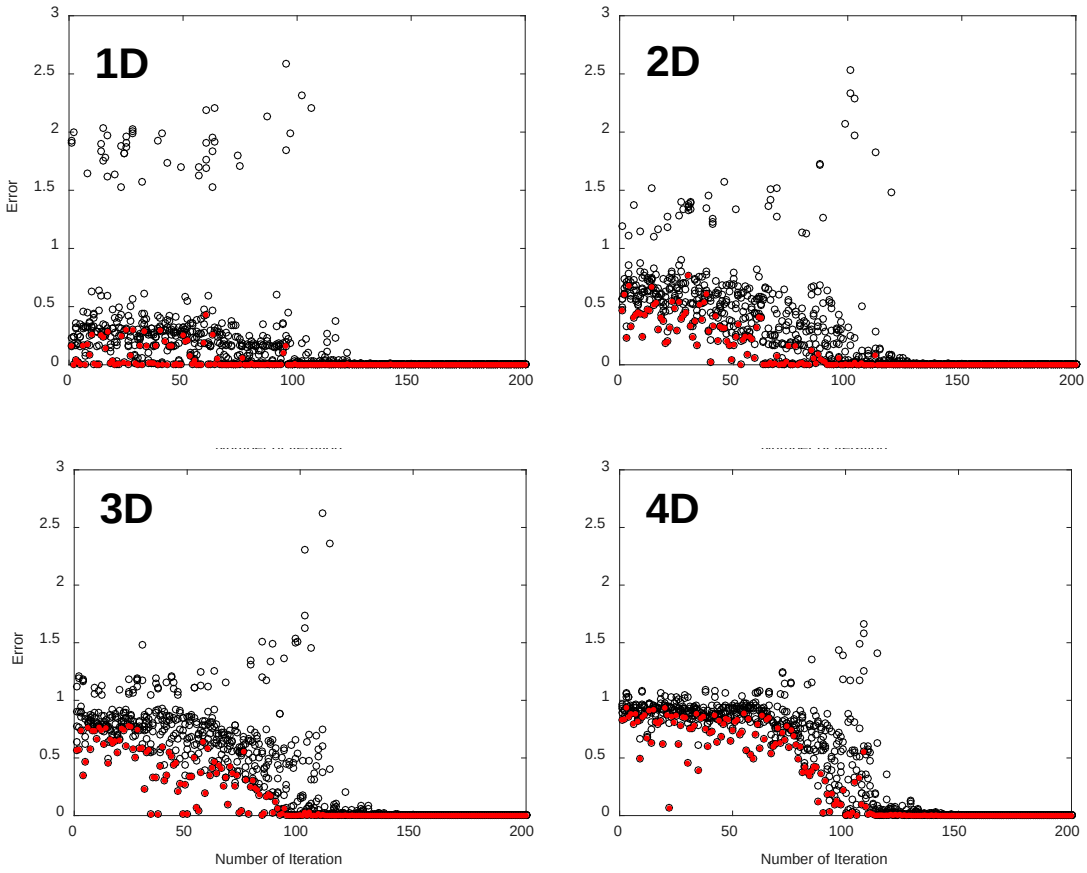

Figure 5.4: Inversion results for the test function in one, two, three, and four dimensions: open circles show errors for all models and red filled circles show a model with the minimum error in the given iteration.

5.2.2. Approximation Based Linear Regression

As discussed in Chapter 2, the approximation introduced in Eq. 2.36 has a linear relationship with the conductance. Implementing this equation into Eq. 2.25 and then into Eq. 1.1, the dependence of the received signal on the conductance for a given location of the tool will be as follows:

$$U_{zz,n}^{\mathrm{sca}} = -j\omega\mu_{\mathrm{o}} N_{\mathrm{rx}} A_{\mathrm{rx}} G \iint_{S} \nabla G_{\mathrm{R}}(\mathbf{r}_n, \mathbf{r}') \times \mathbf{E}^{\mathrm{inc}}(\mathbf{r}')\, dS' \tag{5.11}$$

where n is the receiver number and the differential signal is calculated by subtracting the two receiver signals. If we change the error function to:

$$E_{zz} = \sum_{i} \left(\Delta U_{zz}^{\mathrm{sca},i} - \Delta \widetilde{U}_{zz}^{\mathrm{sca},i}\right)^2 \tag{5.12}$$

and if we take the derivative with respect to conductance, then we can calculate the conductance for the given geometry as follows:

$$G = \sum_{i} \left(\Delta \widetilde{U}_{zz}^{\mathrm{sca},i} \frac{\partial \Delta U_{zz}^{\mathrm{sca},i}}{\partial G} \right) \Bigg/ \sum_{i} \left(\frac{\partial \Delta U_{zz}^{\mathrm{sca},i}}{\partial G} \right)^2 \tag{5.13}$$

Here, i is the sampling point number. This approach will be limited to orthogonal fractures and can be used to reduce the computation time required for the inversion analysis.

5.3. HYDRAULIC FRACTURE IMAGING

In this section, the proposed inversion algorithms are applied to single fracture models, and then an inversion strategy is proposed for use in the presence of neighbor fractures. For all results, the number of iterations is 100, the population is 5, and the number of model parameters is either 2 or 3 depending on the fracture under consideration. The first two model parameters are fracture conductivity and radius. If the observed data has significant signal levels on the cross-polarized configuration, the model parameters include dip-angle as well. Gaussian noise with a mean of one percent of the signal level is added to the "measured data" after calculating them with a node spacing factor of ten. In the inversion analyses, meshes are coarsened and the node spacing factor of four is used.

5.3.1. Single Cluster Analysis

The stochastic inversion results for a single fracture inversion are shown in error figures and box charts. The figures show error values calculated with Eq. 5.2: at the given iteration number, the open circles show errors for all evaluated models, and the red filled circle shows a model with the minimum error. The box plots show the statistical information for the fifty lowest error models. In each box, the central mark indicates the median, and the bottom and top edges of the box indicate the 25th and 75th percentiles, respectively. The whiskers extend to the lower and upper adjacent values, and outliers are shown with the '+' symbol. The approximation based linear regression results are shown only for orthogonal fractures; lines of conductivity values calculated with Eq. 5.13 for short and long coil spacings is shown where the intersection point of lines refers to the estimated result.

5.3.1.1. Circular Fracture

In the first example, the true fracture model is an orthogonal circle with a radius of 8 m and a conductivity of 100 S/m. Fig. 5.5 shows the error and box plots: errors show a decreasing trend with the number of iterations, and the whiskers of both box plots cover the interval which includes the true parameters. The best inversion result (model with the lowest error) has a radius of 8.08 m and a conductivity of 100 S/m.

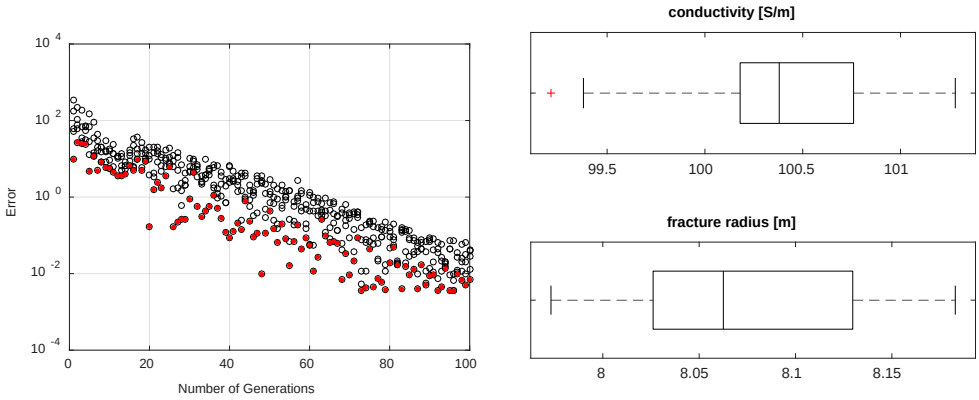

Figure 5.5: Inversion results for a circular and orthogonal fracture: true fracture model has the radius of 8 m and uniform conductivity of 100 S/m. Left figure shows a change in the error with the number of iterations: open circles show errors for all models and red filled circles show a model with the minimum error in the given iteration; and right figures show calculated conductivity and radius box plots for the best 50 cases.

Fig. 5.6 shows a comparison of the differential signals calculated for the true and best inverted models in both short and long coil spacings. As it can be seen in the plots, the curves are essentially indistinguishable showing an excellent agreement for both real and imaginary components.

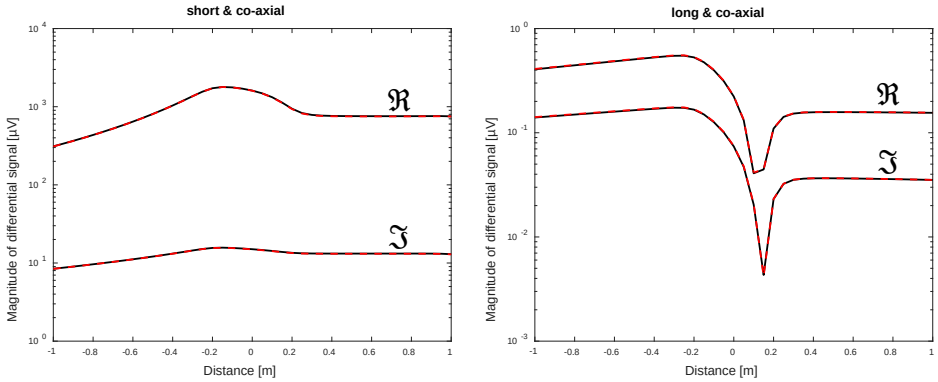

Figure 5.6: The comparison of true (solid black line) and the best inverted (dashed red line) differential signals for a circular and orthogonal fracture with uniform conductivity distribution: true fracture model has the radius of 8 m and constant conductivity of 100 S/m; differential signals are shown for a co-axial coil configuration in short (left) and long (right) coil spacings.

Fig. 5.7 shows results for an approximation based linear regression. The short and long spacing regression lines intersect at a radius of 8.1 m and a conductivity of 100 S/m, and these results are in a good agreement with the stochastic inversion results.

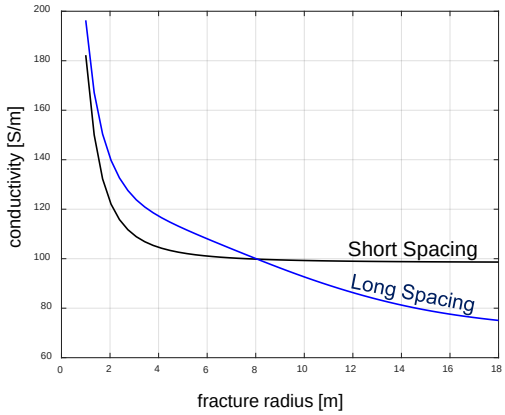

Figure 5.7: Approximation based inversion for a circular and orthogonal fracture: true fracture model has a radius of 8 m and a constant conductivity of 100 S/m; calculated conductivity values are shown for short (red) and long (blue) coil spacings.

5.3.1.2. Rotated Fracture

In this example, the true fracture model is a circle with a radius of 8 m, a constant conductivity of 100 S/m and a dip-angle of 30˚ (rotated about the vertical axis). Fig. 5.8 shows the error and box plots: errors show the same decreasing trend with the number of iterations, and the whiskers of all box plots cover the interval which includes the true parameters. The best inversion result (model with the lowest error) has a radius of 8.09m, a conductivity of 100S/m and a dip-angle of 30.2˚.

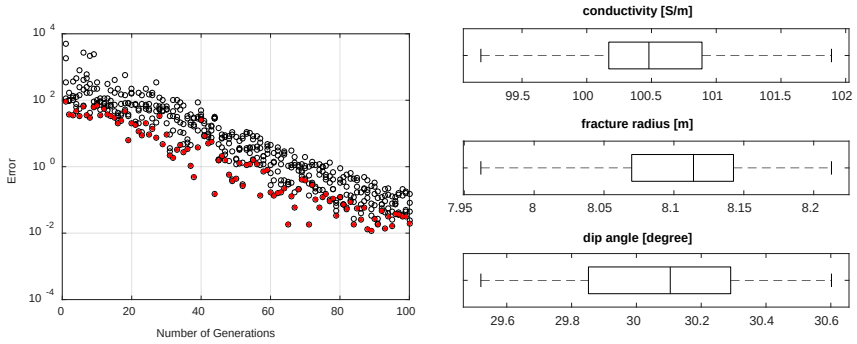

Figure 5.8: Inversion results for a circular and rotated fracture: true fracture model has a radius of 8 m, a uniform conductivity of 100 S/m and a dip-angle of 30^o. Left figure shows a change in the error with the number of iterations: open circles show errors for all models and red filled circles show a model with the minimum error in the given iteration; and right figures show calculated conductivity, radius and dip-angle box plots for the best 50 cases.

Fig. 5.9 shows a comparison of the differential signals calculated for the true and best inverted models for both short and long coil spacing including both co-axial and cross-polarized configurations. As can be seen in the plots, the curves are in good agreement for both real and imaginary components for all spacings and configurations.

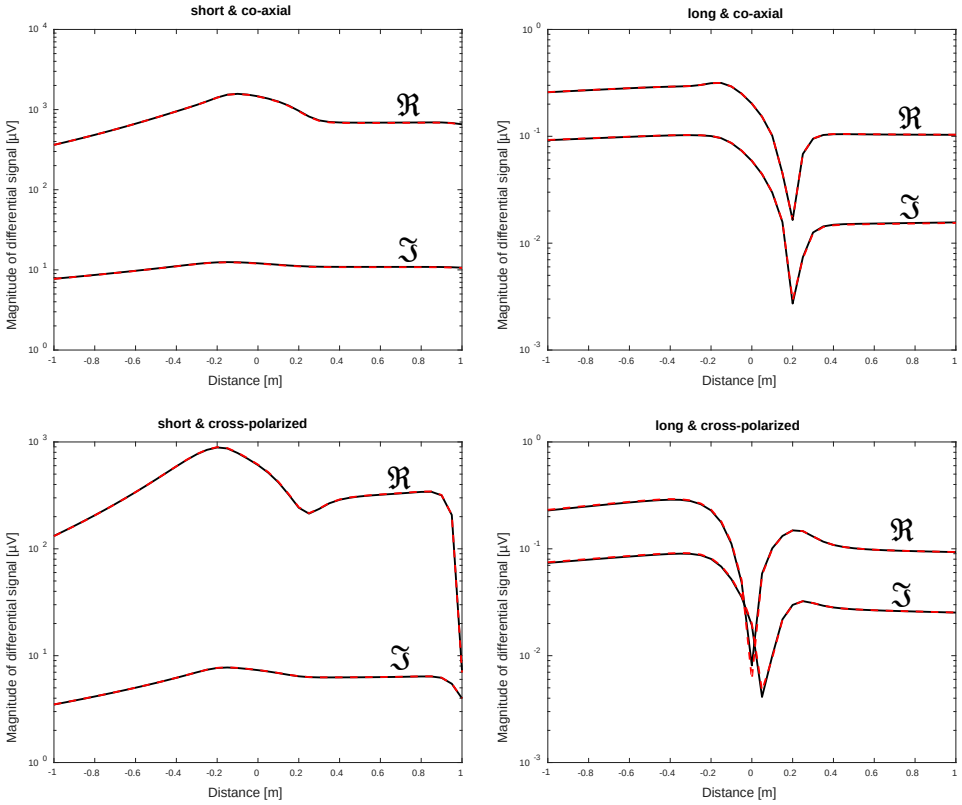

Figure 5.9: The comparison of true (solid black line) and the best inverted (dashed red line) differential signals for a circular and rotated fracture with uniform conductivity distribution: true fracture model has a radius of 8 m, a constant conductivity of 100 S/m and a dip-angle of 30^o; differential signals are shown for co-axial (upper row) and cross-polarized (lower row) coil configurations in short (left column) and long (right column) coil spacings.

5.3.1.3. Elliptical Fracture

In this example, the true fracture model is an orthogonal ellipse with a major radius of 8 m, an aspect ratio of 1.5 and a conductivity of 100 S/m. Fig. 5.10 shows the error and box plots: errors show a decreasing trend with the number of iterations, and the whiskers of the conductivity box plot cover the interval which includes the true parameter. For the box plot of fracture radius, however, whiskers cover the interval which includes the effective radius. The model with the lowest error is a circle with a radius of 6.46 m and a conductivity of 100S/m.

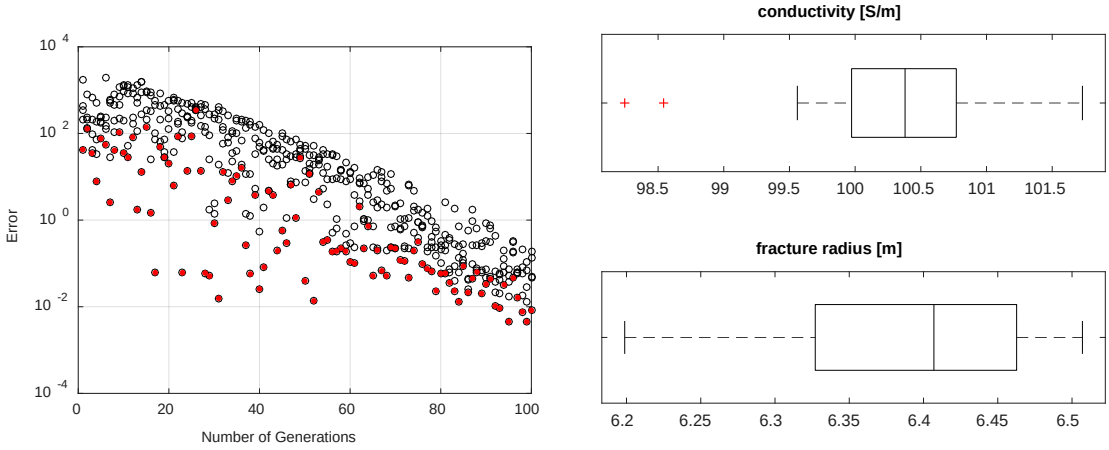

Figure 5.10: Inversion results for an elliptical and orthogonal fracture: true fracture model has a major radius of 8 m, an aspect ratio of 1.5 and a constant conductivity of 100 S/m. Left figure shows a change in the error with the number of iterations: open circles show errors for all models and red filled circles show a model with the minimum error in the given iteration; and right figures show calculated conductivity and radius box-plots for the best 50 cases.

Fig. 5.11 compares the differential signals calculated for the true and best inverted models in both short and long coil spacings. It shows very good agreement for both real and imaginary components.

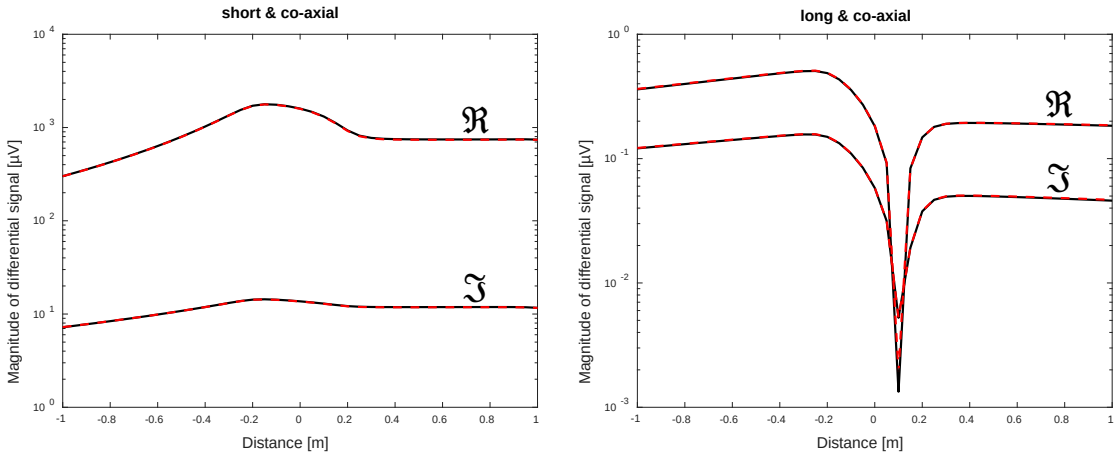

Figure 5.11: The comparison of true (solid black line) and the best inverted (dashed red line) differential signals for an elliptical and orthogonal fracture with uniform conductivity distribution: the true major radius is 8 m, the aspect ratio is 1.5 and the conductivity is 100 S/m. Differential signals are shown for a co-axial coil configuration in short (left) and long (right) coil spacings.

Fig. 5.12 shows results for the approximation based linear regression. The short and long spacing regression lines intersect at a radius of 6.4 m and a conductivity of 100 S/m, and these results are in a good agreement with the stochastic inversion results.

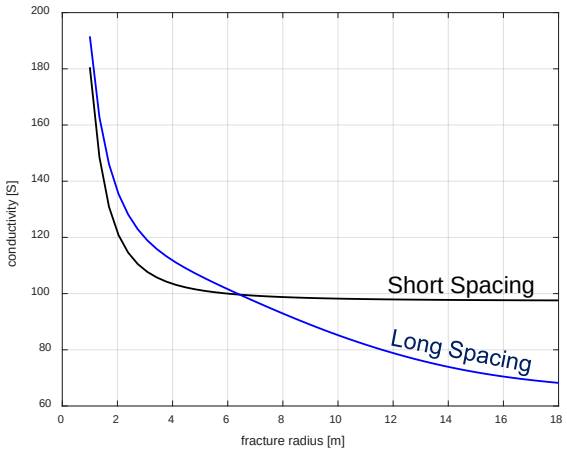

Figure 5.12: Approximation based inversion for an elliptical and orthogonal fracture: the true fracture model has a major radius of 8 m, an aspect ratio of 1.5 and a constant conductivity of 100 S/m; calculated conductivity values are shown for short (red) and long (blue) coil spacings.

To see the effect of rotation in the inversion of elliptical fractures, we run the true model with a major radius of 8 m, an aspect ratio of 1.5, a conductivity of 100 S/m and a dip-angle of 30˚ (rotated about the *x*-axis). Fig. 5.13 shows the error and box plots: errors show a decreasing trend with the number of iterations, and the whiskers of conductivity and dip-angle box plots cover the interval which includes the true model parameters. For the fracture radius box plot, however,

whiskers cover the range for an effective radius. The model with the lowest error is a circle with a radius of 6.47 m, a conductivity of 102 S/m and a dip-angle of 31˚.

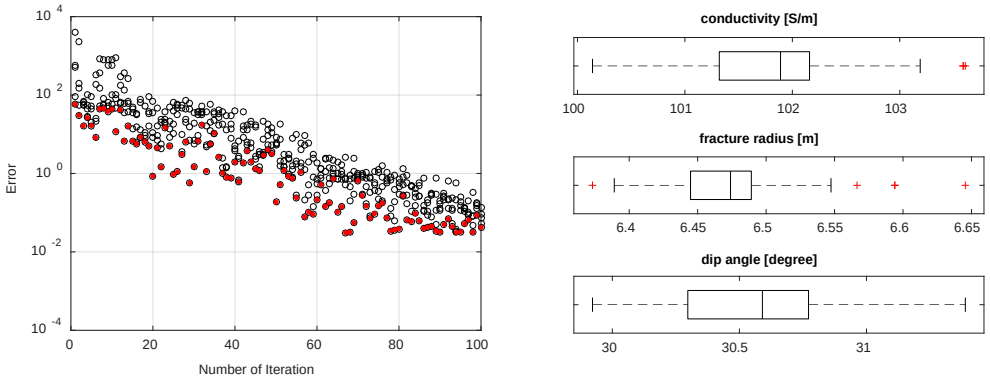

Figure 5.13: Inversion results for an elliptical and rotated fracture: the true fracture model has a major radius of 8 m, an aspect ratio of 1.5, a conductivity of 100 S/m, and a dip-angle of 30˚. Left figure shows a change in the error with the number of iterations: open circles show errors for all models and red filled circles show a model with the minimum error in the given iteration; and right figures show calculated conductivity, radius and dip-angle box plots for the best 50 cases.

Fig. 5.14 shows the comparison of the differential signals calculated for the true and best inverted models in both short and long coil spacings including both co-axial and cross-polarized configurations. It shows very good agreement for both real and imaginary components for all combinations.

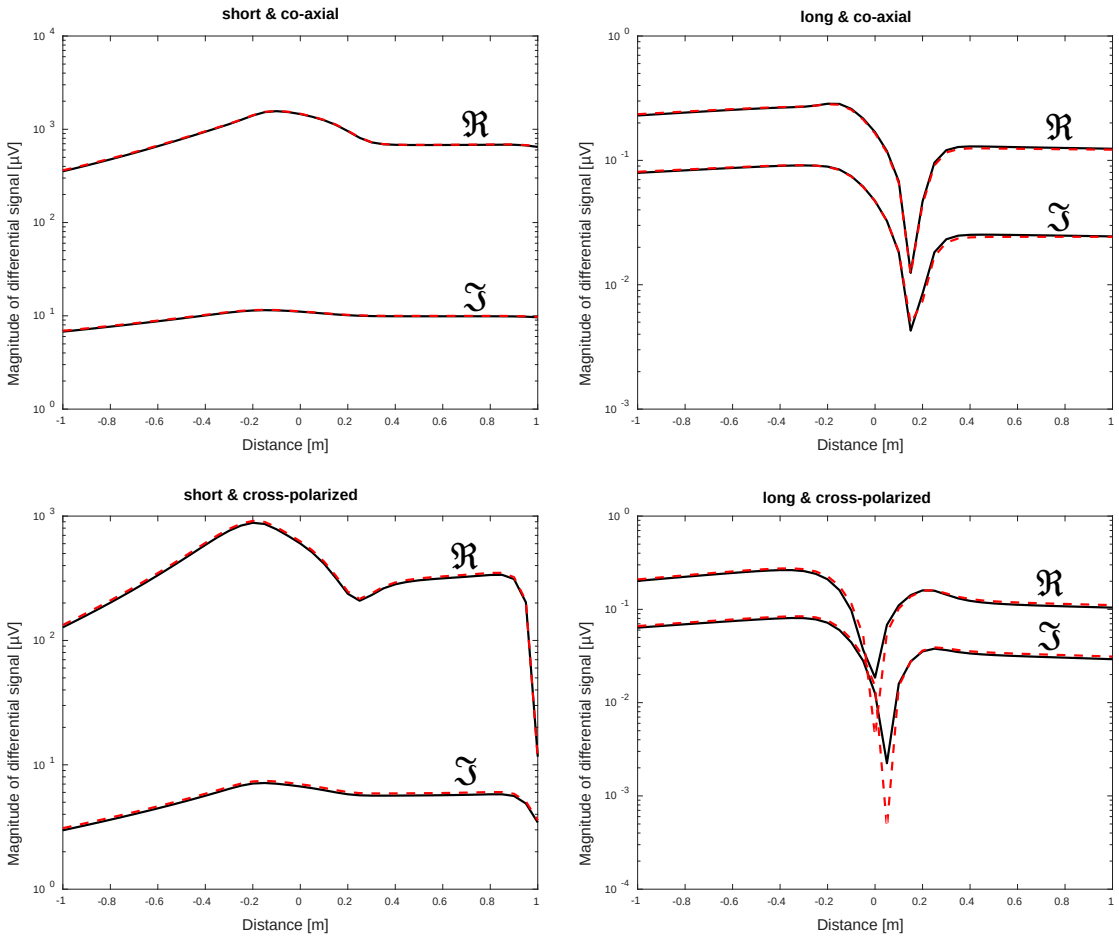

Figure 5.14: The comparison of true (solid black line) and the best inverted (dashed red line) differential signals for an elliptical and rotated fracture with uniform conductivity distribution: the true fracture model has a major radius of 8 m, an aspect ratio of 1.5, a constant conductivity of 100 S/m, and a dip-angle of 30˚; differential signals are shown for co-axial (upper row) and cross-polarized (lower row) coil configurations in short (left column) and long (right column) coil spacings.

5.3.1.4. Conductivity Distribution

In this example, the true fracture model is a circle with a radius of 8 m, and its conductivity decreases linearly in the radial direction (Fig. 5.15); the conductivity is 100 S/m at the wellbore and 0 S/m at the fracture tip.

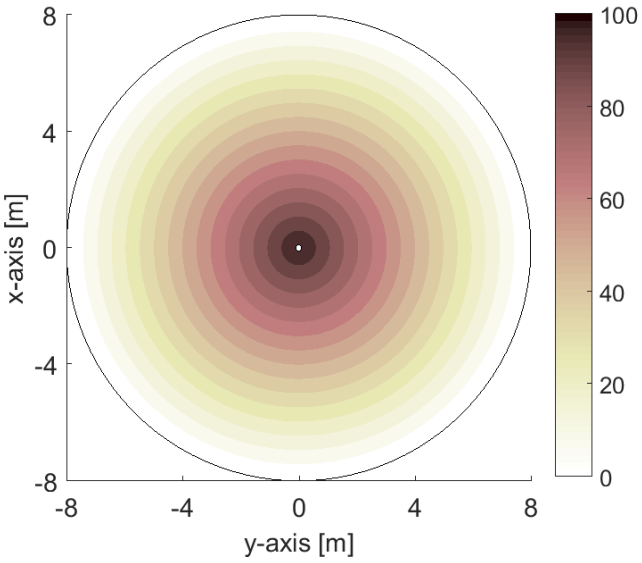

Figure 5.15: A fracture model with varying conductivity: conductivity at the wellbore is 100 S/m and 0 S/m at the fracture tip, decreasing linearly.

Fig. 5.16 shows the error and box plots: errors show a decreasing trend with the number of iterations, and the whiskers of box plots cover the interval which includes the effective parameters. The model with the lowest error is a circle with a radius of 4.37 m and a constant conductivity of 85 S/m.

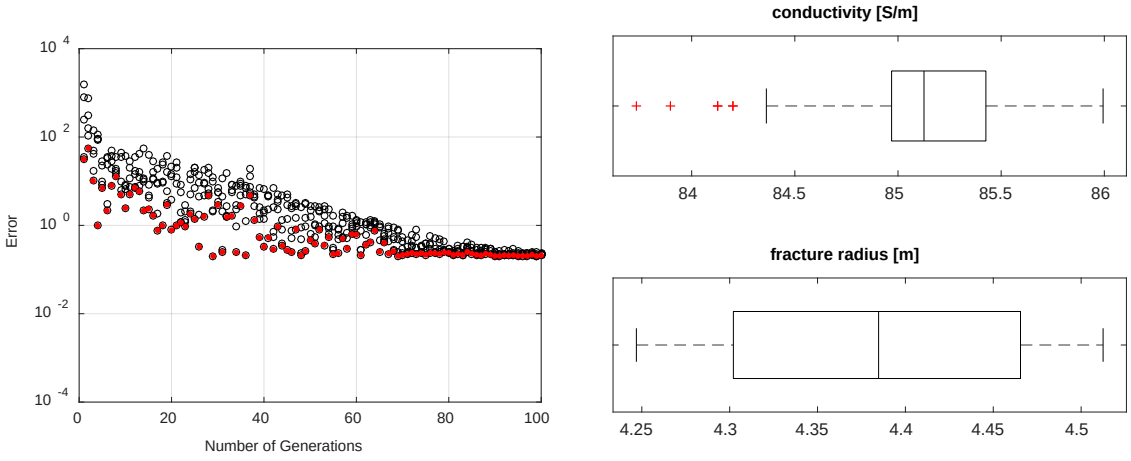

Figure 5.16: Inversion results for a circular and orthogonal fracture with varying conductivity: the true fracture model has a radius of 8 m, and the conductivity at the wellbore is 100 S/m and 0 S/m at the fracture tip, decreasing linearly. The left figure shows a change in the error with the number of iterations: open circles show errors for all models and red filled circles show a model with the minimum error in the given iteration; and right figures show calculated conductivity and radius box plots for the best 50 cases.

Fig. 5.17 shows a comparison of the differential signals calculated for the true and best inverted models in both short and long coil spacings. It shows a good agreement for both real and imaginary components.

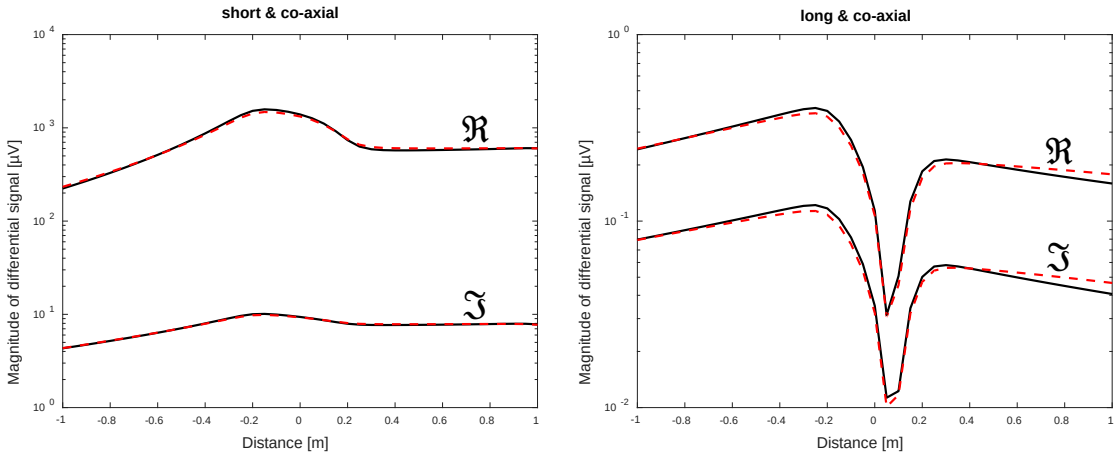

Figure 5.17: The comparison of true (solid black line) and the best inverted (dashed red line) differential signals for a circular and orthogonal fracture with varying conductivity: the true fracture model has a radius of 8 m, and the conductivity at the wellbore is 100 S/m and 0 S/m at the fracture tip, decreasing linearly. Differential signals are shown for a co-axial coil configuration in short (left) and long (right) coil spacings.

Fig. 5.18 shows results for the approximation based linear regression. The short and long spacing regression lines intersect at the radius of 4.5 m and conductivity of 86 S/m, and these results are in a good agreement with the stochastic inversion results.

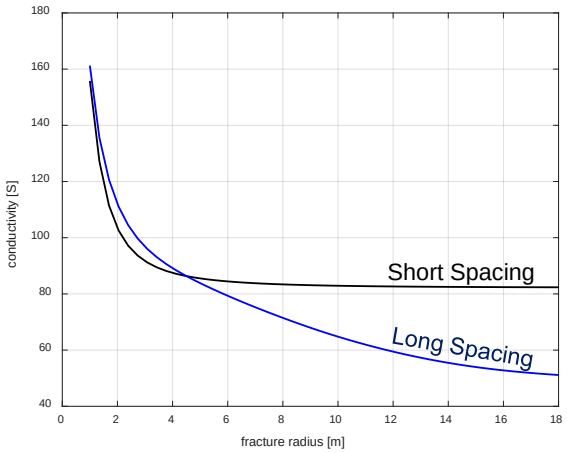

Figure 5.18: Approximation based inversion for a circular and orthogonal fracture with varying conductivity: the true fracture model has a radius of 8 m, and the conductivity at the wellbore is 100 S/m and 0 S/m at the fracture tip, decreasing linearly; calculated conductivity values are shown for short (red) and long (blue) coil spacings.

To see the effect of rotation in the inversion of fractures with varying conductivity, we ran the true circular fracture model with a radius of 8 m and a dip-angle of 30˚ (rotated about the *x*-axis). The conductivity at the wellbore is 100 S/m, and it is decreasing linearly to 0 S/m at the fracture tips. Fig. 5.19 shows the error and box plots: errors show a decreasing trend with iteration numbers, and the whiskers of the dip-angle box plot cover the interval which is very close to the true parameter. For the box plot of fracture radius and conductivity, however, whiskers cover the range which includes the effective parameters. The inverted model with the lowest error has a dip-angle of 29˚, a radius of 4.57 m and a constant conductivity of 84 S/m.

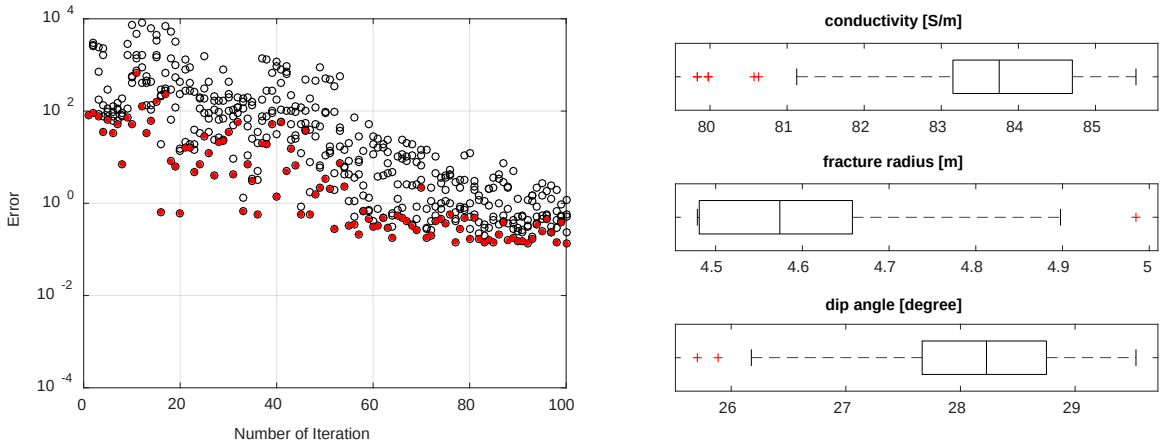

Figure 5.19: Inversion results for a circular and rotated fracture with varying conductivity: the true fracture model has a radius of 8 m and a dip-angle of 30˚, and the conductivity at the wellbore is 100 S/m and 0 S/m at the fracture tip decreasing linearly. The left plot shows a change in the error with the number of iterations: open circles show errors for all models and red filled circles show a model with the minimum error in the given iteration; and right figures show calculated conductivity, radius and dip-angle box plots for the best 50 cases.

Fig. 5.20 compares the differential signals computed for the true and best inverted models in both short and long coil spacings with both co-axial and cross-polarized configurations. The results of both models show very good agreement for both real and imaginary components.

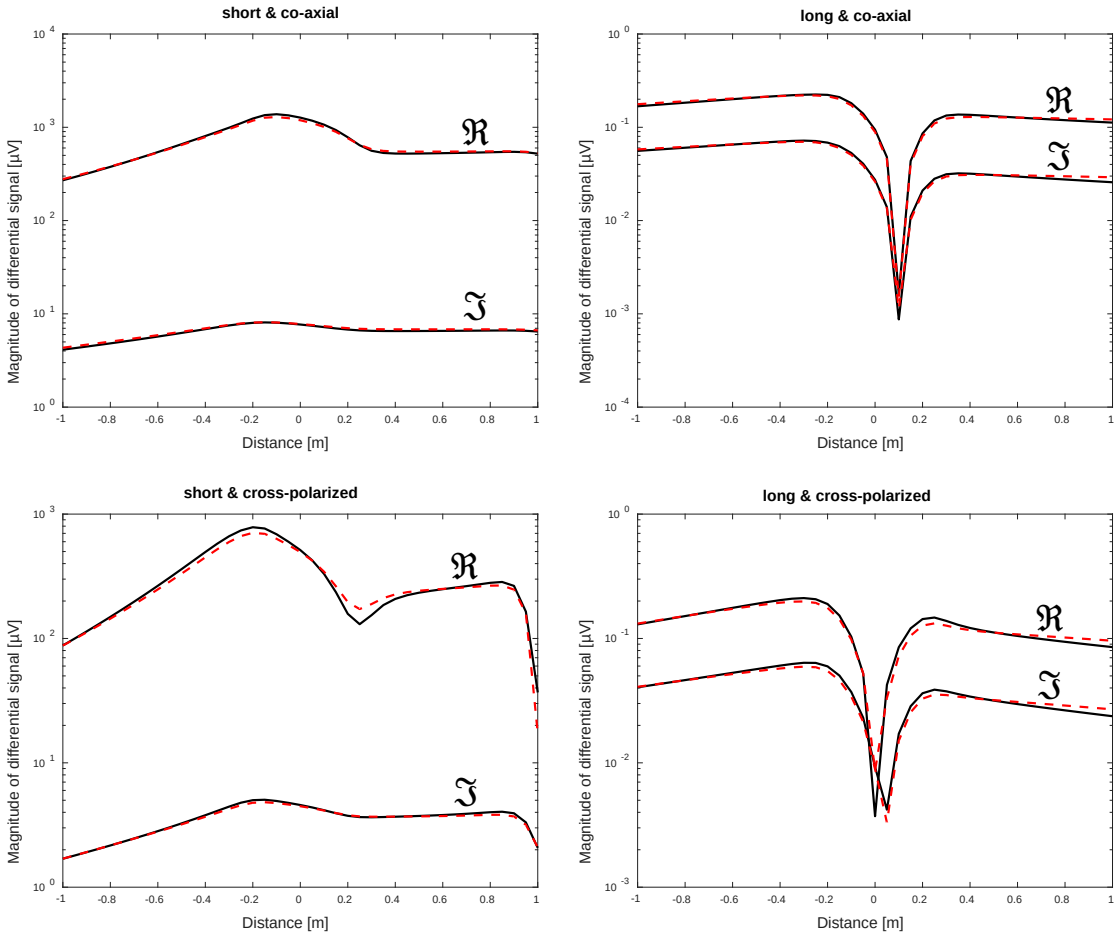

Figure 5.20: The comparison of true (solid black line) and the best inverted (dashed red line) differential signals for a circular and rotated fracture with varying conductivity: the true fracture model has a radius of 8 m and a dip-angle of 30˚, and the conductivity at the wellbore is 100 S/m and 0 S/m at the fracture tip, decreasing linearly; differential signals are shown for co-axial (upper row) and cross-polarized (lower row) coil configurations in short (left column) and long (right column) coil spacings.

5.3.1.5. Heterogeneous Background Conductivity

All the previous forward/inversion models were run with homogeneous background (rock) conductivity. In this section, we simulate heterogeneous background conductivity using the axial hybrid method. Adopting the layering and meshing scheme shown in Fig. 2.13, the uniform region of the mesh is selected between -1 and 1 m with 10 cm intervals. The computation domain is truncated at 100 m on both sides with the grid size ratio of 1.25 in the expanding region. At every grid, in each of the three layers, we use a randomly selected conductivity between 0 and 1 S/m where the overall mean conductivity is 0.49 S/m. Fig. 5.21 shows the primary signals for the formation with the described conductivity properties.

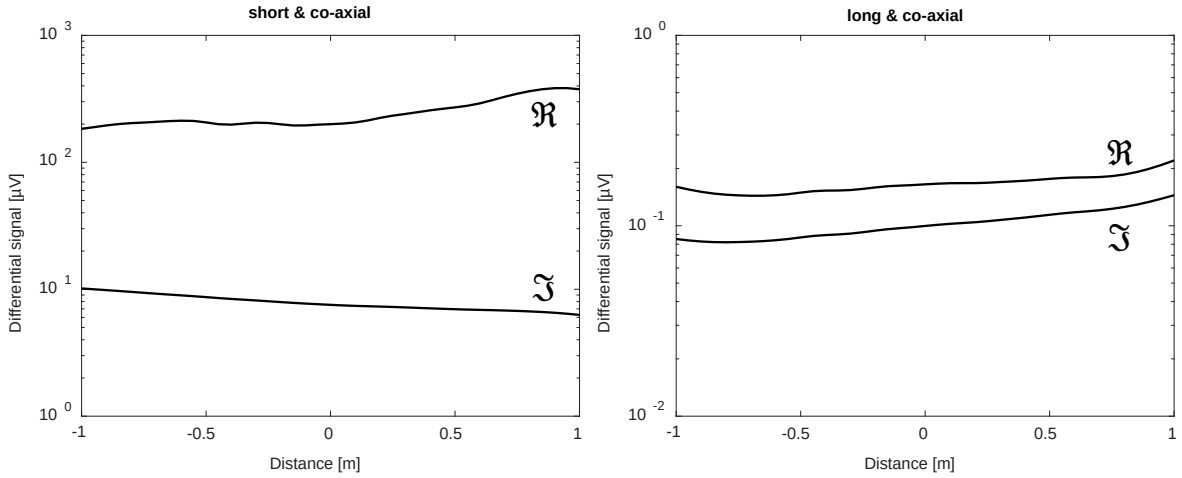

Figure 5.21: Tool response to the heterogeneous background formation; no-fracture case: real and imaginary components of primary signals are shown for co-axial coil configuration in short (left) and long (right) coil spacings.

After introducing a fracture model to the formation with the background conductivity properties described above, we simulate the tool response and subtract the non-fracture case response. The true model of the fracture is an orthogonal circle with a radius of 8 m and a conductivity of 100 S/m. We then run the inversion algorithm with the background (rock) formation conductivity of 0.49 S/m. Fig. 5.22 shows the error and box plots: errors show a decreasing trend with the iteration number, and the whiskers of both box plots cover the intervals which include the true parameters. The model with the lowest error has a radius of 8.1 m and a conductivity of 99.4 S/m.

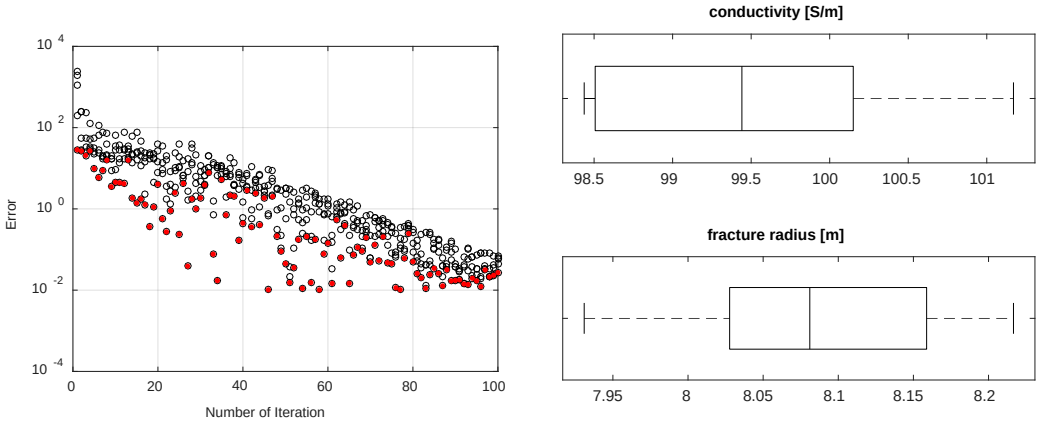

Figure 5.22: Inversion results for a circular and orthogonal fracture in the heterogeneous formation conductivity: true fracture model has a radius of 8 m and a uniform conductivity of 100 S/m. Left plot shows a change in the error with the number of iterations: open circles show errors for all models and red filled circles show a model with the minimum error in the given iteration; and the right figures show calculated conductivity and radius box plots for the best 50 cases.

Fig. 5.23 compares the differential signals computed for the true and best inverted models in both short and long coil spacings. The results show good agreement for both real and imaginary components.

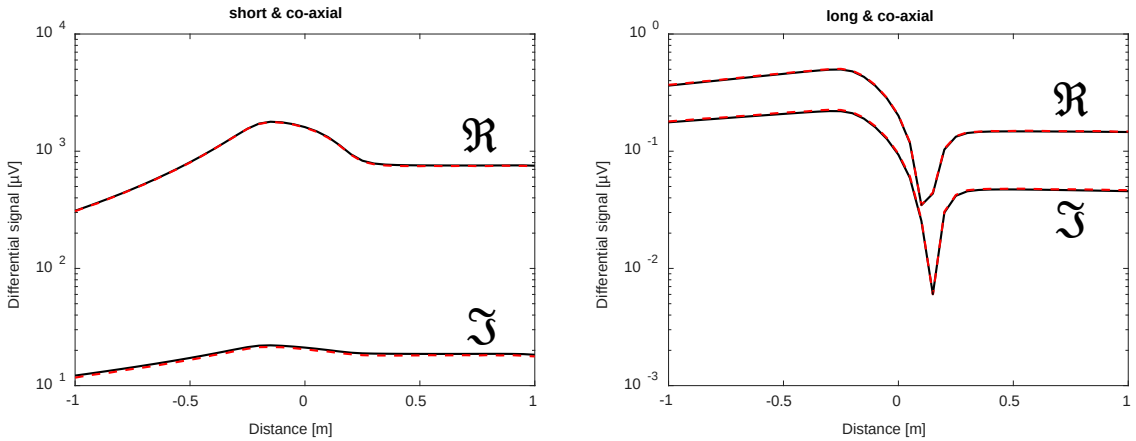

Figure 5.23: The comparison of true (solid black line) and the best inverted (dashed red line) differential signals for a circular and orthogonal fracture in a heterogeneous formation conductivity: true fracture model has the radius of 8 m and uniform conductivity of 100 S/m. Differential signals are shown for a co-axial coil configuration in short (left) and long (right) coil spacings. Measurements with and without fracture are subtracted for the true differential signals; and for the best inverted signals, average formation conductivity is used in the simulation.

This exercise shows the importance of an accurate subtraction of signals before and after fracturing. If we repeat the same analyses without the subtraction, the obtained accuracy is very poor; the result will be a circular fracture with the radius of 2 m and conductivity of 150 S/m.

5.3.2. Multi-Cluster Analysis

In a typical hydraulic fracturing operation, there are more than 20 stages and every stage includes 3 to 10 perforation clusters. Each of these fractures will affect the signals received by the tool. To evaluate this effect, we run many cases varying the number of fractures. Then, we implement a multi-fracture inversion algorithm to get the distribution of proppant in each fracture.

5.3.2.1. Effect of Neighboring Fractures

After completing the single fracture analysis, we ran simulations for a fracturing stage while varying the number of propped fractures to estimate how the neighboring fractures affect the signals coming from the fracture of interest. Fig. 5.24 shows the index number for each fracture.

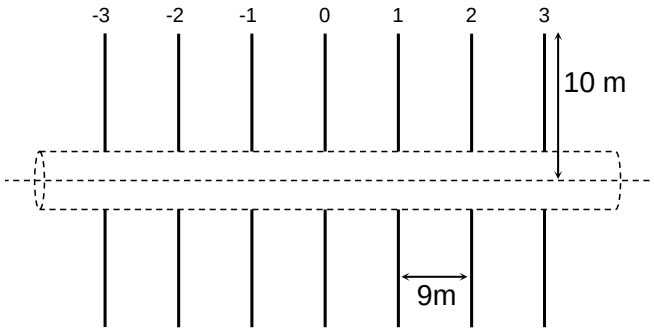

Figure 5.24: Wellbore model used for the evaluation of neighbor effects: fractures are circular and orthogonal with a radius of 10 m and a separation distance of 9 m; fractures are numbered with respect to the fracture of interest (middle fracture).

Fig. 5.25 plots three different cases: a) one neighboring fracture [-1 0 1], b) two neighboring fractures [-2 -1 0 1 2], and c) three neighboring fractures [-3 -2 -1 0 1 2 3]. The following plots show in-phase components of the received signals for short and long coil spacings.

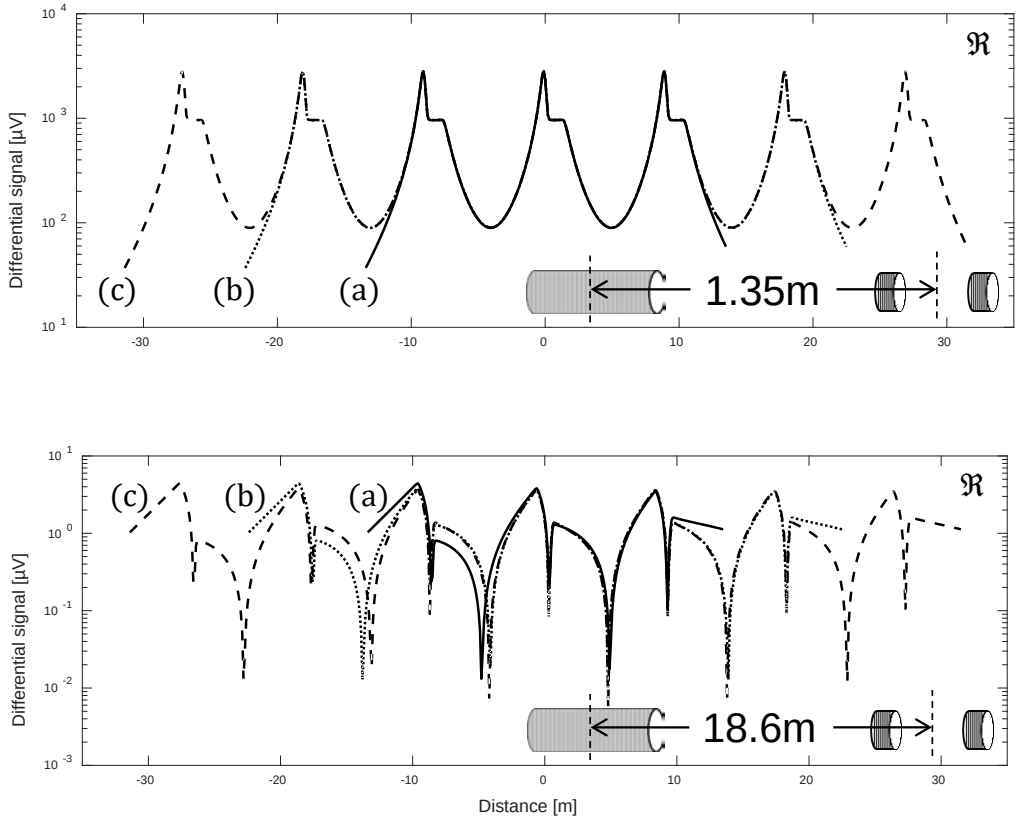

Figure 5.25: The effect of neighbors on the differential signals recorded in short (upper) and long (lower) coil spacings: fractures are shown in Fig. 5.24; plots show differential signals for one (a), two (b) and three (c) neighbors on both sides of the middle fracture.

In the short spacing receiver, we do not see any significant effect of the neighboring fractures. In the long spacing receiver, however, the two closest neighbors are interfering with the signal of interest. The cases with two and three neighbors give almost the same signals around the fracture of interest (with zero index number). Hence, in the next section, we include the effect of only the closest two neighboring fractures in the multi-fracture inversion to minimize the computation time.

5.3.2.2. Multi-Fracture Inversion

The technique used for the inversion is to first invert the data for each fracture assuming that it has no neighbors. Then, we use the best inverted parameters as an initial guess for the inversion with multiple fractures. In this second iterative step, we include the two closest neighbor fractures on both sides of the fracture of interest (maximum of five total fractures in each forward model). To demonstrate this procedure, we use two true models shown in Fig. 5.26.

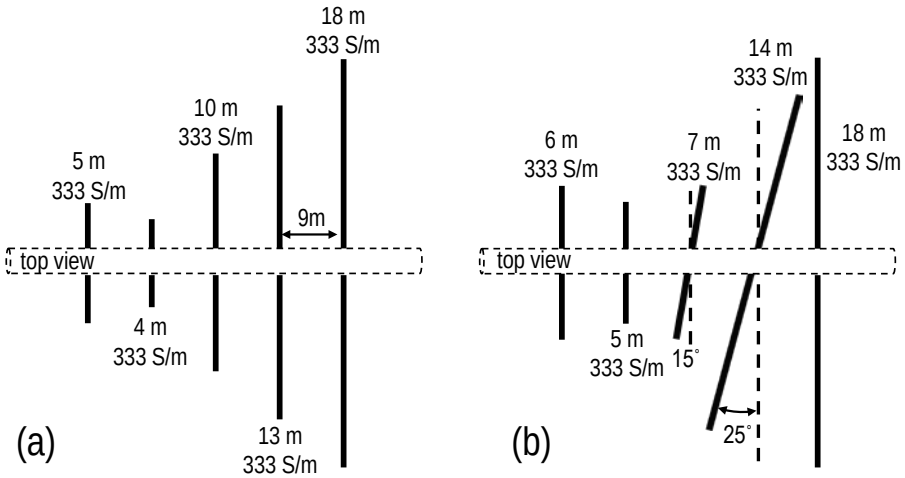

Figure 5.26: Two "true" fracture models used for the multi-fracture inversion analysis: (a) all fractures are orthogonal and (b) third and fourth fractures are tilted.

The differential signals for case (a) are shown in Fig. 5.27. It is not easy to distinguish the distribution of fracture sizes by visual inspection. First, for each fracture, we invert the signals in the interval of (-1, 1) m. Second, the results obtained in the previous step are used as initial guesses for the multi-fracture inversion. We are using two model parameters, fracture conductivity and size.

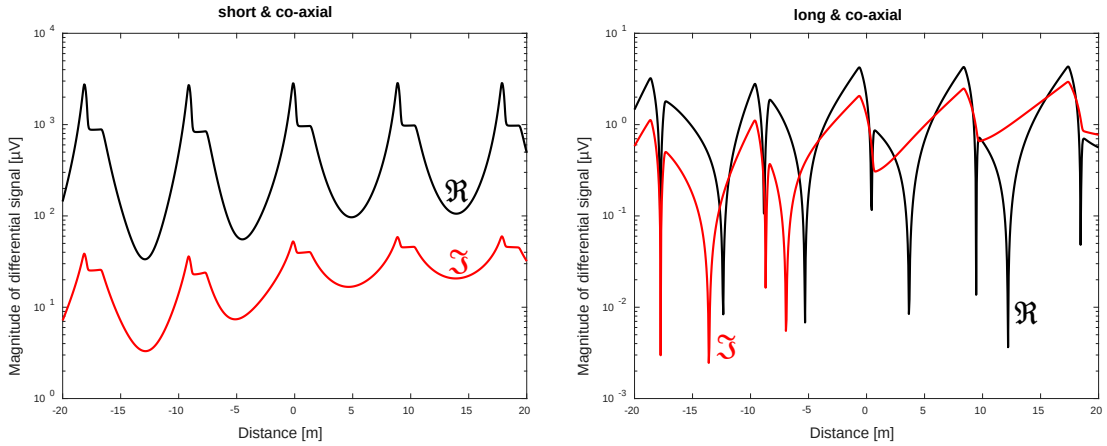

Figure 5.27: Differential signals for the case shown in Fig. 5.26(a): real (black) and imaginary (red) components are shown for co-axial configurations for short (left) and long (right) coil spacings.

After the single fracture inversion, we get the following error vs. iteration for each fracture in case (a). The increase in the error level, as we go from fracture number 1 to 5, can be related to the effect of neighboring fractures.

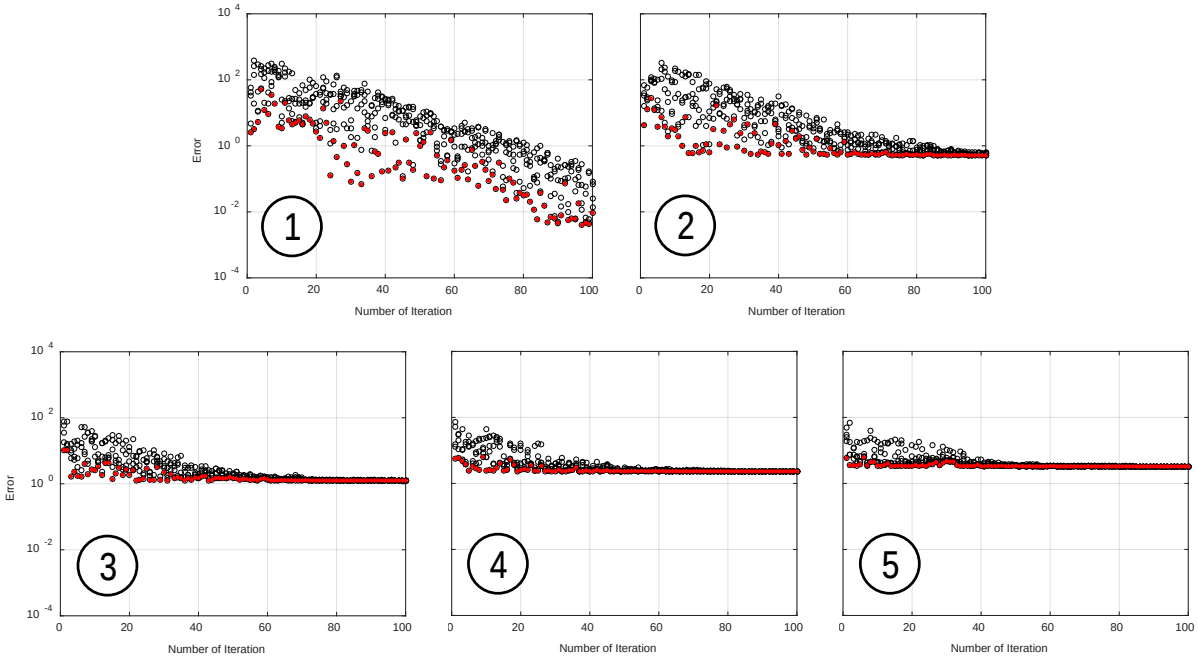

Figure 5.28: Single-fracture inversion results for the case shown in Fig. 5.26(a). A change in the error with the number of iterations is shown for each fracture numbered from left to right: open circles show errors for all models and red filled circles show a model with the minimum error in the given iteration.

The best results for the single fracture inversion (the models with the lowest error) are shown in Fig. 5.30 – middle figure. The evolution of errors after two iterations in the multi-fracture inversion is shown in Fig. 5.29. As can be seen in the plots, final errors are less than the errors in the first step. The final output is shown in Fig. 5.30 – right plot. The calculated fracture parameters are in a sufficiently good agreement with the true parameters.

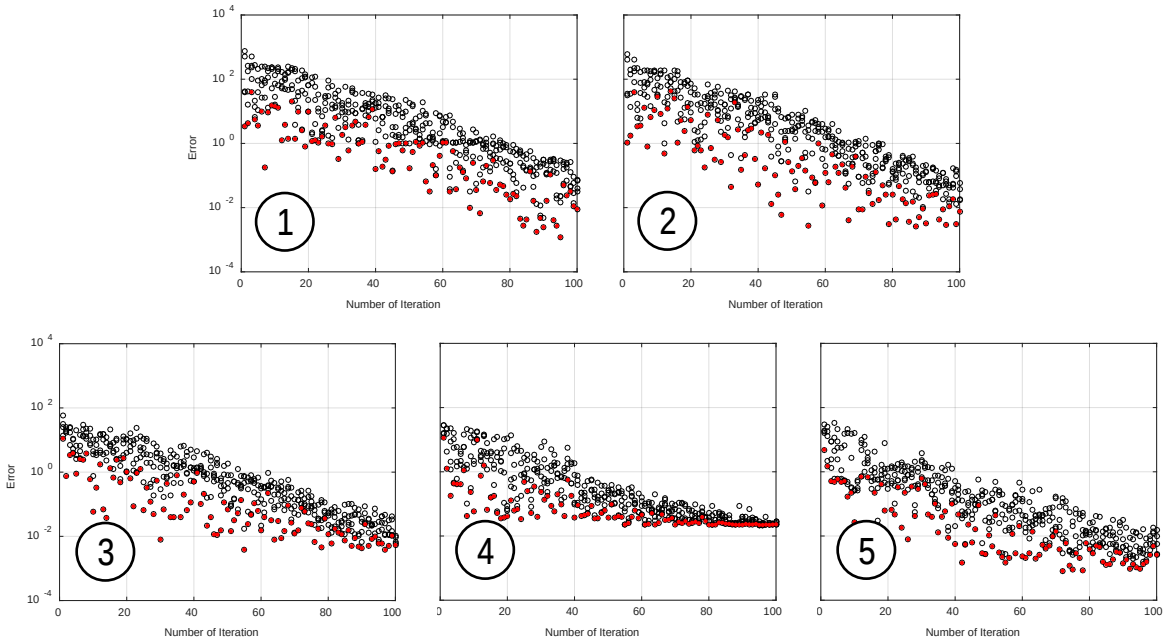

Figure 5.29: Multi-fracture inversion results after two iterations for the case shown in Fig. 5.26(a). A change in the error with the number of iterations is shown for each fracture numbered from left to right: open circles show errors for all models and red filled circles show a model with the minimum error in the given iteration.

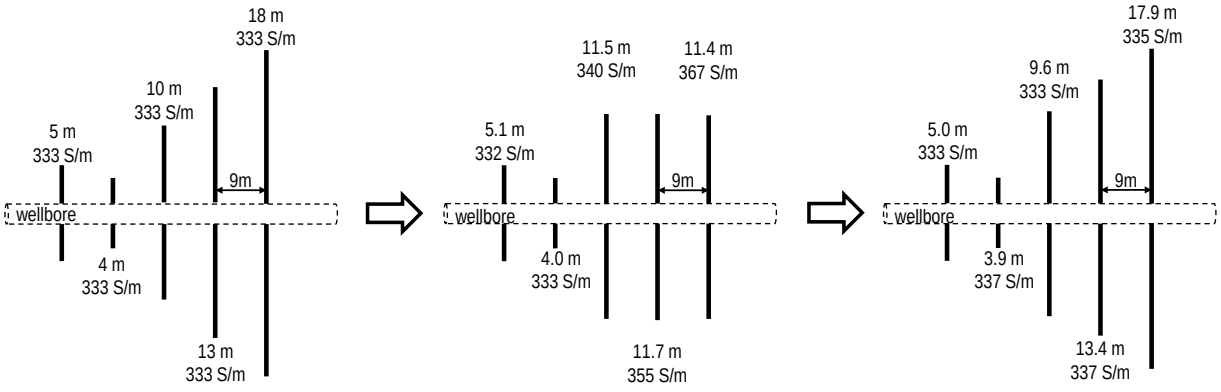

Figure 5.30: Multi-fracture inversion analysis for the model shown in Fig. 5.26(a): left figure shows the true model; middle and right figures show the best result after single- and multi-fracture inversions, respectively.

The differential signals for case (b) are shown in Fig. 5.31. Again, it is not easy to distinguish the distribution of fracture sizes by visual inspection. Based on two peaks in the signal observed in the cross-polarized configuration of short coil spacing (lower-left plot), we use three model parameters (conductivity, size and dip-angle) for the third and fourth fractures and two parameters (conductivity and size) for the rest. We apply the same inversion strategy as in the previous case.

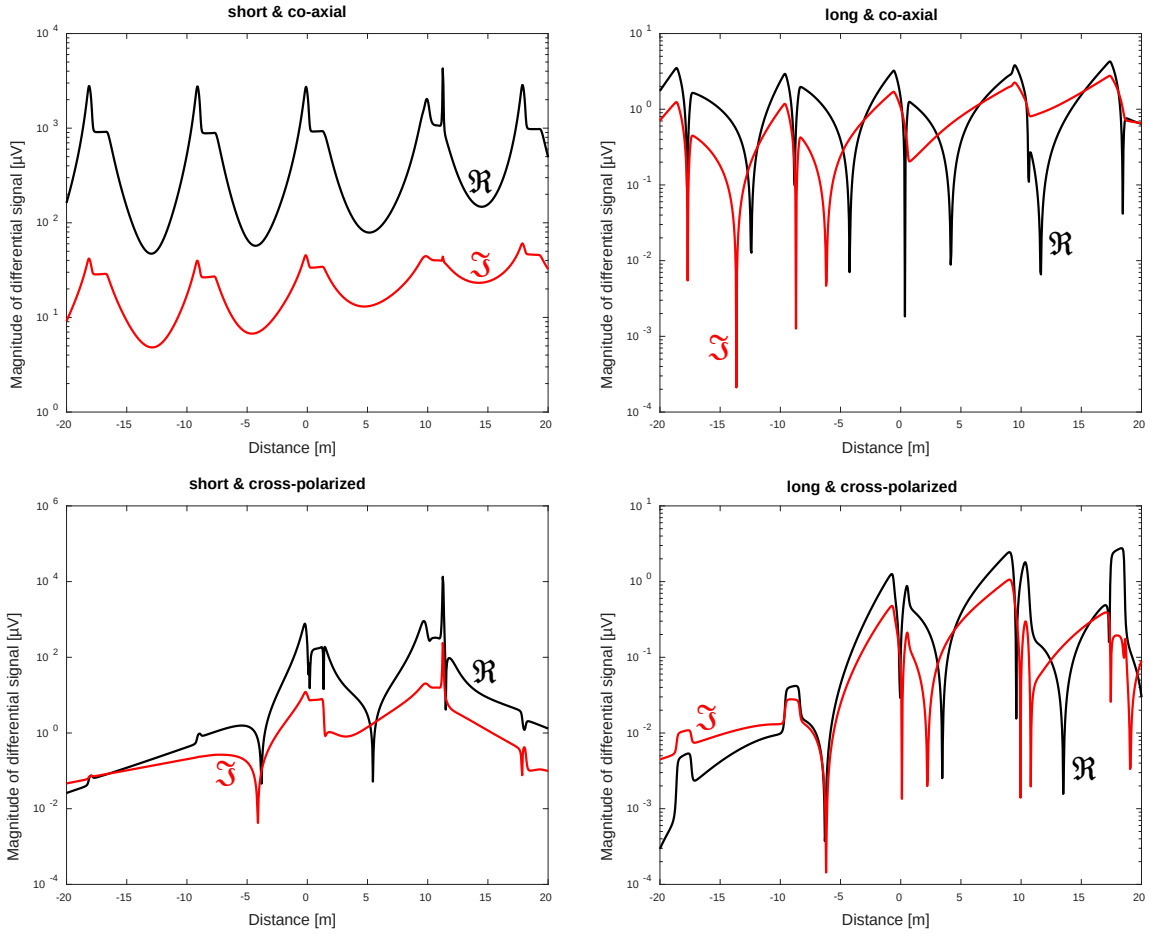

Figure 5.31: Differential signals for the case shown in Fig. 5.26(b): real (black) and imaginary (red) components are shown for co-axial (upper row) and cross-polarized (lower row) configurations for short (left column) and long (right column) coil spacings.

After the single fracture inversion, we get the following error vs. iteration for each fracture in case (b). The high levels of error for all cases can be attributed to the effect of neighboring fractures.

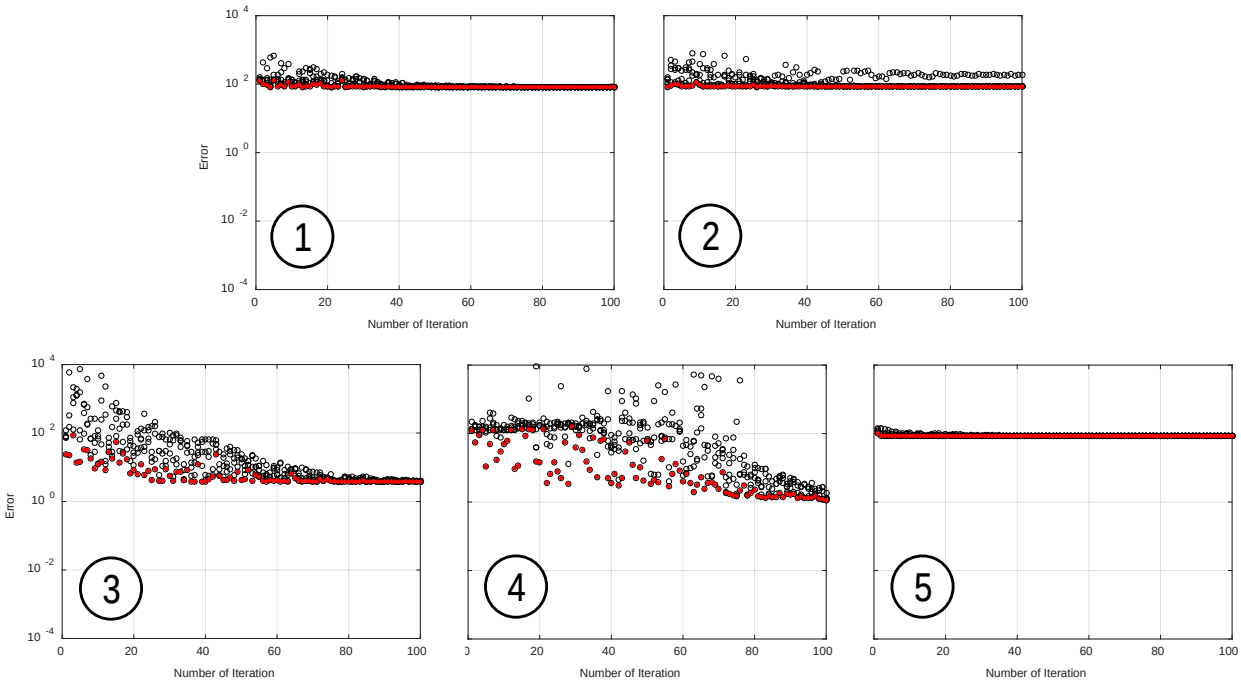

Figure 5.32: Single-fracture inversion results for the case shown in Fig. 5.26(b). A change in the error with the number of iterations is shown for each fracture numbered from left to right: open circles show errors for all models and red filled circles show a model with the minimum error in the given iteration.

The best results for the single fracture inversion (the models with the lowest error) are shown in Fig. 5.34 – middle figure. The evolution of errors after two iterations in the multi-fracture inversion is shown in Fig. 5.33. As can be seen in the plots, final errors are much less than the error of the first step. The final output is shown in Fig. 5.34 – right plot. The calculated fracture parameters are in a sufficiently good agreement with the true parameters.

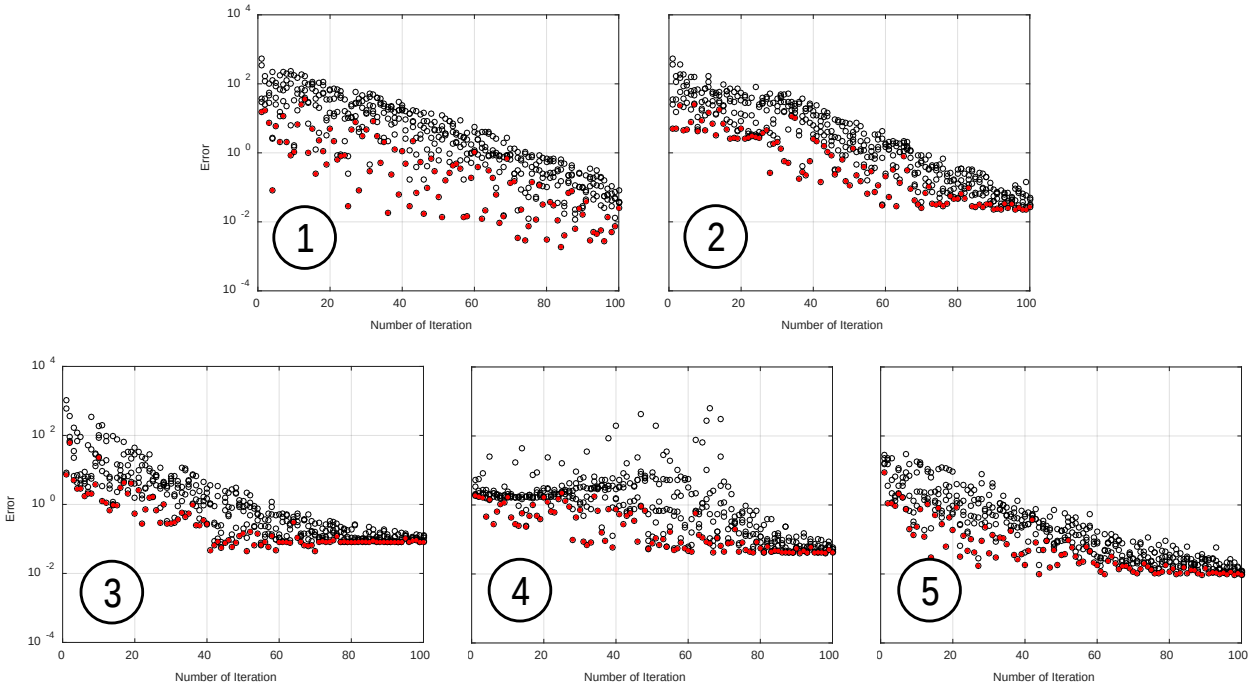

Figure 5.33: Multi-fracture inversion results after two iterations for the case shown in Fig. 5.26(b). A change in the error with the number of iterations is shown for each fracture numbered from left to right: open circles show errors for all models and red filled circles show a model with the minimum error in the given iteration.

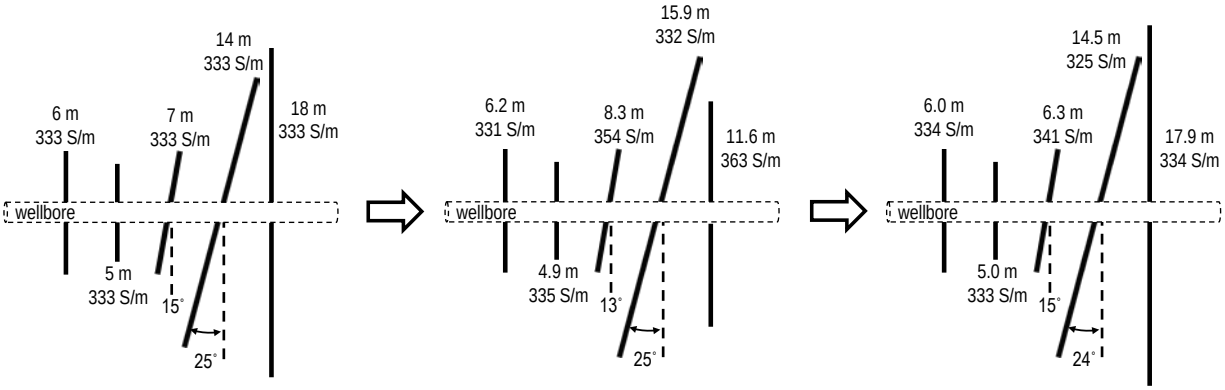

Figure 5.34: Multi-fracture inversion analysis for the model shown in Fig. 5.26(b): left figure shows the true model; middle and right figures show the best result after single- and multi-fracture inversions, respectively.

5.4. CONCLUSIONS

In this chapter, we developed a hybrid stochastic inversion algorithm to process tri-axial induction data to estimate the geometry and conductivity of hydraulic fractures. It is shown that this inversion analysis can successfully provide good estimates of fracture length, conductivity and

dip-angle. The approximation based linear regression is also shown to be a very efficient inversion technique for single orthogonal fractures. When neighboring fractures are considered in the inversion, the hybrid inversion model provides excellent results. In all cases, good agreement is obtained between the true and estimated fracture parameters suggesting that a tri-axial EM tool has excellent potential to map the proppant distribution in hydraulic fractures. The following conclusions are obtained from this study:

- By using a mono-axial transmitter coil and tri-axial receiver coils, it is possible to recover the effective properties of hydraulic fractures; two coil configurations (co-axial and cross-polarized) and two coil spacings (short and long) are essential to provide the complete description of fracture geometries and conductivities.
- For fractures that are assumed to be circular, parameters such as fracture conductivity and radius were shown to be recovered very accurately. For fractures that are assumed to be elliptical, we recover the effective radius for a circle which has the same area as the ellipse. When the proppant concentration varies radially in a fracture (linearly decreasing conductivities towards the fracture tip), the inverted conductivity value is approximately equal to the average conductivity of the fracture. In all these cases, the calculated dip-angle is always close to the true value.
- For heterogeneous conductivity rock, an accurate estimate of fracture parameters is obtained only after the subtraction of the differential signals with and without a hydraulic fracture. The differential signals without a fracture can be large enough to affect the inversion accuracy. This highlights the importance of logging the well before and after fracturing operations.
- For a tool spacing of 18 m, differential signals for the fracture of interest are affected by two neighboring fractures on each side when 9 m spacing is used for the distance between fractures. To invert the results for multiple fractures in a time efficient manner, five fractures should be included in each forward model run. This approach is shown to provide a very accurate estimation of fracture parameters in the given stage.

Chapter 6: Design Specifications and Simulation of a Field Deployable Tool

The final chapter of this report summarizes a suggested design of the commercial Low Frequency Electromagnetic Induction (LFEI) tool and explores its potential based on the numerical models presented in the previous chapters. This design work was initiated by E-Spectrum Technologies, Inc., under this contract (see Appendix A), and was significantly advanced during the subsequent Phase I SBIR/DOR project previously mentioned. Many of the results presented below, therefore, are taken from the Phase I final report (E-Spectrum, 2017). They are presented here for completeness because of the synergistic relationship between the two projects.

The numerical results presented here provide quantitative insight into the differential signals by evaluating the tool properties and proppant characteristics. To minimize power requirements and to investigate large fracture surface areas, we studied the effect of tool operation frequencies. In addition, we studied the effect of tool coil spacing to improve the efficiency of primary field cancellation and suggested a trend-line for selecting the coil separation distances. Later, we present numerical results for an inter-well deployment of the tool where a treatment well is monitored by an offset well. We also showed how proppant settlement can be monitored and how the enhanced electrical permittivity and magnetic permeability of the proppants can improve the differential signals. At the end of the chapter, we suggest a track of future study to improve the tool capabilities.

6.1. COMMERCIAL TOOL SPECIFICATIONS

A detailed system design specification was developed and fully documented in the attachment of a previously submitted report with the title, "LFEI System Design Document". For the purpose of clarity and transparency, it is noted that this document was developed under the Phase I SBIR/DOE project previously mentioned (E-Spectrum, 2017). Highlights of that report are presented in this section.

6.1.1. System Overview

The LFEI System is an induction logging system which utilizes a modular downhole tool featuring multiple, tri-axial transmit and receive coil arrays to facilitate diagnostics measurements and inversion analysis of hydraulic fractures propped with electrically conductive proppants. The system provides the following primary features:

- **Coiled tubing conveyed tool** – allows tool to be tripped in/out quickly, reducing overall time required for fracture diagnostics logging. The coiled tubing has an integral, single-conductor wireline for providing power and two-way communication between the tool and the surface.
- **Modular design –** tool consists of three basic components, Transmitter Sub, Receiver Sub, and Wired Spacer Bar, which can be easily transported and assembled at the job site.
- **Provides multiple investigation depths –** tool provides three investigation formation depths: short space (SS = 1.35m), intermediate space (IS = 5.3m), and long space (LS =

18.6m) and is reconfigurable for different investigation depths by replacing the Wired Spacer Bars.

- **Provides downhole data logging with easy data retrieval for inversion analysis –** each Receiver Sub logs conductivity measurements in non-volatile logging memory during the logging operation. Once on surface, the tool can be quickly disassembled, and a download cable can be connected to each sub to transfer logged data from logging memory to the surface laptop for inversion analysis.
- **Low Frequency, deep penetration operation –** 1 kHz transmitter frequency, coupled with low-noise, lock-in-amplifier (LIA) detection techniques, allows for deep penetration into the formation to facilitate the evaluation of long propped fracture geometries.
- **Bucking-compensated receiver coil arrays –** Receiver Sub features adjustable bucking coil array architecture to provide for reduction of the mutual inductance component in the receiver coil (caused by direct induction of transmitter coil current) to improve LIA receiver dynamic range.
- **Thermally controlled electronics module -** Transmitter and Receiver Subs feature thermally controlled electronics flasks to minimize temperature gradient induced electronic circuit drift and thus improve fracture measurement resolution and stability.

Fig. 6.1 shows an operational schematic of the LFEI system. The system consists of two major component blocks: a surface system and a modular downhole tool. The surface system includes computer hardware that allows the data to be downloaded and analyzed. For EM signals, deeper penetration into the rock is generally obtained by using lower frequencies. In practice, however, lower frequencies require higher power which necessitates a surface power supply. Therefore, the surface system also consists of a power source that delivers currents to the downhole tool. Lastly, considering the depth of reservoirs, it is anticipated that the power loss will be minimized if DC signals are delivered to the downhole tool and then converted to AC.

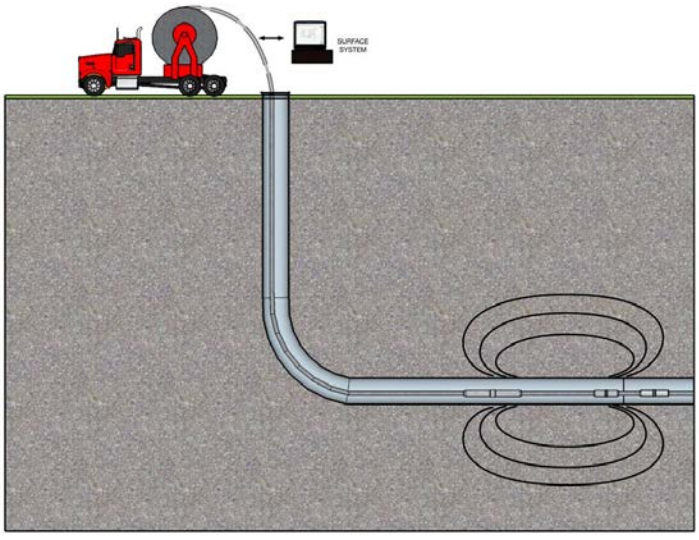

Figure 6.1: Low frequency electromagnetic induction (LFEI) tool consisting of a surface system and a modular downhole tool.

6.1.1.1. Surface System

The Surface System contains the equipment necessary for the operation of the tool and includes a laptop computer, power supplies, and communication equipment:

- Laptop Computer - the main operator interface and processing unit. This is a standard, commercial Windows Laptop running custom application software.
- Wireline Modem - a surface-located wireline modem used to communicate through the wireline to the downhole modem in the Transmitter Control Sub. The modem could either be an off-the-shelf or a custom assembly built to interface to the specific wireline used.
- Power Supply – a surface-located, 600 VDC power is supplied to the Transmitter Control Sub over the wireline. Fig. 6.2 shows the power topology for the system. The power supply is located on the surface, and a wireline cable is used to communicate with the downhole tool. The physics of LC tank shown in red dashed box is described in *Section 6.1.5*.

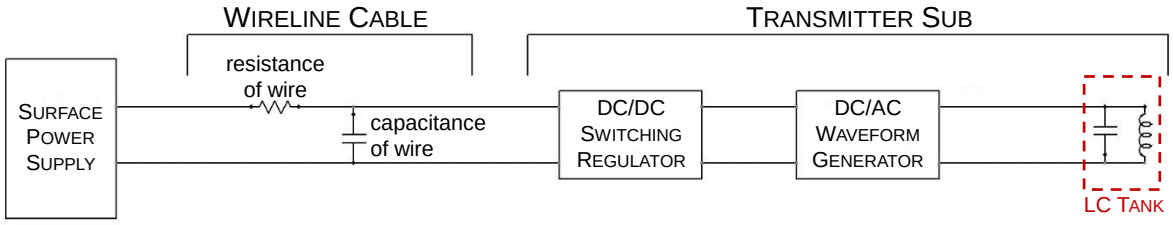

Figure 6.2: Transmitter sub power delivery system.

6.1.1.2. Modular Downhole Tool

Fig. 6.3 shows a block diagram of the LFEI Modular Downhole Tool. The tool consists of three primary components:

- Transmitter Sub
- Receiver Sub
- Wired Spacer Bar

Each of these components includes electronic modules and associated mechanical housings and interconnects.

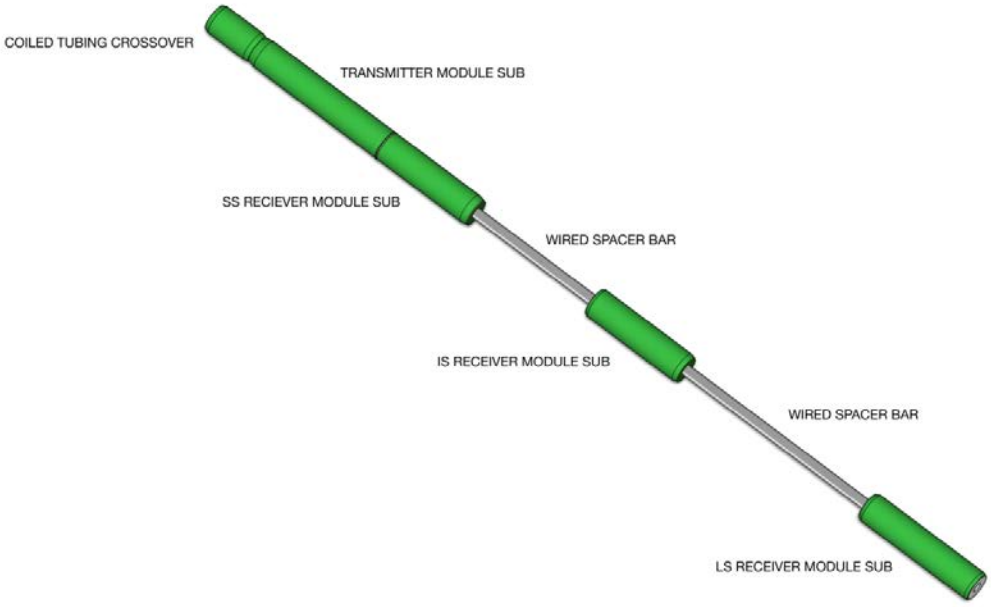

Figure 6.3: Downhole tool configuration

The downhole tool is designed to be deployed as the Bottom Hole Assembly (BHA) of a coiled tubing rig via connection to the tubing using a mechanical crossover adaptor. The tool is designed to be transported to the job site in nine pieces (one Transmitter Control Sub, one Transmitter Coil Sub, three Receiver Subs, and four Wired Spacer Bars), and assembled onsite prior to run-in. After formation/fracture imaging, the tool is tripped out and disassembled, and the logging data is downloaded from each Receiver Sub's logging memory using a download cable which connects directly to the Receiver Sub's wired spacer connection port.

Each Receiver Sub contains a replaceable bucking/receiver coil pair, the spacing of which can be manually adjusted for bucking calibration purposes. Once adjusted, the Receiver Sub coil pair spacing can be locked in place, and any misalignment of the coil pair with respect to the transmitter coil is monitored and logged, by the sub CPU, using an Orientation Module (OM) located in the sub. The OM contains a tri-axial magnetometer and a tri-axial accelerometer, and provides the orientation of the Receiver coil pair with respect to the earth's magnetic and gravity field vectors (note that the Transmitter Control Sub also contains an OM). This information can be combined with the tool geometry to correct for any bucking induced misalignment errors when the logged conduction data is post-processed prior to inversion.

The Wired Spacer Bars are used to space the Receiver Subs, and are also used to electrically connect the LIA synchronization clock and tool command/control bus. Multiple-conductor rotary connectors in sealed metal housings are screwed together to electrically and mechanically connect the various modules and spacer bars in the tool assembly.

6.1.2. Tool Electronics

Fig. 6.4 shows a top-level schematic of the LFEI tool electronic topology.

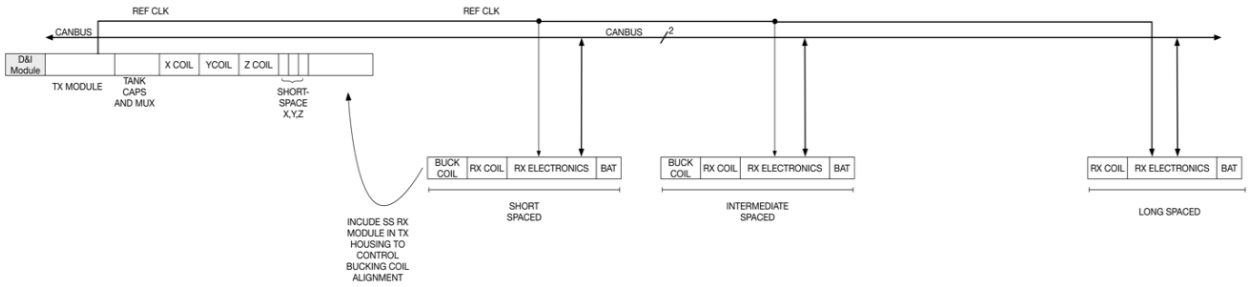

Figure 6.4: LFEI tool electronics block diagram

The Transmitter Module electronics consist of the following functional blocks:

- CPU – a highly integrated, high performance microcontroller that serves as the digital control element of the Transmitter Module. ESTI has used the selected microcontroller for other downhole tools, and as such, has an extensive peripheral firmware driver library in place and many custom firmware modules written to handle various type of signal processing algorithms.
- Coil-driver Power Supply – takes DC power from the wireline and converts it to a signal suitable to drive the transmit coils.
- Wireline Communications Interface – an embedded wireline modem that provides a mechanism for communicating with the surface controller via modulated signals coupled to the single conductor mono-cable power line.
- Tank Capacitor Module – a capacitor module that forms a tank circuit with the transmit coils. The tank circuit functions as a current multiplier when it is driven by a signal at the resonant frequency. By making use of a tank circuit, the power demand on the power supply is reduced.
- Transmitter Coil Multiplexer – a solid-state mux, consisting of high-temperature, high-voltage, silicon carbide junction FETs, used to sequentially connect the coil-driver power supply to the *x*-, *y*-, *z*- oriented transmitter coils.
- Long- and Short-Spacing Transmitter Coils – four different coils that generate magnetic fields in different directions and over different ranges. These magnetic fields are the sources for all detected receive signals.
- Receiver Module Interface – a wiring bus that allows the Transmitter Control Sub to communicate with the Receiver Subs in order to exchange command and control information and provide an optically isolated clock signal to sync the Receiver Sub lock-in amplifiers to the coil transmitter drive current frequency.

- Transmitter Orientation Module – an off-the-shelf directional package that provides digitized values of inclination, azimuth, tool-face angle, temperature, total gravitational field, and total magnetic field. This provides a means for determining the downhole spatial orientation of the Induction Tool Transmitter module and Receiver modules, and thus, can be used to detect/correct for misalignment bucking errors between the Transmitter Sub and the Receiver Subs.

The three Receiver Modules contain electronics that consist of the following functional blocks:

- Receiver and Bucking Coils – coils of various designs and orientations that, respectively, sense the magnetic fields generated by the transmit coils and improve performance by reducing the mutual inductance component in the receiver coils caused by direct induction of the transmitter coil current.
- Signal Conditioning Electronics – the receiver coil bucking circuitry, which consists of three Instrumentation Amplifier (IA) blocks, a 4th order bandpass filter, and a gain adjust circuit controlled by the CPU.
- Delta Sigma ADC – a 24-bit delta-sigma analog to digital converter that converts the analog receive signals to digital signals that can be read and stored in the Receiver CPU.
- Receiver CPU – the digital control element for the Receiver Sub. The same high performance microcontroller used in the Transmitter CPU will be used here.
- Receiver Orientation Module – a directional package used to detect/correct for misalignment bucking errors between the Transmitter Sub and the Receiver Subs. The same off-the-shelf directional package used in the Transmitter Module will be used here.
- Battery Pack – replaceable lithium thionyl chloride batteries to break-up ground loops and minimize the conducted transmitter noise within the tool string.

6.1.3. Tool Mechanical

Fig. 6.5 shows cross-sectional sketches of the mechanical architecture of the various tool subs. These subs are transported in modular form and assembled piece-by-piece, from bottom to top, in the wellhead. The maximum diameter of the tool is 4 inches, and the entire assembled tool is estimated to be about 76 feet long and to weigh about 800 lb. The subs and their mechanical components include:

- Transmitter Control Sub – a sealed metallic, non-magnetic tool section that includes the necessary electronics and hardware to communicate with the surface, communicate with the Receiver Subs, and generate and control the transmit signals sent to the transmit coils. This sub includes:
    - Transmitter Control Pressure Housing – a metallic, non-magnetic pressure barrel and bulkheads rated for 20,000 psi external pressure. The bulkheads seal each end of the pressure barrel and employ Stub Acme threads and double O-rings for reliability and ease of assembly.
    - Rolling Tube Crossover – the top bulkhead on the pressure housing, which connects the tool to the bottom end of the coiled tubing. Metal rollers built into the

crossover's exterior surface are used to reduce the sliding friction of the tool in inclined and horizontal sections of the wellbore.

- High-Temperature Electronics Backbone – a chassis used to mount the portions of the Transmitter Module Electronics that are not temperature sensitive, such as the Coil-Driver Power Supply and the Wireline Communications Interface.
- Transmitter Dewar Flask – a non-magnetic Dewar flask with phase-change material to house the Transmitter CPU, Transmitter Orientation Module, and other electronics that are temperature sensitive. A thermal analysis conducted in Phase I shows that this flask can provide at least a 27-hour operating window where the CPU temperature stays below 100˚ C in a 175˚ C well.
- Tank Capacitor and Coil MUX Backbones – chasses used to mount the tank capacitor bank and coil MUX.
- Lower Rolling Bulkhead and Wet Connector Housing – the lower bulkhead on the pressure housing, which houses the receptacle end of a multiple-conductor rotary connector mounted on its internal end surface for electrical connection with the Coil MUX as the lower bulkhead is screwed onto the pressure barrel. The bulkhead exterior surface also has built-in metal rollers similar to those on the Rolling Tube Crossover to reduce tool drag in inclined and horizontal wells.

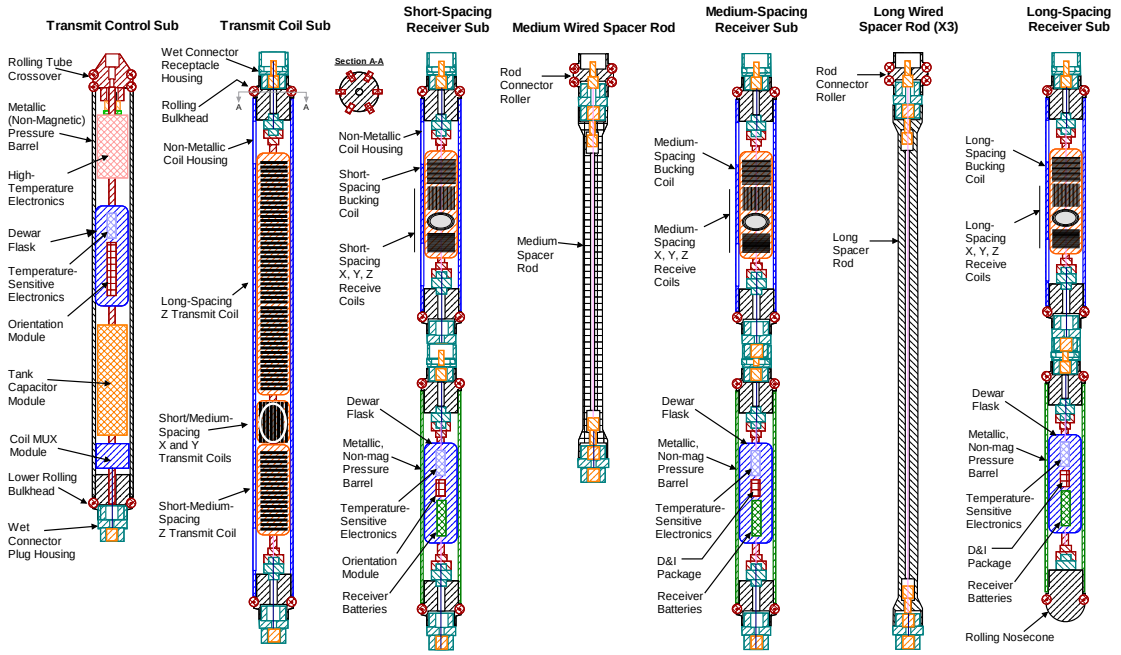

Figure 6.5: Conceptual design of the LFEI tool

- Transmitter Coil Sub – a tool section with a non-metallic housing the seals the transmitter coils. This sub includes:

- Transmitter Coil Housing – a non-metallic (fiberglass or high-temperature plastic) pressure housing employing either a pressure-compensated design or solid potting of the contents to withstand wellbore pressure and exclude wellbore fluids.
- Non-Metallic Rolling Bulkheads – the top and bottom bulkheads on the Transmitter Coil Sub that connect with the non-metallic pressure housing or protective sleeve with Stub Acme threads and contain multiple-conductor rotary connectors to electrically connect the Transmitter Coil Sub to the subs above and below it. Non-metallic rollers will again be incorporated into the exterior surface to reduce tool drag in inclined and horizontal wellbores. These bulkheads will likely be made of high-temperature plastic.
- Transmitter Coil Backbone – a single non-metallic backbone for mounting the transmitter coils to facilitate packaging and provide strength and rigidity to package, whether it is potted or pressure-compensated. This backbone will likely be made of fiberglass.

- Receiver Sub – a tool section with a non-metallic housing that seals the receiver coils and a metallic, non-magnetic housing that seals the temperature-sensitive receiver electronics. This sub includes:
  - Receiver Coil Housing - a non-metallic (fiberglass or high-temperature plastic) pressure housing employing either a pressure-compensated design or solid potting of the contents to withstand wellbore pressure and exclude wellbore fluids. Similar to the Transmitter Coil Housing.
  - Non-Metallic Rolling Bulkheads - similar to those used in the Transmitter Coil Sub.
  - Receiver Coil Backbone – similar to that used in the Transmitter Coil Sub.
  - Receiver Electronics Pressure Housing – a metallic, non-magnetic pressure housing used to protect the Receiver Dewar Flask from wellbore pressures and fluids.
  - Receiver Dewar Flask - a non-magnetic Dewar flask with phase-change material to house the temperature-sensitive receiver electronics, orientation package, and batteries. A thermal analysis conducted in Phase I shows that this flask can provide at least a 7-hour deployment window in a 175˚ C well, a 10+-hour operational window where the payload temperatures to stay constant at 60˚ C, and another 10-hour retrieval period where the payload temperatures stay below 100˚ C. The constant-temperature period allows the receiver electronics to operate with greatly improved performance.
- Spacer Rods – mon-metallic tool sections that space the Medium- and Long-Spacing Receiver Subs at specified distances downhole from the transmitter coils. The Medium and Long Spacer Rods are identical, except for length. The Medium Spacer Bar is about 12 feet long and positions the Medium-Spacing Receive Coils 20 feet from the Short-/Medium- Transmit Coils. The Long Spacer Bars are about 9-ft long, and three of them are connected together to place the Long-Spacing Receive Coils 60 feet from the Long-Transmit Coil. Each Spacer Rod includes:

- Rod Connector Roller - non-metallic bulkheads on the end of each spacer rod that mechanically and electrically connect the spacer rods with other subs and with each other. Multiple-conductor rotary connectors will be molded into each bulkhead.
- Rod - rods that span between the connectors are made of non-metallic materials such as fiberglass, high-temperature plastic, and rubber potting material. To ensure strength and rigidity, these connector rods may be as large as 2-3 inches diameter. Multiple-conductor wires running through the center of the spacer rods are potted inside the rods for additional strength and sealing efficacy.

6.1.4. Primary Field Cancellation

In this report, we have focused on single frequency analyses which allow us to use the frequency domain in all the experimental and computational set-ups. As already mentioned in the beginning of this report, in the frequency domain, the primary fields need to be canceled in co-axial and co-planar configurations (the primary field in cross-polarized configuration is theoretically zero) to improve the tool's sensitivity to small variations in the total magnetic field. The cancellation technique we have used is detailed both in Chapter 1 and 4. Another approach was implemented in Yu et al. (2016) where a transmitter coil is utilized as the bucking unit to cancel direct coil coupling in a small area near the receiving coil without affecting the primary field at other locations. This bucking coil is in a concentric arrangement with the receiver coil and minimizes incident field such that the total magnetic flux density at receiver locations can be approximated to the scattered field. They suggest this approach to have the capabilities of performing in situ bucking adjustments which can further increase the sensitivity of the tool in the downhole measurements (Liu et al., 2015).

The implementation of the same electromagnetic induction concept in the time domain eliminates the need to cancel the primary field where the responses are measured in the absence of it. Measurements in the time domain, however, are more susceptible to noise which can easily be filtered out in the frequency domain. If wide band analyses are required, the implementation of time domain methods will be more efficient because the same analyses in the frequency domain are overwhelming requiring many separate measurements.

6.1.5. LC Tank

The EM-based approach we are using for the hydraulic fracture monitoring supports many different types of waveforms: Gaussian, sinusoidal, square, etc. (Palisch et al., 2016). In this report, we have considered a signal generator which pulses sinusoidal waves to the LC tank (Fig. 6.6) which is one of the main components of the tool. The tank circuit, which consists of transmitting coils and capacitors, is an energy storage device which stores energy in the magnetic field of coils and the electric field of capacitors. During each cycle, this field energy is circulated between these two components. In an ideal case, when the DC resistance of its components is negligible, no energy is lost per cycle, so no further energy needs to be supplied. In a real application, however, the tank circuit will lose energy in every cycle due to DC resistance, and this loss must be compensated for by the AC voltage source. The loss can be minimized if the tank is operated at a resonant frequency defined as:

$$\omega = \frac{1}{\sqrt{LC}} \tag{6.1}$$

where ω is the angular frequency, L is the inductance and C is the capacitance of the tank. It is possible to adjust the capacitance (number of capacitors in parallel, p) to maintain a required operation frequency for a given inductor (Fig. 6.6). In space limited tools, however, the addition of more capacitors is not always an easy task. The additional practical challenge is the temperature constraint of the capacitors.

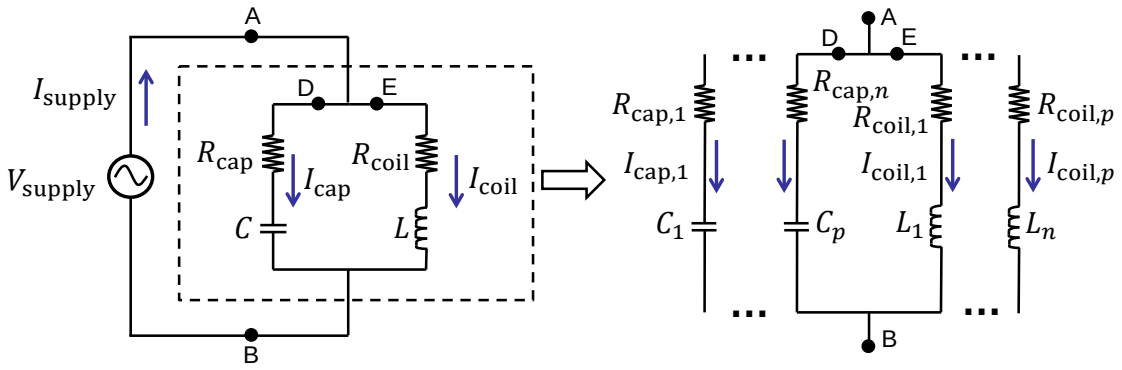

Figure 6.6: LC transmitter tank diagram.

For the induction coils used in the tank, the quality factor (Q) is an important design parameter to determine the efficiency of a coil's power storage. It is defined by the ratio of the inductive reactance (X) and the DC resistance (R) as shown below:

$$Q_{\text{coil}} = \frac{X_{\text{coil}}}{R_{\text{coil}}} = \frac{2\pi f L}{R_{\text{coil}}} \tag{6.2}$$

As is the case for dipole moment, the larger the value of quality factor, the better the design. It is possible to connect several inductor coils in parallel to decrease the total resistivity of a coil and to produce higher quality factors. The number of inductor coils in parallel (n), however, decreases the total inductance (L):

$$L < \frac{L_i}{n} \tag{6.3}$$

where inductance on each coil is calculated as:

$$L_i = \frac{\mu_{\text{core}} A_{\text{coil}} N_{\text{coil}}^2}{nh} \tag{6.4}$$

This is due to mutual inductance. The lower inductivity not only gives a lower quality factor but it also requires a higher capacitance for the given resonant frequency (Eq. 6.1). As previously mentioned, this is a mechanical challenge for a tool development.

In summary, for a low frequency electromagnetic induction tool, coils can be designed with a thicker gauge wire with fewer turns to reduce the losses and to lower the driving source power. Another important design consideration for this application is the use of a ferrite core which acts as a magnetic field multiplier. We get more benefit from a ferrite core as the length to diameter ratio of the coil increases, and this ratio is very small for coils oriented orthogonal to the wellbore. Therefore, a coil core oriented in the wellbore direction (*z*-oriented transmitter coil) will produce the strongest magnetic field.

6.2. MODELING TOOL SPECIFICATIONS

In this application, scattered signal levels are proportional to the frequency and inversely proportional to the distance between the coils. As we decrease the operation frequency, the signals get too weak to be detected (in the frequency range of interest signal levels decrease $\sim\omega^2$ as the frequency decreases). Hydraulic fractures, however, can be large and penetrate deep into the reservoir requiring large investigation areas which need lower operating frequencies and larger tool spacing. In this section, we provide optimum tool spacing maps to maximize received signals and to evaluate the bucking efficiency. Then, the investigation area of the tool is demonstrated by using the optimized spacing and frequency. The same analysis can be carried out for other frequencies and spacings with the numerical forward and inversion models provided in this report. In the last sub-section, we performed a numerical study to appraise the applicability of the inter-well tool deployment where a transmitter coil is logging a fracture in a treatment well and observations are made in an offset well.

6.2.1. Tool Spacing

From the previous chapter on inversion analyses, we know that the calculation of fracture parameters require responses both from relatively short and long coil spacings. Therefore, it is very important to have detectable differential signals in all spacings. The detectability of the signal depends on its absolute and relative values. In this sub-section, we evaluate the effect of tool aperture on the strength of signals of interest (presented in absolute and relative level). First, we look at the incident and scattered signals detected with one receiver coil at different background conductivities. Then, we compare the incident and scattered signals when the fracture size is changed. Finally, the same comparison is performed when we include the bucking-receiver coil into the system.

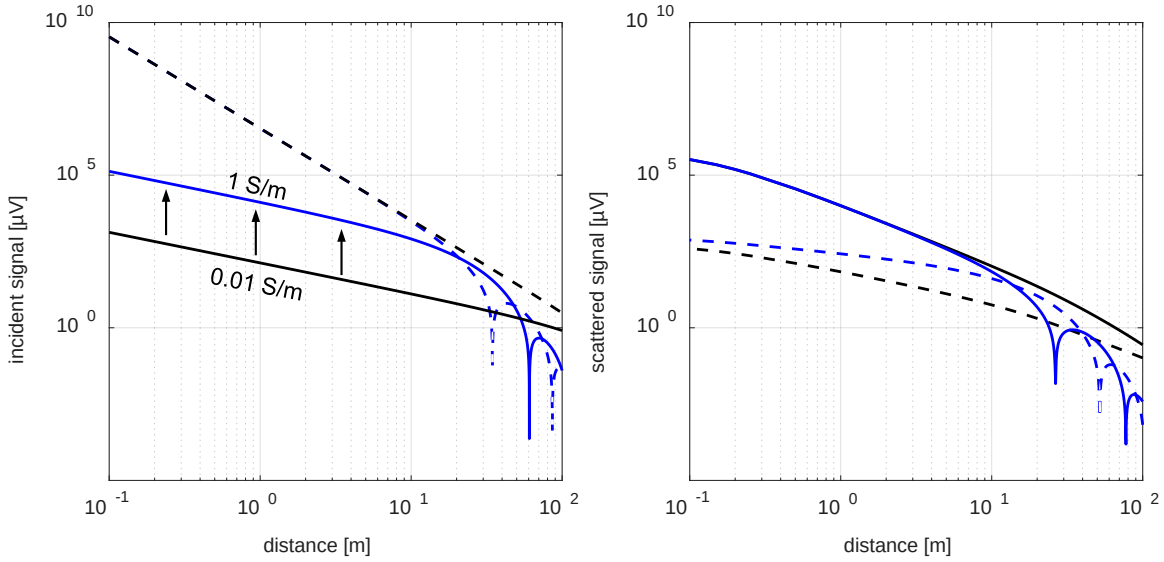

Figure 6.7: The effect of background conductivity on the incident (left) and scattered (right) signals: *x*-axis is the distance between transmitter and receiver coil; solid and dashed lines show real and imaginary components, respectively; black and blue lines are for a background formation conductivity of 0.01 S/m and 1 S/m, respectively. The tool is operated at 1 kHz frequency and 1500 $\mathbf{A \cdot m^2}$ transmitting moment; the cross-sectional area of the receiver coil is 30 $\mathbf{mm^2}$ with 600 turns. For the scattered field calculation, fracture is assumed to be a disc with 30 m radius, 333 S/m conductivity and 5 mm thickness.

Fig. 6.7 shows the change of incident signals with the change of background conductivity and transmitter-receiver spacing. The interval selected for the formation conductivity covers the minimum and maximum electrical conductivities of shale (Adisoemarta, 1999). For the scattered signals, the receiver is positioned at the fracture location, and we adjust the distance between the transmitter and the receiver coils. Obviously, as the distance between coils increases both incident and scattered signals weaken. An increase in the background conductivity of the formation, however, increases the real component of incident signals and the imaginary component of scattered signals keeping the other components the same for most of the transmitter-receiver spacing. Note that for a majority of the region that covers the nominal tool spacings, imaginary signals are stronger than the real signals for incident fields and vice versa for scattered fields.

Fig. 6.8 shows incident and scattered signals for fractures with a radius of 1 m and 20 m, and the background (rock) formation conductivity is 0.333 S/m. As already noted in Fig. 6.7, there is a phase difference between the dominant components of incident and scattered signals, however, in all cases, the real component of incident signals is significantly stronger compared to that of scattered signals. This suggests the importance of the bucking coil for both short and long coil spacings. For the short spacing receiver, even signal decomposition will improve the quality of detection and adding the bucking coil will improve it further. For the long spacing receiver, however, the implementation of the bucking coil is more vital. Further plots are proposed for the optimum spacing between the receiver and bucking coil.

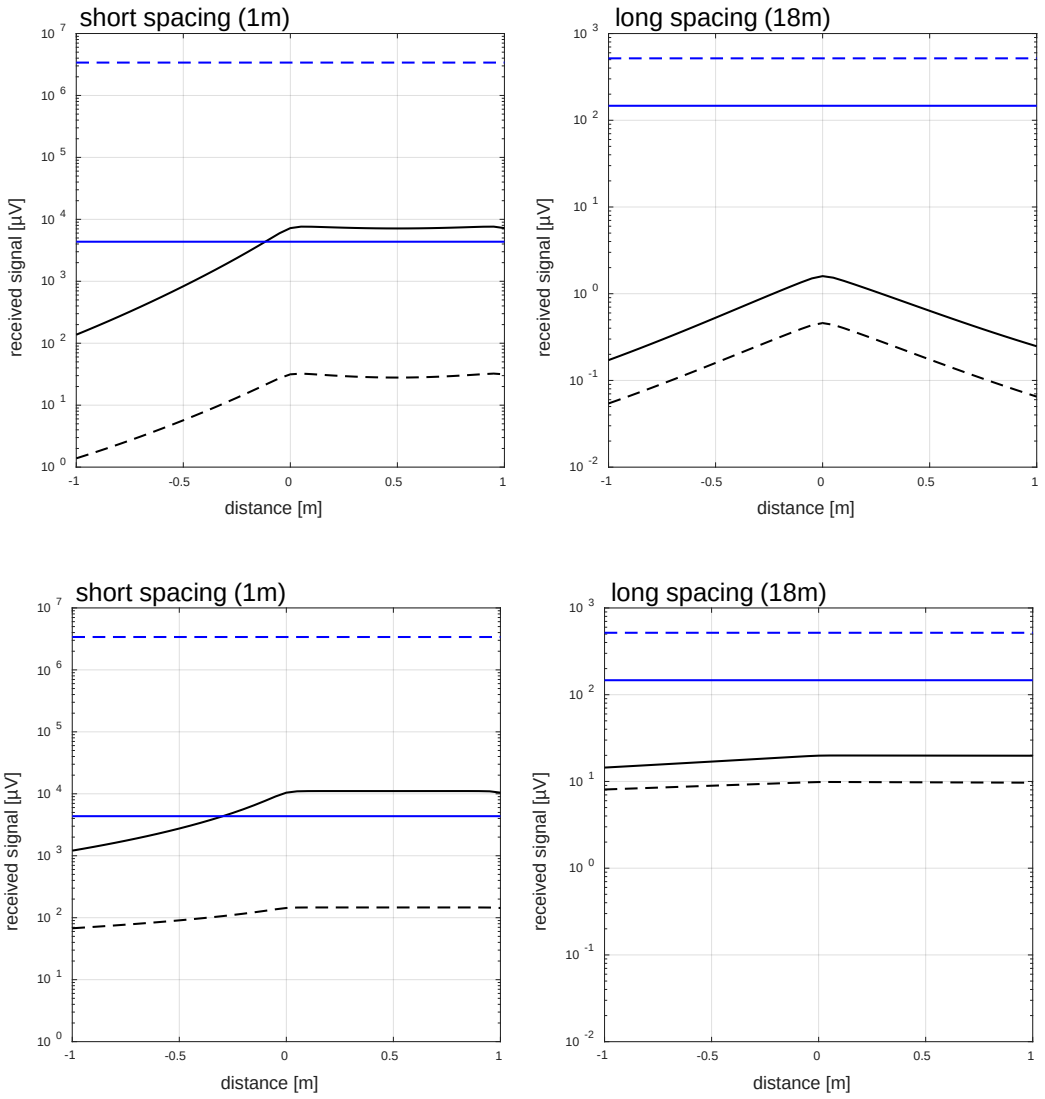

Figure 6.8: Incident (blue) and scattered (black) signals for short (left column) and long (right column) coil spacings: real (solid lines) and imaginary (dashed lines) components of signals are shown for the background formation with 0.333 S/m conductivity. The tool is operated at 1 kHz frequency and 1500 $\mathbf{A \cdot m^2}$ transmitting moment; the cross-sectional area of the receiver coil is 30 $\mathbf{mm^2}$ with 600 turns. For the scattered field calculation, a fracture is assumed to be a disc with 1 m (upper row) and 20 m (lower row) radius, 333 S/m conductivity and 5 mm thickness.

To find the optimum bucking and receiver coil distances for the long coil spacing, we plotted the absolute and relative signal levels for the 30 m radius fracture in Fig. 6.9. The *y*-axis of the plots is the distance between the transmitter and the center of the receiver couples, and the relative signal is calculated by dividing the secondary signals by primary signals. Based on these absolute and relative signals, we suggest a trend-line (shown with a dashed line) to select the distance between coils. The dashed line is the region where differential signals are strong enough to be detected and their ratio to the primary signals is sufficiently large.

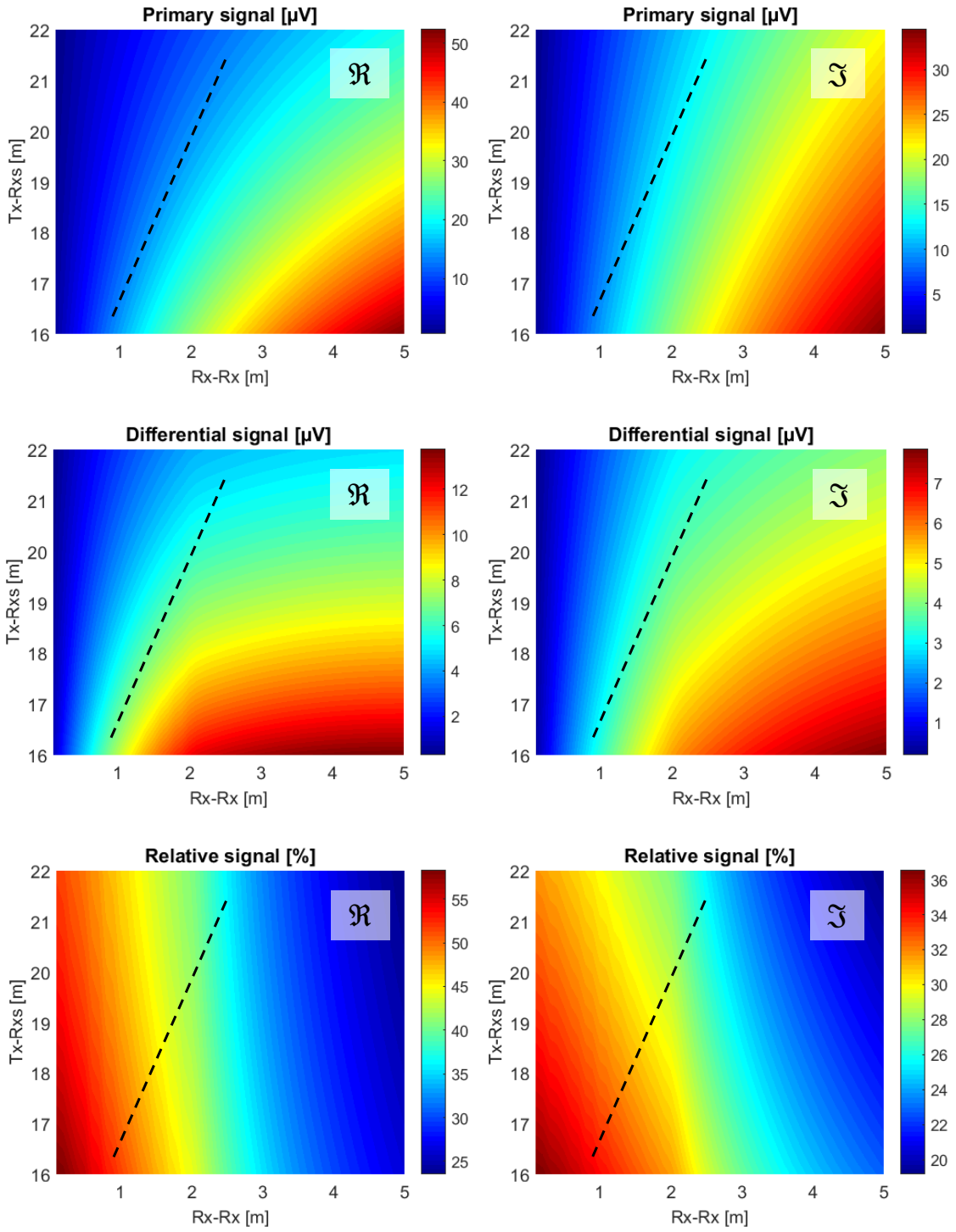

Figure 6.9: The primary (top row), differential (middle row) and relative (bottom row) signals for different transmitter-receiver and receiver-receiver spacings: real (left column) and imaginary (right column) components of signals are shown for the background formation with the conductivity of 0.333 S/m. For the differential and relative signal calculation, the fracture is a disc with 30 m outer radius, 10 cm inner radius, 333 S/m conductivity and 5 mm thickness.

6.2.2. Depth of Investigation

In this section, we estimate the investigation area of the tool by using the inversion algorithm developed in the previous chapter. We run multiple realizations by increasing the radius of fractures and calculating a variation in the inverted fracture parameters. Fig. 6.10 shows results for the tool with nominal spacings and properties. After running the forward model for the orthogonal and circular fractures with the node spacing factor of ten, we added one percent of random noise to the differential signals. A node spacing factor of four was used in the inversion analysis. There are at least five realizations for the given radius of a fracture and 300 of the most successful results are plotted in the figure. The measured variation is calculated by subtracting the true model parameter from the calculated value. In the runs, the fracture conductivity for the true model is 100 S/m.

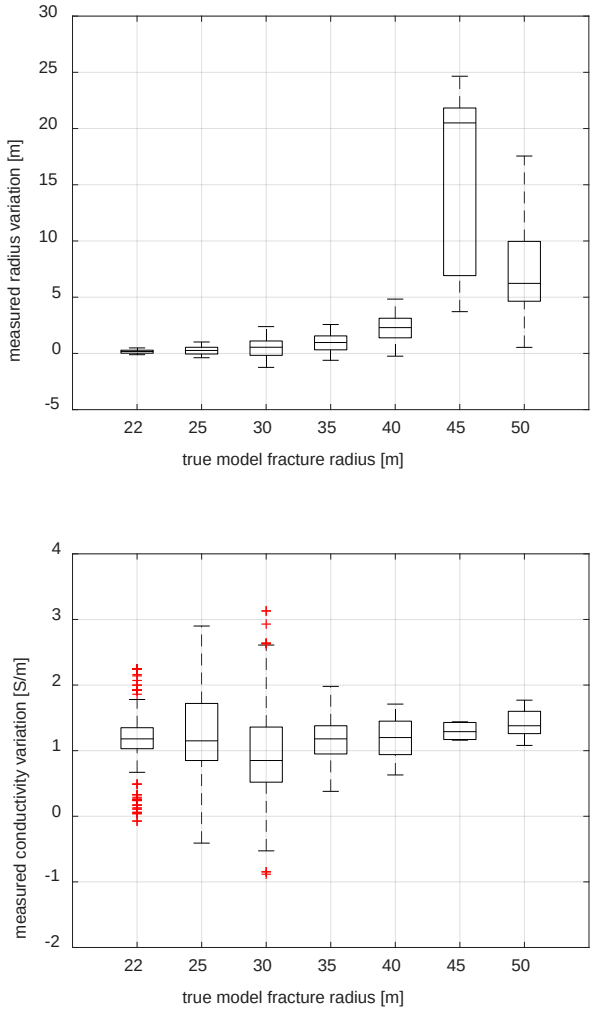

Figure 6.10: Box plots for the inverted vs. actual parameters: calculated variation of fracture radius (upper) and fracture conductivity (lower) vs. the fracture radius of the true model. The boxes include 300 of the lowest error results from 5 different realizations.

The results show that once the radius surpasses 40 m, the tool with the nominal spacing and properties loses resolution. The variation of fracture conductivity, however, is not increasing for this uniformly distributed conductivity case. To determine fracture sizes larger than 40 m we can use longer spacings for the tool but we need to make sure that signals are detectable. One way to increase these signal levels is to deploy a receiver coil with a higher magnetic dipole moment (not taking into account the noise level in the field). Another way is to use proppants with further enhanced electromagnetic properties (see Section 5.3.4).

6.2.3. Inter-well Testing

To diagnose larger fractures, another potential deployment of the tool is the inter-well monitoring of the treatment well. In this part, we numerically evaluate signal levels detected with receivers in an observation well while logging a treatment well with a transmitter coil. The fracture is an orthogonal circle with a radius of 30 m, conductivity of 333 S/m and thickness of 5 mm. The upper drawing of Fig. 6.11 shows the scheme used in the simulation, and in the lower graph, secondary (scattered) signals are plotted. Two separate lines are shown for the transmitter fracture distance: the lower line is the secondary signals when the transmitter coil is 30 m away from the fracture and the upper line shows signals when the transmitter coil is at the center of the fracture. The receiver is in the observation well where its *z*-coordinate is always the same as that of the fracture. The tool is operated at 1 kHz frequency and 1500 $\mathrm{A \cdot m^2}$ transmitting moment; the cross-sectional area of the receiver coil is 30 $\mathrm{mm^2}$ with 600 turns.

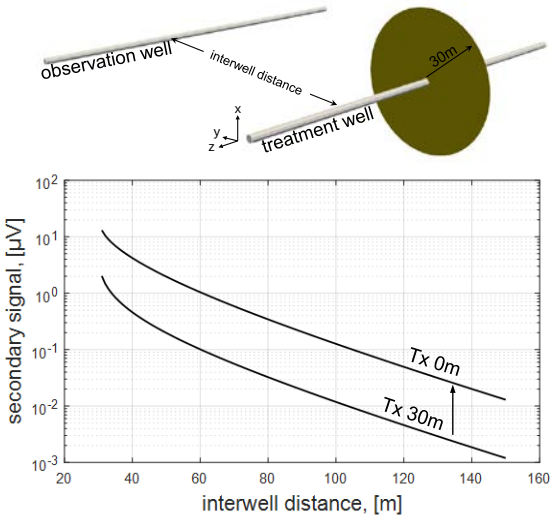

Figure 6.11: Inter-well hydraulic fracture monitoring: scattered signals are calculated for a receiver coil in the observation well and a transmitter coil in the treatment well (upper drawing). In the plot, upper and lower lines show signals when the transmitter coil is 0 m and 30 m away from the fracture, respectively. The fracture is a disc with an outer radius of 30 m, inner radius of 10 cm, conductivity of 333 S/m and thickness of 5 mm. The background formation (rock) conductivity is 0.333 S/m. The tool is operated at 1 kHz frequency and 1500 $\mathbf{A \cdot m^2}$ transmitting moment; the cross-sectional area of the receiver coil is 30 $\mathbf{mm^2}$ with 600 turns.

As it can be seen in the plot of Fig. 6.11, for the transmitter coil at the center of the fracture (upper line), the scattered signals fall below 1 μV when the observation well is 60 m away from the treatment well. To detect weak signals is practically challenging and this limits the deployment of the tool for inter-well diagnosis.

6.3. SIMULATING FIELD DEPLOYABLE TOOL

In this section, we numerically investigate the tool's potential to detect proppant settling. Later, a numerical study is carried out to see how proppants can be upgraded to scatter stronger signals.

6.3.1. Proppant Settling: Imaging Proppant Banks

There has been a great deal of research conducted on the proppant transport in hydraulic fractures (Blyton et al. 2015). Investigating favorable conditions leading to efficient proppant delivery to induced fractures without letting them settle has been a long-standing challenge. Independent proppant monitoring techniques assist in these studies and improve operational efficiencies. Therefore, in this section, we evaluate the potential of the induction tool for settlement detection by changing the geometry of fractures, as shown in Fig. 6.12, and recording the variation in the differential signals. For all cases, we assume that the injected proppant volume is the same; as the area of fracture decreases, we linearly increase the conductivity. The surface area of fractures is 201 m^2, 162 m^2, 101 m^2 and 67 m^2, hence the conductivity is selected as 100 S/m, 124 S/m, 200 S/m and 300 S/m for the fractures from left to right (Fig. 6.12), and the thickness of fractures is 5 mm for all cases.

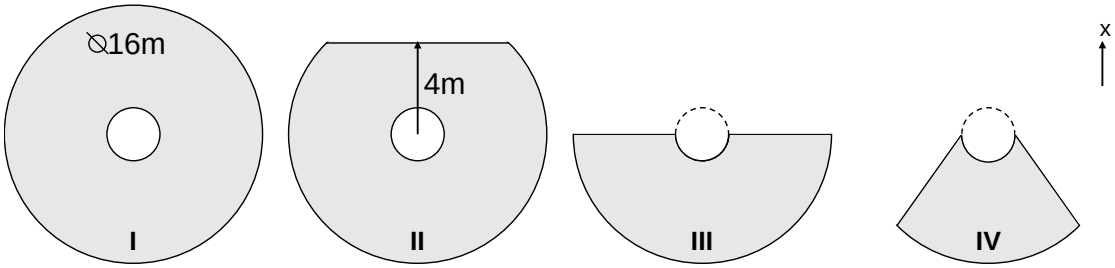

Figure 6.12: Fracture models used in the proppant settlement simulation: models are orthogonal to the wellbore, and the injected volume of proppant is constant.

Differential signals for the four different cases of fractures are plotted in Fig. 6.13. In the computation, the distances for the short spacing receivers are 0.8 m and 1.2 m, and 17.8 m and 18.2 m for the long spacing receivers. The operational frequency is 1 kHz, and transmitting magnetic dipole moment is 1500 $A.m^2$. The cross-sectional area of receiver coils is 30 cm^2 with 600 turns. The formation (rock) conductivity is 0.333 S/m.

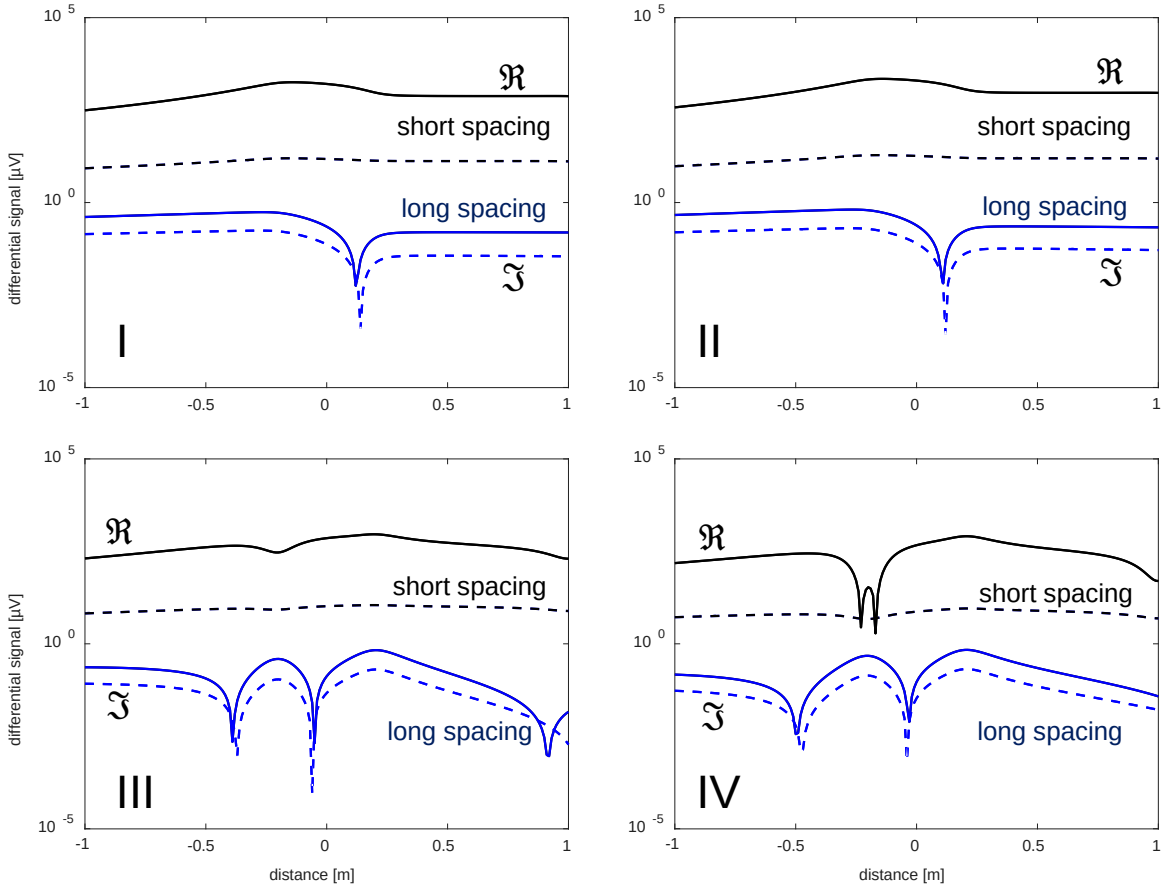

Figure 6.13: Monitoring proppant settling: fracture models shown in Fig. 6.12 are used to compute the real (solid line) and imaginary (dashed line) components of differential signals in short (black) and long (blue) coil spacings.

As the shape of fracture becomes more irregular, differential signals vary from that of the regular circle response. This proves that there is good potential for the tool to evaluate proppant settlement.

6.3.2. Enhanced Electrical Permittivity

Till now, all results are demonstrated for the electrical conductivity of proppants where both the relative permittivity and magnetic permeability are one. In this sub-section, we investigate how proppants with enhanced electrical permittivity affect the differential signals. In the next sub-section, the effect of enhanced magnetic permeability is studied.

To evaluate the effect of enhanced electrical permittivity, we need to implement the boundary condition shown in Eq. 3.13. In the equation, shunt admittance is due to two parallel sheets: a resistive sheet with the admittance σt and a pure reactive sheet (the right component of the summation). In Fig. 6.14, we plot those components over a wide frequency range. The fracture conductivity is 333 S/m and thickness is 5 mm. As can be seen from the plot, in the 1 Hz - 1 MHz

range of frequency, the resistive sheet strongly dominates shunt admittance and consequently surface impedance. As the relative permittivity of proppants increases the signals of interest will not be affected.

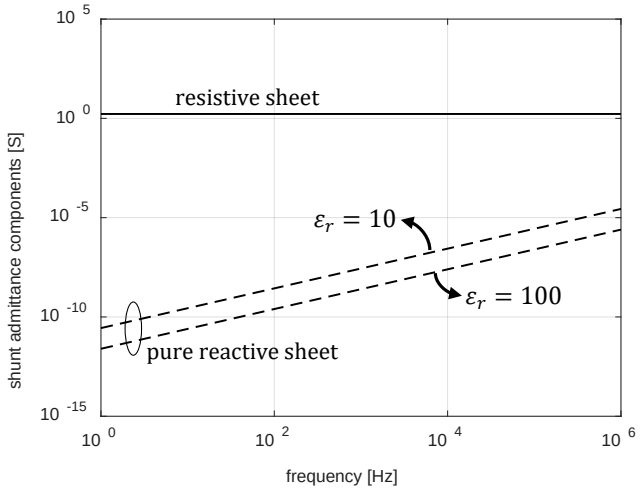

Figure 6.14: Dependence of shunt admittance (Eq. 3.13) on the resistive (solid line) and pure reactive (dashed lines) sheet.

6.3.3. Enhanced Magnetic Permeability

For evaluating the effect of enhanced relative magnetic permeability, we have used the axial hybrid method and the values are adjusted between 1, 5, 10, 20 and 50. In the simulation, the fracture has an outer radius of 8 m, inner radius of 10 cm, conductivity of 333 S/m and thickness of 5 mm, and the background formation (rock) conductivity is 0.333 S/m. The uniform section of meshing ranges from -1 to 1 m with the step sizes of 10 cm (Fig. 3.13). In the expanding mesh section, grid expansion ratio is 1.1, and the computation domain is truncated at 100 m on both edges. The operation frequency is 1 kHz, and the magnetic dipole moment of transmitter coil is 1500 A.m^2. The cross-sectional area of receiver coil is 30 cm^2, and the number of turns on the receiver coil is 600. The distance between the transmitter and the first and second receivers is 0.8 and 1.2 m, respectively. Fig. 6.15 shows real and imaginary components of differential signals for all relative permeabilities.

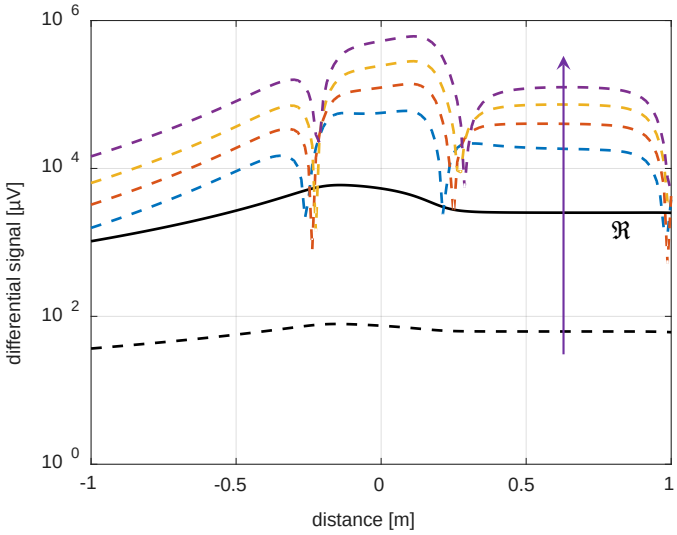

Figure 6.15: The effect of fracture relative magnetic permeability on the differential signals calculated with co-axial configuration of short coil spacing: relative magnetic permeability increases in the direction of arrow, and the values are selected as 1, 5, 10, 20 and 50; black solid line shows real component of signals for all simulated cases and dashed lines are imaginary components.

It can be seen from the plot that the real part of the differential signal does not change while increasing the relative permeability; however, imaginary components increase significantly. A 50 times increase in the relative permeability results in imaginary differential signals 100 times stronger than the real components.

6.4. CONCLUSIONS

In this chapter, first, we presented the current design of the induction tool. Then, we demonstrated the capabilities of the current tool with nominal spacings and properties. The signal levels for a range of shale rock electrical conductivities are presented and the improvement made with the bucking coil is evaluated to establish a trend-line to calculate the distance between the receiver and bucking coil for the given transmitter-receiver distance. For the investigation area, the resolution of the tool is sufficiently high, up to 40 m radii. Further improvement can be obtained by sustaining detectable signal levels for the increased tool spacings. This can be achieved with better coil design, large EM contrast proppants or both. We also evaluated an inter-well deployment of the tool and found it practically challenging to detect the signals from the observation well.

In the last part, we demonstrated the potential of the induction tool in monitoring proppant settling. By changing the shapes and keeping the total injected proppant volume the same, we have shown that the differential signals are distinguishable. Finally, to improve the differential signals we can increase the magnetic permeability of the proppants. The differential signals are indifferent to the enhanced electrical permittivity.

6.5. FUTURE WORK

In this last section, we provide a list of several additional efforts that could be made to make the tool more efficient:

- The current design of the tool cannot handle in-situ bucking. This is a practical challenge which can cause a loss of accuracy in the measured signals. The surface control of the bucking, which is suggested in Yu et al. (2016), can be studied and incorporated into the current tool.
- Proppants with enhanced magnetic permeability can be used in the field which was shown to further increase the signal levels compared to the case when only electrical conductivity is the contrast agent.
- The capability of multi frequency analysis can be added to the tool which may produce more information on a conductivity distribution inside the fracture. Although this may require only slight changes in the tool itself, significant changes in the computational study will be necessary. This may require time-domain analyses for the computation efficiency.
- In the inversion study, different shapes of fractures can be parametrized and used in the simulation to envision capabilities of the tool. This will be more meaningful after obtaining field data.
- Current inversion analysis will recover information about the main branch of fractures. They can be extended to the generation of a conductivity map where secondary branches of fractures can also be monitored. The use of axial hybrid methods will be less costly because of lower computation dimensions, and the study can be further extended to three-dimensional numerical solutions where variable background formation conductivities can be computed.

List of Tables

List of Figures

References

Adisoemarta, P.S., 1999, Complex electrical properties of shale as a function of frequency and water content: Ph.D. dissertation, Texas Tech University.

Balan, H.O., A. Gupta, and D.T. Georgi, 2017, Feasibility of predicting long-term shale gas production and EURs based on early-time data: Presented at the SPE Middle East Oil & Gas Show and Conference, doi: 10.2118/183754-MS.

Balanis, C.A., 2005, Antenna theory analysis and design: John Wiley & Sons, Inc.

Basu, S., 2014, Fracture diagnostics using low-frequency electromagnetic induction: M.S. thesis, The University of Texas at Austin.

Basu, S., and M.M. Sharma, 2014, A new method for fracture diagnostics using low-frequency electromagnetic induction: Presented at the SPE Hydraulic Fracturing Technology Conference, doi: 10.2118/168606-MS.

Batchelor, A.S., R. Baria, and K. Hearn, 1983, Monitoring the effects of hydraulic stimulation by microseismic event location: a case study: Presented at the SPE-AIME Annual Technical Conference and Exhibition, doi: 10.2118/12109-MS.

Bhatnagar, A., 2016, Overcoming challenges in fracture stimulation through advanced fracture diagnostics: Presented at the SPE Asia Pacific Hydraulic Fracturing Conference, doi: 10.2118/181802-MS.

Blyton, C.A.J., D.P. Gala, and M.M. Sharma, 2015, A comprehensive study of proppant transport in a hydraulic fracture: Presented at the SPE Annual Technical Conference and Exhibition, doi: 10.2118/174973-MS.

Carey, M.A., S. Mondal, and M.M. Sharma, 2015, Analysis of water hammer signatures for fracture diagnostics: Presented at the SPE Annual Technical Conference and Exhibition, doi: 10.2118/174866-MS.

Carey, M.A., S. Mondal, M.M. Sharma, and D.B. Hebert, 2016, Correlating water hammer signatures with production log and microseismic data in fractured horizontal wells: Presented at the SPE Hydraulic Fracturing Technology Conference, doi: 10.2118/179108-MS.

Catlett, R.D., J.D. Spencer, E. Lolon, and D. Bucior, 2013, Evaluation of two horizontal wells in the eagle ford using oil-based chemical tracer technology to optimize stimulation design: Presented at the SPE Hydraulic Fracturing Technology Conference, doi: 10.2118/163846-MS.

Cipolla, C.L., and C.A. Wright, 2000, State-of-the-art in hydraulic fracture diagnostics: Presented at the SPE Asia Pacific Oil and Gas Conference and Exhibition, doi: 10.2118/64434-MS.

Davidson, D.B., 2011, Computational electromagnetics for RF and microwave engineering: Cambridge University Press.

Dawson, M., and G. Kampfer, 2016, Breakthrough in hydraulic fracture & proppant mapping: achieving increased precision with lower cost: Presented at the Unconventional Resources Technology Conference, doi: 10.15530/URTEC-2016-2432330.

Duenckel, R.J., H.D. Smith, S. Hao, D. Gao, T.T. Palisch, and X. Han, 2011, A new method to identify proppant location in induced fractures: Presented at the International Petroleum Technology Conference, doi: doi.org/10.2523/IPTC-14369-MS.

Duesterhoeft, W.C., R.E. Hartline, and H.S. Thomsen, 1961, The effect of coil design on the performance of the induction log: Journal of Petroleum Technology, **13**, no. 11, 1137-1150, doi: 10.2118/1558-G-PA.

Eftekhari, B., M. Marder, and T.W. Patzek, 2018, Field data provide estimates of effective permeability, fracturing spacing, well drainage area and incremental production in gas shales: Journal of Natural Gas Science and Engineering, **56**, 141-151, doi: 10.1016/j.jngse.2018.05.027.

Eisner, L., T. Fischer, and J.H. Le Calvez, 2006, Detection of repeated hydraulic fracturing (out-of-zone growth) by microseismic monitoring: The Leading Edge, **25**, no. 5, 548-554, doi: 10.1190/1.2202655.

Elahi, S.H., and B. Jafarpour, 2018, Dynamic fracture characterization from tracer-test and flow-rate data with ensemble Kalman filter: SPE Journal, **23**, no.2, 449-466, doi: 10.2118/189449-PA.

E-Spectrum Technologies, Inc., and The University of Texas, April 2017, An Enhanced Extermely Low Frequency Triaxial Induction Tool for Fracture Diagnostics in Open Wellbores, SBIR/DOE Phase I Final Report, Grant No. DE-SC0015774 .

Fisher, M.K., C.A. Wright, B.M. Davidson, A.K. Goodwin, E.O. Fielder, W.S. Buckler, and N.P. Steinsberger, 2002, Integrating fracture mapping technologies to optimize stimulations in the Barnett Shale: Presented at the SPE annual technical conference and exhibition, doi: 10.2118/77441-MS.

Fluke 1625, 2006, Earth/ground tester user manual: Fluke Corporation.

Fouskakis, D., and D. Draper, 2002, Stochastic optimization, a review: International Statistical Review, 70, no. 3, 315-349, doi: 10.1111/j.1751-5823.2002.tb00174.x.

Frischknecht, F.C., 1988, Electromagnetic physical scale modeling, *in* M.N. Nabighian, ed., Electromagnetic methods in applied geophysics: Theory: SEG, 365-469.

Gianzero, S., Y. Lin, and S. Su, 1985, A new high-speed hybrid technique for simulation and inversion of resistivity logs: SPE Formation Evaluation, **3**, no. 1, 55-61, doi: 10.2118/14189-PA.

Gore, G.L., and L.L. Terry, 1956, Radioactive tracer techniques: Journal of Petroleum Technology, **8**, no. 9, 12-17.

Grae, A., R.J. Duenckel, J.R. Nelson, H.D. Smith, X. Han, and T.T. Palisch, 2012, Field study compares hydraulic fracture diagnostic technologies: Presented at the SPE Hydraulic Fracturing Technology Conference, doi: 10.2118/152169-MS.

Gul, S., and V. Aslanoglu, 2018, Drilling and well completion cost analysis of geothermal wells in turkey: Presented at the 43rd Workshop on Geothermal Reservoir Engineering.

Haustveit, K., K. Dahlgren, H. Greenwood, T. Peryam, B. Kennedy, and M. Dawson, 2017, New age fracture mapping diagnostic tools - A STACK case study: Presented at the SPE Hydraulic Fracturing Technology Conference and Exhibition, doi: 10.2118/184862-MS.

Heagy, L.J., and D.W. Oldenburg, 2013, Investigating the potential of using conductive or permeable proppant particles for hydraulic fracture characterization: 83rd Annual International Meeting, SEG, Expanded Abstracts, 576-580.

Hibbs, A.D., 2014, Evaluation of deep subsurface resistivity imaging for hydrofracture monitoring, https://www.netl.doe.gov/File%20Library/Research/Oil-Gas/Natural%20Gas/fe0013902-qpr-jan-mar-2014.pdf, accessed 1 November 2015.

Hoversten, G.M., M. Commer, E. Haber, and C. Schwarzbach, 2015, Hydro-frac monitoring using ground time-domain electromagnetics: Geophysical Prospecting, **63**, 1508-1526, doi: 10.1111/1365-2478.12300.

Iriarte, J., J. Merritt, and B. Kreyche, 2017, Using water hammer characteristics as a fracture treatment diagnostic: Presented at the SPE Oklahoma City Oil and Gas Symposium doi: 10.2118/185087-MS.

Jin, J.M., 2010, Theory and computation of electromagnetic fields: John Wiley & Sons, Inc.

Kampfer, G., and M. Dawson, 2016, A novel approach to mapping hydraulic fractures using poromechanic principles: Presented at the 50th US Rock Mechanics/ Geomechanics Symposium, ARMA-2016-843.

Kaur, G., and A.E. Yilmaz, 2011, A practical implementation and comparative assessment of the radial-angular-transform singularity cancellation method: IEEE Transactions on Antennas and Propagation, **59**, no. 12, doi: 10.1109/TAP.2011.2165516.

LaBrecque, D., R. Brigham, J. Denison, L. Murdoch, W. Slack, Q.H. Liu, Y. Fang, J. Dai, Y. Hu, Z. Yu, A. Kleinhammes, P. Doyle, Y. Wu, and M. Ahmadian, 2016, Remote imaging of

proppants in hydraulic fracture networks using electromagnetic methods: results of small-scale field experiments: Presented at the SPE Hydraulic Fracturing Technology Conference, doi: 10.2118/179170-MS.

Le Calvez, J.H., M.E. Craven, R.C. Klem, J.D. Baihly, L.A. Bennett, and K. Brook, 2007, Real-time microseismic monitoring of hydraulic fracture treatment: a tool to improve completion and reservoir management: Presented at the SPE Hydraulic Fracturing Technology Conference, doi: 10.2118/106159-MS.

Li, J., and L.C. Shen, 1993, Vertical eigenstate method for simulation of induction and MWD resistivity sensors: IEEE Transactions on Geoscience and Remote Sensing, **31**, no. 2, 399–406, doi: 10.1109/36.214916.

Lindell, I.V., 1992, Methods for electromagnetic field analysis: Clarendon Press.

Liu, Q.H., Z. Yu, J. Zhou, 2015, Electromagnetic (EM) well logging tools and related methods: U.S. Patent WO/2016/144457.

Lovell, J.R., 1993, Finite element methods in resistivity logging: Ph.D. dissertation, Delft University of Technology.

Mayerhofer, M.J., E. Lolon, N.R. Warpinski, C.L. Cipolla, D.W. Walser, and C.M. Rightmire, 2010, What is stimulated reservoir volume?: SPE Production & Operations, **25**, no. 1, 89-98, doi: 10.2118/119890-PA.

Mayerhofer, M.J., N.A. Stegent, J.O. Barth, and K.M. Ryan, 2011, Integrating fracture diagnostics and engineering data in the marcellus shale: Presented at the SPE Annual Technical Conference and Exhibition, doi: 10.2118/145463-MS.

Pai, D.M., 1991, Induction log modeling using vertical eigenstates: IEEE Transactions on Geoscience and Remote Sensing, **29**, no. 2, 209–213, doi: 10.1109/36.73661.

Palisch, T., W. Al-Tailji, L. Bartel, C. Cannan, M. Czapski, and K. Lynch, 2016, Recent advancements in far-field proppant detection: Presented at the SPE Hydraulic Fracturing Technology Conference doi: 10.2118/ 179161-MS.

Pardo, D., and C. Torres-Verdin, 2013, Sensitivity analysis for the appraisal of hydrofractures in horizontal wells with borehole resistivity measurements: Geophysics, **78**, no. 4, D209-D222, doi: 10.1190/geo2013-0014.1.

Qian, Z.G., W.C. Chew, and R. Suaya, 2007, Generalized impedance boundary condition for conductor modeling in surface integral equation: IEEE Transactions on Microwave Theory and Techniques, **55**, no. 11, doi: 10.1109/TMTT.2007.908678.

Rao, S.M., D.R. Wilton, and A.W. Glisson, 1982, Electromagnetic scattering by surfaces of arbitrary shape: IEEE Transactions on Antennas and Propagation, 30, no. 3, doi: 10.1109/TAP.1982.1142818.

Ren, Y., W.F. Huang, Q.H. Liu, and Y.P. Chen, 2016, Accurate fracture scattering simulation by thin dielectric sheet-based surface integral equation: IEEE Geoscience and Remote Sensing Letters, **13**, no. 10, 1448-1451, doi: 10.1109/LGRS.2016.2591079.

Saldungaray, P., T.T. Palisch, and R. Duenckel, 2012, Novel traceable proppant enables propped frac height measurement while reducing the environmental impact: Presented at the SPE/EAGE European Unconventional Resources Conference and Exhibition, doi: 10.2118/151696-MS.

Salies, N.G., 2012. Study on the feasibility of using electromagnetic methods for fracture diagnostics: M.S. thesis, The University of Texas at Austin.

Sambridge, M., 1999, Geophysical inversion with a neighborhood algorithm – I. searching a parameter space, Geophysical Journal International, 138, no. 2, 479-494, doi: 10.1046/j.1365-246X.1999.00876.x.

Scott, M.P., R.L. Johnson, A. Datey, C.B. Vandenborn, and R.A. Woodroof, 2010, Evaluating hydraulic fracture geometry from sonic anisotropy and radioactive tracer logs: Presented at the SPE Asia Pacific Oil and Gas Conference and Exhibition, doi: 10.2118/133059-MS.

Sen, M., and P. Stoffa, 2013, Global optimization methods in geophysical inversion: Cambridge University Press.

Sharma, M.M., and R. Manchanda, 2015, The role of induced un-propped (IU) fractures in unconventional oil and gas wells: Presented at the SPE Annual Technical Conference and Exhibition, doi: 10.2118/174946- MS.

Shiriyev, J., Y. Brick, P. Zhang, A.E. Yilmaz, C. Torres-Verdin, M.M. Sharma, T. Hosbach, M.A. Oerkfitz, and J. Gabelmann, 2018, Experiments and simulations of a prototype tri-axial electromagnetic induction logging tool for open-hole hydraulic fracture diagnostics: Geophysics, **83**, no. 3, D73-D81, doi: 10.1190/GEO2017-0354.1.

Shrivastava, K., and M.M. Sharma, 2018, Proppant transport in complex fracture networks: Presented at the SPE Hydraulic Fracturing Technology Conference and Exhibition, doi: 10.2118/189895-MS.

Sierra, J.R., J.D. Kaura, D. Gualtieri, G. Glasbergen, D. Sarker, and D. Johnson, 2008, DTS monitoring of hydraulic fracturing: experiences and lessons learned: Presented at the SPE Annual Technical Conference and Exhibition, doi: 10.2118/116182-MS.

Sinclair, G., 1948, Theory of models of electromagnetic systems: Proceedings of the IEEE, **36**, no. 11, 1364-1370, doi: 10.1109/JRPROC.1948.232289.

Smolen, J.J., and A. Spek, 2003, Distributed temperature sensing, http://w3.energistics.org/schema/witsml_v1.3.1_data/doc/Shell_DTS_Primer.pdf, accessed 30 May 2017.

Sookprasong, P.A., C.C. Gill, and R.S. Hurt, 2014, Lessons learned from DAS and DTS in multicluster, multistage horizontal well fracturing: interpretation of hydraulic fracture initiation and propagation through diagnostics: Presented at the IADC/SPE Asia Pacific Drilling Technology Conference, doi: 10.2118/170512-MS.

Sookprasong, P.A., R.S. Hurt, and C.C. Gill, 2014, Downhole monitoring of multi-cluster, multi-stage horizontal well fracturing with fiber optic distributed acoustic sensing (DAS) and distributed temperature sensing (DTS): Presented at the International Petroleum Technology Conference, doi: 10.2523/IPTC-17972-MS.

Swift, C.M., 1988, Fundamentals of the electromagnetic method, *in* M.N. Nabighian, ed., Electromagnetic methods in applied geophysics: Theory: SEG, 5-13.

Ugueto, G.A., Huckabee, P.T., Molenaar, M.M., Wyker, B., and Somanchi, K., 2016, Perforation cluster efficiency of cemented plug and perf limited entry completions; insight from fiber optics diagnostics: Presented at the SPE Hydraulic Fracturing Technology Conference, doi: 10.2118/179124-MS.

Wang, G.L., C. Torres-Verdin, and S. Gianzero, 2009, Fast simulation of tri-axial borehole induction measurements acquired in axially symmetrical and transversely isotropic media: Geophysics, **74**, no. 6, E233-E249, doi: 10.1190/1.3261745.

Warpinski, N.R., 1996, Hydraulic fracture diagnostics: Journal of Petroleum Technology, 48, no. 10, 907-910, doi: 10.2118/36361-JPT.

Warpinski, N.R., and J. Du, 2010, Source-mechanism studies on microseismicity induced by hydraulic fracturing: Presented at the SPE Annual Technical Conference and Exhibition, doi: 10.2118/135254-MS.

Warpinski, N.R., and P.T. Branagan, 1989, Altered stress fracturing: Journal of Petroleum Technology, **41**, no. 9, 990-997, doi: 10.2118/17533-PA.

Webster, P., B. Cox, and M. Molenaar, 2013, Developments in diagnostic tools for hydraulic fracture geometry analysis: Presented at the Unconventional Resources Technology Conference, URTEC-1619968-MS.

Wheaton, B., K. Haustveit, and W. Deeg, 2016, A case study of completion effectiveness in the Eagle Ford Shale using DAS/DTS observations and hydraulic fracture monitoring: Presented at the SPE Hydraulic Fracturing Technology Conference, doi: 10.2118/179149-MS.

Wright, C.A., E.J. Davis, G.M. Golich, J.F. Ward, S.L. Demetrius, W.A. Minner, and L. Weijers, 1998b, Downhole tiltmeter fracture mapping: finally measuring hydraulic fracture dimensions: Presented at the SPE Western Regional Meeting, doi: 10.2118/46194-MS.

Wright, C.A., E.J. Davis, L. Weijers, G.M. Golich, J.F. Ward, S.L. Demetrius, and W.A. Minner, 1998a, Downhole tiltmeter fracture mapping: a new tool for directly measuring hydraulic fracture dimensions: Presented at the SPE Annual Technical Conference and Exhibition, doi: 10.2118/49193-MS.

Wu, C., S. Yi, and M.M. Sharma, 2017, Proppant distribution among multiple perforation clusters in a horizontal wellbore: Presented at the SPE Hydraulic Fracturing Technology Conference and Exhibition, doi: 10.2118/184861-MS.

Wu, W., R. Russell, and M.M. Sharma, 2017, An experimental method to study the impact of fracturing fluids on fracture conductivity in heterogeneous shales: Presented at the Unconventional Resources Technology Conference, doi: 10.15530/URTEC-2017-2669936.

Yang, K., and A. E. Yilmaz, 2014, An FFT-accelerated integral equation solver for analyzing scattering in rectangular cavities: IEEE Transactions on Microwave Theory and Techniques, **62**, no. 9, 1930-1942, doi: 10.1109/TMTT.2014.2335176.

Yang, K., A.E. Yilmaz, and C. Torres-Verdin, 2016, Efficient 3D parametric inversion of hydraulic fractures with low frequency borehole tri-axial electromagnetic measurements: 86th Annual International Meeting, SEG, Expanded Abstracts, 954-958.

Yang, K., C. Torres-Verdin, and A.E. Yilmaz, 2015, Detection and quantification of three-dimensional hydraulic fractures with horizontal borehole resistivity measurements: IEEE Transactions on Geoscience and Remote Sensing, **53**, no. 8, 4605-4615, doi: 10.1109/TGRS.2015.2402656.

Yu, Z., J. Zhou, Y. Fang, Y. Hu, and Q. H. Liu, 2016, Through-casing hydraulic fracture evaluation by induction logging II: the inversion algorithm and experimental validations: IEEE Geoscience and Remote Sensing, **55**, no. 2, 1189-1198, doi: 10.1109/TGRS.2016.2621002.

Zhang, G.J., G.L. Wang, and H.M. Wang, 1999, Application of novel basis functions in a hybrid method simulation of the response of induction logging in axisymmetrical stratified media: Radio Science, **34**, no. 1, 19-26, doi: 10.1029/98RS02767.

Zhang, P., J. Shiriyev, C. Torres-Verdin, M.M. Sharma, Y. Brick, J. Massey, and A.E. Yilmaz, 2016, Fracture diagnostics using a low-frequency electromagnetic induction method: Presented at the 50th US Rock Mechanics/Geomechanics Symposium.

Zhang, S., and D. Zhu, 2017, Inversion of downhole temperature measurements in multistage fracture stimulation in horizontal wells: Presented at the SPE Annual Technical Conference and Exhibition, doi: 10.2118/187322-MS.

List of Acronyms and Abbreviations

Symbol	Definition	Unit
$\mathbf{E}$	electric field	V-m
$\mathbf{H}$	magnetic field	A-m
$\mathbf{J}$	electric current density	A-m^2
$\mathbf{J}_s$	surface electric current density	A-m
$\mathbf{M}$	magnetic current density	V-m^2
$\hat{\mathbf{n}}$	unit normal vector	-
$\mathbf{r}$	observer point	m
$\mathbf{r}'$	source point	m
A	area	m^2
B	magnetic field	mG
D	core diameter	cm
F	formation factor	
F_{CD}	dimensionless fracture conductivity	
G	conductance	S
G_{R}	Green's function	1-m
H	magnetic flux density	A-m
$\hat{H}_n^{(1)}$	normalized Hankel function of the first kind	
$H_n^{(2)}$	regular Hankel function of the second kind	
$\check{H}_n^{(2)}$	spherical Hankel function of the second kind	
I	peak current	A
$\Im$	imaginary component of complex voltage	V
J_n	regular Bessel function	
$\hat{J}_n$	normalized Bessel function	
$\check{J}_n$	spherical Bessel function	
M	magnetic dipole moment	A·m^2
N	number	-

Symbol	Definition	Unit
N^i	induction number	-
P	power	W
P_n	Legendre polynomial	
P_n^1	associated Legendre polynomial	
Q	flow rate	cm^3-s
$\Re$	real component of complex voltage	V
R_o	resistivity of a core saturated by brine	Ω·m
R_w	resistivity of brine	Ω·m
S	surface	m^2
U, V	voltage	V
X, Y	lock-in amplifier readings	V
Z_s	surface impedance	Ω
d	diameter	m
f	frequency	Hz
g_η	one dimensional basis function	
h	coil height	m
j	complex number	-
k	wave number	1-m
k_f	fracture permeability	Darcy
l	length, distance	m
r	radius	m
t	thickness	m
w	weight factor	
w_f	fracture width	cm
ΔP	pressure drop	atm
Λ	RWG basis function defined over the triangle	-
Λ_η	eigenvalues	-
γ	propagation constant	-
δ	skin depth	m

Symbol	Definition	Unit
ε	permittivity	F-m
ε_{o}	free space permittivity	F-m
ε_{r}	relative permittivity	-
$\tilde{\varepsilon}$	complex permittivity	F-m
η	wave impedance	Ω
η_{o}	free space wave impedance	Ω
λ	node spacing factor	-
μ	magnetic permeability	H-m
μ_f	fluid viscosity	cp
μ_{o}	free space magnetic permeability	H-m
μ_{r}	relative magnetic permeability	-
ρ_{e}	electric charge density	C-m^3
ρ_{m}	magnetic charge density	Wb-m^3
σ	conductivity	S-m
φ	electric scalar potential	V
ω	angular frequency	Hz
x, y, z	Cartesian coordinate system	
r, θ, ϕ	spherical coordinate system	

Symbol	Definition	Unit

u and v show the coil orientation in the equation of U_{uv}

u	orientation of receiver coil
v	orientation of transmitter coils

SI derived unit	Definition	SI base units
C	Coulomb	$s \cdot A$
F	Farad	$s^4 \cdot A^2 - m^2 \cdot kg$
T	Tesla	$kg - A \cdot s^2$
H	Henry	$kg \cdot m^2 - s^2 \cdot A^2$
Hz	Hertz	1-s
Ω	Ohm	$kg \cdot m^2 - s^3 \cdot A^2$
S	Siemens	$s^3 \cdot A^2 - kg \cdot m^2$
V	Volt	$kg \cdot m^2 - s^3 \cdot A$
W	Watt	$kg \cdot m^2 - s^3$
Wb	Weber	$kg \cdot m^2 - s^2 \cdot A$
G	Gauss	$1E-4[kg - A \cdot s^2]$

Appendix A

Detailed Evaluation and Design of Prototype Tool

A.1. SCOPE

This document describes some of the details of the work done under Cost-Reimbursable Subaward Agreement No. UTA16-000787 between the University of Texas (UT) at Austin and E-Spectrum Technologies, Inc. (ESTI). The University of Texas was the Prime Sponsor of the original work under the Department of Energy Prime Award No.: DE-FE0024271. ESTI received the initial subaward from UT on June 1, 2017. This initial subaward was amended (Amendment No. 2) on September 18, 2017 to increased total funding by $70,394.80 making the total subaward amount not to exceed $165,693.38. A third amendment (Amendment No. 3) was added June 11, 2018 to extend the period of performance to September 30, 2018.

A.2. SUMMARY OF WORK

ESTI was brought into the original project to replace an existing subcontractor who had exited the project due to financial insolvency. As such, much of the initial work involved analyzing the existing design and offering suggestions as to how to best proceed given the constraints of the remaining award funding. Subsequent amendments to the award (Amendment No 2) involved ESTI supporting the building and testing of alternate, related technical concepts regarding fracture diagnostic measurements.

Initial Subaward

- Detailed engineering analysis of existing Gearhart Induction Tool design.
- Development of Requirement Specification Document for recommended tool redesign.
- Analysis and modification of existing Gearhart Coil Design Model.
- Coil construction and testing to validate revised Gearhart Coil Design Model.

Amendment No. 2

- Building the tool electronics (hardware design)
- Battery Hazard Analysis
- System Architecture Analysis
- Assist in tool testing and evaluation (lab and shallow earth test)

A.3. DETAILED ENGINEERING ANALYSIS OF GEARHART TOOL

A detailed engineering analysis of the design of the previous Induction Tool was conducted. The original design engineering was done by the Gearhart Company, and a design package and partially completed prototype were delivered to the University of Texas at Austin during Q1 of 2016. The analysis included herein provides both analytical and empirical results and provides detailed recommendations regarding remediation of the shortcomings found in the existing

Gearhart design. It should be noted that a significant amount of the remediation work that was suggested in this analysis was subsequently undertaken in a Phase I Small Business Innovative Research project, resulting in new circuits and hardware that overcome the shortcomings of the Gearhart design. The conclusions and recommendations from the analysis conducted under this contract were made before the Phase I SBIR project began and are summarized below in their original form for the purpose of historical perspective and transparency.

A.3.1. Summary of Findings

1. The tank circuit will not produce the requisite dipole moment for the long-spaced conductivity measurement. The measured Q of the Gearhart tank circuit is low, and thus the tank circuit is very lossy and requires much more energy per cycle than the existing supply can deliver. This finding was verified through both theoretical analysis and empirical testing of the tank circuit. This basic design flaw means that the coil and the coil driver circuitry must be redesigned, and the packaging of the downhole electronics must be re-engineered to accommodate the thermal and power dissipation issues associated with the increased energy requirements for the tank and tool.
2. The existing design for the Induction Tool transmitter and receiver electronics and firmware is insufficient and incomplete. The electronics and firmware for the existing Gearhart design contain fundamental flaws that will be difficult to remediate without substantial changes to the basic system architecture.
3. The existing mechanical design for the Induction Tool is insufficient and incomplete. Moreover, the drawing package for the existing Gearhart mechanical design is not machine shop ready. The existing mechanical design lacks provisions for pressure compensation/packaging, inter-tool wiring, and it is not practical with regards to field assembly and tool deployment.

The following sections provide details on the engineering analysis results.

A.3.2. Coil and Tank Circuit Analysis

The Gearhart design specifies that a parallel resonant LC tank circuit, consisting of a custom wound coil and a 20-unit capacitor bank, will be used to generate the approximately 160Arms of drive current necessary to supply the 150Am2 dipole moment required for the medium and long-spaced conductivity measurements. The Gearhart design assumes that the drive current can be gradually injected into the tank, by slowly ramping the tank voltage, using a variable output DC to AC convertor tank-driver circuit. This driver circuit, which is located in the downhole tool, will be capable of delivering a maximum of 300Vrms at 2Arms for a total output power of 600Wrms. The basic premise of the Gearhart design is that the tank circuit, once energized at resonance, will maintain the requisite energy for 150Am2 dipole, with minimal subsequent energy being required from the drive source to maintain the requisite dipole moment. The following sections provide an analysis of this technique.

A.3.2.1. Tank Circuit Theory of Operation

Fig. A.1 shows a schematic diagram of the parallel LC tank circuit used to generate the induction tool dipole moment. A tank circuit is an energy storage device which, when driven at resonant frequency by an AC voltage source, stores energy in the magnetic field of the inductor and the electric field of the capacitor. Resonant frequency of the tank circuit is given by:

$$\omega = \frac{1}{\sqrt{LC}} \tag{A.1}$$

When driven at resonance, the field energy in the tank is circulated between the inductor and capacitor during each cycle of the AC voltage source. If the inductor and capacitor are ideal circuit elements (i.e. the impedance is purely reactive with no internal DC resistance), no energy is lost per cycle during the field energy transfer, and thus no further energy would be required from the source to maintain the energy circulating in the tank. In other words, once the requisite energy is injected into the tank circuit, via initially charging the tank circuit with current drawn from the AC voltage source, the subsequent current drawn from the AC voltage source would be zero because no energy would be lost in the tank, and the magnitude of the current circulating in the tank would remain constant. Therefore, if the tank circuit elements were ideal (purely reactive), the inductor current required to generate the induction tool dipole moment could be gradually injected into the tank circuit, via ramping up the supply voltage to the target value given by Ohm's law (Vs = IS/Ztank), and the supply voltage could be held constant while the tank circuit circulated the inductor current indefinitely. In reality, the inductor and capacitors used in the tank circuit are not ideal elements, and thus the tank circuit will lose energy every cycle. This lost energy must be replenished from the AC voltage supply.

For a resonant circuit, the ratio of the power dissipated in the circuit reactance to the power dissipated in the circuit resistance is called the Quality Factor (Q):

$$Q = \frac{\text{Power Stored in Reactance}}{\text{Power Dissipated in Resistance}} = \frac{I^2 X_{\text{tank}}}{I^2 R_{\text{tank}}} \tag{A.2}$$

It can be seen from this equation that a higher Q indicates a lower rate of per-cycle energy loss relative to the energy stored in the resonant circuit. It can also be seen that a tank circuit containing purely reactive elements (R=0) would have infinite Q, and a circuit containing elements with higher internal resistance (i.e. with a complex impedance, Z=R+jωx) will give a lower Q. Low Q resonant circuits are inefficient, and therefore require more energy per cycle from the source to maintain their output power.

For a parallel resonant LC tank, the energy losses of the tank will normally be dominated by the Q of the inductor. This is because the inductor has a much higher series internal resistance than that of each individual capacitor, and all of the individual capacitor's series internal resistances are in parallel within the tank circuit making the total resistance of the capacitor branch of the tank a fraction of each individual capacitor's ESR. This gives the inductor a larger resistive

component within its complex impedance (ZL = RL + jωL), making the Q of the inductive branch much lower than the total Q of the capacitive branch, and thus lowering the overall Q of the tank.

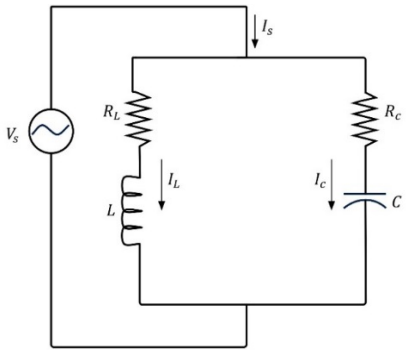

Figure A.1: Tank Circuit Schematic.

A.3.2.2. Circuit Analysis

Figure A.1 shows the schematic of the parallel LC tank circuit. The impedance of the inductor L is given by:

$$Z_{\mathrm{L}} = R_{\mathrm{L}} + j\omega L \tag{A.3}$$

and the impedance of the capacitor is given by:

$$Z_{\mathrm{C}} = R_{\mathrm{C}} + \frac{1}{j\omega C} = R_{\mathrm{C}} - j\frac{1}{\omega C} \tag{A.4}$$

Figure A.2 shows a phasor diagram of the tank impedances Z_C and Z_L.

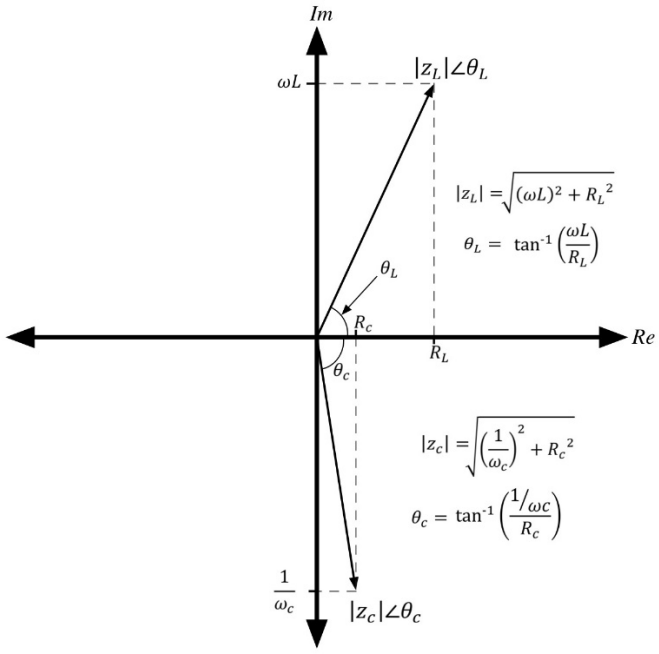

Figure A.2: Tank Circuit Impedances.

The current in the inductor branch of the tank is given by:

$$I_{\mathrm{L}} = \frac{V_{\mathrm{S}}}{Z_{\mathrm{L}}} \tag{A.5}$$

and the current in the capacitor branch is given by:

$$I_{\mathrm{C}} = \frac{V_{\mathrm{S}}}{Z_{\mathrm{C}}} \tag{A.6}$$

Figure A.3 shows a phasor diagram of the supply current (IS) and the tank branch currents IL and IC. Note that the supply current (IS) is the vector sum of IC and IL.

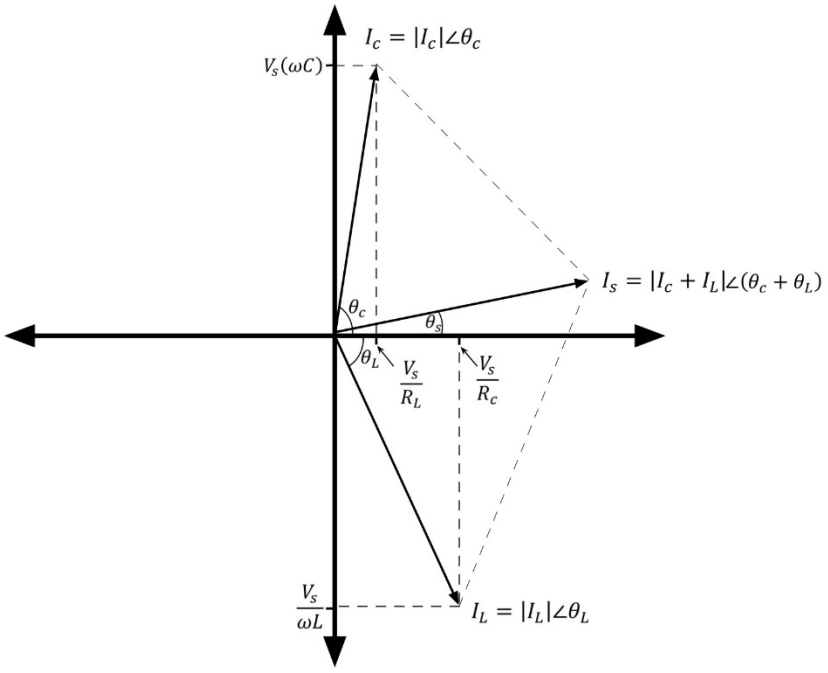

Figure A.3: Tank Circuit Currents.

The phasor diagrams of Figs. Figure A.2 and Figure A.3 graphically illustrate the following points:

- as the branch series resistances (RL and RC) of the inductor and capacitor become smaller (or accordingly, as the absolute value of the phase angles Θ_C and Θ_L becomes larger) the magnitude of the supply current (IS) becomes smaller, and
- as the series resistances of the tank circuit elements approach zero ohms (i.e. as the phase angle of the capacitor current (Θ_C) approaches 90^0 and the phase angle of the inductor current (Θ_L) approaches -90^0), the tank circuit becomes more resonant (i.e. the tank circuit becomes more reactive and the circuit Q becomes larger), and the magnitude of the current drawn from the supply (I_S) approaches zero.

Note that when the tank circuit is at resonance, the reactive component (XC $=-j\frac{1}{\omega C}$) of the capacitor impedance and the reactive component (XL = jωC) of the inductor impedance will be equal.

The resistive component of the inductor impedance is determined by the physical characteristics of the inductor winding (i.e. the number of turns of wire, the diameter of the core bobbin, the gauge of the wire, etc.). The resistive component of the capacitor impedance is determined by the capacitor equivalent series resistance (ESR) specification, which, depending on the capacitor dielectric material and physical size, is typically much smaller than that of the inductor winding resistance. Due to the finite resistive components of both the inductor and capacitor impedances, it can be seen from Figure A.3 that the phase angles of the current waveforms will never equal 90^0, and thus, the vector sum of the inductor and capacitor branch currents will never equal zero. Furthermore, because the inductor resistance (RL) is larger than

the capacitor resistance (RC), the phase angle of the inductor current (θ_L) will be smaller than the phase angle of the capacitor current (θ_C), making the phase angle of the source current (IS) waveform slightly positive (i.e. indicating a capacitive load).

Table A.1 shows the theoretical (i.e. derived using Gearhart "Coil Calculator" spread sheet) circuit values for the existing induction tool tank circuit.

Magnetic Moment	148.4 Am^2
Inductance	1700 μH
Coil resistance	0.2 Ω
Total # coil windings	15,000
Parallel coil count	80
Coil diameter	3.8 "
Coil length	4.75 "
Coil Area	0.005027 m^2
Coil winding current (for dipole moment)	1.97 Arms
Resonant frequency	100 Hz
Tank Capacitor	1520 μF
Capacitor ESR (estimated value)	0.08 Ω

Table A.1: Tank Circuit Theoretical Values.

Table A.2 shows the calculated voltage, current, and power for the various tank circuit elements using the theoretical values taken from
Table A.1. Note that, for the purpose of clarity,

Table A.2 shows the calculated values in both polar and rectangular notation. Also note that the total current that must be sourced by the power supply to the inductor branch (Icoil) of the tank is the product of the inductor winding current times the number of parallel coils:

$$I_{coil} = 1.97A_{rms} \times 80 = 157.5\ A_{rms}$$

	Polar		Rectangular		
	magnitude	***angle***	***real***	***imaginary***	
Icoil	157.46	-79.4	28.979	-154.768	
Zcoil	1.09	79.4	0.200	1.068	
Vsupply	171.11	0.0	171.110	0.000	*Zcoil * Icoil*
Zcap	1.05	-85.6	0.080	-1.047	
Icap	162.94	85.6	12.413	162.469	*Vsupply / Zcap*
Isupply	42.10	10.5	41.392	7.701	*Icap + Icoil*
Iratio	3.74				*Icoil /Isupply*
Psupply	7204.1	10.5	7082.6	1317.7	*Vsupply*Isupply*
Pcoil	26942.4	-79.4	4958.6	-26482.2	*Vsupply*Icoil*
Pcap	27880.98	85.6	2124.0	27800.0	*Vsupply*Icap*
Qcoil	5.34				*Pxcoil/Prcoil*
Qcap	13.09				*Pxcap/Prcap*
Qtank	3.79				

Table A.2: Tank Circuit Calculated Values.

The

Table A.2 circuit analysis results show that, in order to supply the requisite dipole moment of 148.8 Am2, the tank will require a supply voltage of $171.1\angle 0^0$ Vrms at $42.1\angle 10.5^0$Arms, for a total power supply output rating of $7204.1\angle 10.5^0$ Wrms. This data indicates that the 2.0 Arms, 600 Wrms rating of the existing power supply will not be adequate to source enough current to generate the requisite 148.8 Am2 dipole moment.

Table A.3 shows the calculated circuit values for the tank circuit when driven by a maximum output current source of 2.0 Arms. This data shows that the tank circuit will deliver a maximum dipole moment of 6.97 Am2 when driven by a 2 Arms source, as proposed in the existing coil driver design.

Table A.4 shows the calculated circuit values for the tank circuit when driven by a 199Vpeak (141Vrms) voltage source. This voltage is the tank drive voltage specified in the Gearhart "Coil Calculator" spread sheet for the existing proposed coil. The

Table A.4 data shows that the power supply must source 35 Arms at a 199Vpeak drive voltage. Note that the Gearhart design philosophy for the tank drive circuit is to slowly ramp-up the tank to this voltage, using a 2Arms source current, to gradually build energy in the tank circuit. The data in

Table A.4 indicates the proposed ramp-up technique will not work with the existing coil and power supply design.

The circuit analysis data presented in this section illustrates a fundamental design flaw with the existing Gearhart tank and tank drive circuitry:

a) the Q of the tank circuit is very low (3.79), and thus

b) the tank circuit will not store energy efficiently at resonance, and thus

c) will require that a large amount of complex power be injected into the tank to replace the "real" component of the power lost during each cycle

	Polar		Rectangular		
	magnitude	***angle***	***real***	***imaginary***	
Icoil	7.40	-79.4	1.362	-7.274	
Zcoil	1.09	79.4	0.200	1.068	
Vsupply	8.04	0.0	8.042	0.000	*Zcoil * Icoil*
Zcap	1.05	-85.6	0.080	-1.047	
Icap	7.66	85.6	0.583	7.636	*Vsupply / Zcap*
Isupply	1.98	10.5	1.945	0.362	*Icap + Icoil*
dipole moment	**6.97**				*area*#turns*(Icoil/parallel coil count)*

Table A.3: Dipole Moment with 2A Power Supply.

	Polar		Rectangular		
	magnitude	***angle***	***real***	***imaginary***	
Icoil	129.75	-79.4	23.880	-127.534	
Zcoil	1.09	79.4	0.200	1.068	
Vsupply	141.00	0.0	141.000	0.000	*Zcoil * Icoil*
Zcap	1.05	-85.6	0.080	-1.047	
Icap	134.27	85.6	10.229	133.880	*Vsupply / Zcap*
Isupply	34.69	10.5	34.108	6.346	*Icap + Icoil*
dipole moment	**122.29**				*area*#turns*(Icoil/parallel coil count)*

Table A.4: Diploe Moment with 233Vrms Power Supply.

Another important thing to note from the

Table A.2 data is the calculated "real" power value of the coil. The data shows that the coil will produce 4,959 Wrms of real power in the winding resistance, which must be dissipated as radiated or conducted heat within the downhole tool. This amount of thermal energy will be very difficult to dissipate downhole, and would most likely result in premature tool failure, or manifest as intermittent field reliability issues.

One final comment regarding the existing Gearhart design concerns personnel safety issues.

Table A.2 results indicate that a 171 Vrms, 42 Arms power supply is required to drive the existing coil. This supply would be extremely dangerous and could deliver lethal amounts of current in the event of a circuit fault within the tool. The design of such a supply would require that several safety features be present in the system hardware and firmware including:

a) safety interlocks

b) double-fault electrical insulation

c) ground-fault interrupter type circuit breaker protection

A.3.2.3. Tank Circuit Bench Testing

The existing Gearhart tank circuit was bench tested to validate the circuit analysis results.

Table A.5 shows the measured values for the tank circuit.

Parameter	**Value**	**Measurement Method**
Inductance	1247 μH	HP4263B LCR meter
Coil resistance	0.24 Ω	HP4263B LCR meter
Tank Capacitor	1600 μF	Rated (+/-5%)
Resonant frequency	117 Hz	Sweep method for max inductor current

Table A.5: Tank Circuit Measured Values.

During testing, the tank circuit was driven with the ESTI Drill Dog Surface Transceiver power amplifier unit, and the power amplifier source current, current in the capacitor branch, and current in the inductor branch of the tank was measured.

Table A.6 shows the measured data. Note that the supply voltage to the tank was not raised beyond the indicated 13.4Vrms because the coil began to show indications of thermal heating.

V_{supply}	$13.4\angle 0^0$ V_{rms}
I_{supply}	$6.4\angle 16.9^0$ I_{rms}
I_{coil}	$14.6\angle -71.0^0$ I_{rms}
I_{cap}	$15.7\angle 88.0^0$ I_{rms}

Table A.6: Tank Circuit Bench Test Results.

Table A.7 shows the calculated circuit values, derived using the bench test measured V_{supply} and I_{supply} data from

Table A.6. The

Table A.7 calculated results correlate with the measured bench test results of

Table A.6, and also correlate reasonably well with the calculated results from

Table A.2. The primary difference between the

Table A.2 results and the

Table A.7 results is the difference in the measured resistive component (RC) of the capacitor impedance (ZL). The

Table A.7 data shows an RC of 0.137Ω versus 0.08Ω shown in

Table A.2. Note that the RC from

Table A.7 is a measured value, derived from the measured VS and measured Zcoil values. This measured value of RC is larger than the estimated 0.08Ω due to the resistance of the wiring used to connect the twenty, parallel 80μF capacitors that makeup the 1600μF tank-circuit capacitor. This larger value of capacitor branch resistance causes more real power to be generated in the capacitor branch of the tank, causing the Q of the capacitor branch to go from 13.09 (

Table A.2) to 6.11 (

Table A.7). This lower capacitor Q lowers the overall theoretical Q of the tank from 3.79 to the measured bench value of 2.35 (

Table A.7).

	Polar		Rectangular		
	magnitude	***angle***	***real***	***imaginary***	
Isupply	6.40	16.9	6.124	1.860	*measured*
Vsupply	13.40	0.0	13.400	0.000	*measured*
Zcoil	0.95	75.3	0.240	0.917	*measured*
Icoil	14.14	-75.3	3.581	-13.680	*Vs / Zcoil*
Icap	15.75	80.7	2.542	15.540	*Isupply - Icoil*
Zcap	0.85	-80.7	0.137	-0.840	*Vs / Icap*
Psupply	85.76	16.9	82.056	24.931	*Vsupply*Isupply*
Pcoil	189.49	-75.3	47.992	-183.310	*Vsupply*Icoil*
Pcap	211.01	80.7	34.065	208.240	*Vsupply*Icap*
Qcoil	3.82				*Pxcoil/Prcoil*
Qcap	6.11				*Pxcap/Prcap*
Qtank	2.35				

Table A.7: Calculated Bench Test Results.

A.3.2.4. Potential Alternate Design

A potential alternate design, that uses the existing coil, might consist of locating the DC to AC convertor tank driver circuitry on the surface and driving the coil through the wireline. This has the advantage of allowing a much higher drive current and makes cooling of the drive circuitry much easier.

Table A.8 lists the relevant mono-conductor cable specifications and Figure A.4 shows an equivalent schematic of the wireline connected to the tank circuit.

DC conductor Resistance	2.8 Ω/Kft
DC Armor Resistance	2.1 Ω/Kft
Capacitor Conductor to Armor	45pF/ft

Table A.8: Mono Conductor Wireline Cable Specification.

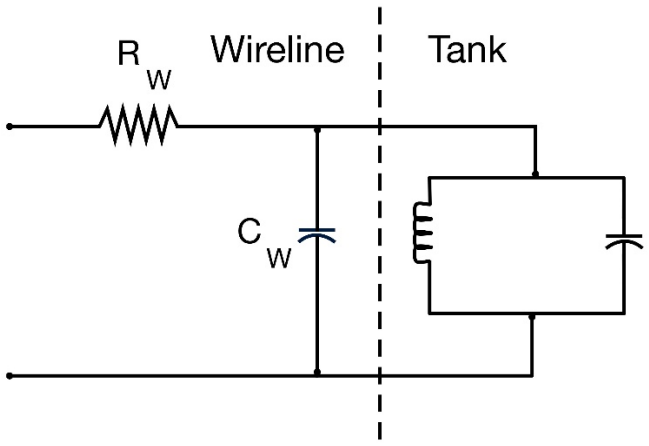

Figure A.4: Schematic: LC Tank Circuit Driven by Wireline.

Table A.9 shows the total resistance and capacitance values for a 15,000' wireline.

Wireline length	15,000 ft
Total Wireline Resistance	73.5 Ω
Capacitor Conductor to Armor	67.5 μF

Table A.9: 15,000 ft. Wireline Total R and C.

Table A.10 shows the calculated results for driving 15,000' of wireline using a 1500Vrms DC to AC power supply located on the surface. It can be seen from the

Table A.10 data that the wireline impedance causes 1454Vrms to be lost in the wireline, resulting in a maximum dipole moment of 48.7Am2. Note that almost 29,000Wrms is lost in the wireline impedance. Also note that the requisite DC to AC power supply would require a 1500Vrms at 19.8Arms rating making it a physically very large, and extremely dangerous power supply.

	Polar		Rectangular		
	magnitude	*angle*	*real*	*imaginary*	
Vsupply	1500.00	0.0	1500.0	0.000	
Vtank	48.96	-20.4	45.883	-17.092	*Vsupply*Zp/(Rwire+Zp)*
Icoil	51.67	-95.8	-5.186	-51.409	*Vtank/Zcoil*
Icap	57.34	64.2	24.962	51.619	*Vtank/Zcap*
Icw	0.02	69.6	0.008	0.023	*Vtank/Zcw*
Isupply	19.79	0.7	19.784	0.233	*Icoil + Icap + Icw*
V lost in wire	1454.22	0.7	1454.117	17.092	*Vsupply-Vtank*
Pwire	28772.09	1.3	28764.1	676.312	*Vlost*Isupply*
Dipole Moment	**48.70**				

Table A.10: Dipole Moment for Tank Driven from Surface via 15,000' Wireline.

A.3.2.5. ESTI Recommended Tank Circuit Design

ESTI recommends that the coil, tank, and tank drive circuity be redesigned to facilitate lowering the downhole power requirements for the tool to make the tool more thermally efficient, reliable, and safer to operate.

Lowering the downhole power will be facilitated by:

- Redistributing the power supply circuitry between the surface support equipment and the tool,
- Lowering the drive voltage and current requirements for the tank by redesigning the coil, and
- Replacing the large, individual tank capacitors with circuit board mounted high-temperature ceramic capacitors.

The tank coil will be redesigned such that the parallel coil count will be lowered from 80 coils to 20 coils. A lower parallel coil count will decrease the total current required in the inductive branch of the tank. The advantages of lowering the total inductive branch current include:

a) the tank can be driven with a lower source voltage, which allows

b) physically smaller, high-temperature compatible tank capacitors to be used, and the

c) lower coil voltage/current will create less DC resistive losses in the coil, providing

d) less coil heating

Table A.11 shows the specifications for the redesigned tank circuit components. Note that the coil wire gauge was increased from 30AWG to 20AWG to accommodate the increased winding current while keeping the coil DC resistance low. Note that the 20AWG wire has a larger outer diameter (O.D.), and thus the length of the coil must increase from 4.75" to 30" in order to keep the O.D. of the coil less than 4".

Magnetic Moment	158 Am^2
Inductance	2514 μH
Coil resistance	0.272 Ω
Total # coil windings	12,615
Parallel coil count	20
Coil diameter	3.8 "
Coil length	30 "
Coil Area	0.005027 m^2
Coil winding current (for dipole moment)	2.34 Arms
Resonant frequency	100 Hz
Tank Capacitor	1007 μF
Capacitor ESR (estimated value)	0.08 Ω

Table A.11: Revised Tank Circuit Values.

Figure A.5 shows a block diagram of the redistributed power supply circuitry and

Table A.12 contains the circuit analysis data.

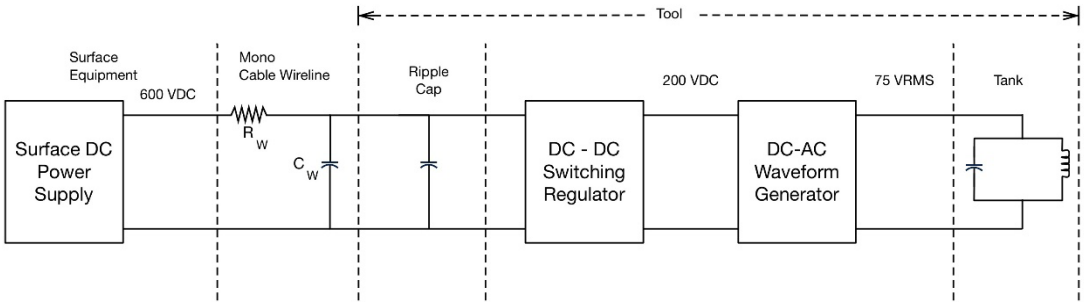

Figure A.5: Tank Circuit Driver Block Diagram.

The

Table A.12 data shows that the revised tank circuit requires an AC drive of 75 Vrms at 9.53 Arms to produce a 158 Am2 dipole moment. The total “real” power produced in the coil windings is 596 Wrms, which, while still being a large amount of power to be dissipated downhole, is a manageable amount given proper tool mechanical design techniques. Note that this contrasts with the 5000 Wrms of power (

Table A.2) which must be dissipated by the coil in the existing tool design.

The tank circuit drive voltage is generated from a 200Vdc, 1000Wrms supply which is located in the downhole tool. Fig. A.5 shows that the 200Vdc downhole supply is sourced by a second, larger DC supply which is located on the surface (600 Vdc, 3000Wrms). Note that, assuming 70% conversion efficiency, the downhole supply must dissipate 306 Wrms of power. Although this amount of power will be challenging to thermally manage downhole, this number is certainly more reasonable than the 2000Wrms of power (Pdis = Psupply – Pcoil. Refer to

Table A.2) which must be dissipated downhole using the existing coil design.

Table A.12 shows that the impedance of the 15,000’ mono-cable causes a voltage drop of 375Vdc, measured from surface to tool, with a total power loss of almost 2000 Wrms within the cable. Again, while this amount of lost power is large, it is considerably more practical than the 29,000 Wrms (refer to

Table A.10) which would be lost in the cable assuming the existing coil is driven from the surface as described in Section 0.

		Polar		Rectangular		
		magnitude	***angle***	***real***	***imaginary***	
	Icoil	46.80	-80.2	7.942	-46.121	
	Zcoil	1.60	80.2	0.272	1.580	
	Vtank	75.01	0.0	75.013	0.000	*Zcoil * Icoil*
	Zcap	1.58	-88.2	0.050	-1.580	
	Icap	47.44	88.2	1.500	47.414	*Vtank / Zcap*
	Itank	9.53	7.8	9.442	1.293	*Icap + Icoil*
	Dipole Moment	**158.00**				*Icoil /Itank*
	Ptank	714.9	7.8	708.3	97.0	
	Pcoil	3510.6	-80.2	595.7	-3459.7	*Vtank*Icoil*
	Pcap	3558.5	88.2	112.5	3556.7	*Vtank*Icap*
(input downhole)	Vsupply	200.0	Vdc			
	Supply efficiency	0.70				
(input downhole)	Isupply	5.1	Adc			
(input downhole)	Vripple	25.5	Vrms			*I=C(dV/dt)*
(downhole)	Psupply	1021.3	Wrms			
	Pdissipated	306.4	Wrms			*Psupply-Ptank*
cable Vdrop	Vcable	375.3	Vdc			*15,000' cable*
	Pcable	1916.4	Wrms			
	Vsurface	575.3	Vdc			
	Psurface	2937.7	Wrms			

Table A.12: Revised Tank Circuit Calculated Values.

An important issue to note is that the redesigned coils are 30” long. A tri-axial coil set using coils this long could cause spatial resolution issues for the short-spaced conduction measurement. We propose addressing this issue by using a second set of smaller tri-axial transmitter coils for the short-spaced measurement and using the 30” set of tri-axial coils for the medium and long-spaced measurements. Refer to Section 0 for short-spaced coil details.

The existing tank-circuit capacitor branch consists of twenty, 80uF capacitors connected in parallel. Each capacitor has a voltage rating of 370Vac and an operating temperature rating of 85^0C. The individual capacitors are very large, and when connected together form a sub-unit which is approximately 12’ long. The redesign of the tank coil, for a drive voltage of 75Vrms, will allow for the usage of high temperature ceramic capacitors in the tank. We propose using the Kemet HT16 series of X7R ceramic capacitors. These capacitors are rated at 200^0C with a rated operating voltage of 200V, and are designed for through-hole mounting on a printed circuit board. Unfortunately, the largest capacitance available in this voltage/temperature rating is 1.5µF, requiring 680 capacitors for a total capacitance of 1020uF. While not impossible, packaging these capacitors into a mechanical form-factor suitable for mounting in a downhole tool will be challenging. Figure A.6 shows one possible mounting configuration for the ceramic capacitors. This modular configuration consists of 40 circular printed circuit boards, with each board containing 17 individual capacitors. The module would be encased in a thermally conductive encapsulate and mounted in a pressure housing.

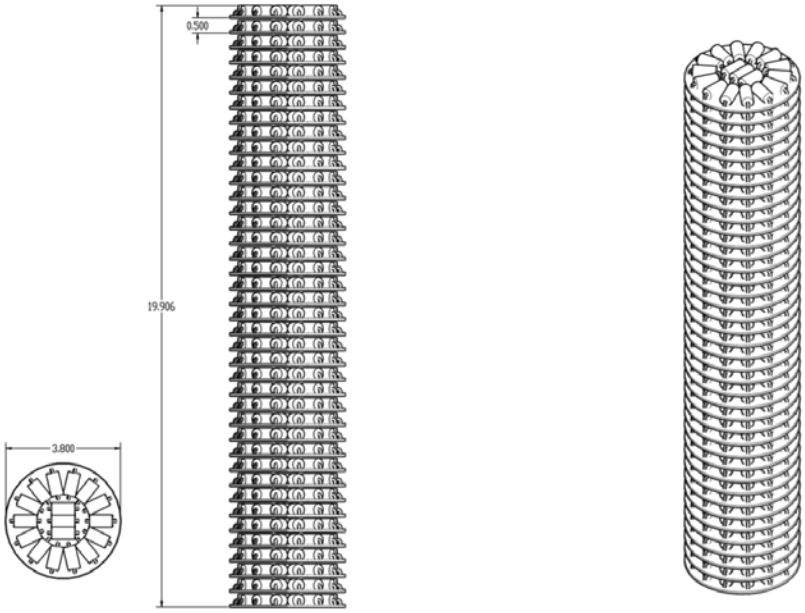

Figure A.6: Ceramic Capacitor Module.

A.3.3. Gearhart Tool Firmware Analysis

Both the Transmitter and Receiver code files had missing files (no header for the EEProm assembly) and did not have any build instructions. MPLab X IDE was used to compile both applications, which included using XC16 compiler and dsPic peripheral libraries. A few

modifications were required to build and there still exists numerous compiler warnings. Both the Transmitter and Receiver source files have had some modifications (mostly comments and variable name changes) and a few code changes to remove some of the warnings. The logic (program flow) in both applications has not been changed.

A.3.3.1. Transmitter Analysis

The hardware design appears to be based on an application note from Microchip
App Note AN144 Grid-Connected Solar Micro inverter Reference Design

The firmware design might be loosely based on the code from the application note but it is difficult to tell as the Transmitter code logic is very different than the application note and looks to be ported from another project. There are many unused variables, constants, bad code style etc. that appear to be from other project. In general the code base is "At best" development level code and not production ready. The PWM logic appears to have numerous math errors and bad assumptions but might be able to be fixed to drive the tank circuit. The other option is start over on the transmitter PWM drive logic and use the App Note as the starting code base and import other required functionality from the transmitter code base or redesign that functionality as needed. These design requirements might change depending on the status of the hardware and other requirements provided by the university.

Transmitter Application

The transmitter application is responsible for controlling LC Tank circuit output power as well as logging captured data to storage. A simple command line interface provides for additional commands. The application is designed to control one coil (not three) and no provisions are made for controlling the other coils. When the Transmitter board is powered on after a 75 second delay (not sure why??) the PWM starts and attempts to drive the Tank circuit and will run until the board is turned off, an over current or voltage detection or until a console "Stop" command is issued or until the cpu blows up. Logging, MWD Sensor monitoring are incomplete or missing. There does not appear to be any technical documentation in the code or elsewhere about the "Memory Tool" or the external D&I package the Transmitter is attempting to use. The PWM logic has a number of potential math errors and might need some debug time in order to make it perform as intended.

Processor Details

- Processor: dspPIC30F6015
- Main Oscillator (FOsc): 8 MHz
- Pre-scaler: 16
- Instruction Frequency: (FCy) = FOsc/4 * Prescaler = 8/2*16 = 32 MHz
- Instruction Period: (TCy) = 1/FCy = 31.25 ns

LC Tank Control

The PWM is used to control the power delivered to the LC Tank circuit with feedback from the tank for monitoring over voltage/current and fly back current. The PWM drives the DC to DC converter which generates a half wave rectified sine wave and then generates a full sine wave via the H-Bridge. The LC tank circuit is designed to run at approximately 100 Hz with a maximum power rating of 600 Watts.

The PWM circuit will attempt to drive close to the maximum power and adjust the frequency +/- approximately 10%. See below for more details.

PWM Details

- PWM Mode : Up/Down, counts up then back down
- PWM Frequency: PTPER is initially set to 270 and can range from 250 to 290.
  - Using Up/Down counter mode which doubles the period to 500, 540 and 580 (Min, Start, Max)
  - Starting PWM Frequency is 59.259 KHz
  - Min PWMF = 32E6/580 = 55.172 KHz
  - Max PWMF = = 32E6/500 = 64 KHz
  - Corresponding target frequency ranges from 93 Hz to 108 Hz
- Code: There appears to be several math errors in PWM calculations and might need some adjustments to generate the 100 Hz as well as the Dead Time control of the PWM outputs. Additional adjustments might be required depending the hardware design.
- See new comments in code for additional details on PWM initialization.

ADC Details

The ADC monitors the following signals and is used in reporting as well as feedback to the PWM logic control.

- 2.5 Volt Reference
- Supply Voltage
- L Voltage
- I Inv
- Flyback current 1C, 2C, 3C and 4C

MWD Sensor Data

Looks like there are 2 ways to get MWD Sensor data – from the hardware board (not implemented) and from a 3rd party D&I. Details and specifications are unknown and cannot determine the completeness or functionality of the code.

Interface to Wireline

Unknown due to lack of information provided. There is a PLD that converts serial data to wireline modulated data, but the functional state of this function is unknown.

Transmitter Console Commands

Outlined below are the commands available via a console interface. The original design was to provide a command line interface via the wireline to the surface. Technical specifications to the wireline interface are unknown and thus it is unknown whether the interface is functional.

Many of the commands appear to be left over from another product.

IDLE

STAR

CONN

EEPROM

ANGLS

BATTV

TEMPS

ADC

ACCUA - Accurate Angle

SLA

VERS

SERI

SELF

HARD

MEMO

MMEM

LOG

LR - Log Reset

SLEEP

SLEEPxx

WR

RD

INIT - Load EE Prom coefs

PARA - Coefficients to Master Computer

EXIT

AZIM : Compute Azimuth

SURV - Computes Survey

STOP - Turns off survey

CALI - Dump Mag/Grav + Inc, AZIM,G TOT, Mag T

ACCUM - Accurate Mags

DIP - Dip Angle

XMAG

YMAG

ZMAG

MOFF - Magnetometer Off

MON - Mag On

A.3.3.2. Receiver Analysis

Source Code

The receiver code is a copy and paste of the transmitter code with changes to the main loop, timer interrupt and various hardware peripherals and the main method for receiving data. This code did not compile as delivered and some assumptions had to be made as well additional header files created to get the code to compile. Again, there are a very large number of compiler warnings and poor coding practices, poor, missing or wrong comments and documentation. The D&I code is an exact duplicate and appears to use the same D&I as the transmitter.

Receiver Design

The receiver performs the following tasks:

- Process diagnostic commands from the command line interface
- Read and store D&I and receive data
- Write data to the “Memory Tool” (every 15 seconds?)

Processor Details

- Processor: dspPIC30F6014a
- Main Oscillator (FOsc): 8 MHz
- Pre-scaler: 16
- Instruction Frequency: (FCy) = FOsc/4 * Prescaler = 8/2*16 = 32 MHz

Receiver Console Commands

The list of commands:

IDLE	ACCUA	LR	AZIM
STAR	SLA	SLEEP?	SURV
CONN	VERS	SLEEP	STOP
RESE	SERI	WR	CALI
EEPROM	SELF	RD	ACCUM
ANGLS	HARD	INIT	DIP

ZDVAL	MEMO	PARA	XMAG
BATTV	DATEP	FOSC	YMAG
TEMPS	MMEM	EXIT	ZMAG
ADC	LOG		

A.3.3.3. Firmware Analysis Conclusions

Common

There are number of common issues with both transmitter and receiver applications:

- D&I: Missing specifications, documentation, as minimum requires validation. Unknown if code works as designed.
- Memory tool and logging: Missing specifications, documentation. Very likely both applications require additional design, validation and testing.
- Console interface: Might work, again, requires validation and debugging
- Wireline interface: Missing design specifications, documentation. Probably requires additional development to communicate to surface via Wireline.
- No provisions have been made for calibrating the tool.

Transmitter

The transmitter application success depends on the hardware functioning as designed. There are other issues including the ability of the DC to DC to deliver enough power to the tank circuit to achieve the required receive levels meaningful for the model. The PWM logic might not work as designed and will require testing at the minimum, most likely redesign. For example, the PWM controller will attempt to "Lock" into the resonant frequency. Currently the range is from 93 to 107 Hz. From the testing in the lab in the LC resonant frequency is closer to 114 Hz, a strong indication the transmitter code has never been tested with the tank circuit. Also, the transmitter process blew after 1 second of enabling the DC to DC power converter. This might be a hardware or firmware issue or both. This will require additional research and testing.

Receiver

There are a number of possible reasons the receiver code might not work as intended and possibly considerable development time will be required to get the receiver code to function as intended.

- Receiver success depends on the hardware, especially receive coils and bucking coil, if this hardware does not perform as designed then the receiver will not work, not to mention all the other unknowns, D&I, Memory Tool, Wireline interface etc.
- No specifications provided for the actual data and format required for the model. This issue is related to lack of tool calibration provisions.
- Bucking coil implementation is incomplete and most likely based on incorrect assumptions.

A.4. Development of Requirement Specification Document for Recommended Tool Redesign

The existing design for the Induction Tool transmitter and receiver electronics and firmware is insufficient and incomplete. Major design issues include:

- The transmitter DC to AC coil driver circuitry lacks sufficient output power to generate the requisite dipole moment for the medium and long spaced coil measurements (refer to Section 0 for details).
- The hardware and firmware infrastructure to support the tool orientation functionality is incomplete.
- The transmitter and receiver source code contains numerous errors and omissions and will require additional design, validation, and testing.

Overall, our analysis has found that the electronics and firmware for the existing Gearhart design are incomplete and contain fundamental flaws that will be difficult to remediate without substantial changes to the basic system architecture.

A.4.1. Recommended Tool Electronic Design

ESTI recommends that a new system architecture be adopted to correct the large number of deficiencies inherent in the existing tool design. Figure A.7 shows a system level functional block diagram of the revised Induction Tool electronic infrastructure. The revised tool will consist of three primary electronic modular elements:

- Orientation Module
- Transmitter Module
- Receiver Module (used for short, medium, and long spaced readings)

The following sections describe the functional details of each module. Refer to Section 4.20 for the specific mechanical package details for each module.

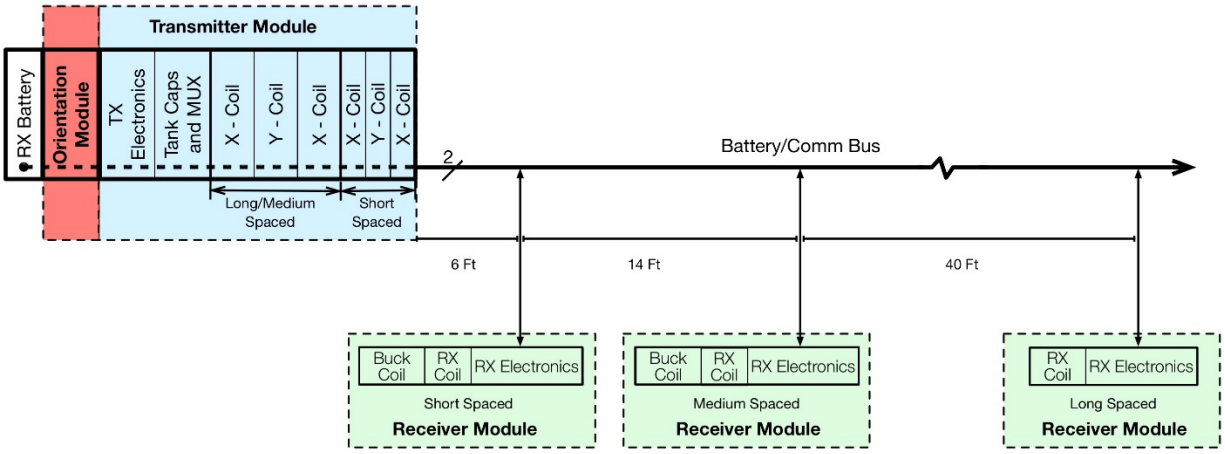

Figure A.7: Induction Tool Electronic Module Block Diagram.

A.4.1.1.1. Orientation Module

The Orientation Module provides a means for determining the downhole spatial orientation of the Induction Tool, and thus, can be used to determine the orientation of transmitter and receiver coils with respect to the rock matrix being imaged. The Orientation Module will consist of an off-the-shelf directional package, supplied by a third-party vendor, which will provide digitized values of inclination, azimuth, tool-face angle, temperature, total gravitational field and total magnetic field. The Orientation Module will interface to the Transmitter Module CPU via a standard TTL serial interface. There are many third-party vendors that offer industry-standard, MWD style directional module packages.

A.4.1.1.2. Transmitter Module

Figure A.8 shows a block diagram of the Transmitter Module electronics. The Transmitter Module electronics consist of the following functional blocks:

- CPU
- Coil-driver Power Supply
- Wireline communications interface
- Tank Capacitor Module
- Transmitter coil multiplexer
- Long and short spaced transmitter coils (not shown in Figure A.8)
- Receiver Module interface

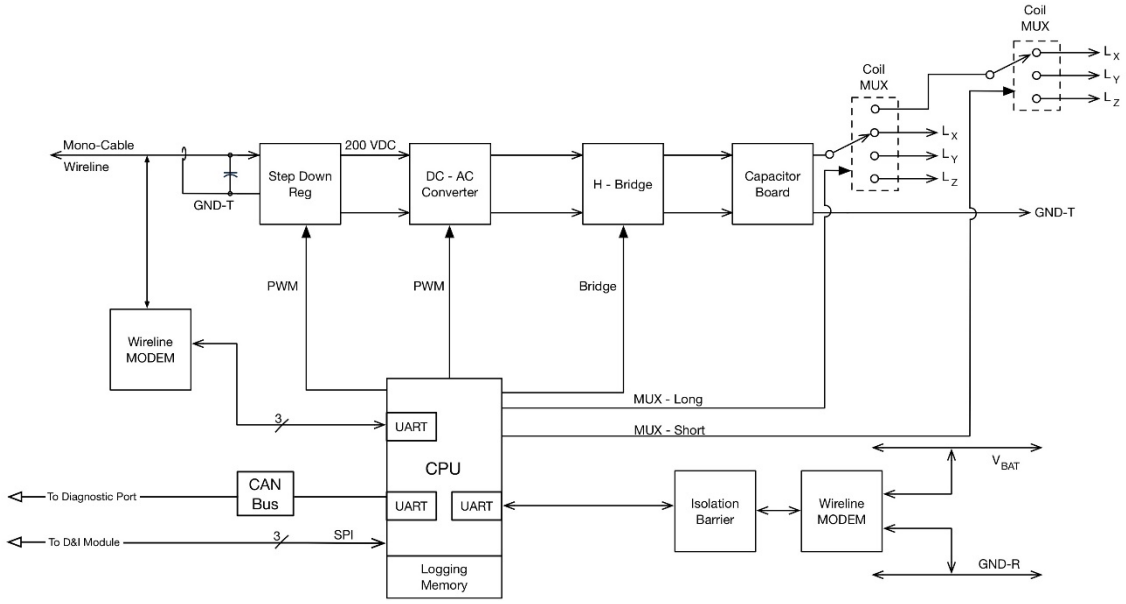

Figure A.8: Transmitter Module Block Diagram.

A.4.1.1.2.1. CPU

The Central Processing Unit (CPU) is the digital control element for the Transmitter Module. The basic element of the CPU block will be a highly integrated, high performance microcontroller. The microcontroller will provide a diverse peripheral component set and will provide access to 1Mbyte of logging memory (off-chip).

A.4.1.1.2.2. Coil-driver Power Supply

Refer to Section 0 for coil-driver power supply details.

A.4.1.1.2.3. Wireline Communications Interface

The communications interface block is an off-the-shelf wireline modem, supplied by a third-party vendor, which provides a mechanism for communicating with the surface controller via modulated signals coupled to the single conductor mono-cable power line.

A.4.1.1.2.4. Tank Capacitor Module

Refer to Section 0 for tank capacitor module details.

A.4.1.1.2.5. Coil Multiplexer

The coil multiplexor is used to sequentially connect the coil-driver power supply to x,y,z transmitter coils. The coil multiplexer will be a solid-state mux, consisting of high-temperature, high-voltage, silicon carbide junction FETs. Note that the same type of HT-FET will be used in the coil-driver power supply circuitry.

A.4.1.1.2.6. Long and Short-spaced Transmitter Coils

As described in Section 0, a separate set of transmit coils will be required for the short-spaced induction measurement.

Table A.13 shows the specification details for the short-spaced transmitter coil.

Magnetic Moment	15.8 Am^2
Inductance	5853 μH
Coil resistance	0.2 Ω
Total # coil windings	1680
Parallel coil count	8
Coil diameter	3.8 “
Coil length	2 “
Coil Area	0.005027 m^2
Coil winding current (for dipole moment)	1.58 Arms
Resonant frequency	100 Hz
Tank Capacitor	433 μF

Table A.13: Short-spaced Coil Specification.

Note that the tank circuit capacitance for the short-spaced transmitter coil set is different than that of the long-spaced coil tank. It is possible that the long-spaced capacitor module could be tapped to provide capacitance for both the short and long spaced tanks.

A.4.1.1.2.7. Receiver Module Interface

In order to minimize the conducted transmitter noise within the tool, a replaceable lithium thyonal chloride battery will be used to power the receiver modules. The battery will provide power to the receivers via a mono-cable bus wire which extends the length of the tool. Communications between the Transmitter Module and the Receiver Modules will be facilitated via modulated signals coupled to the single conductor mono-cable battery bus line

A.4.1.1.3. Receiver Module

Figure A.9 shows a block diagram of the Receiver Module electronics. The Receiver Module electronics consist of the following functional blocks:

- CPU
- Coil signal conditioning
- Wireline communications interface

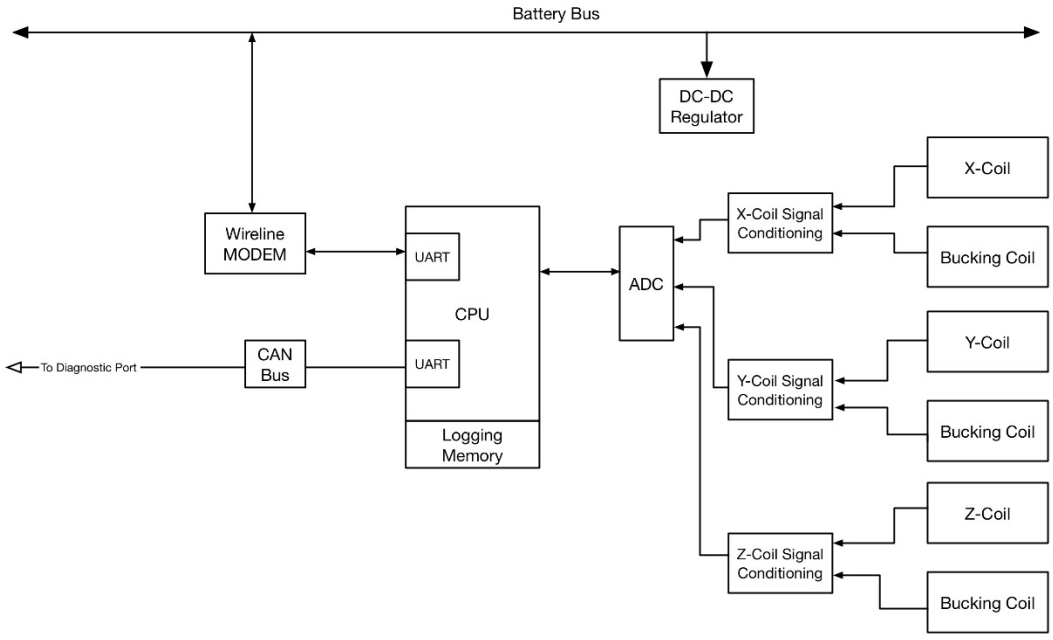

Figure A.9: Receiver Module Block Diagram.

A.4.1.1.4. CPU

The Central Processing Unit (CPU) is the digital control element for the Receiver Module. The basic element of the CPU block will be a highly integrated, high performance microcontroller. The microcontroller will provide a diverse peripheral component set, and will provide access to 1Mbyte of logging memory (off-chip).

A.4.1.1.4.1. Coil Signal Conditioning

The coil signal conditioning block provides noise filtering and gain to the received signal. Note that it is anticipated that the long-spaced Receiver Module will not require bucking coils.

A.4.1.1.4.2. Wireline Communications Interface

The communications interface block is an off-the-shelf wireline modem, supplied by a third party vendor, which provides a mechanism for communicating with the Transmitter Module via modulated signals coupled to the single conductor mono-cable battery bus line.

A.4.2. Recommended Tool Mechanical Design

The existing Gearhart mechanical design for the Induction Tool is insufficient and incomplete. Major design issues include:

- Lack of details regarding field assembly and deployment of tool.
- Incomplete pressure compensation methods regarding the design of the non-metallic sections of the tool.
- Insufficient detail on inter-module tool wiring.
- Incomplete drawing set including missing dimensions and material specifications. Note that very few, if any, of the machine drawings are machine shop ready.
- Seal designs are not fully defined, and provisions for anchoring the electronic backbones are not included.
- No methods for protecting the coil assemblies from wellbore fluids and wall abrasion are provided.

A new conceptual design for the Induction Tool is proposed as shown in Figs.
Figure A.10,
Figure A.11 and Figure A.12. This design builds on the basic layout of the Gearhart design, but addresses major requirements and design challenges not previously addressed. The following assumptions were used in developing this new design:

1) The induction tool will be run on e-line coiled tubing without the use of a downhole tractor.
2) A horizontal orientation of the tool during operation is normal, but the tool must operate in any orientation, from vertical to horizontal.
3) The long-range x, y, and z transmit coils are each approximately 30 inches long in the tool's axial direction.
4) A separate short-range transmit coil assembly will be used to couple with the short-range receiver assembly.

5) The short- and long-range receiver coil assemblies will be placed at 6-, 20-, and 60-ft distances, respectively, from the transmit coils.

6) The maximum diameter of any section of the tool is 4 inches.

Starting at the top of the tool, on the left side of

Figure A.10, is the Rolling Tubing Head, which attaches the induction tool to the coiled tubing. In addition to serving as the attachment point for the tool, this head serves as a bulkhead for the Receiver Battery Pressure Barrel and has built-in rollers that facilitate movement of the tool in a horizontal borehole. Sliding the tool without rollers could significantly abrade tool surfaces and compromise the life of the tool. Placing rollers at strategic points along the tool's entire length would minimize tool abrasion, reduce emplacement friction, and allow the tool to be inserted farther into a horizontal wellbore for a given weight string above the tool.

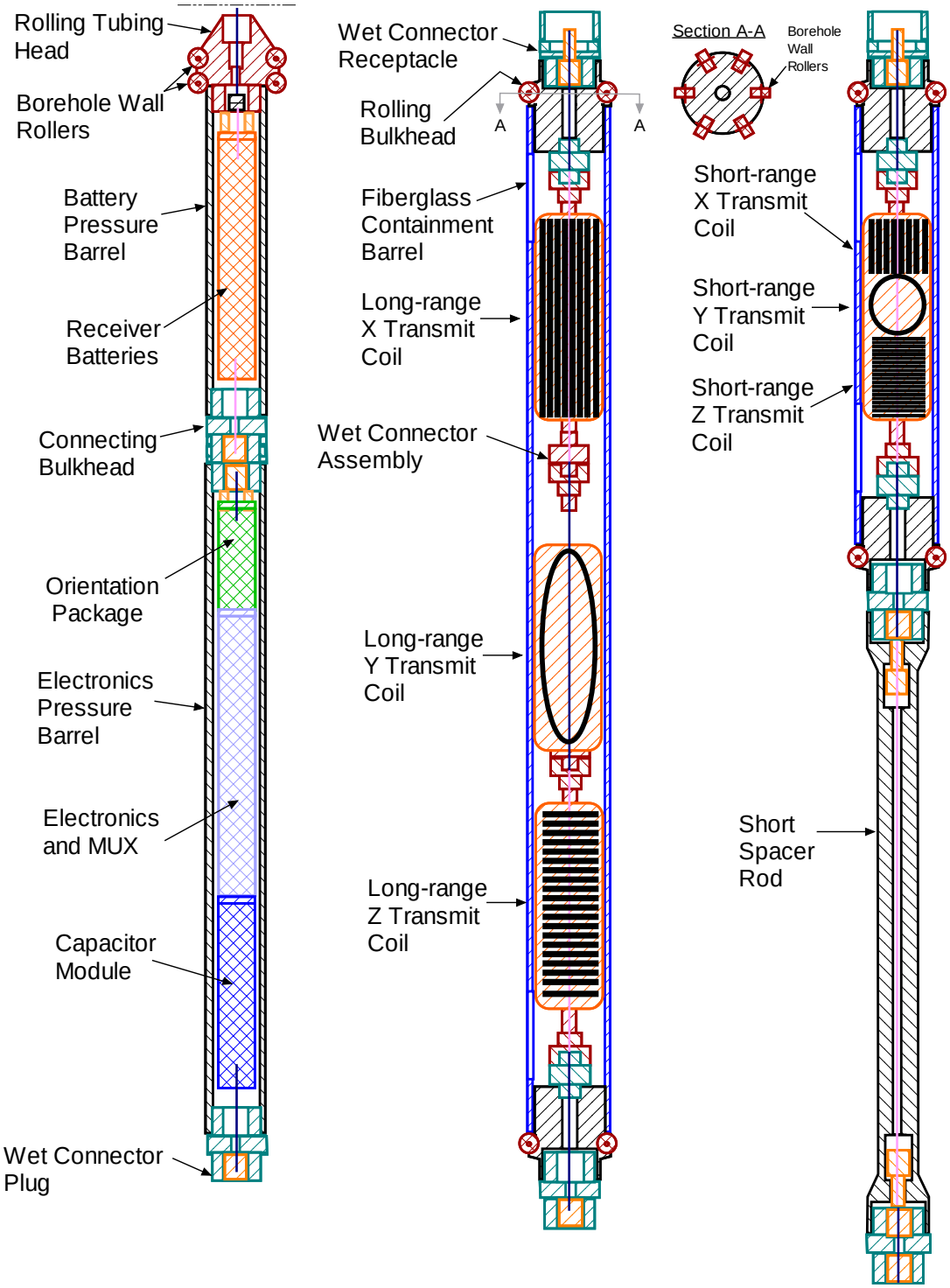

Figure A.10: Top three sections of proposed UT Induction Tool.

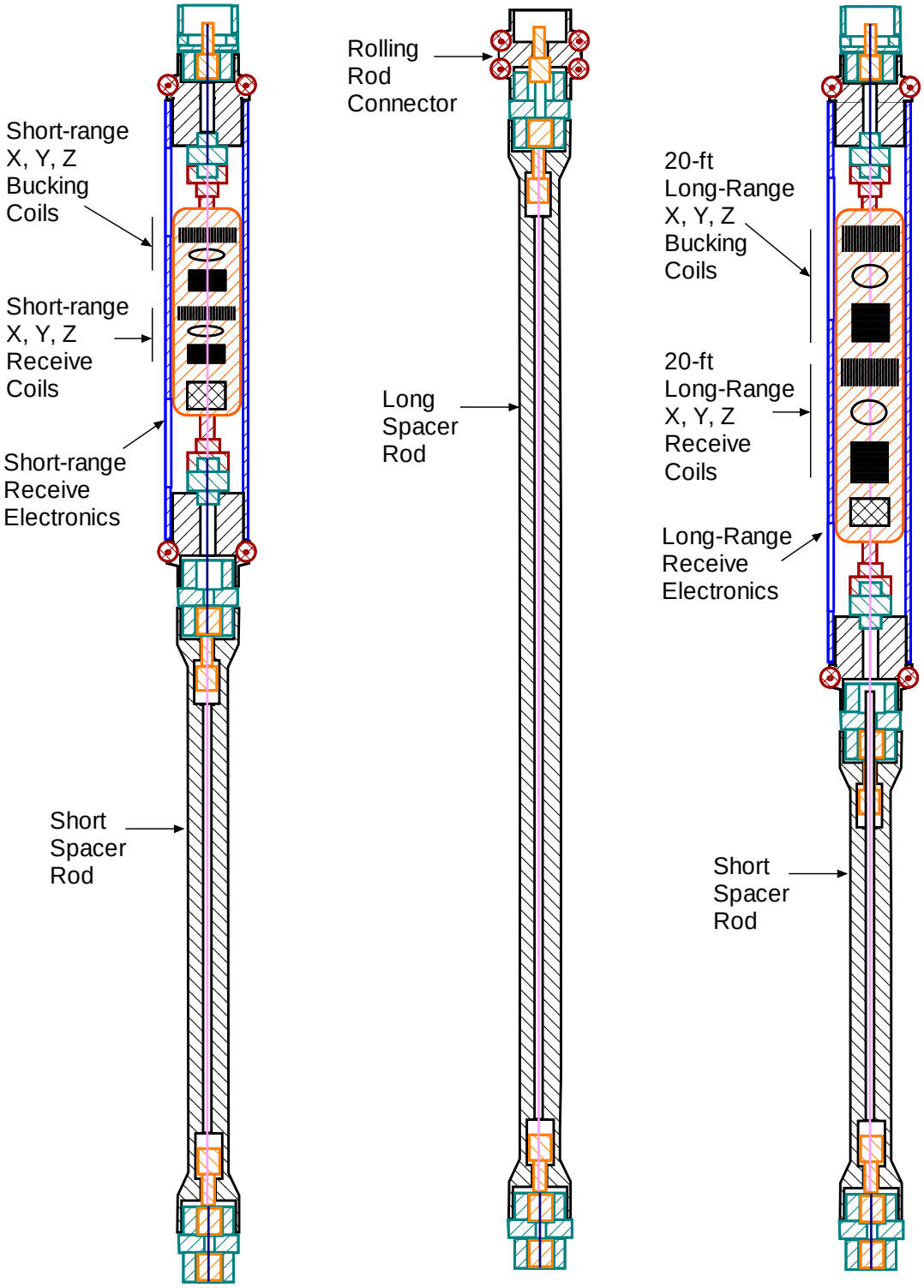

Figure A.11: Middle three sections of proposed UT Induction Tool.

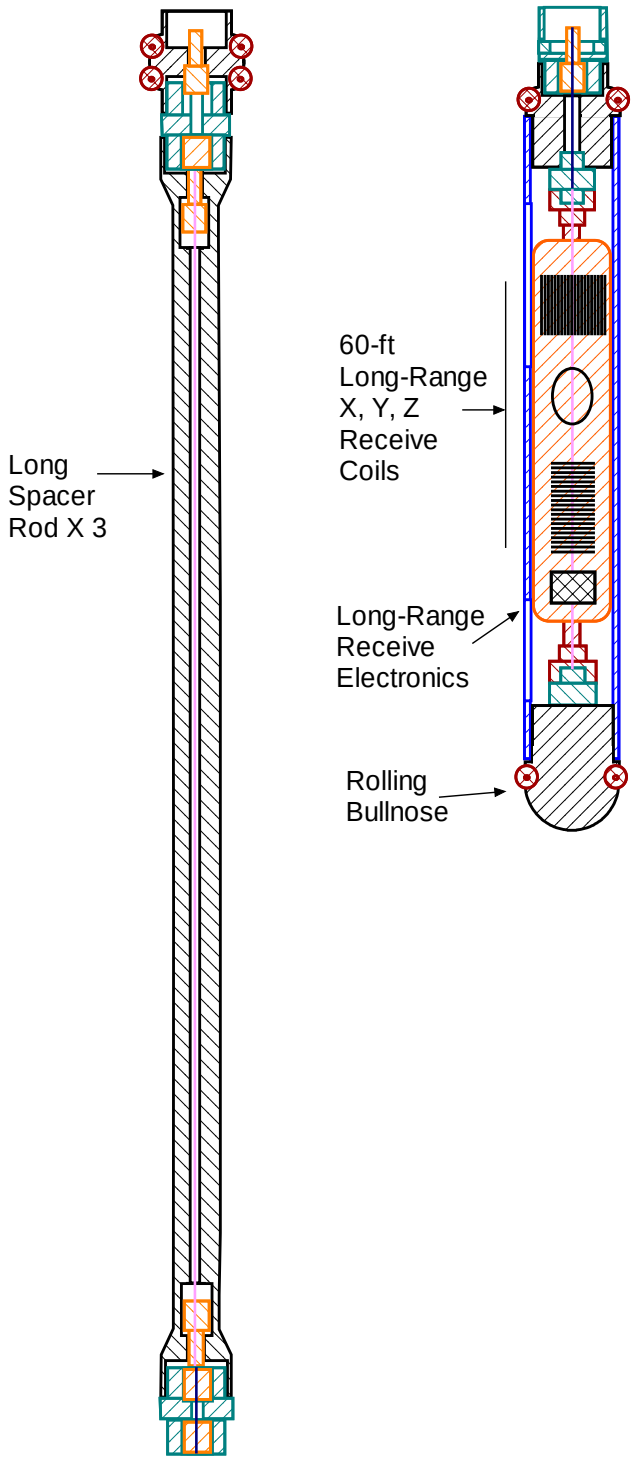

Figure A.12: Lower four sections of proposed UT Induction Tool.

The Receiver Battery Pressure Barrel is a pressure housing containing the Receiver Batteries, which provide power for the three Receiver Modules. Note that the receiver battery is housed in a separate pressure housing in order to allow for the receiver battery to be easily replaced in the

field. The Orientation Module, transmitter electronics, tank capacitor, and transmitter coil mux are housed in the Transmitter Module pressure housing. The pressure barrels, bulkheads and electronics all contain a significant amount of metal but will be located uphole of both the transmitting and receiving coils. This will cause a small and well-characterized perturbation to the portions of the magnetic fields measured with the receive coils.

Closing off the bottom of the Transmitter Module pressure barrel is a bulkhead incorporating a Wet Connector Plug, which mates with the Wet-Conductor Receptacle to form a sealed, multi-conductor electrical connector as well as a pressure-tight mechanical connection to the rest of the tool.

The next tool section houses the Long-Range x, y, and z Transmit Coils. Each coil is potted in a sealed container made of non-metallic, non-conductive, non-magnetic material such as plastic and/or fiberglass. Because of the high downhole pressures to be encountered and the relatively low strengths of plastic and fiberglass, the design of the containers will need to incorporate some sort of pressure compensation system that transfers the container stresses from its shell to its contents. As envisioned in the concept of

Figure A.10, this pressure compensation function would result from potting the coil inside a flexible, but volumetrically incompressible material such as EPDM (a high-temperature, rubber-like material). Assuming all vacant spaces within such a volume are filled with potting material, subjecting the resulting pod to elevated hydrostatic pressures would not cause it to deform, nor would wellbore fluid be able to force its way inside.

Wiring from and through each coil pod terminates inside a wet connector assembly, which connects each pod with its uphole and downhole neighbors. The Fiberglass Containment Barrel serves to hold the coil pods in place and protect them from the abrasive wellbore wall. Pressure relief vents in the containment barrel ensure that the pressure inside the barrel is equal to that in the wellbore, thereby relieving the containment barrel from differential pressure stresses.

Another approach to pressure compensation around the coil assemblies would be to use a sealed Fiberglass Containment Barrel and fill the vacant volume inside the barrel with a non-conductive liquid, such as mineral oil. In this case, bellows or a spring-loaded piston and cylinder system would be needed to maintain inside liquid pressure at a level near the wellbore pressure so that the containment barrel is not overstressed. Such a pressure compensation system must respond to not only changes in wellbore pressure but also to thermal expansion of the non-conductive liquid as it heats up. Previous experience in designing such systems suggests that using a non-conductive liquid in this tool would greatly increase the complexity of the tool and its operation in the field. However, it would have the advantage that heat from the large transmit coils would be more effectively removed by the non-conductive liquid than by a solid potting material. It is possible that the optimal approach would be to use a liquid-filled pressure compensation system for the transmit coils and a solid-potting system for the receive coil assemblies and spacer rods.

Next in line is the short-range transmit coil assembly. This assembly is similar to that of the long-range coils, but conceivably much smaller since the short-range coils will not deliver as much power. If a liquid-filled pressure compensation system is used, the long- and short-range coil assemblies could be located in the same pressure-compensated housing.

The Transmitter Module and short-spaced Receiver Module are separated by a Short Spacer Rod, which is an extension rod carrying the mono-cable wire bus that connects the Receiver

Modules to the receiver battery and Transmitter Module wireline modem. Since the spacer rods must be constructed of non-conductive, non-magnetic materials, a solid-potted pressure compensation design is foreseen for these parts. Wet connector assemblies would be built into the ends of the spacer rods to facilitate assembling the tool in the field.

Figure A.11 continues the tool assembly with the short-range Receiver Module, followed by another short spacer rod, a long spacer rod, and the 20-ft mid-range Receiver Module. At the top end of every long spacer rod is a Rolling Rod Connector, which connects two spacer rods together and provides a 4-inch diameter platform that both centralizes the rods and allows them to roll freely along the wellbore wall.

Next, another Short Spacer Rod and three Long Spacer Rods are connected together, followed by the 60-ft long-range Receiver Module. The rolling bull nose at the bottom of the 60-ft Receiver Module and, all the borehole wall rollers along the length of the tool facilitate emplacement of the induction tool in a long section of horizontal borehole.

A.4.2.1. Proposed Tool Assembly Procedure

The overall length of the proposed design is at least 75 ft. Even with a crane that could lift the tool that high, it is doubtful that a 4-inch diameter tool of that length could be successfully transitioned to a vertical position if it were assembled horizontally on the ground. It is, therefore, proposed that the induction tool be assembled in pieces at the wellhead.

A slotted plate can be used to catch a narrowed neck at the top of each tool section as that section is lowered into the wellbore. The slotted plate, resting on the top of the wellhead valve, would hold that tool section while the next tool section is lowered on top and connected. The slotted plate would then be removed, the tool lowered further into the well, and the process repeated until all sections of the tool were assembled in the top of the well. The slotted plate would then be used to hold the tool while the BHA and coil tubing are connected to the top of the tool. A reverse process would be used to remove the tool from the well, breaking the tool down in pieces and laying them down one section at a time.

A.5. Analysis and Modification of Gearhart Coil Design Model

The Gearhart Company had developed a detailed model (implemented in Excel spreadsheet format) used to design the receiver and high-power transmitter coils. This model was analyzed and found to contain several basic design issues and calculation errors including:

- Model did not account for the thickness of the wire insulation in coil diameter calculation.
- Coil power calculation was incorrect.
- A wire gauge user input was added to the model to make wire gauge effect analysis easier to calculate
- Model was modified so coil physical parameters would automatically be applied to all analysis result screens throughout the user interface.

A.6. COIL CONSTRUCTION AND TESTING TO VALIDATE GEARHART COIL DESIGN MODEL

To validate the modified coil design model, a coil design for a small transmit coil was input and the resulting calculations were used to build a prototype coil. This transmit coil was fabricated and bench tested (using the procedure described in the following section) and the empirical test results were found to match those predicted by the model.

Once the model was validated a 150 Am2, 100Hz transmitter coil was designed and fabricated and tested using the existing Gearhart receiver coils. Note that this transmitter coil design became the precursor for the 1000Hz design developed under the "Enhanced Extremely Low Frequency Tri-axial Induction Tool for Fracture Diagnostics in Open Wellbores" Phase I work conducted under DOE Award Number DE-SC0015774.

Coil Bench Testing setup

Equipment List

- Tektronix MSO2024 Mixed Signal Oscilloscope
- Model 3100D audio power amplifier
- FJW 50BR-001 Switched Attenuator
- Wavetek Function Generator
- Fluke 80i-110s Current Probe

Block Diagram

Figure A.13 shows the coil bench testing setup.

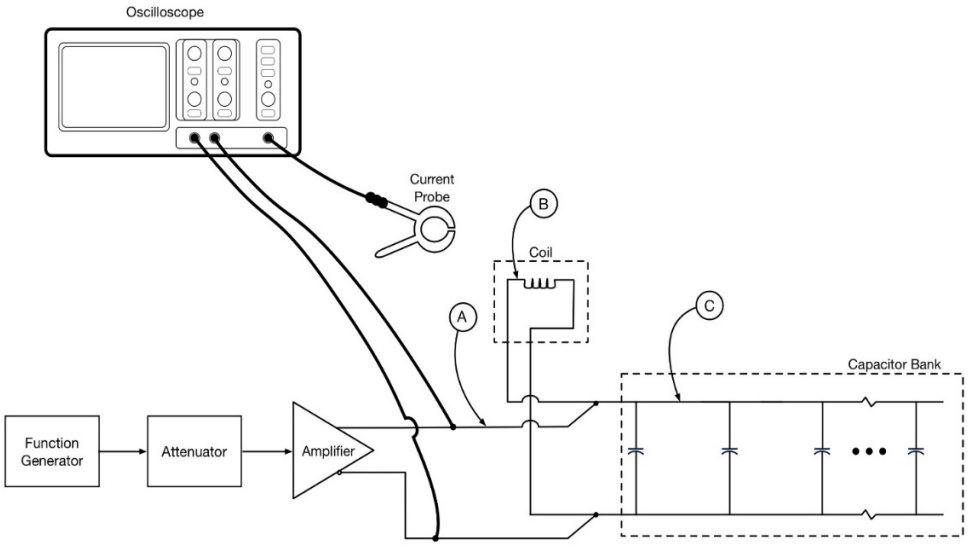

Figure A.13: Coil Bench Test Setup.

Test Procedure

Tank Circuit Resonant Frequency

1) Connect the tank circuit to test equipment according to Figure A.13.
2) Set function generator for sinusoidal output. Set function generator to 100Hz and adjust output level (may have to use attenuator) to get a moderate level of current in the tank circuit, around 20A.
3) Connect current probe to coil wire (Point B).
4) While measuring the current probe signal on the oscilloscope, adjust the function generator frequency to get maximum coil current.
5) Record the frequency at maximum coil current. This is the resonant frequency of the tank circuit.

Tank Circuit Current and Phase Angles

1) Connect the tank circuit to test equipment according to Figure A.13.
2) Set function generator for sinusoidal output. Set function generator to the resonant frequency and adjust output level (may have to use attenuator) to produce the desired tank circuit current. This may be limited by the output voltage or power of the amplifier and available AC input power. Also, be aware that coil will become very hot at moderate power.
3) Connect the one current probe to the signal input wire (Point A).
4) Measure and record the source voltage amplitude on the oscilloscope probe inputs.
5) Measure and record the source current amplitude on the current probe input.
6) Using the oscilloscope cursers, measure and record the phase angle between the voltage and current waveforms. By definition, the voltage is the reference phase and is phase angle 0.
7) Connect the current probe to the coil wire (Point B).
8) Measure and record the coil current amplitude on the current probe input.
9) Using the oscilloscope cursers, measure and record the phase angle between the source voltage and coil current waveforms.
10) Connect the current probe to the capacitor wire (Point C).
11) Measure and record the capacitor current amplitude on the current probe input.
12) Using the oscilloscope cursers, measure and record the phase angle between the source voltage and capacitor current waveforms.
13) Using the oscilloscope cursers, measure the total cycle period (in milliseconds). Use this value to compute the phase angles in degrees.